Discrete Element Modeling of the Mechanical Response of Cemented Granular Materials

by:

Pu Yang

A Dissertation Presented in Partial Fulfillment
of the Requirements for the Degree
Doctor of Philosophy

Approved October 2018 by the
Graduate Supervisory Committee:

Narayanan Neithalath, Chair
Edward Kavazanjian
S. D. Rajan
Barzin Mobasher
Yang Jiao

ARIZONA STATE UNIVERSITY

December 2018

ABSTRACT

With the growth of global population, the demand for sustainable infrastructure is significantly increasing. Substructures with appropriate materials are required to be built in or above soil that can support the massive volume of construction demand. However, increased structural requirements often require ground improvement to increase the soil capacity. Moreover, certain soils are prone to liquefaction during an earthquake, which results in significant structural damage and loss of lives. While various soil treatment methods have been developed in the past to improve the soil's load carrying ability, most of these traditional treatment methods have been found either hazardous and may cause irreversible damage to natural environment, or too disruptive to use beneath or adjacent to existing structures. Thus, alternative techniques are required to provide a more natural and sustainable solution. Biomediated methods of strengthening soil through mineral precipitation, in particular through microbially induced carbonate precipitation (MICP), have recently emerged as a promising means of soil improvement. In MICP, the precipitation of carbonate (usually in the form of calcium carbonate) is mediated by microorganisms and the process is referred to as biomineralization. The precipitated carbonate coats soil particles, precipitates in the voids, and bridges between soil particles, thereby improving the mechanical properties (e.g., strength, stiffness, and dilatancy). Although it has been reported that the soil's mechanical properties can be extensively enhanced through MICP, the micro-scale mechanisms that influence the macro-scale constitutive response remain to be clearly explained.

The utilization of alternative techniques such as MICP requires an in-depth understanding of the particle-scale contact mechanisms and the ability to predict the improvement in soil

properties resulting from calcite precipitation. For this purpose, the discrete element method (DEM), which is extensively used to investigate granular materials, is adopted in this dissertation. Three-dimensional discrete element method (DEM) based numerical models are developed to simulate the response of bio-cemented sand under static and dynamic loading conditions and the micro-scale mechanisms of MICP are numerically investigated. Special focus is paid to the understanding of the particle scale mechanisms that are dominant in the common laboratory scale experiments including undrained and drained triaxial compression when calcite bridges are present in the soil, that enhances its load capacity. The mechanisms behind improvement of liquefaction resistance in cemented sands are also elucidated through the use of DEM. The thesis thus aims to provide the fundamental link that is important in ensuring proper material design for granular materials to enhance their mechanical performance.

Dedicated to my parents and my wife for their support and encouragement

ACKNOWLEDGMENTS

I would like to specially acknowledge my advisor Dr. Narayanan Neithalath for guiding me throughout my dissertation work and helping me to overcome all the challenges and develop innovative ideas. The dissertation work would never have been accomplished without his timely and patient support and suggestions. I would like to thank my committee members: Dr. Kavazanjian, Dr. Rajan, Dr. Mobasher and Dr. Jiao for dedicating their guidance to my dissertation work.

I would also like to express my gratitude to my dear colleagues and friends, Yiming, Sumanta, Akash, Matt, Aashay, Naman, Sooraj, Hussam, Kirk, Ben, Swaptik, Ahmet for their help and support.

I would like to express my most sincere gratitude to my wife and my parents, for their love, encouragement and support.

TABLE OF CONTENTS

Page

LIST OF TABLES xi

LIST OF FIGURES xiii

1. INTRODUCTION 1

1.1. Objectives 2

1.2. Dissertation Layout 3

2. LITERATURE REVIEW 6

2.1. Background of Discrete Element Method (DEM) 6

2.1.1. Available Resources of DEM Solvers 7

2.1.2. General Modeling Procedure 9

2.1.3. Contact Model Used to Simulate the Mechanical Behavior of Sands 11

2.1.4. Applications of DEM Models on Simulating the Behavior of Granular Materials 13

2.2. Bio-mediated Methods of Strengthening Soil Through Mineral Precipitation 14

2.3. Laboratory Tests to Determine the Mechanical Response of Soil 18

2.3.1. Triaxial Compression Test 18

2.3.2. Direct Simple Shear Test 21

2.3.3. Cone Penetration Test 23

3. 3D DEM SIMULATIONS OF DRAINED TRIAXIAL COMPRESSION OF SAND STRENGTHENED USING MICROBIALLY INDUCED CARBONATE PRECIPITATION 25

3.1. Introduction 25

CHAPTER Page

3.2. Discrete Element Method (DEM) Modeling Framework for Triaxial Compression…. 27

3.2.1. Contact Law 28

3.2.2. Sphere Packing and Drained Triaxial Compression Simulation 31

3.3. Microscale Parameters, Their Relative Effects, and Model Calibration 33

3.3.1. Preliminary Simulations 34

3.3.2. Influence of Microscale Parameters (kn, ks, μ, β and η) 37

3.4. Numerical Simulation of the Constitutive Response of Sand Strengthened Using MICP Under Consolidated Drained Triaxial Compression 43

3.4.1. Simulation of MICP Strengthened Sand Containing Low Calcite Contents (~0.5% by mass) 44

3.4.2. Simulation of MICP Strengthened Sand Containing High Calcite Contents (> 1% by mass) 47

3.5. Summary and Conclusions 54

4. PARTICLE-SCALE MECHANISMS IN UNDRAINED TRIAXIAL COMPRESSION OF BIO-CEMENTED SANDS: INSIGHTS FROM 3D DEM SIMULATIONS WITH FLEXIBLE BOUNDARY 57

4.1. Introduction 57

4.2. Numerical Modeling Using Discrete Element Method (DEM) 59

4.3. Simulation of Undrained Triaxial Response of Saturated Sand 63

4.3.1. Simulation with Rigid Boundaries 63

4.3.2. Simulation with Flexible Boundaries 68

CHAPTER Page

4.3.3. Comparison Between Simulated Results Under Different Boundary Conditions 72

4.4. Simulating Undrained Triaxial Compression Test of MICP-Strengthened Sand 76

4.5. Summary and Conclusions 86

5. DISCRETE ELEMENT SIMULATIONS TO PREDICT RESPONSE OF UNCEMENTED AND CEMENTED SANDS: INFLUENCE OF MATERIAL AND TEST PARAMETERS, AND BOUNDARY CONDITIONS 89

5.1. Introduction 89

5.2. Mathematical Background 91

5.2.1. A Brief Overview of the Discrete Element Method 91

5.2.2. Contact Law 93

5.2.3. The Pore-scale Finite Volume (PFV) Method 95

5.2.4. PFV-DEM Coupling 98

5.3. Simulation of Triaxial Compression of Uncemented and Lightly Cemented Sands Using Rigid Boundaries with and without PFV Coupling 98

5.3.1. Classical DEM Method 99

5.3.2. Coupled PFV-DEM Method 100

5.3.3. Comparison of Response from both the Methods 101

5.4. Simulation of Triaxial Compression of Cemented Sands Using Flexible Boundaries 104

5.4.1. Introducing PFacet-based Flexible Membrane 105

CHAPTER Page

5.4.2. Simulating Undrained Triaxial Compression of Cemented Sands Under Different Confining Stress Levels 106

5.4.3. Simulating Unconfined Compressive Strength (UCS) Test of Bio-Cemented Sand…… 112

5.4.4. Simulating the Response of Multi-Phase Particulate Systems: A Preliminary Investigation 115

5.5. Summary and Conclusions..... 122

6. DEM SIMULATIONS ON THE INFLUENCE OF CARBONATE PRECIPITATION ON LIQUEFACTION MITIGATION OF SAND 125

6.1. Introduction..... 125

6.2. Simulating the Cyclic Direct Simple Shear (DSS) Test Using DEM 128

6.2.1. General Modeling Process for Shear Box and Stacked Ring DEM Tests 129

6.2.2. Comparing the Performance of the Shear Box and Laminar Wall DEM Models… 132

6.2.3. 3D Shear Box Model Validation Using Cyclic DSS Test of Fraser River Sand…… . ……136

6.2.4. Criteria for Determining the Onset of Liquefaction 139

6.3. DEM Simulations of Sands Strengthened Using Carbonate Precipitation 140

6.3.1. DEM Model Parameter Identification for Cyclic DSS Simulation of MICP-Cemented Sands 142

6.3.2. Simulating Cyclic DSS Test of Cemented and Reconstituted Sands 146

6.4. Summary and Conclusions..... 152

CHAPTER Page

7. A PRELIMINARY STUDY ON THE CONE PENETRATION TEST (CPT) WITH DISCRETE ELEMENT METHOD (DEM) 154

7.1. Introduction 154

7.2. Preliminary Study with 2D DEM Model 155

7.2.1. Particle Packing and Model Preparation 156

7.2.2. Influence of Penetrometer Advance Speed 158

7.2.3. Influence of Cone-diameter to Particle-size Ratio 159

7.2.4. Influence of Boundary Conditions 161

7.3. Conclusions and Future Work 163

8. PREDICTING THE MECHANICAL RESPONSE OF ULTRA-HIGH PERFORMANCE CONCRETE (UHPC) WITH DISCRETE ELEMENT METHOD (DEM) 165

8.1. Introduction 165

8.2. DEM Methodology 166

8.2.1. Contact Model 167

8.2.2. Preparing the Numerical Particle Packing 169

8.3. Simulating the Mechanical Performance of UHPC 170

8.3.1. Calibrating the Contact Model Using Compression and Flexure Results 170

8.3.2. Predicting the Tension Behavior 177

8.4. Summary and Conclusions 180

9. CONSCLUSIONS AND FUTURE WORK 181

9.1. Conclusions 181

CHAPTER Page

9.2. Future Work 183

REFERENCES 186

APPENDIX

A. PYTHON SCRIPT FOR SIMULATING UNDRAINED TRIAXIAL COMPRESSION TEST WITH FLEXIBLE MEMBRANE..... 205

LIST OF TABLES

Table Page

3.1: DEM parameters used to simulate the macroscale response of Labenne sand reported by Belheine et al. (2009). 35

3.2: Summary of the 2^3 factorial design to evaluate the influence of the microscale rupture parameters μ, β and η on the stress-strain response of the DEM simulation 40

3.3: DEM parameters used to simulate the macroscale response of Karlsruhe sand reported by Widuliński (2009). 43

3.4: DEM parameters used to simulate the macroscale response of untreated and treated Ottawa 50/70 sand reported by Montoya and DeJong (2015). 46

3.5: DEM parameters used to simulate the macroscale response of untreated and treated Ottawa 50/70 sand reported by Feng and Montoya (2015a)..... 50

3.6: Comparison of friction angle between DEM simulation and experimental results... 54

4.1: DEM parameters used to simulate the macroscale response of untreated and treated Ottawa 50/70 sand under undrained triaxial compression (Montoya and DeJong 2015). 66

4.2: DEM parameters used to simulate the macroscale response of untreated and treated Ottawa 50/70 sand reported by (Montoya and DeJong 2015). 77

5.1: DEM parameters used to simulate the drained/undrained triaxial compression test of plain and lightly cemented sands. 101

5.2: DEM parameters used to simulate the undrained triaxial compression test. 107

5.3: DEM parameters used to simulate the UCS test. 114

5.4: DEM parameters used to simulate the undrained triaxial compression test of the virtual specimen. 118

Table Page

5.5: Simulation parameters: variation in cohesive strength of particle types. 120

5.6: Simulation parameters: variation in volume fraction of particle types..... 122

6.1: DEM parameters used to simulate the Fraser River sand (Wijewickreme et al. 2005). 134

6.2: DEM input parameters used to simulate the macroscopic response of cyclic DSS tests. 145

7.1: Geometries information and material properties used for simulation. 157

8.1: Parameters used in DEM simulations..... 172

LIST OF FIGURES

Figure Page

2.1: Typical interaction loop of DEM simulations (Šmilauer et al. 2018). 11

2.2: Two spheres in contact, showing the normal (Fn) and tangential (Fs) contact force vectors, the contact moment vector (M) and the unit normal vector (n). 12

2.3: SEM images showing calcite carbonate precipitation (a) on the soil particle surface (Kavazanjian and O'Donnell 2015a) and (b) concentrated at particle contacts (Li 2015) 15

2.4: General set-up of a soil specimen inside a triaxial cell (Rees 2013). 18

2.5: Typical response obtained from a CU test of dilatant soil. 20

2.6: Typical apparatus for direct simple shear test: (a) Cambridge DSS device (Roscoe 1953), (b) NGI DSS device and (c) modified NGI-type DSS device (Li et al. 2016) 22

2.7 : Typical response of soil under cyclic DSS test: (a) cyclic stress-path and (b) stress-strain response (Wijewickreme et al. 2005). 23

2.8 : A schematic plot of in-filed cone penetration test and the ingredients of cone penetrometer (Mayne 2007). 24

3.1: Two spheres in contact, showing the normal (Fn) and tangential (Fs) contact force vectors, the contact moment vector (M) and the unit normal vector (n). 29

3.2: (a) Initial volume of spherical particles with random positions, (b) virtual specimen after radii expansion with desired void ratio and confining stress, (c) virtual specimen with deviator loading and (d) distribution of internal forces in the virtual sample. 32

3.3: Typical response obtained from a drained triaxial compression test of dilatant sand. 33

Figure Page

3.4: Comparison of DEM simulation (solid lines) to experimental data points for deviator stress-axial strain and volumetric strain-axial strain response of Labenne sand (Belheine et al. 2009). 35

3.5: (a) Influence of number of particles, and (b) influence of the initial randomization of particles on deviator stress-axial strain and volumetric strain-axial strain response of Labenne sand (Belheine et al. 2009). 37

3.6: Influence of: (a) normal stiffness kn, and (b) stiffness ratio α on the elastic modulus E_0 and Poisson's ratio ν of Labenne sand in drained triaxial compression from DEM simulations. 38

3.7: (a) Deviator stress versus axial strain and (b) volumetric strain versus axial strain for the DEM simulations summarized in Table 3.2..... 41

3.8: Effect of local friction angle on: (a) deviator stress-axial strain and (b) volumetric strain-axial response for DEM simulations of Labenne sand in drained triaxial compression. 42

3.9: Comparison of DEM simulation (solid lines) to experimental data for macroscale response of Karlsruhe sand reported by Widuliński (2009). 43

3.10: Calcite cladding the surface of a sand grain after microbial treatment (Kavazanjian and O'Donnell 2015a)..... 45

3.11: Comparison of DEM simulation (solid line) to experimental data for the deviator stress-axial strain and volumetric strain-axial strain response of untreated and treated (calcite content = 0.6% by mass) Ottawa 50/70 sand in drained triaxial compression reported by Montoya and DeJong (2015). 47

Figure Page

3.12: Calcite bridges between sand grains (Li 2015)..... 48

3.13: DEM simulation (solid lines) compared to experimental data from Feng and Montoya (2015a) for the deviator stress-axial strain and volumetric strain-axial strain response of MICP-modified Ottawa 50/70 sand (calcite content ≥ 0.9%)..... 51

3.14: Contact force distribution in the DEM simulation volume at 1% axial strain for: (a) untreated sand, and (b), (c), (d) MICP-modified sand with 0.9%, 3%, and 4.3% calcite by mass..... 52

3.15: Mohr circles for: (a) peak friction angle, and (b) residual friction angle extracted from the DEM simulation for untreated and MICP-modified sands. 53

4.1: Two spheres in contact, showing the normal (Fn) and tangential (Fs) contact force vectors, the contact moment vector (M) and the unit normal vector (n). 61

4.2: (a) Initial volume of spherical particles with random positions; (b) virtual specimen after radii expansion with desired void ratio and confining stress; and (c) deviator loading with constant volume method. 65

4.3: Deviator stress and excess pore pressure predicted by the DEM model (continuous lines) for uncemented sand and heavily cemented sand and its comparison with experimental data (symbols) from (Montoya and DeJong 2015). 67

4.4: (a) PFacet element, and (b) cylindrical membrane created using PFacet elements. Spheres form the vertices of the triangular facet and deformable cylinders, the sides..... 69

Figure Page

4.5: Flowchart depicting numerical simulation of undrained compression test using a flexible membrane boundary. (1): particle packing for desired porosity in a rigid container; (2): replacing the rigid container with a PFacet flexible membrane wall; (3) arriving at isotropic confinement, and (4) applying deviator loading and implementing the constant volume condition in every step. 70

4.6: Deviator stress and excess pore pressure predicted by the DEM models employing rigid or flexible boundaries, for uncemented sand and heavily cemented sand. The experimental data comes from (Montoya and DeJong 2015). In the legend, UT indicates untreated, and HT, heavily treated. 73

4.7: Force chains in highly cemented sand samples subjected to unconfined triaxial compression: (a) rigid boundary, (b) flexible membrane boundary. Line thickness and colors are indicative of contact force magnitude. 75

4.8: Strain localization predicted by the DEM model for heavily cemented sand: (a) rigid boundary, and (b) flexible membrane boundary. The red color represents the heavily rotated particles while light blue represent particles with a lower rotation degree. A tentative shear band is shown here; however this is by no means an accurate representation. This is used only for illustration. 76

4.9: Simulation of constitutive response of sand strengthened using different amounts of carbonates through MICP. The symbols indicate the experimental results and the continuous lines, the simulated response. The numbers next to the legend indicates the shear wave velocity through the samples. Experimental results from (Montoya and DeJong 2015). 78

Figure Page

4.10: Relationships between initial shear wave velocity (which is a function of the degree of cementation) and the shear stiffness of particles and cohesion bond strength between the contacted particles used in the simulations. Experimental values of shear wave velocity from (Montoya and DeJong 2015). 79

4.11: Particle rotations obtained from DEM simulations at different cementation levels: (a) untreated (UT190), (b) lightly treated (LT300), (c) moderately treated (MT450), (d) moderately treated (MT650), with likely conjugate shear banding and (e) heavily treated (HT1400), with a narrow shear band. Note that the shear band locations are determined from a visual observation since the use of 1000 particles for simulation is not enough to clearly delineate the shear bands. However one can easily discern the gradual localization from these figures as the cementation increases. 81

4.12: Force chains at 6% axial strain for specimens with different cementation levels: (a) untreated (UT190), (b) lightly treated (LT300), (c) moderately treated (MT450), (d) moderately treated (MT650), and (e) heavily treated (HT1400). 82

4.13: Evolution of force chains for lightly treated (low cementation, LT300) and heavily treated (high cementation, HT1400) specimens. 84

4.14: Average coordination number as a function of axial strain for the simulated samples. 86

5.1: Two spheres in contact, showing the normal (Fn) and tangential (Fs) contact force vectors, the contact moment vector (M) and the unit normal vector (n). 94

5.2: Tetrahedral element of the finite volume discretization (Chareyre et al. 2012). 96

5.3: Boundary conditions during the deviator loading stage for: (a) DEM simulation of drained triaxial compression test, (b) DEM simulation of undrained triaxial compression test, (c) coupled PFV-DEM simulation of drained triaxial compression test, and (d) coupled PFV-DEM simulation of undrained triaxial compression test..... 100

5.4: Comparison of DEM and PFV-DEM methods for: (a) drained triaxial compression test and (b) undrained triaxial compression test, for uncemented sands. 102

5.5: Comparison of DEM and PFV-DEM methods for: (a) drained triaxial compression test and (b) undrained triaxial compression test, for lightly cemented sands. Note that the data for (a) and (b) came from different sources. 102

5.6: Comparison of the computational cost (time) of DEM and PFV-DEM models for the drained and undrained compression tests on plain and lightly cemented sands. 104

5.7: (a) Geometric construction of PFacet element, (b) Sphere-PFacet contact and (c) Diagram representing decomposition of sphere-PFacet interaction. 105

5.8: Deviator stress and excess pore pressure predicted by DEM model under varying confining stresses. 107

5.9: Force chains at 0% axial strain for cemented sand specimens (~1% by mass of calcite) at different confining stresses: (a) 100 kPa, (b) 200 kPa and (c) 300 kPa. 109

5.10: Force chains at 6% axial strain for cemented sand specimens (~1% by mass of calcite) at different confining stresses: (a) 100 kPa, (b) 200 kPa and (c) 300 kPa. 109

5.11: Particle rotations obtained from DEM simulations of undrained triaxial compression tests on cemented sand (~1% by mass of calcite) at different confining levels: (a) and (b) 100 kPa, (c) and (d) 200 kPa, and (e) and (f) 300 kPa. Figures (b), (d), and (f) are thresholded images that show only the particles with the highest rotation. A less random organization of these particles can be noticed with increasing confining stress, and at a confining stress of 300 kPa, a reasonably well-formed shear band can be seen. 110

5.12: Particle rotations obtained from DEM simulations of undrained triaxial compression tests at different cementation levels: (a) and (b) lightly cemented (LT190), (c) and (d) moderately cemented (MT450) and (e) and (f) heavily cemented (HT1400) (Yang et al. 2018). Figures (b), (d), and (f) are thresholded images that show only the particles with the highest rotation, which shows a more organized distribution of these particles with increasing cementation levels. A distinct shear band can be seen for the highly cemented case. All virtual specimens subjected to a confining pressure of 100 kPa. The identifiers LT190, MT450, and HT1400 refer to lightly, moderately, and highly treated sands, with the numbers representing the shear wave velocities through the sample. Please refer to (Yang et al. 2018) for more details. 111

5.13: (a) 3D visualization of particle rotations and sample deformation under unconfined compression at 4% axial strain, and (b) deviator stress-strain relationship predicted by DEM model and its comparison with experimental data from (van Paassen et al. 2009). 115

5.14: Packing in a multi-phase system with three particle types, each having different cohesive bond strengths. 118

5.15: Deviator stress-axial strain-excess pore pressure relationships for simulated systems when the cohesive strengths of phases are varied (case number corresponds to that listed in Table 5.5). 120

5.16: Deviator stress-axial strain-excess pore pressure relationships for simulated systems when the volume fraction of phases are varied (case number corresponds to that listed in Table 5.6). 122

6.1: Simulation schemes for the shear box and cylindrical models: (a) loose packing state before radii growth process, (b) confined state along with boundary conditions applied for cyclic DSS simulation, (c) contact force network as the end of consolidation for shear box model and (d) loose packing state before radii growth process, (e) confined state along with boundary conditions, (f) contact force network after consolidation for cylindrical model. 131

6.2: Results of numerical simulation of the cyclic DSS test at a CSR of 0.10 for Fraser river sand: (a) stress path, and (b) shear stress-shear strain response. 134

6.3: Numerically simulated contact force network for the shear box model: (a) after consolidation, (b) after shearing, and (c) side view (right side) of (b); and for the model: (d) after consolidation, (e) after shearing, and (f) side (right side) of (e). 136

6.4: Simulated stress path and shear stress-strain response under cyclic DSS tests for Fraser river sand at different CSR: (a) 0.12, and (b) 0.08. Please refer to Figure 6.2 for simulation results corresponding to a CSR of 0.10. 138

6.5: Cyclic shear resistance predicted by the numerical simulation and its comparison with experimental results from (Wijewickreme et al. 2005). 138

6.6: Numerically simulated excess pore water pressure ratio (r_u) as a function of number of cycles to reach 3.75% strain..... 140

6.7: Particle size distribution of Ottawa 20-30 sand the corresponding simplified PSD used for simulations. 142

6.8: SEM images showing CaCO3 precipitation concentrated at particle contacts (O'Donnell et al. 2017b). 144

6.9: Experimental (O'Donnell et al. 2017b) and numerically predicted constitutive relationships for untreated (UT) and treated (T) samples under CIUC test. Note that the experimental data for the actual treated sample used in cyclic DSS test is not available, and a specimen with very similar characteristics is used for DEM parameter identification.146

6.10: Cyclic strength curves developed using the DEM simulations and compared to the experimental data reported in (O'Donnell et al. 2017b). The closed symbols correspond to experimental data and the open symbols to DEM simulations. 149

6.11: Simulated stress path and shear stress – shear strain relationship under cyclic DSS test for untreated, cemented and reconstituted sands with CSR = 0.30, for 10 cycles. .. 150

6.12: Predicted average coordination number of untreated, cemented and reconstituted sands, for the first 10 cycles of cyclic DSS simulation with a CSR of 0.3. 152

7.1: (a) Initial loose-state packing, (b) prepared 2D DEM model for CPT simulation, (c) model after CPT simulation (with a cone-diameter/particle-size ratio of 15), and (d) force chain network after simulation of CPT. 158

7.2: Effect of loading speed on: (a) cone penetration resistance and (b) coordination number. 159

Figure Page

7.3: Simulated cone penetration resistance for different cone-diameter/particle-size ratios. 161

7.4: Influence of boundary conditions and chamber width..... 163

8.1: Inter-particle contact model used in DEM simulations (Cundall 2004). 168

8.2: Mechanical response of contact law used in DEM simulations: (a) bonded normal contact, (b) bonded tangential contact and (c) bonded failure envelope (Cundall 2004). 169

8.3: Numerically designed and experimentally obtained particle size distributions for cement paste and aggregate, where solid lines represent PSDs obtained experimentally and dot lines with marks represent numerical PSDs. 170

8.4: Schematic showing: (a) initially distributed particle packing with significant overlaps, (b) particle packing restricted by rigid boundaries after attaining the balanced state, and (c) the prepared numerical specimen before the flexural loading. 173

8.5: Numerically simulated flexural stress-strain response against reported experimental result (Arora 2018)..... 174

8.6: (a) Schematic illustration of the numerical specimen, and (b) the simulated stress-strain response under compression against experimental data (Arora 2018). 175

8.7: (a) Simulated crack patterns and (b) Contact force network distribution at the end of uniaxial compression simulation..... 176

8.8: The measurement sections indicated in a 2D DEM model for the tension test. 178

8.9: Numerically simulated tension behavior of UHPC. 179

Figure Page

8.10: (a) Particle displacement and (b) Contact force (in vertical direction) network at the end of the tension simulation. 179

1. INTRODUCTION

With the growth of global population, the demand for sustainable infrastructure is significantly increasing. Substructures with appropriate material are required to be built in or above soil that can support the massive volume of construction demand. However, increased structural requirements often require ground improvement to increase the soil capacity. Moreover, certain soils are prone to liquefaction during an earthquake, which results in significant structural damage and loss of lives. Physical and chemical methods have been developed in the past to improve the soil's ability, including mechanically densifying the soil, or using binding agents such as cement, epoxy, or silicates. Most of these traditional treatment methods have been found either hazardous and may cause irreversible damage to natural environment (Mortensen and DeJong 2011), or are too disruptive to use beneath or adjacent to existing structures (Kavazanjian and O'Donnell 2015a). Thus, alternative techniques are required to provide a more natural and sustainable solution. Biomediated methods of strengthening soil through mineral precipitation, in particular through microbially induced carbonate precipitation (MICP), have recently emerged as a promising means of soil improvement. In MICP, the precipitation of carbonate (usually in the form of calcium carbonate) is mediated by microorganisms and the process is referred to as biomineralization. The precipitated carbonate coats soil particles, precipitates in the voids, and bridges soil particles, thereby improving its mechanical properties (e.g., strength, stiffness, and dilatancy). It has been reported that the mechanical properties of soil can be extensively enhanced through MICP (Kavazanjian and O'Donnell 2015a; Li 2015; Montoya and DeJong 2015; Mortensen and DeJong 2011;

O'Donnell and Kavazanjian 2015), however the micro-scale mechanisms that influence the macro-scale constitutive response remains to be clearly explained.

To help understand the particle-scale mechanisms that govern the macro-scale constitutive response of bio-cemented sand, discrete element method (DEM) (Cundall and Strack 1979, 2013) is employed in this thesis to model the physical processes at the particle-scale. Considering the inherently discontinuous and heterogeneous nature of soils, DEM is a powerful and appropriate modeling tool since it simulates the macro-scale mechanical response of granular materials by computing the individual motion and interactions of discrete elements with certain micro-scale properties (Belheine et al. 2009; Cundall and Strack 2013; Kozicki et al. 2014; Widuliński et al. 2009). 3D DEM models are used in this thesis to simulate the behavior of bio-cemented sand under triaxial compression and extract the microstructural features during the triaxial test to provide fundamental insights into the behavior of bio-cemented sand. DEM has been implemented to study several important phenomena such as strain localization (i.e., shear band formation), variation in the number of nearest neighbor particles (i.e., coordination numbers), and the evolution of force chains between the particles. Furthermore, the dynamic behavior of bio-cemented sand under cyclic loading is also numerically studied with DEM, which will help better predict the performance of bio-cemented sand.

1.1. Objectives

The primary objective is devoted to understanding the particle-scale mechanisms that govern the macroscale constitutive response of bio-cemented sand. The discrete element method (DEM) has been employed to develop a 3D model that can predict the macroscale

behavior of bio-cemented sand with micro-scale properties under varying loading conditions. The specific objectives of this dissertation are:

(a) Development of a three-dimensional discrete element method (DEM) based numerical model to simulate the response of bio-cemented sand under drained triaxial compression, and validate its ability to simulate the performance of granular materials.

(b) Refining the existing DEM models with advanced flexible boundary conditions and simulate the response of bio-cemented sand under undrained triaxial compression, and investigate the influence of cementation levels on the mechanical response.

(c) Characterization of the influence of boundary conditions and material types on the response of bio-cemented sands as well as evaluate the difference between different simulation strategies, with an aim of providing guidance on appropriate simulation types for undrained and drained triaxial compression of granular materials.

(d) Simulation of the dynamic response of bio-cemented sand subjected to cyclic loading and conduct a numerical investigation on the resistance of bio-cemented sand to earthquake-induced liquefaction and cone penetration.

1.2. Dissertation Layout

This dissertation is primarily composed of four research papers that are published, submitted or is ready to be submitted for publication. These papers are presented in Chapters 3-6, where each chapter corresponds to a research paper. Chapters 3-7 focus on simulating the static and dynamic mechanical responses of bio-cemented sands and investigating the particle-scale mechanisms with DEM whereas Chapter 8 extends the application of DEM to study of the response of ultra-high-performance concrete (UHPC) in compression, flexure, and tension.

Chapter 2 consists of extensive literature review on (1) the development and applications of discrete element method (DEM), (2) existing methodologies available for carbonate precipitation, and (3) laboratory tests to study the mechanical responses of sands.

Chapter 3 reports the development of a 3D discrete element method (DEM) based numerical model used to simulate the triaxial compression response of a sand strengthened using microbially induced carbonate precipitation (MICP). A parameter identification approach is employed to evaluate the influence of microscale parameters of the DEM model. A particle homogenization approach is employed to model the particles strengthened with low amounts of calcium carbonate (<1% by mass). The particle contacts are assigned a cohesive bond strength when higher amounts of calcium carbonate (≥1% by mass) are present to model the effect of cementation between sand grains.

Chapter 4 introduces a modified version of the 3D DEM model presented in chapter 3 by introducing flexible membrane boundaries created with particle facets (PFacets). A methodology to implement virtual undrained triaxial compression using PFacet-based membrane boundaries is developed. The macroscale response of sands with varying degrees of cementation is simulated by this model under undrained triaxial compression conditions. The failure process (i.e., formation of shear band) of sands with varying degrees of cementation is studied by measuring particle rotations during simulations. The relationship between the cohesive bond strength and the shear wave velocity is evaluated.

Chapter 5 details the available methodologies that can be used to simulate the constitutive response of uncemented and bio-cemented sands and the influence of boundary conditions, loading and testing conditions, and material types. Both the classical DEM model and the pore scale finite volume (PFV)-coupled DEM model are used to simulate the response of

saturated uncemented and lightly cemented sands with a rigid wall boundary under both drained and undrained triaxial compression. The DEM model with flexible boundaries is used to simulate undrained triaxial compression of moderately cemented sands, including the influence of confining stress. A classical DEM model is used to simulate the uniaxial compression response of a sand with an extremely high degree of cementation. A multi-phase particle-packing model for cemented sands is presented in this chapter.

Chapter 6 numerically studies the dynamic response of bio-cemented sands. In this chapter, DEM-based simulations of the cyclic direct simple shear (DSS) tests are carried out using a 3D shear box geometry to evaluate the liquefaction resistance of untreated, MICP-cemented, and reconstituted sands. Verification of the DEM model are implemented through experimental DSS results on a loose river sand at different cyclic stress ratios (CSR). The validated model is used for bio-cemented sands subjected to multiple liquefaction cycles.

Chapter 7 preliminarily simulates the cone penetration test (CPT) with two-dimensional DEM models. Parametric studies are carried out to investigate the influence of non-material factors on the performance of numerical models. The effect of loading speed, cone-diameter to particle-size ratio and the boundary conditions are numerically studied.

Chapter 8 extends the application of DEM-based models to study the mechanical properties of a highly dense cemented material - ultra-high-performance concrete (UHPC). A 2D DEM model is developed in this chapter and used to simulate flexural, compression, and tension response of UHPC.

2. LITERATURE REVIEW

The literature review chapter is divided into three sections: the first section introduces discrete element method (DEM) and the DEM software used in this dissertation. The second section is focused on the existing methods for strengthening soil through mineral precipitation and the third section briefly reviews the available laboratory tests commonly used to determine the mechanical behavior of sands.

2.1. Background of Discrete Element Method (DEM)

The Discrete Element Method (DEM), initially developed by (Cundall and Strack 1979), has captured increased interest in the last few decades. DEM simulates the macro-mechanical response of granular materials by computing the individual motion and interactions of a large number of discrete elements (Cundall and Strack 1979). One of the significant benefits of using DEM for constitutive modeling of granular materials is its capability to capture the local response which influences the global behavior of the material. The solid constituents are represented by a collection of interacting particles, which is a more realistic representation compared to continuum analyses. However, the application of DEM remained limited in the 1980s and 1990s due to its relatively high computational demand. Post that era, the rapid increase in computational power (e.g., higher clock rate of central processing unit (CPU), availability of multi-core systems) made it possible to model mechanical problems with larger number of particles and more complex contact models. This prompted a rapid evolution of DEM models as well as widespread increase in the use of DEM in chemical and process engineering, food technology, civil engineering, and pharmaceutical sciences (O'Sullivan 2011).

2.1.1. Available Resources of DEM Solvers

During the development of discrete element method, multiple DEM solvers have been released as both commercial and open-source products. For instance, the EDEM software first introduced to the market in 2006 by DEM Solutions Ltd., is a commercial DEM solver that focuses on virtually testing the performance of equipment which handles or processes bulk materials under varying industrial environments and thus help optimize the industrial design of these equipment. EDEM is able to simulate granular materials with different shapes by accessing the Generic EDEM Material Model (GEMM) database, which contains a significant number of material models that can be used to represent a wide range of granular materials. EDEM is also able to perform fast and scalable computations using the double precision graphics processing unit (GPU) solver, which is an advanced GPU-accelerated technique to facilitate process-intensive operations.

The Particle Flow Code (PFC), developed by Itasca Consulting Group and initially released in 1994, is an advanced, fast and extremely versatile DEM-based software that is widely used by both industry and academia. By distinguishing the software into PFC2D and PFC3D versions, the software can simulate two-dimensional and three-dimensional problems separately with different particle geometries and degree of freedoms (DOFs) (e.g., disk particle with 3 DOFs in 2D and sphere particle with 6 DOFs in 3D). PFC can also simulate select multi-physics problems (e.g., thermal coupled and fluid coupled phenomena) with the built-in thermal solution analysis and the ability to connect with third-party computational fluid dynamics (CFD) software. The software functions are controlled by either FISH scripting (the default scripting system) or Python scripting language. By providing a built-in material framework together with default contact models, PFC also

enables users to customize new contact models based on specific modeling requirement. Stable and fast simulation is insured by adoption of auto time-step selection algorithm as well as implementation of parallel-processing optimization.

While the above described commercial software typically require purchase of license permission, several open-source solvers are also available for DEM simulations. The distinct element method code BALL & TRUBAL that was originally written by P. Cundall, is the first operational code that was designed to solve discrete element problems. Other open-source DEM solvers such as LIGGGHTS, ESyS-Particle and YADE are also widely used by researchers around the world.

Among all these DEM software, this dissertation uses the open-source platform YADE (J. Kozicki and F.V. Donzé 2009; Šmilauer et al. 2018), which is an extensible open-source framework for 3-dimensional DEM models, to simulate the mechanical response of bio-cemented sand. Developed and maintained under selected Linux platforms (Debian and Ubuntu), YADE is an extremely powerful DEM solver that can be implemented to solve mechanical as well as multi-physics problems of granular materials. Serving as an open-source framework, YADE allows for a high degree of customization (e.g., development of new contact models and new particle geometries) with the accessibility of source code. By writing the computational code with a flexible object model, YADE allows independent implementation of new algorithms and interfaces. The fluid-coupled DEM model can be utilized with the built-in pore finite volume (PFV) module available in YADE. Further, YADE is also capable of coupling with open-source FEM code Escript to implement parallel hierarchical multiscale modeling of granular materials (a FEM-DEM coupled modeling procedure). Since YADE is controlled by Python scripting language, it is easy to

construct a designed scene, control the simulation progress by adding user-defined functions as well as record and export simulation results. YADE provides the ability to consistently record the modeling state information such as particle positions, particle velocities and inter-particle forces during simulations. Thus, post processing can be easily carried out by exporting these information into third-party post processing software (e.g., paraview3D). In addition, parallel-computing is available in YADE to enhance simulation speed. More details on YADE can be found in (Belheine et al. 2009; J. Kozicki and F.V. Donzé 2009; Šmilauer and Chareyre 2010).

2.1.2. General Modeling Procedure

A typical simulation loop for a DEM solver is illustrated in Figure 2.1. First of all, all the particle-related information (e.g., particle location, particle size, and particle density as well as contact properties) is stored to bodies that corresponding to each individual particle. During the simulation loop, all the forces acting on bodies from previous step are reset. An approximate collision detection is executed to fast detect possible collisions and filter away impossible collisions. A more exact but expensive collision detection algorithm is then run on the remaining possible interactions to accurately detect the exact collisions of bodies. This refreshed collision state is then used to update the inter-particle interactions (e.g., elimination of no-longer existing contacts and establish new contacts). The contact model stored in bodies is then used to solve interactions to obtain contact forces acting on all bodies. The contact forces, together with other external conditions (e.g., gravitational force), are used to update the accelerations, velocities and finally positions of bodies by integrating the equations of motion (Newton's second law). These steps are repeated with either pre-determined or auto-selected time increment Δt until the end of the simulation.

Since DEM adopts an explicit solution scheme (Cundall 2004; Šmilauer et al. 2018), the selection of an appropriate time increment (Δt) for analysis is necessary for obtaining reasonable results. While different DEM software may have different criteria of critical time step determination (Cundall 2004; Šmilauer et al. 2018), the selection of time increment Δt is always related to the critical time step of the simulation. For example, according to the YADE (an open-source DEM solver) user manual (Šmilauer et al. 2018), a time increments that are equal to 30% or less of the critical time increment (defined in Equation 2.1) is always recommended to ensure the stability of the solution. It is noted that the critical time step is a function of the contact stiffness and particle mass (i.e., particle density). Thus a decrease in contact stiffness and an increase in particle density can both increase the critical time step and accelerate the simulation.

$$\Delta t_{cr} = \sqrt{2}\sqrt{\frac{m}{k}} \tag{2.1}$$

where Δt_{cr} is the critical time step used for simulations, m is the mass of a particle, and k is its contact stiffness.

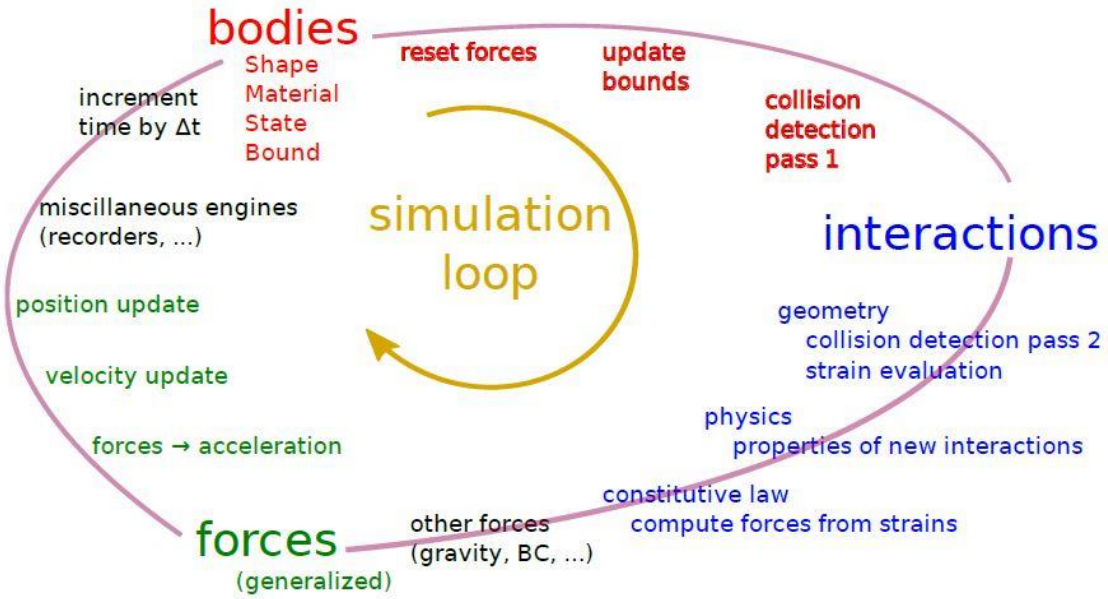

Figure 2.1: Typical interaction loop of DEM simulations (Šmilauer et al. 2018).

To simulate quasi-static phenomena, it is necessary to dissipate kinetic energy of particles during simulation. Local non-viscous damping scheme is commonly adopted (Cundall and Hart 1995) in DEM simulations where the damping scheme acts on forces without constraining uniform motion and can damp all the particles uniformly (Šmilauer et al. 2018).

2.1.3. Contact Model Used to Simulate the Mechanical Behavior of Sands

Pioneered by (Cundall and Strack 1979), two-dimensional DEM model is constructed with disk-like particles. A linear contact model following the Mohr-Coulomb rupture criterion is used to describe the normal and tangential interactions between particles. The "soft contacts" approach which allows finite overlap distance between particles in contact is used. It is noted that the use of the "soft contacts" approach violates the compatibility requirement. As such, DEM assumes that the overlapping volume between the entities in contact is very small and therefore is of negligible significance from a practical perspective.

While such simplifications can keep calculation costs low (Plassiard et al. 2009), excessive rolling during shear displacement has been observed by (Mahboubi et al. 1996) where the stress-softening behavior that occurrs in experiments after peak stress was not reproduced adequately. On the other hand, experimental observation strongly suggests that rolling, rather than sliding, dominants the dilatancy (Iwashita and Oda 1998). Thus, rolling contact is introduced to modify the contact model so that the inter-particle contacts have rolling resistance and can transfer rolling motions. The modified contact model, often recognized as the moment transfer law (MTL), has been extended to the three-dimensional case with the development of 3D DEM models (Plassiard 2007) and has been widely used to simulate the mechanical behavior of sands.

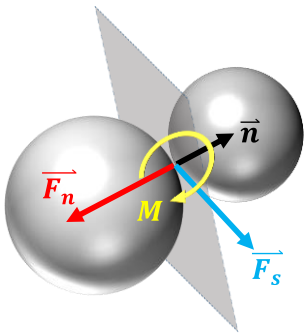

Figure 2.2: Two spheres in contact, showing the normal ($\vec{F}_n$) and tangential ($\vec{F}_s$) contact force vectors, the contact moment vector ($\vec{M}$) and the unit normal vector ($\vec{n}$).

Figure 2.2 shows two spheres with radii of r_A and r_B in contact. The interaction force between the particles can be decomposed into a normal force, a shear force and a contact moment, represented by vectors $\vec{F}_n$, $\vec{F}_s$ and M, respectively. The normal force follows a linear relationship with a zero-tension contact and shear forces follows the Mohr-Coulomb law. The rolling contact follows a linear elastic plastic relationship that limits the rolling

moment and can be sustained by the inter-particle contact. Detailed description of the contact model is discussed in the following chapters.

2.1.4. Applications of DEM Models on Simulating the Behavior of Granular Materials

The discrete element method has been widely used to study the mechanical behavior of granular materials. A variety of inter-particle contact laws have been developed to capture the characteristics of particle contacts in granular media, facilitating robust DEM models for predictive purposes (Iwashita and Oda 1998, 2000). The development of fluid-coupled DEM models has enabled accurate description of fluid-particle contacts (Catalano et al. 2014; Chareyre et al. 2012; Liu et al. 2015; Shafipour and Soroush 2008; Tong et al. 2012). DEM models that consider particle shape and roughness, clumped particles, packing density, and microscopic stress states have been developed (de Bono et al. 2015; Kozicki and Tejchman 2011; Lee et al. 2012; Sayeed et al. 2011; Shen et al. 2016; Wang and Leung 2008b). DEM has been extensively used to model the behavior of non-cohesive materials (e.g., sand) (Belheine et al. 2009; Widuliński et al. 2009; Kumara et al. 2013) and of cohesive materials (e.g., concrete, cemented sand) (Wang and Leung 2008b; a; Utili and Nova 2008; Tran et al. 2011; de Bono et al. 2015; Camusso and Barla 2009; Feng et al. 2017, 2014; Obermayr et al. 2013; Vallejos et al. 2016).

Both the drained and undrained triaxial compression tests, which are most common laboratory tests used to determine the properties of soil, have been simulated with DEM-based models as well as fluid coupled DEM models (Belheine et al. 2009; Cil and Alshibli 2014; Gong 2008; Kozicki et al. 2014; Lee et al. 2012; Liu et al. 2015; Wang and Li 2014; Widuliński et al. 2009). These studies have demonstrated the immense potential of DEM simulations to predict the behavior of soil during triaxial compression.

Modeling of the dynamic response of water saturated granular materials is a complex problem requiring complex multi-physics models. Despite these continuum formulations based on phenomenological observations of the soil skeleton and the pore water phase, DEM based models are used to study the liquefaction of saturated soil during cyclic loading with a constant volume method (El Shamy et al. 2010; El Shamy and Abdelhamid 2014; El Shamy and Zeghal 2007; Gong and Zha 2012; Shi et al. 2010; Vinod et al. 2013; Wang and Wang 2017; Wei and Wang 2016). The commonly used direct simple shear (DSS) test has also been extensively modeled with discrete element method (Bernhardt et al. 2014; Bernhardt and Biscontin 2016; Dabeet 2014; Dabeet et al. 2012, 2014). DEM has been comprehensively used to simulate the cone penetration test (CPT), a widely used in-situ test to determine soil properties (Bakunowicz and Ecemis 2014; Ciantia et al. 2016; Ecemis and Bakunowicz 2018; Falagush et al. 2015; Huang et al. 1993; Janda and Ooi 2016; Kotrocz et al. 2016; Kouretzis et al. 2014; Poganski et al. 2017).

During the last few years, the application of DEM has rapidly extended to simulate the fracture as well as fatigue response of cementitious materials (such as concrete) due to its distinct nature (Nagai and Matsumoto 2010; Nitka and Tejchman 2015a; b; Skarzyn´ski et al. 2015; Suchorzewski et al. 2018; Tran et al. 2011). The reported studies indicate the appropriateness of using DEM to simulate the failure behavior of cementitious materials.

2.2. Bio-mediated Methods of Strengthening Soil Through Mineral Precipitation

Bio-mediated methods of strengthening granular soil through mineral precipitation, in particular through microbially induced carbonate precipitation (MICP), have recently emerged as a promising means of soil improvement (DeJong et al. 2006, 2010; van Paassen et al. 2010). In MICP, the precipitation of carbonate (usually in the form of calcium

carbonate) is mediated by micro-organisms. This process is referred to as biomineralization. The precipitated carbonate coats soil particles, precipitates in the voids, and forms bridges between sand particles (as shown in Figure 2.2), thereby improving the mechanical properties (e.g., strength, stiffness, and dilatancy) through inter-particle cementation and particle roughening (DeJong et al. 2006, 2013; van Paassen et al. 2010).

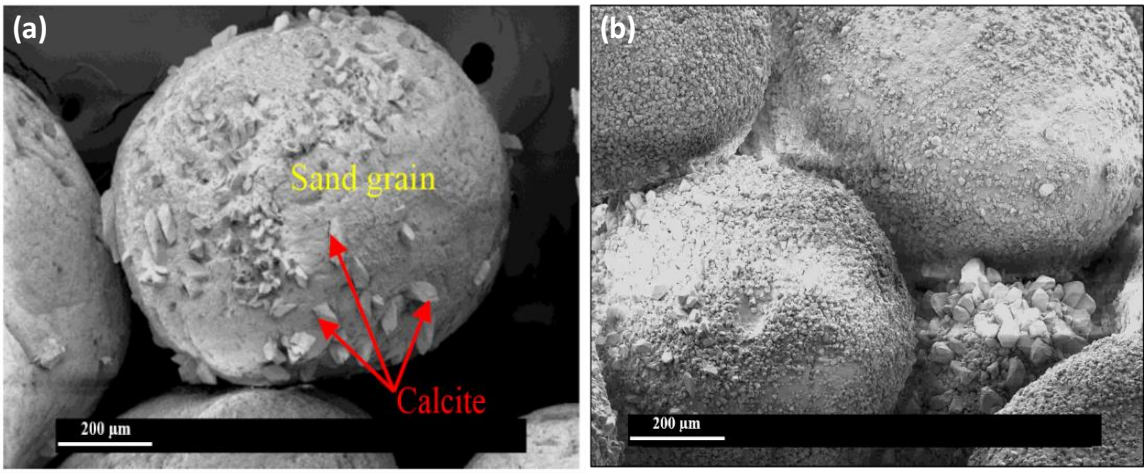

Figure 2.3: SEM images showing calcite carbonate precipitation (a) on the soil particle surface (Kavazanjian and O'Donnell 2015a) and (b) concentrated at particle contacts (Li 2015)

The occurrence of carbonate precipitation requires significant activity of carbonate and high content of suitable cation (e.g., calcium, magnesium, manganese, iron, cobalt) to surpass the solubility product of the resulting carbonate mineral (Ehrlich et al. 2015). While different kinds of carbonate minerals such as calcite ($CaCO_3$), aragonite ($CaCO_3$), magnesite ($MgCO_3$), dolomite ($CaMg(CO_3)_2$) and siderite ($FeCO_3$) are commonly available (Ehrlich et al. 2015), the microbially induced precipitation of calcite draws most of the interest due to its low solubility, thermodynamic stability, and high strength (O'Donnell 2016).

The activities of micro-organisms (such as bacteria) can alter the geochemical conditions by increasing the pH and the total carbonate content of the aqueous environment and thus favor the precipitation of carbonate minerals (DeJong et al. 2010). Both the higher pH environment and higher total carbonate content can increase the carbonate concentration and hence cause the precipitation of carbonate minerals in the presence of a high enough concentration of a suitable cation (Karatas et al. 2008). Overall, MICP enhances the mechanical properties of soils using the byproducts of a chemical reaction network within the soil that is controlled by biological activity.

A wide variety of microbial processes have been reported to be able to induce carbonate precipitation (Karatas 2008). For example, sulfate reducing bacteria can induce carbonate precipitation by consuming sulfuric acid during the anaerobic metabolism. During this biochemical process, the pH level can be increased by continuous consumption of the sulfuric acid and the total carbonate content can be increased by generating aqueous carbon dioxide, which can contribute to the precipitation of carbonates (DeJong et al. 2010). However, the application of sulfate reducing bacteria in carbonate precipitation is limited by the fact that large quantities of hydrogen sulfide, a potentially toxic gas, are generated during the biochemical reaction. Photosynthetic microbes such as cyanobacteria can induce carbonate precipitation by consuming dissolved carbon dioxide under the effect of photosynthesis (Bundeleva et al. 2014). While such carbonate precipitation has been observed in both nature and laboratory experiments, the feeble existence of sunlight energy within soil limits its potential application in soil strengthening.

Apart from these bio-mediated methods with inherent limitations, urea hydrolysis is a microbial process capable of inducing carbonate precipitation. The common ureolysis

process is an important approach through which plants and micro-organisms can scavenge nitrogen, an essential nutrient, by hydrolyzing urea. Ureolysis can also result in an increase in the pH level through the production of ammonia and an increase in the total carbonate content by producing carbon dioxide. Thus such bio-chemical reaction can favor the precipitation of carbonate mineral effectively (Whiffin et al. 2007). Significant improvement in peak strength has been observed for ureolytic MICP-treated soil with a carbonate content of 4 wt% or higher (Whiffin et al. 2007). In a study conducted (van Paassen et al. 2010), a large box experiment with fine to medium poorly graded sand showed that ureolysis can be used to quickly induce the precipitation of calcite carbonate in large amounts (0.8 – 24 wt% $CaCO_3$). However, the byproduct of ureolysis, ammonium chloride, is considered as a potentially toxic product. A large-scale field test on ureolytic MICP reported that additional treatment was required to remove ammonium chloride to meet regulatory groundwater requirements (Van der Star et al. 2011).

Microbial denitrification is also considered to be capable of inducing the precipitation of carbonate minerals. By microbially consuming nitric acid and producing nitrogen gas and carbon dioxide, the nitrogen reduction process can raise the pH level as well as increase the total carbonate content of the chemical environment and finally result in the precipitation of carbonate minerals (Hamdan et al. 2017; Karatas 2008). While it has been reported that MICP through denitrification is significantly slower than that via ureolysis with lower content of participated calcite carbonate (1% -- 9 .5% by weight) (Hamdan et al. 2017; Van Paassen et al. 2010), the denitrification induced carbonite precipitation showed a significant improvement of soil properties with relatively low content of calcite carbonate (O'Donnell et al. 2017a, 2017b). In addition, denitrification produces nontoxic

byproducts such as nitrogen and carbon dioxide gases, which do not incur any environmental cleanup costs (Van Paassen et al. 2010).

2.3. Laboratory Tests to Determine the Mechanical Response of Soil

Multiple laboratory tests are available for determining the properties of soil and measuring the response of soil under varying loading conditions.

2.3.1. Triaxial Compression Test

The triaxial compression test is one of the most versatile and widely adopted laboratory tests used to determine the shear strength and stiffness of soil. Figure 2.4 illustrates a general experimental setup of the triaxial compression test. A cylindrical specimen of soil with an approximate 2:1 height-to-diameter ratio is placed on the pedestal inside a cell that can be pressurized. A rubber membrane, porous discs and O-rings are used to seal the specimen while allowing drainage. The internal submersible load cell is connected with the load ram to measure the axial load change during shear.

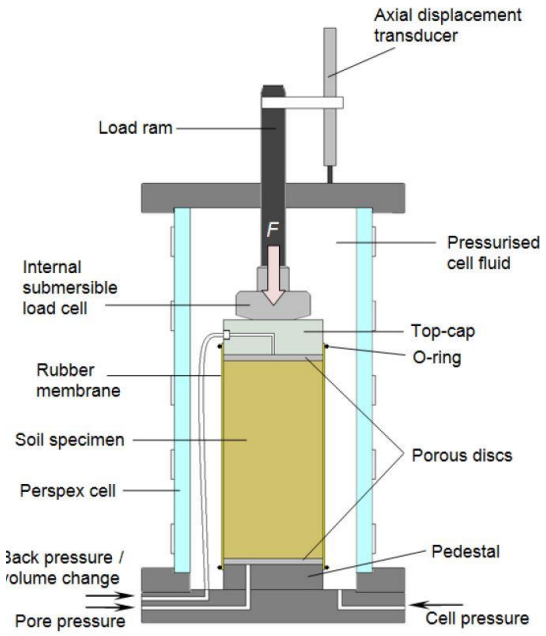

Figure 2.4: General set-up of a soil specimen inside a triaxial cell (Rees 2013).

There are three primary triaxial tests conducted in the laboratory, including the unconsolidated undrained test (UU), consolidated undrained test (CU) and consolidated drained test (CD). Each of the test represents different engineering applications.

The unconsolidated undrained (UU) test is the simplest and fastest procedure that is generally performed on cohesive soil specimens. During the shearing stage, the drainage is closed and only total stresses are controlled and recorded, which allows the undrained shear strength to be determined. Thus the short-term (e.g., during construction projects) stability of soil can be determined through this test.

The consolidated drained (CD) test is designed to access long-term loading response. While maintaining the open drainage condition with a constant back pressure, the volume change of the specimen is measured during the test. The shear rate is maintained to be slow enough to allow the pore water pressure built up during shearing the dissipate.

The consolidated undrained (CU) test is the most common triaxial procedure which can determine the strength parameters with a faster shear rate. The drainage is closed during the test and the excess pore pressure change is recorded.

A triaxial compression test typically consists of four main stages: specimen preparation, saturation, consolidation, and shearing. First, the test specimen is prepared on the pedestal using a split-part mold with minimum disturbance.

Once the specimen has been placed and the assembled triaxial cell is filled with fluid, the saturation process is required to fill all the voids within the specimen with water, as well as to de-air the pore pressure transducer and drainage lines properly. This process typically contains two steps: an initial partial vacuum of specimen to remove air and draw water into the transducer and drainage lines followed by a linear increase of the cell and back

pressures with a constant effective stress. De-aired water should be used during the saturation process to reach full saturation. To check the degree of specimen saturation, the so-called B-check test is performed to determine Skempton's B-value. The test result of $B \geq 0.95$ is typically used to confirm full specimen saturation condition.

The consolidation stage is designed to prepare the specimen to the effective stress state required for shearing. This process is typically conducted by increasing the cell pressure while maintaining a constant back pressure until the volume change of the specimen is no longer significant and significant portion of the excess pore pressure has dissipated.

The soil is then sheared under constant axial strain rate through movement of the load frame platen and the stress state of the specimen is measured by recording the change of axial load and pore water pressure. The applied loading rate and the specimen drainage condition depends on the type of triaxial test being performed, as discussed earlier.

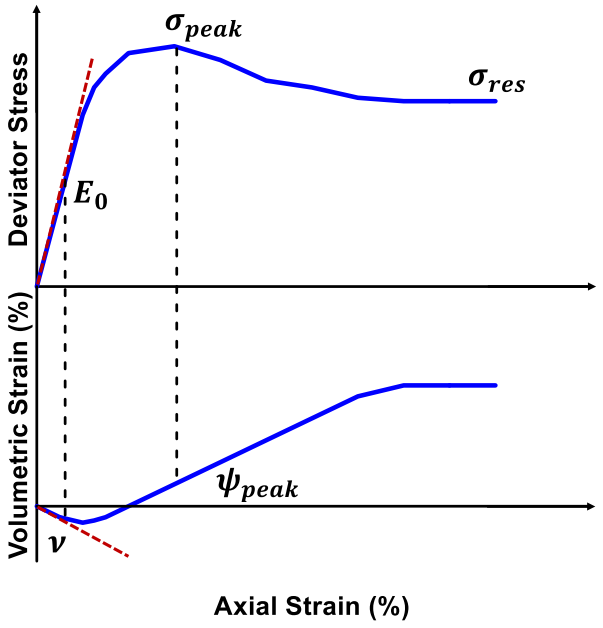

Figure 2.5: Typical response obtained from a CU test of dilatant soil.

A typical response of non-cohesive soil under consolidated drained triaxial compression loading is shown in Figure 2.5. The deviator stress versus axial strain, and volumetric strain versus axial strain curves yield the following properties: Young's modulus E_0, Poisson's ratio ν, the peak and residual (large displacement) friction angles, ϕ_{peak} and ϕ_{res} (determined from the peak and post-peak shear stresses), and the peak dilatancy angle, ψ_{peak}.

2.3.2. Direct Simple Shear Test

The direct simple shear (DSS) test, initially developed to overcome significant stress non-uniformities imposed by the direct shear test (Dabeet 2014), is another widely adopted laboratory test used to characterize the properties of soil under horizonal loadings. There are mainly two apparatus that are commonly used for direct simple shear tests: the Cambridge-type apparatus and the NGI-type apparatus.

The Cambridge apparatus, initially developed by (Roscoe 1953), is suitable for cubical specimens with a dimension of 60 x 60 x 20 mm. The apparatus is bound with rigid frictionless side boundaries and rough top and bottom boundaries. Starting with the initial Cambridge apparatus, the researchers from Cambridge University developed a long series of improved apparatus during the following decades. Considering the major drawback of these apparatus (no back pressure can be applied for full saturation), the direct simple shear test device with enclosed in a pressurized cell was developed (Franke 1979, Dyvik 1987) to ensure a full saturation condition and provide accurate pore pressure measurements in the soil specimen. It can be expected that the Cambridge apparatus provides an accurate estimate of the behavior of soil under monotonic loading if stress measurements are taken at the center of the sample (Budhu 1984).

The Norwegian Geotechnical Institute (NGI) apparatus (Bjerrum and Landva 1966), improved upon the Kjellman's apparatus (Kjellman 1951), and is equipped with wire-reinforced membrane providing lateral confinement to enforce constant area and can accept cylindrical specimens. Lately, the NGI apparatus has been modified with stacked steel rings that slide over each other and are placed around a typical rubber membrane to provide lateral confinement. These three types of apparatus are schematically shown in Figure 2.6. The NGI-type apparatus is more commonly used in direct simple shear test due to its relatively simple setup and the ability to incorporate a cylindrical specimen.

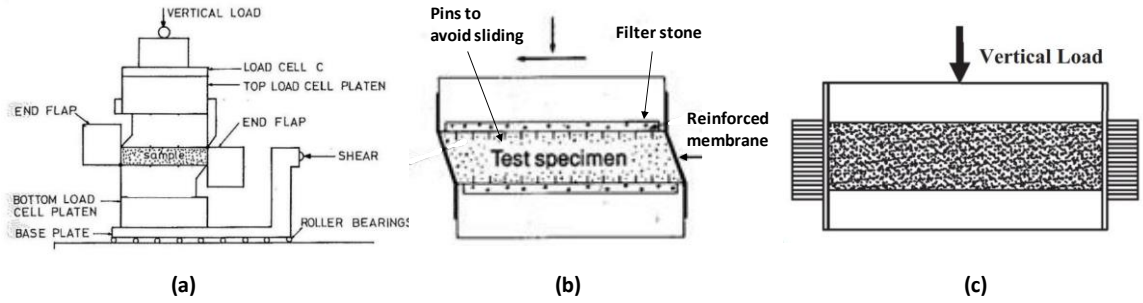

Figure 2.6: Typical apparatus for direct simple shear test: (a) Cambridge DSS device (Roscoe 1953), (b) NGI DSS device and (c) modified NGI-type DSS device (Li et al. 2016).

To investigate earthquake-induced hazards, primarily the earthquake-induced soil liquefaction that causes the loss of load capacity of soil, the cyclic direct simple shear test is commonly implemented on soil specimen with undrained condition (which enforces a constant volume condition). During cyclic direct simple shear test, repeated horizontal loading is applied to consolidated soil specimen under either stress or strain controlled condition with a low frequency (typically 1Hz) to simulate the seismic loading that occurs during an earthquake. The effective vertical stress, the shear stress, the shear strain (defined as the horizontal displacement divided by the height of the specimen) as well as the excess

pore pressure (which is essentially equivalent to the change of the effective vertical stress for undrained cyclic DSS test) are recorded during the test. A typical response of soil subjected to cyclic DSS test is illustrated in Figure 2.7.

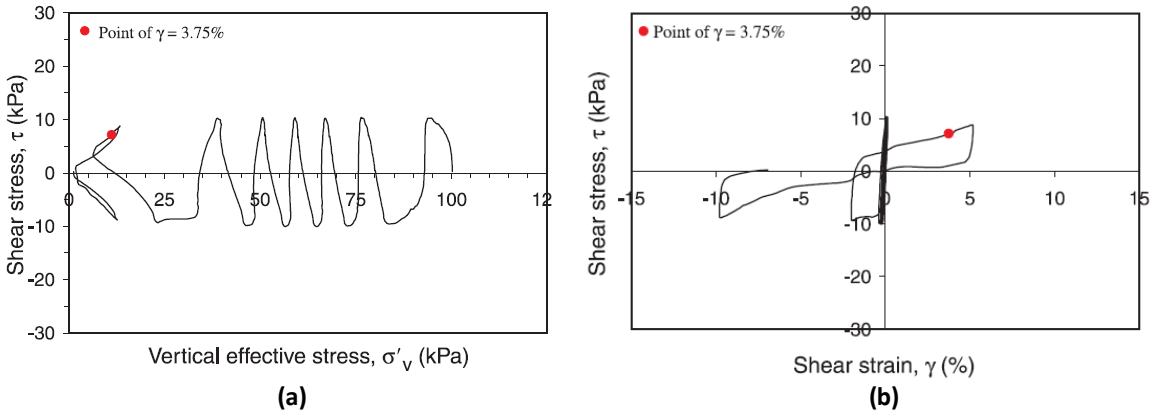

Figure 2.7 : Typical response of soil under cyclic DSS test: (a) cyclic stress-path and (b) stress-strain response (Wijewickreme et al. 2005).

2.3.3. Cone Penetration Test

The cone penetration test (CPT) is an in-situ testing method used to determine geotechnical properties of soils. The cone penetration test has become one of the most widely used and accepted in-situ testing techniques for investigating the soil properties due to its repeatability and reliability and is mainly applied to establish sub-surface stratigraphy and identify material presence, estimate geotechnical parameters and obtain data required for direct geotechnical design (Lunne et al. 1997). The testing method consists of driving instrumented rods connected with cone penetrometers into the ground at a controlled rate (usually 15-25 mm/s). Three main types of penetrometers are available for cone penetration test, which are mechanical cone penetrometers, electric cone penetrometers and piezocone penetrometers. Figure 2.8 illustrates typical filed cone penetration test together with the prominent elements of a typical cone penetrometer - cone tip, friction sleeve, pore pressure filters and connector with rod (located at the top of the penetrometer). A cone penetrometer

with a 35.6 mm diameter cone and 55° to 60° apex angle is recommended as the standard penetrometer and is specified in the International Reference Test Procedure (ISSMGE, 1989).

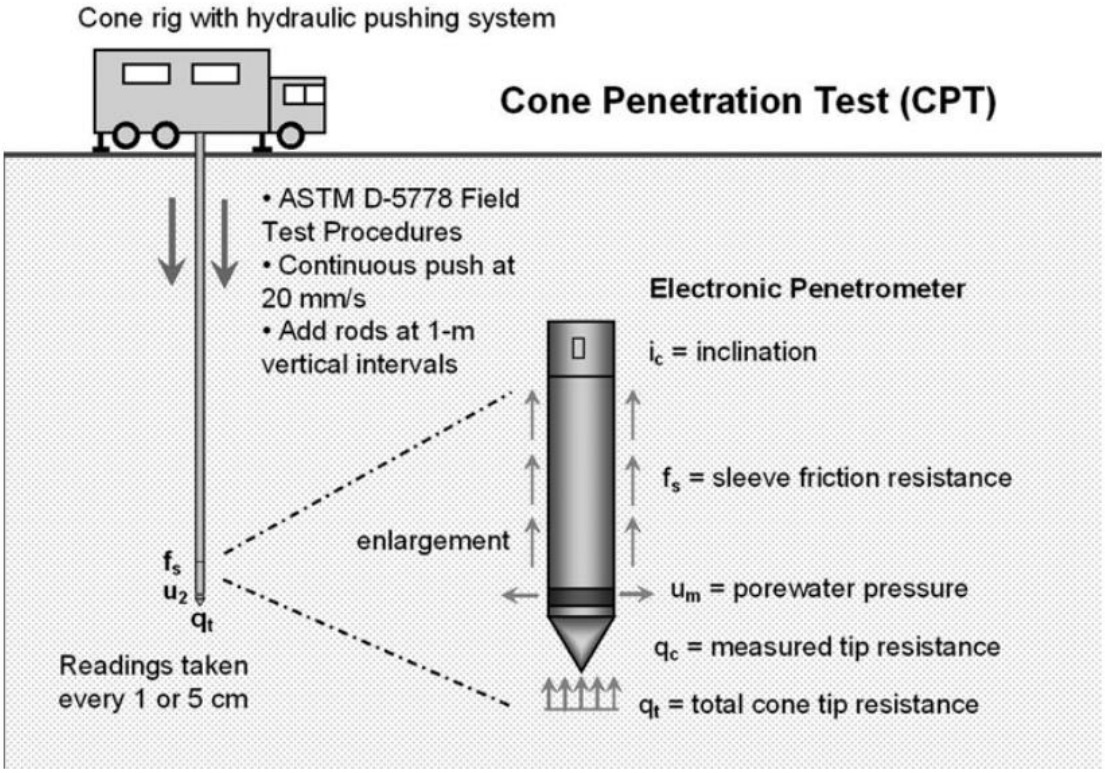

Figure 2.8 : A schematic plot of in-filed cone penetration test and the ingredients of cone penetrometer (Mayne 2007).

During CPT, the penetration resistance of the cone, the local friction resistance on a friction sleeve and pore pressure in the vicinity of the cone and sleeve are measured either continuously or at selected depth intervals. The penetration resistance of the cone is obtained by dividing the total force acting on the cone by the projected cone area. The local friction resistance on friction sleeve is calculated by dividing the total force acting on the friction sleeve by the surface area of the friction sleeve.

3. 3D DEM SIMULATIONS OF DRAINED TRIAXIAL COMPRESSION OF SAND STRENGTHENED USING MICROBIALLY INDUCED CARBONATE PRECIPITATION

3.1. Introduction

Bio-mediated methods of strengthening granular soil through mineral precipitation, and in particular through microbially induced carbonate precipitation (MICP), have recently emerged as a promising means of soil improvement (DeJong et al. 2006, 2010; van Paassen et al. 2010). In MICP, the precipitation of carbonate (usually in the form of calcium carbonate) is mediated by micro-organisms. This process is referred to as biomineralization. The precipitated carbonate coats soil particles, precipitates in the voids, and bridges between soil particles, thereby improving the mechanical properties (e.g., strength, stiffness, and dilatancy) (DeJong et al. 2006, 2013; van Paassen et al. 2010). Preferably, the carbonate precipitates as calcite, since calcite is the strongest and most durable of calcium carbonate polymorphs. Thus in this chapter, it will be assumed that the precipitated carbonate species is calcite. The chemistry of carbonate precipitation, including the dosage of the reagents and treatment conditions, has been reported in detail by Montoya 2012.

In order to design an efficient calcite biomineralization scheme, it is important to be able to predict the improvement in soil properties resulting from calcite precipitation. This improvement is a direct function of the mode (e.g., particle coating, bridging between particles, void filling) and extent of carbonate precipitation. Mathematical models that describe the observed phenomena at the macroscopic scale cannot represent the discrete nature of precipitated calcite, which plays a major role in the behavior of MICP-improved

soils (Belheine et al. 2009). Thus, the discrete element method (DEM) (Cundall and Strack 1979) is used here to model the physical processes at the particle-scale that govern the macroscale constitutive response. DEM has been extensively used to model the behavior of non-cohesive materials (e.g., sand) (Belheine et al. 2009; Widuliński et al. 2009; Kumara et al. 2013) and of cohesive materials (e.g., concrete, cemented sand) (Wang and Leung 2008a; 2008b; Utili and Nova 2008; Tran et al. 2011).

A five-parameter DEM model is employed in this study to model the behavior of MICP-modified sands. This model uses two elastic and three rupture parameters. The microstructural nature of the MICP-modified sand is modeled based on the volume fraction of precipitated calcite. A homogenized particle model is used for sand improved by small amounts of precipitated calcite, wherein most of the calcite simply precipitates on the sand particle surfaces. A cohesive shear strength assigned to the particle contacts is employed to model the behavior of sand containing higher amounts of calcite, wherein precipitated calcite bridges between particles. The micromechanical model is applied to drained triaxial compression tests of both unimproved and MICP-improved sand. The influence of the five microscale parameters on the macroscale response of the MICP-modified sand under triaxial compression is investigated to establish appropriate values for these parameters. The DEM model developed in this chapter is shown to be a reliable method to predict the performance of MICP-strengthened sand under drained triaxial compression through a series of numerical simulations and their comparison to experimental results. The model is expected to useful in identifying the desired levels of cementation for the design of MICP treatment strategies without a large number of trial-and-error experiments.

3.2. Discrete Element Method (DEM) Modeling Framework for Triaxial Compression

This section briefly describes the general DEM modeling approach used in this chapter. DEM simulates the macro-mechanical response of granular materials by computing the individual motion and interactions of a large number of discrete elements with certain microscale properties (Cundall and Strack 1979). One of the benefits of using DEM for constitutive modeling of granular materials is its capability to capture the local response which influences the global behavior of the material. The solid constituents are represented by a collection of normally and tangentially interacting particles for which the translational and rotational motions under an applied load are numerically solved. While different particle geometries can be employed in DEM modeling, spherical elements are commonly used to keep the computational cost low (Belheine et al. 2009; Widuliński et al. 2009).

Several commercial DEM solvers are available. This chapter uses the open-source platform YADE (J. Kozicki and F.V. Donzé 2009), which is a 3-dimensional DEM code with a Python interface. YADE enables the implementation of particle generation/packing algorithms and boundary schemes to simulate laboratory tests under different boundary conditions (e.g., drained and undrained triaxial compression). YADE is an open source code, which makes it widely accessible. Other common DEM codes are proprietary and needs to be licensed from the software supplier. YADE also allows for a degree of customization not possible in other common DEM codes. Also, several researchers have noted that YADE is slightly faster than other codes for systems with a large number of particles ("Comparisons with PFC3D - Yade"). More details on YADE can be found in (Belheine et al. 2009; J. Kozicki and F.V. Donzé 2009; Šmilauer and Chareyre 2010).

3.2.1. Contact Law

Cundall and Strack (1979) developed the local constitutive law for classical DEM modeling of smooth spherical particles. Figure 3.1 shows two spheres, A and B, with radii of r_A and r_B, in contact. The interaction force (representing the effect of particle A on particle B) can be decomposed into a normal force and a shear force, represented by vectors $\vec{F}_n$ and $\vec{F}_s$. Both the normal and shear forces are related to displacements through the normal stiffness k_n and shear stiffness k_s as:

$$\vec{F}_n = k_n U \vec{n} \tag{3.1}$$

$$\Delta \vec{F}_s = k_s \Delta \vec{U}_s \tag{3.2}$$

where, U is the relative normal displacement between two spheres, $\vec{n}$ is the unit normal vector and $\Delta \vec{U}_s$ is the incremental tangential displacement. The tangential force $\vec{F}_s$ is obtained by summation of Equation 3.2.

The normal and shear stiffness are given by:

$$k_n = \frac{K_n^A r_A \cdot K_n^B r_B}{K_n^A r_A + K_n^B r_B} \tag{3.3}$$

$$k_s = \frac{K_s^A r_A \cdot K_s^B r_B}{K_s^A r_A + K_s^B r_B} \tag{3.4}$$

Here, K_n^A and K_n^B represent the normal stiffness for the two particles (i.e., particles A and B) involved in the contact. K_s^A and K_s^B represent the corresponding tangential stiffness.

For a single phase system, every particle has the same properties and Equations 3.3 and 3.4 can be written as:

$$k_n = K_n \frac{r_A \cdot r_B}{r_A + r_B} \tag{3.5}$$

$$k_s = K_s \frac{r_A \cdot r_B}{r_A + r_B} = \alpha K_n \frac{r_A \cdot r_B}{r_A + r_B} = \alpha k_n \tag{3.6}$$

The ratio between the shear and normal stiffness k_s/k_n is defined as α.

For non-cohesive materials, shearing (sliding) begins at the contact point where $\vec{F}_n$ and $\vec{F}_s$ satisfies the Mohr-Coulomb rupture criterion:

$$\|\vec{F}_s\| - \|\vec{F}_n\| tan\, \mu \leq 0 \tag{3.7}$$

Here, μ is the inter-particle friction angle.

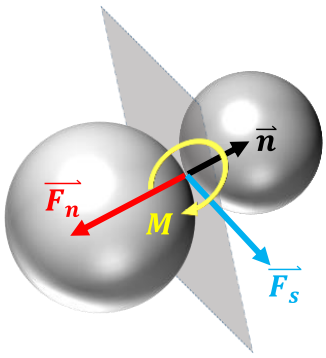

Figure 3.1: Two spheres in contact, showing the normal ($\vec{F}_n$) and tangential ($\vec{F}_s$) contact force vectors, the contact moment vector ($\vec{M}$) and the unit normal vector ($\vec{n}$).

To represent the surface roughness and irregularity of sand grains, the local constitutive law of classical DEM is modified by introducing an additional component at contact points referred to as the Moment Transfer Law (MTL) (Belheine et al. 2009). The contact moments account for the increase the rolling resistance. Only the normal force contributes to rolling resistance. The contact moment increments are calculated by multiplying the rolling stiffness k_r with the rotational increment between two spheres, $\Delta\theta$.

$$\Delta M = k_r \Delta\theta \tag{3.8}$$

The rolling stiffness is a function of tangential stiffness and a dimensionless coefficient, β, defined as the rolling stiffness coefficient, and given by Equation 3.9.

$$k_r = \beta k_s r_A r_B \tag{3.9}$$

The elastic moment (M_e) can be represented as:

$$M_e = k_r \theta_r \tag{3.10}$$

where θ_r is the rotation angle between two particles.

The elastic moment, and thus elastic rolling, can be limited (to simulate plasticity) by the introduction of a plastic moment (M_p) as:

$$M_p = \eta \bar{r} \left\| \vec{F}_n \right\| \tag{3.11}$$

Here, $\bar{r}$ is the average radii of two particles in contact and η is a dimensionless coefficient called the plastic moment limit coefficient. Once the plastic moment is reached, the rotation angle between two spheres is recalculated as:

$$\theta_r = \frac{M_p}{k_r} \tag{3.12}$$

Thus, the rolling moment can be represented as:

$$M_r = min\left(M_e, M_p\right) \tag{3.13}$$

The normal, tangential and rolling contact relationships for the MTL model are elucidated in detail by Belheine et al. (2009).

No forces or moments are transmitted between particles when the particles are separated. In total, five microscale input parameters are required for this DEM model: the normal and

tangential contact stiffness (k_n,k_s), the inter-particle friction angle (μ), the rolling stiffness coefficient (β), and the plastic moment limit coefficient (η). These five microscale parameters require calibration so that macroscale performance is realistically captured.

3.2.2. Sphere Packing and Drained Triaxial Compression Simulation

There are various methods for generating 3D sphere packing for a DEM simulation including dynamic compaction, radius growth, and solution of geometrical equations for sphere placement (Bagi 2005; Chang and Misra 1990; Fazekas et al. 2005; Jerier et al. 2008). In DEM model developed herein, a radii expansion method (Belheine et al. 2009; J. Kozicki and F.V. Donzé 2009) is used. The DEM specimen is generated by assigning random positions to a fixed number of spheres within a prismatic volume, as illustrated in Figure 3.2(a). The particles are initially finer than those in the target size distribution. The growth of the particles eventually results in the target void ratio and grain size distribution of the virtual specimen. The gravity-free growth process, which increases the particle radii, is constrained by the isotropic boundary wall stress applied to represent the isotropic compression stage of a triaxial compression test. The configuration of the target virtual specimen, i.e., the DEM specimen at the isotropic compression stage, is shown in Figure 3.2(b). A packing parameter which is analogous to the inter-particle friction angle is adjusted to obtain the desired initial void ratio during the confining (or particle growth) stage (for example, a high value for the packing parameter leads to a loose packing and a lower value for this parameter leads a denser packing) (Widuliński et al. 2009).

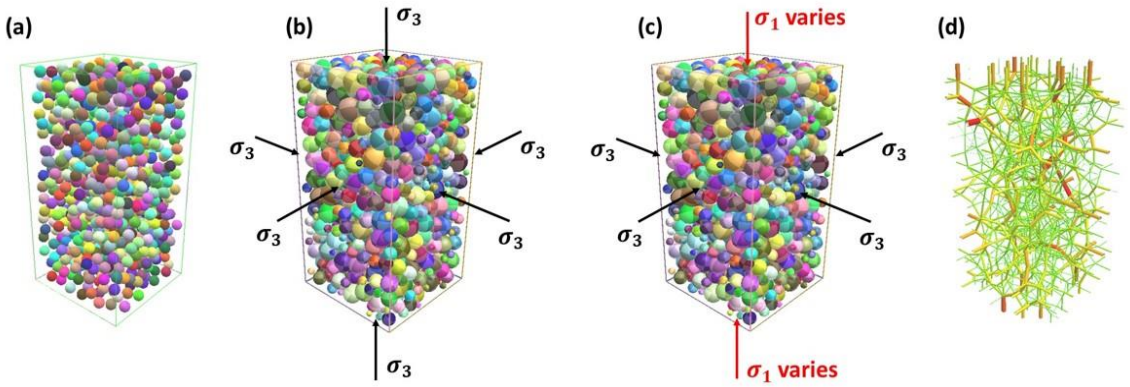

Figure 3.2: (a) Initial volume of spherical particles with random positions, (b) virtual specimen after radii expansion with desired void ratio and confining stress, (c) virtual specimen with deviator loading and (d) distribution of internal forces in the virtual sample.

After the generating the target virtual specimen, deviatoric loading is imposed on the specimen under a gravity free condition to simulate triaxial compression loading. The bottom boundary is fixed against translation normal to the boundary while the top boundary moves vertically (simulating the loading platens in a strain-controlled test). The lateral boundaries are controlled by a servo mechanism that maintains a constant confining stress within the sample (Belheine et al. 2009). The boundary walls are assumed frictionless, which ensures that the stresses applied on the walls remain normal. Figure 3.2(c) shows the loading process with a constant confining stress. The time steps are automatically controlled by the simulation environment to maintain stability. All the simulations are carried out at a strain rate of 0.1/s. Based on the applied boundary conditions and the gravity free assumption, the global stress and strain states within the sample can be assumed to be homogeneous. Strain is calculated directly from the wall displacements and the corresponding stress is obtained from boundary forces. Figure 3.2(d) shows a typical contact force distribution within the sample. The thickness and color of the solid lines is proportional to the magnitude of contact forces.

3.3. Microscale Parameters, Their Relative Effects, and Model Calibration

A series of analyses were conducted to establish the value of the five microscale parameters required for DEM simulation and to investigate their influence on simulation results. A typical macro-mechanical response for drained triaxial compression loading is shown in Figure 3.3. The deviator stress-axial strain, and volumetric strain-axial strain curves yield the following macroscale properties: Young's modulus E_0, Poisson's ratio ν, the peak and residual (large displacement) friction angles, ϕ_{peak} and ϕ_{res} (determined from the peak and post-peak shear stresses), and the peak dilatancy angle, ψ_{peak}.

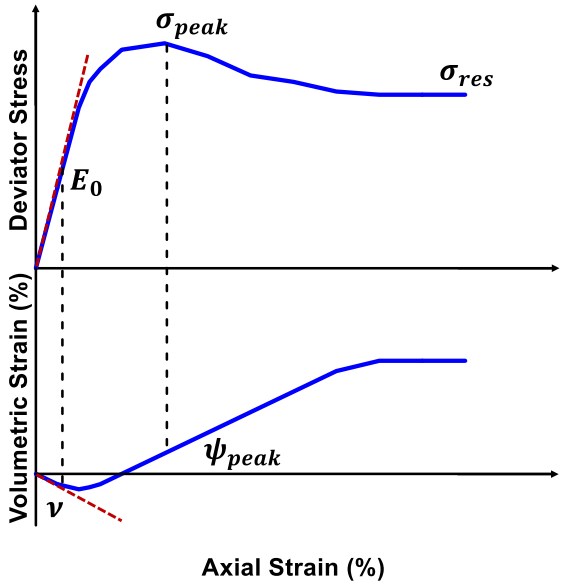

Figure 3.3: Typical response obtained from a drained triaxial compression test of dilatant sand.

The five DEM model parameters are the normal and tangential contact stiffness (k_n, k_s), the inter-particle friction angle (μ), the rolling stiffness coefficient (β) and the plastic moment limit coefficient (η). Note that the inter-particle friction angle required for DEM modeling of mechanical response is different from the arbitrary friction angle used in the particle packing simulation. It has been shown that the local elastic parameters k_n and α

($= k_s/k_n$) influence the macroscale elastic response and the rupture parameters (μ, β and η), either individually or in combination, influence the inelastic properties (J. Kozicki and F.V. Donzé 2009; Plassiard et al. 2009; Widuliński et al. 2009). It is not always easy to obtain accurate estimates of these microscale parameters for simulation. Past studies on numerical modeling of granular materials have relied on multiple stages of calibration in order to obtain results that are comparable with those of experiments. The microscale parameters for the DEM model developed herein were evaluated in a single stage of calibration for two different sands using experimental results for drained triaxial compression tests reported in the literature.

3.3.1. Preliminary Simulations

The experimental results of triaxial drained compression tests on Labenne sand reported by Belheine et al. (2009) were used to understand the influence of the DEM microscale parameters on macroscale response. It has been reported that the stiffness ratio (α) relates to the Poisson's ratio (J. Kozicki and F.V. Donzé 2009; Plassiard et al. 2009). The initial (small strain) value of Poisson's ratio (ν) can be directly obtained from the initial linear elastic portion of the volumetric strain-axial strain plot, as illustrated in Figure 3.3. Using an initial estimate for α ($= k_s/k_n$, which is generally between 0.15 and 0.35), arbitrary values of k_s and k_n were chosen. Initial estimates of the rupture parameters (i.e., μ, β, η) were also chosen such that they are in the corresponding ranges published in the literature (Belheine et al. 2009; Widuliński et al. 2009). A least-squares error minimization procedure was then adopted to match the predicted macroscale response to the experimental results. During this process, the value of k_n was adjusted until the experimental elastic modulus (the initial slope of the deviator stress-axial strain curve) was matched. Table 3.1 provides

the microscale elastic and rupture parameters thus obtained to simulate the macroscale response of Labenne sand. Figure 3.4 shows the experimental and simulated response under a confining stress of 100 kPa.

Table 3.1: DEM parameters used to simulate the macroscale response of Labenne sand reported by Belheine et al. (2009).

Parameters	Labenne sand (Belheine et al. 2009)
Void ratio (e_0)	0.58
Normal stiffness (k_n) (MPa)	600
Stiffness ratio ($\alpha = k_s/k_n$)	0.30
Inter-particle friction angle (μ) (°)	20
Rolling stiffness coefficient (β)	0.025
Plastic moment limit coefficient	0.15
Confining stress (kPa)	100
Number of particles	1000
Sample size (mm)	90 x 180 x 90

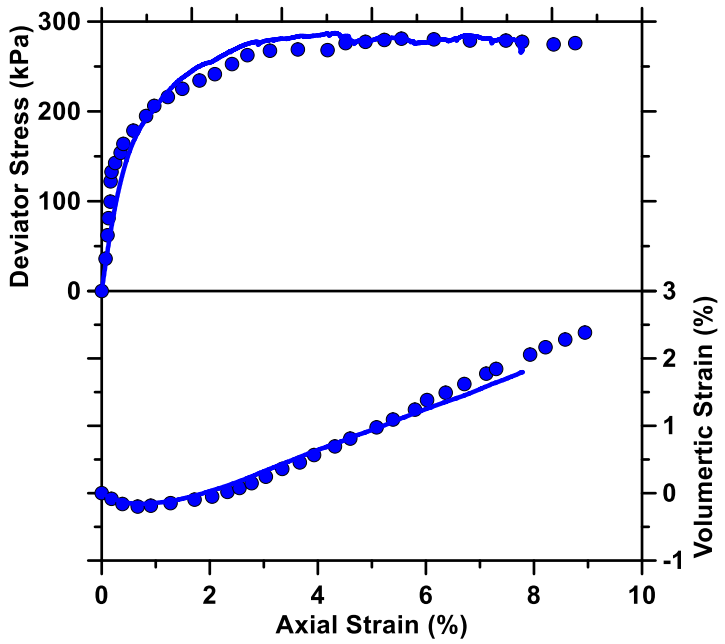

Figure 3.4: Comparison of DEM simulation (solid lines) to experimental data points for deviator stress-axial strain and volumetric strain-axial strain response of Labenne sand (Belheine et al. 2009).

In the simulations described above, the virtual sample contained 1000 particles, which is not uncommon for particle-scale modeling (Zeng 2014). This number of particles was chosen for computational expediency. However, a series of drained triaxial compression simulations were carried out with 1000, 5000 and 10000 particles. The target specimen volume was varied to accommodate the desired number of particles and the initial void ratio was maintained at the same target value for all the three cases. The triaxial compression response of each virtual specimen was then evaluated using the microscale elastic and rupture parameters presented in Table 3.1. Figure 3.5(a) shows the macroscale response of the virtual specimens as a function of number of particles. It is clearly seen that as long as at least 1000 particles are employed, the number of particles has a minimal influence on the simulation results. Hence the all subsequent simulations presented in this study employ 1000 particles in the simulation volume. A series of analyses were also conducted to evaluate the influence of the initial randomization of particles within the virtual specimen on the triaxial response. Five different initial random realizations of particles within a 1000 particle virtual specimen were generated and subject to triaxial compression as described above. Results presented in Figure 3.5(b) indicate that the behavior of the virtual specimen is essentially independent of the initial randomization of particles.

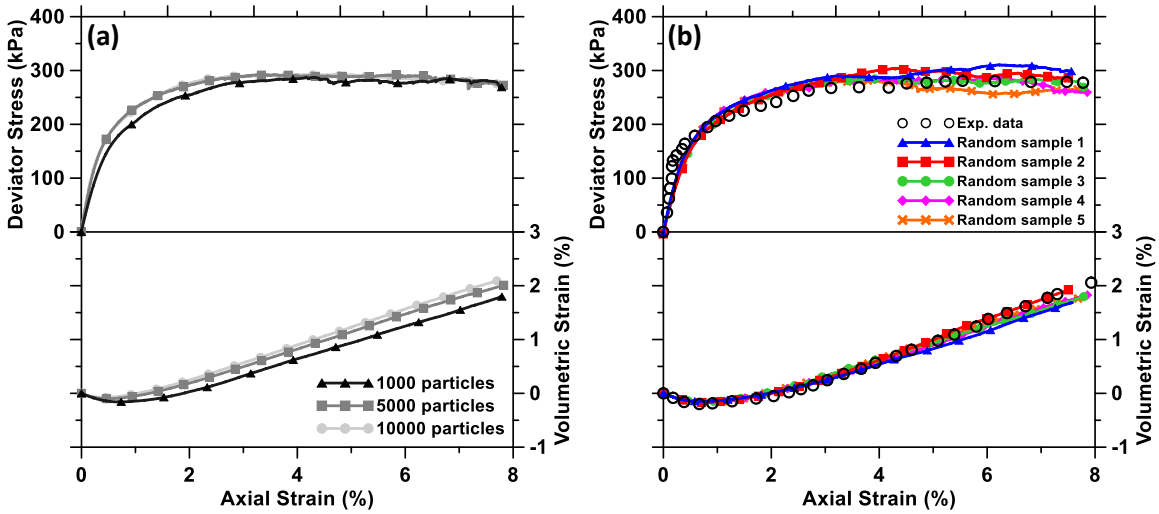

Figure 3.5: (a) Influence of number of particles, and (b) influence of the initial randomization of particles on deviator stress-axial strain and volumetric strain-axial strain response of Labenne sand (Belheine et al. 2009).

3.3.2. Influence of Microscale Parameters (k_n, k_s, μ, β and η)

To understand the influence of the five microscale DEM parameters on the macroscale response of a virtual specimen subject to drained triaxial compression loading, a series of simulations were carried out, first by varying the elastic parameters (k_n and k_s) and then the rupture parameters (μ, β, η). The optimized values reported in Table 3.1 from the initial simulations were used as the baseline values for this analysis.

3.3.2.1. Microscale elastic parameters (k_n and k_s)

First, k_n and α ($= k_s/k_n$) were changed separately to predict the macroscale response. The macroscale elastic properties (elastic modulus E_0 and Poisson's ratio ν) were extracted from the simulations by considering linear elastic behavior persisted up to deviatoric strains up to 0.2%. Figure 3.6(a) shows the influence of the microscale normal stiffness k_n on E_0 and ν. E_0 increases with increasing microscale normal stiffness k_n. The log-linear relationship between E_0 and k_n reported by Kozicki and Donzé (2009) was also observed in this simulation. However, the small strain value of Poisson's ratio, ν, derived from the

numerical simulations decreases as k_n increases until k_n equals 300 MPa, beyond which ν remains relatively unchanged. The influence of the tangential stiffness k_s was examined by changing the value of α while keeping k_n constant at 600 MPa. Figure 3.6(b) shows the influence of varying k_s from 6 MPa to 300 MPa with k_n equal to 600 MPa on the value of E_0. It can be seen that increasing α (increasing k_s) leads to an increase in E_0 and a decrease in ν. The E_0 - α relationship presented in Figure 3.6(b) bears a very close resemblance with the E_0-k_n relationship shown in Figure 3.6(a), indicating that k_s (which is equal to αk_n) also should then influence the elastic response. Comparing the effects of k_n and α, it can be concluded that while both of these microscale elastic parameters can influence the macroscale Young's modulus, α has a dominant influence on the macroscale value of Poisson's ratio. Thus the value of α should be determined first to obtain the observed Poisson's ratio, after which k_n can be adjusted to match E_0 as described in previous section. This approach will be used in the modeling of sand improved by carbonate precipitation in a later section.

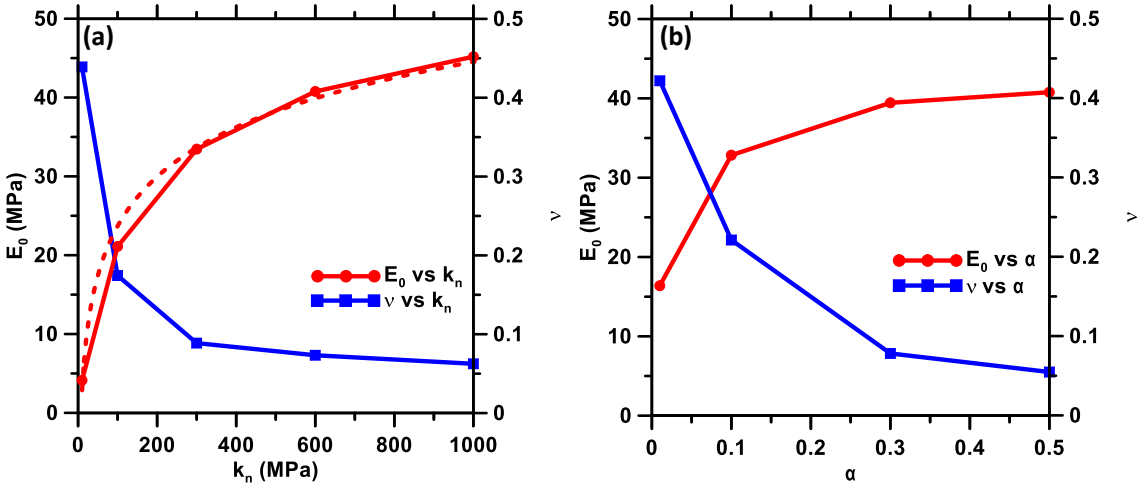

Figure 3.6: Influence of: (a) normal stiffness k_n, and (b) stiffness ratio α on the elastic modulus E_0 and Poisson's ratio ν of Labenne sand in drained triaxial compression from DEM simulations.

3.3.2.2. Microscale rupture parameters (μ, β and η)

To understand the influence of the rupture parameters on simulated drained triaxial compression behavior, a 2^3 factorial design was used. The elastic parameters were the same as given in Table 3.1 for all of these simulations. Two levels of μ (20^o and 40^o), β (0.025 and 0.10), and η (0.15 and 0.50) were used in the statistical analysis. Table 3.2 shows the eight different combinations that were employed in this analysis. Simulation A, which is the control, uses the rupture parameters from Table 3.1 that were used in the simulation shown in Figure 3.4. In simulations B to H, one or more of the rupture parameters are changed.

Figure 3.7 shows the deviator stress-axial strain, and volumetric strain-axial strain plots for the eight microscale rupture parameter combinations presented in Table 3.2. In the small strain range (<1%), none of the rupture parameters influence the macroscale response, as expected. To characterize the influence of the rupture parameters on the overall stress-strain response in each simulation, the relative deviation (δ_r) from simulation A (the baseline case) was calculated (as a percentage) as:

$$\delta_r = avg\left(\frac{\sigma_{d-i} - \sigma_{d-A}}{\sigma_{d-A}}\right).100 \tag{3.14}$$

where σ_{d-A} is the deviator stress at a certain strain for the simulation A, and σ_{d-i} is the corresponding value for simulation i. Table 3.2 presents the relative deviation of macroscale stress response of the each of the eight simulations.

Table 3.2: Summary of the 2^3 factorial design to evaluate the influence of the microscale rupture parameters μ, β and η on the stress-strain response of the DEM simulation

Simulation	Microscale rupture parameters			Relative deviation in deviatoric stress
	μ	β	η	
A (-)	20	0.025	0.15	--
B (μ)	40	0.025	0.15	47.1
C (β)	20	0.1	0.15	1.4
D (μ β)	40	0.1	0.15	46.7
E (η)	20	0.025	0.5	19.4
F (μ η)	40	0.025	0.5	101.2
G (β η)	20	0.1	0.5	30.8
H (μ β η)	40	0.1	0.5	135.3

As illustrated by the values in Table 3.2, changing the rolling stiffness coefficient β or the plastic moment limit coefficient η alone or in combination does not have a large influence on the stress-strain response, while any combination of parameters that includes a change in the microscale friction angle μ results in significant deviation from the control case. Figure 3.7(b) also clearly shows that the volumetric strain response is dominated by the microscale inter-particle friction angle μ. A comparison of the volumetric strain response from simulations A, C, E and G (which use a low friction angle of 20° and vary β and η) shows that the effect of both β and η is negligible when the friction angle is kept low. A comparison of simulations B, D, F and H shows that the effect of rolling stiffness coefficient β is also negligible when the friction angle is high (40°), but the plastic moment limit coefficient η has some influence on the volumetric strain response at high friction angle. Thus it can be safely stated that the microscale friction angle μ is mainly responsible for the macroscale deviatoric strain response predicted by the DEM numerical model while

a combination of the rupture parameters influences the macroscale volumetric strain response.

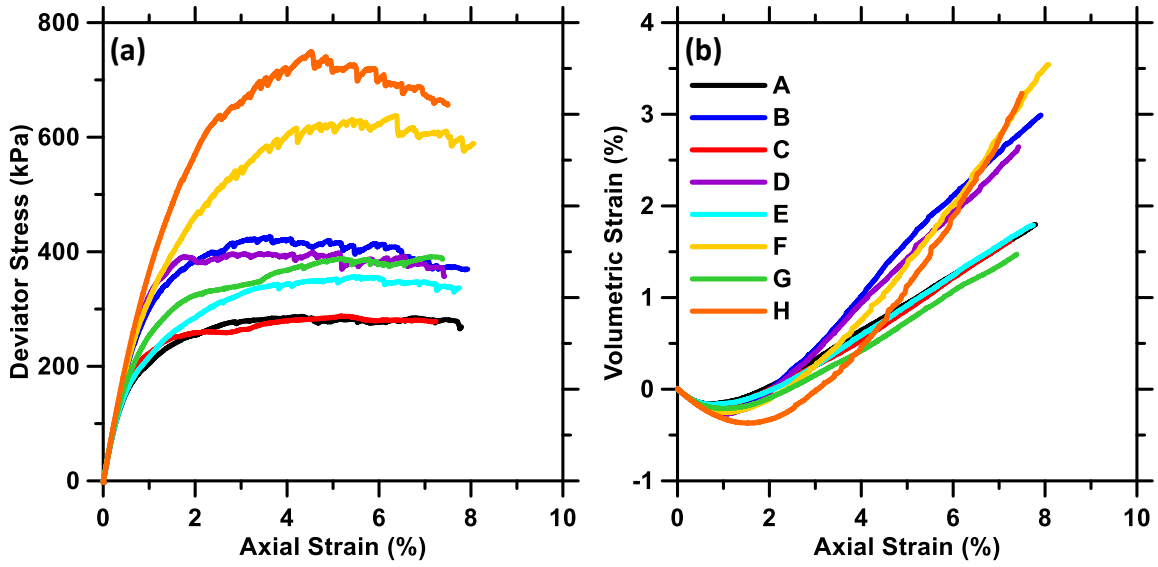

Figure 3.7: (a) Deviator stress versus axial strain and (b) volumetric strain versus axial strain for the DEM simulations summarized in Table 3.2.

Since the microscale friction angle (μ) is observed to be most important rupture parameter with respect to deviatoric stress-strain behavior based on the previous set of simulations, the influence of μ on the macroscale response was investigated. Figure 3.8 shows the influence of μ on the deviatoric stress-strain resposne when none the other parameters are changed from the baseline values. The value of μ was varied from 10^o to 50^o in the analyses presented in Figure 3.8. It is clear that increasing the microscale friction angle μ significantly influences both the deviatoric stress-strain and volumetric strain response. This observation emphasizes the need to obtain accurate microscale friction values for DEM simulations. The other rupture parameters, β and η, are more forgiving and some error in their estimation will likely not influence the simulation results to a large degree.

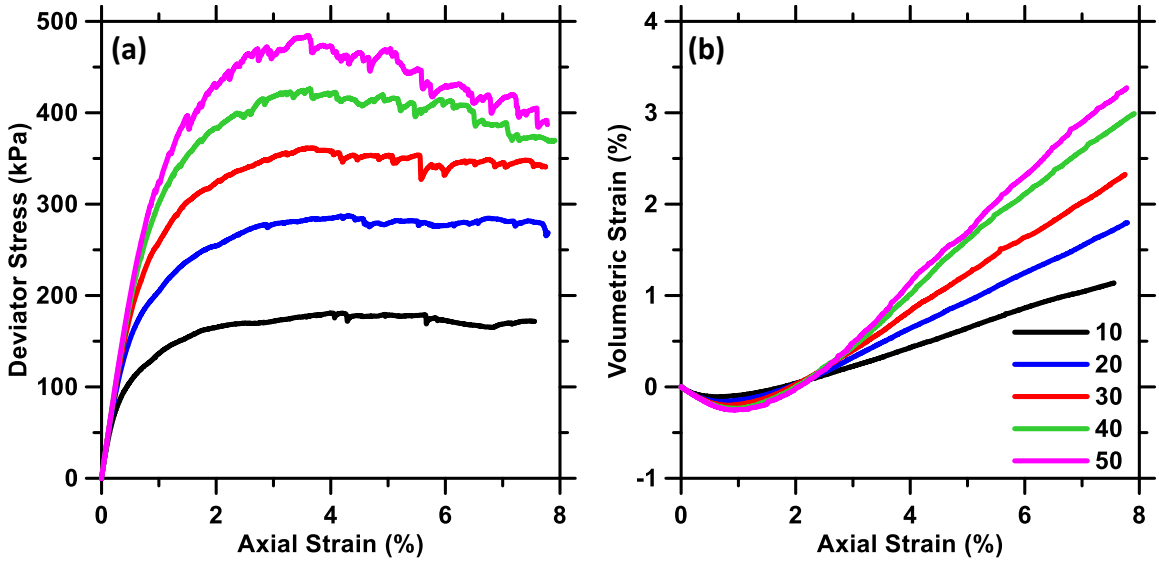

Figure 3.8: Effect of local friction angle on: (a) deviator stress-axial strain and (b) volumetric strain-axial response for DEM simulations of Labenne sand in drained triaxial compression.

The methodology discussed above was also used in the simulation of drained triaxial test on Karlsruhe sand (Widuliński 2009). The properties and microscale input parameters of Karlsruhe sand employed in the simulation are listed in Table 3.3. Figure 3.9 compares the simulation results to the experimental results. The good agreement between model predictions and experimental results indicates that the model can be employed to simulate the drained triaxial compression test of sands effectively. This understanding will be extended to the simulation of sands strengthened using microbial calcite precipitation in the next section of this chapter.

Table 3.3: DEM parameters used to simulate the macroscale response of Karlsruhe sand reported by Widuliński (2009).

Parameters	Karlsruhe sand (Widuliński
Void ratio (e_0)	0.53
Normal stiffness (k_n) (MPa)	120
Stiffness ratio ($\alpha = k_s/k_n$)	0.30
Inter-particle friction angle (μ) (°)	19
Rolling stiffness coefficient (β)	0.05
Plastic moment limit coefficient	0.5
Confining stress (kPa)	100
Number of particles	1000
Sample size (mm)	90 x 180 x 90

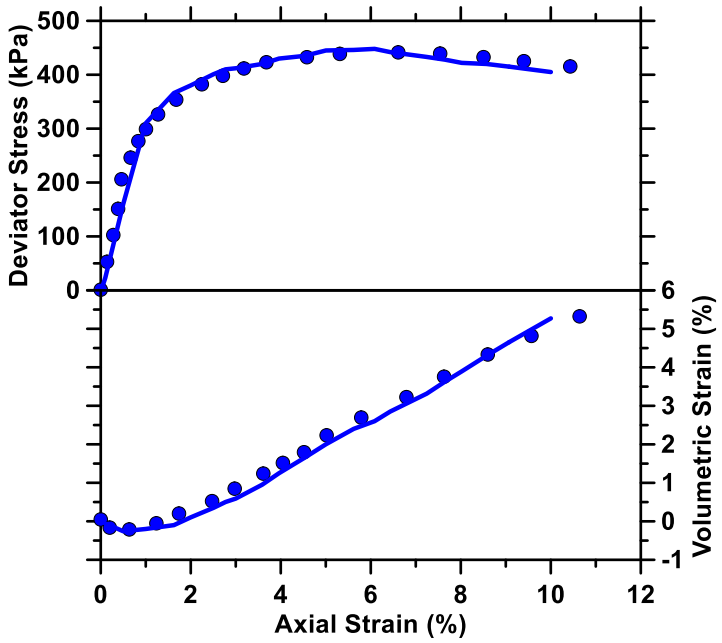

Figure 3.9: Comparison of DEM simulation (solid lines) to experimental data for macroscale response of Karlsruhe sand reported by Widuliński (2009).

3.4. Numerical Simulation of the Constitutive Response of Sand Strengthened Using MICP Under Consolidated Drained Triaxial Compression

The process of soil improvement via MICP is explained in detail by Montoya and DeJong (2015). MICP strengthens sand through the precipitation of calcite crystals on the surface of the sand particles, at the interparticle contacts, and in the void space. The calcite content,

morphology and spatial distribution of the precipitated calcite in a MICP-treated sand influences the stiffness, shear strength, and dilatancy of the improved soil (Kavazanjian and O'Donnell 2015a; Montoya and DeJong 2015). The constitutive behavior of MICP strengthened sand was evaluated using the DEM model as a function of calcite content and compared to experimental data. The simulations and experimental data were all for triaxial compression tests at a confining stress of 100 kPa.

3.4.1. Simulation of MICP Strengthened Sand Containing Low Calcite Contents (~0.5% by mass)

Kavazanjian and O'Donnell (2015) report that in their experiments on Ottawa 20-30 sand improved by MICP via microbial denitrification, when only a small amount of calcite (i.e., less than 1% by mass) was precipitated, no cementation between particles was observed and the precipitated calcite was expressed primarily as discrete crystals cladding the surface of the sand particles, as illustrated in Figure 3.10. Therefore, as the presence of small amounts of calcite does not contribute significantly to bridging between sand particles, the DEM numerical modeling scheme for MICP-treated sand with a small calcite content considers the sand grains together with the calcite crystal cladding as homogenized particles with microscale properties that are different from those of pure (untreated) sand grains. The DEM modeling approach described in the previous section is therefore used to model such systems.

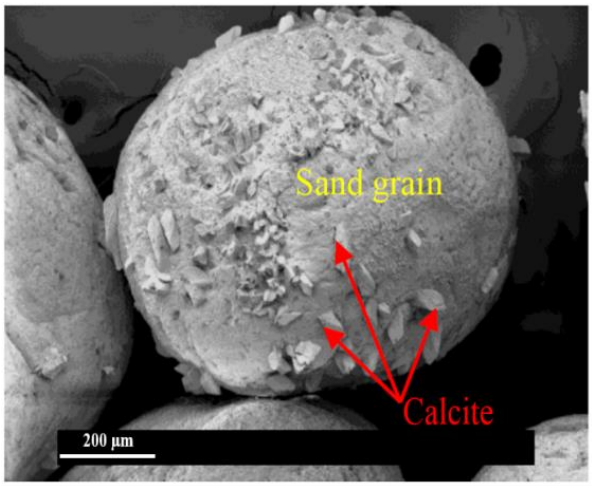

Figure 3.10: Calcite cladding the surface of a sand grain after microbial treatment (Kavazanjian and O'Donnell 2015a).

Simulations were conducted based on experimental results for MICP-modified 50/70 Ottawa sand presented in Montoya and DeJong (2015). The MICP modified sand modeled herein contained 0.6% by mass of calcite (~0.25% by volume). The simulation volume was generated using the sphere packing technique described previously to obtain the desired initial void ratio (0.73 for both the untreated and treated cases, as reported by Montoya and DeJong (2015). The microscale elastic and rupture parameters for the untreated sample, established using the methodology described in the previous section, are presented in Table 3.4. For the MICP-treated sand, the microscale parameters need to be modified to account for the effect of the calcite precipitates that roughen the particle surface and increase the strength, stiffness, and dilatancy of the sand. A closer look at the changes in the microscale parameters required to adequately model the constitutive response of the improved sand provides fundamental insights into the microscale changes brought about by MICP.

Table 3.4: DEM parameters used to simulate the macroscale response of untreated and treated Ottawa 50/70 sand reported by Montoya and DeJong (2015).

Microscale parameters	Experimental data set	
	Untreated	Treated
Void ratio (e_0)	0.73	0.73
Normal stiffness (k_n) (MPa)	100	300
Stiffness ratio ($\alpha = k_s/k_n$)	0.3	0.3
Inter-particle friction angle (μ) (°)	14.5	30
Rolling stiffness coefficient (β)	0.2	0.2
Plastic moment limit coefficient (η)	0.5	0.12
Confining stress (kPa)	100	

Figure 3.11 shows the numerical simulation results for both untreated and treated Ottawa 50/70 sand specimens together with the experimental results from Montoya and DeJong (2015). The calcite content of the treated sand was 0.6% by mass. To model the behavior of the MICP-treated sand, the stiffness ratio α was left unchanged, since the elastic stage (i.e., the initial small strain stage) of the volumetric strain-axial strain response is essentially unchanged with treatment, as can be seen in Figure 3.11. However the normal stiffness k_n was increased from 100 MPa to 300 MPa to account for the increase in stiffness of the treated soil compared to the untreated soil. Even though the calcite content is quite low, it is interesting to note that the normal and shear stiffness of the particles are significantly impacted, presumably by the change in particle roughness. Also, the inter-particle friction angle doubled (from 14.5^o to 30^o) as a result of the presence of calcite, resulting in the increases in both the peak stress and dilatancy angle necessary to match the experimental data. This observation is important since it indicates that MICP increases the dilatant properties of the treated sand by increasing the particle surface roughness. Finally, the plastic moment limit coefficient is reduced from 0.50 to 0.12 to simulate the post-peak phase of the treated sand. It also should be mentioned that although the rolling stiffness

coefficient is kept unchanged, due to the increase in shear stiffness the rolling stiffness (Equation 9) increases, again presumably due to the increase in the surface roughness of the particles.

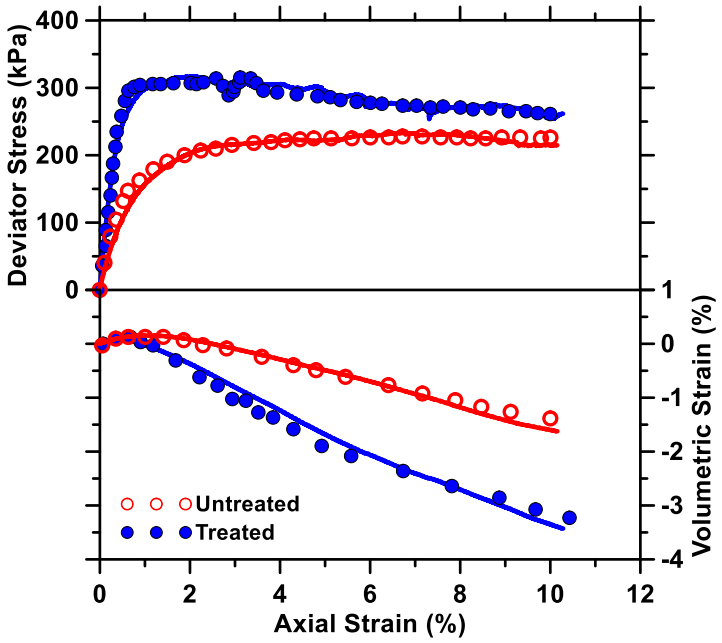

Figure 3.11: Comparison of DEM simulation (solid line) to experimental data for the deviator stress-axial strain and volumetric strain-axial strain response of untreated and treated (calcite content = 0.6% by mass) Ottawa 50/70 sand in drained triaxial compression reported by Montoya and DeJong (2015).

3.4.2. Simulation of MICP Strengthened Sand Containing High Calcite Contents (> 1% by mass)

Modifications to the DEM model were required to account for the effects of the bridging of the precipitated calcite between particles (i.e., inter-particle cementation). O'Donnell (2016) observed that at calcite concentrations greater than ~1% by mass calcite crystals not only clad the particle surfaces but also bridge between sand grains, as shown in Figure 3.12. The aforementioned DEM model cannot be directly applied to describe the constitutive response of such systems.

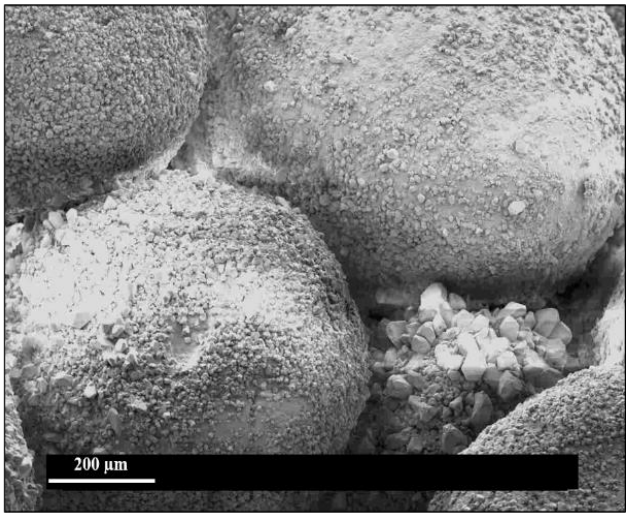

Figure 3.12: Calcite bridges between sand grains (Li 2015).

Several different DEM models have been employed to simulate cemented granular materials. One model employs breakable bonds formed by elastic beams connecting the center of spherical particles to represent cementation (Jiang et al. 2014; Obermayr et al. 2013). The bond is assumed to fail when a specified stress level in the beam is reached. In addition to the microscale elastic and rupture parameters detailed earlier, the elastic bond model requires several other parameters describing the bond elements including their elastic and shear moduli, a breakage stress, and a bond radius, to simulate soil behavior. More realistic microstructural scenarios where the cementing particles are modeled as tiny particles deposited around the larger sand grains have also been reported (Wang and Leung 2008b).

In order to simplify the DEM numerical model and minimize the number of model parameters, this study adopted a 'cohesive model' (Šmilauer et al. 2010) to describe the bridging effect of calcite between sand particles. After packing the particles under the desired confining stress, a cohesive shear strength is assigned to all of the existing interparticle contacts. It is therefore assumed that calcite bridges exist between all

contacted particles. The strength of each calcite bridge is represented by a shear cohesion (c_s) defined as:

$$c_s = C_s min(r_A, r_B)^2 \tag{16}$$

where, C_s is the unit shear strength of the bonds. In the case of regular packing of uncemented sand grains, $C_s = 0$.

To represent the effect of calcite bridges, which restricts the sliding and rotation between the particles, the frictional effects at bridged contacts (i.e., the cohesive contacts) are ignored as long as the contact is active and the maximum shear force that can be carried by the contact is equal to the shear cohesion of the contact.

$$\left\|\overrightarrow{F_s}\right\|_{max} = c_s \tag{17}$$

This assumes that at particle contacts connected by the calcite bridges, the shear stress is completely carried by the calcite bridge until the bridge breaks. Once the shear force between any two particles exceeds $\left\|\overrightarrow{F_s}\right\|_{max}$, the link ruptures and c_s between those particles is set to zero, at which point the state of contact between those particles is similar to the case where there is no inter-particle cementation. The particle contacts after the breaking of calcite bridges, together with any other new contacts generated during the simulation, are cohesionless and follow the Mohr-Coulomb failure criterion.

The modified DEM numerical model was implemented in YADE and used to simulate the influence of the calcite precipitation level using this cohesive model. Three MICP-modified specimens at calcite precipitation levels varying from 0.9% to 4.3% of calcite by mass (0.37% to 1.76% by volume) from Feng and Montoya (2015a) were modeled. The simulation volume again consisted of 1000 particles and a confining stress of 100 kPa was

employed. The total number of particle contacts after the packing stage for the three MICP-modified specimens was similar in each virtual specimen because of the similar initial void ratio (as shown in Table 3.5). The microscale parameters used to simulate the experimental results of Feng and Montoya (2015a) are presented in Table 3.5. Figure 3.13 compares the results of the numerical simulations to the experimental data.

Table 3.5: DEM parameters used to simulate the macroscale response of untreated and treated Ottawa 50/70 sand reported by Feng and Montoya (2015a).

Microscale parameters	Untreated	Mass % of calcite in the treated samples		
		0.9%	3.0%	4.3%
Void ratio (e_0)	0.727	0.728	0.725	0.721
Normal stiffness (k_n) (MPa)	180	2000	2500	3000
Stiffness ratio ($\alpha = k_s/k_n$)	0.15	0.15	0.15	0.15
Inter-particle friction angle (μ) (°)	18	18.5	22	30
Rolling stiffness coefficient (β)	0.12	0.12	0.12	0.25
Plastic moment limit coefficient	0.25	0.12	0.10	0.07
Shear strength C_s (MPa)	0	0.8	1.3	5.5
Confining stress (kPa)	100			

As shown in Table 3.5, the shear strength of the bonds (i.e., C_s) is increased as the calcite content increases to represent the enhanced bridging effect. It should be noted that, for the sample with 4.3% calcite, the value of shear strength required to reproduce the high peak stress observed in the experimental data is very high (5.5 MPa). Breakage of the contacts between particles results in the sharp drop in the deviatoric stress after the peak stress is exceeded, as observed in the experimental data. The post-peak stress decrease is also influenced by the confining pressure: higher confining pressures result in more ductile post-peak behavior (Feng and Montoya 2015a). At higher confining pressures, the translation and slip of particles are less dilative, and the cementation has less of an influence on stress-strain behavior (Hamidi and Haeri 2008). It was also found that the significant

increase in the elastic modulus of the specimen required to match the experimental data necessitated an increase in normal stiffness from 180 MPa for the untreated case to 2000-to-3000 MPa for the MICP-modified sands while keeping the stiffness ratio constant. The rolling stiffness coefficient β either remains unchanged or increases for higher calcite contents, but an increase in shear stiffness (k_s) (because of an increase in normal stiffness and constant α) effectively ensures that the rolling stiffness (k_r), and thus the resisting moment (Equation 9), increases with calcite content.

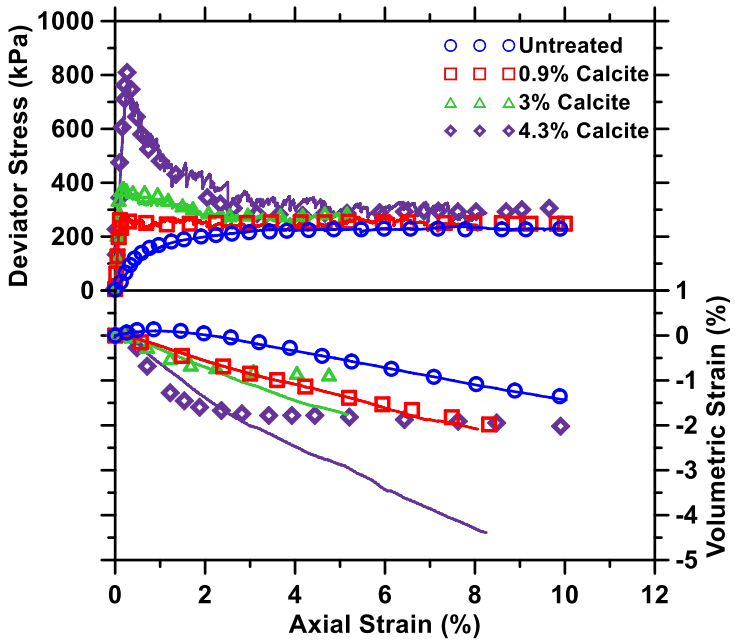

Figure 3.13: DEM simulation (solid lines) compared to experimental data from Feng and Montoya (2015a) for the deviator stress-axial strain and volumetric strain-axial strain response of MICP-modified Ottawa 50/70 sand (calcite content ≥ 0.9%).

The fact that a high β value was needed to accurately simulate the macroscale response of the sample with the highest calcite content, together with the high value of inter-particle friction angle for this case, indicate the extremely high roughness on the surface of sand grains due to the generation of calcite crystals. Figure 3.13 shows that the simulation is capable of matching the experimental results adequately. The exception to this finding is

the volumetric strain response for the samples strengthened with 3% and 4.3% calcite, which are not matched adequately by the model at larger axial strains. It is not clear if this is a model deficiency or if it may be attributed to strain localization and shear banding or some other facet of the experiments. More investigation is needed on this point. Figure 3.14 illustrates the distribution of the three-dimensional contact network and the compressive normal contact force distribution at the microscale in the untreated and MICP-modified sands containing calcite ranging from 0.9% to 4.3% by mass. All the visualizations in Figure 3.14 are at 1% axial strain, which is in (or very close to) the elastic range. For the untreated sand, the normal contact forces are rather small, and the distribution of forces is relatively uniform, attesting to the homogeneous nature of the medium. With increasing calcite content, the force distribution becomes increasingly non-uniform, with a few heavily loaded particle contacts transmitting a large share of the load at the portrayed axial strain level. The strengthening effect introduced by the calcite bridges enable the transmission of such high loads.

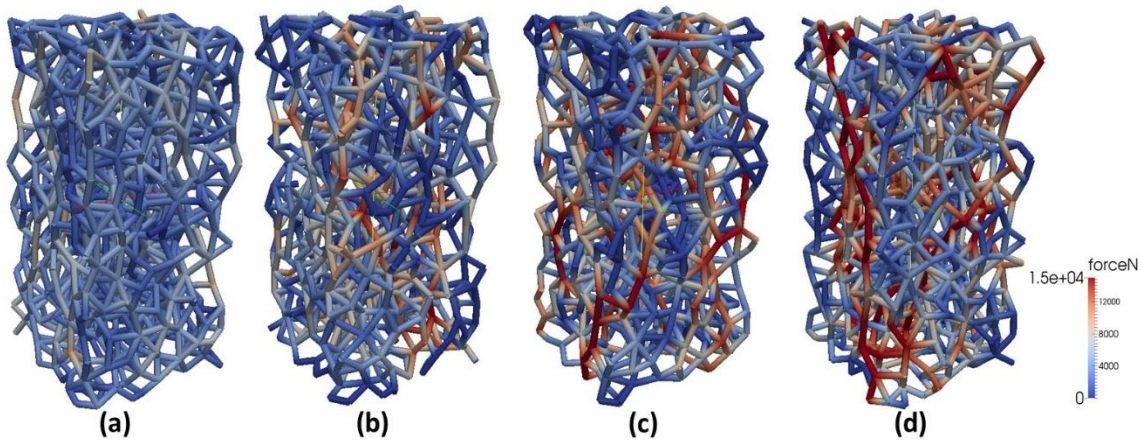

Figure 3.14: Contact force distribution in the DEM simulation volume at 1% axial strain for: (a) untreated sand, and (b), (c), (d) MICP-modified sand with 0.9%, 3%, and 4.3% calcite by mass.

Mohr circles constructed for the untreated and MICP-modified sands are shown in Figure 3.15. The peak and residual friction angles predicted by the DEM numerical model for the untreated and MICP-modified sands are compared in *Table 3.6* to those from experiments of Feng and Montoya (2015b). The simulations, through the use of judicious input parameters, are capable of predicting the peak and residual friction angles for four of the calcite contents evaluated in this work. Both the numerical and experimental data show that increasing calcite content enhances the peak friction angle more than the residual friction angle.

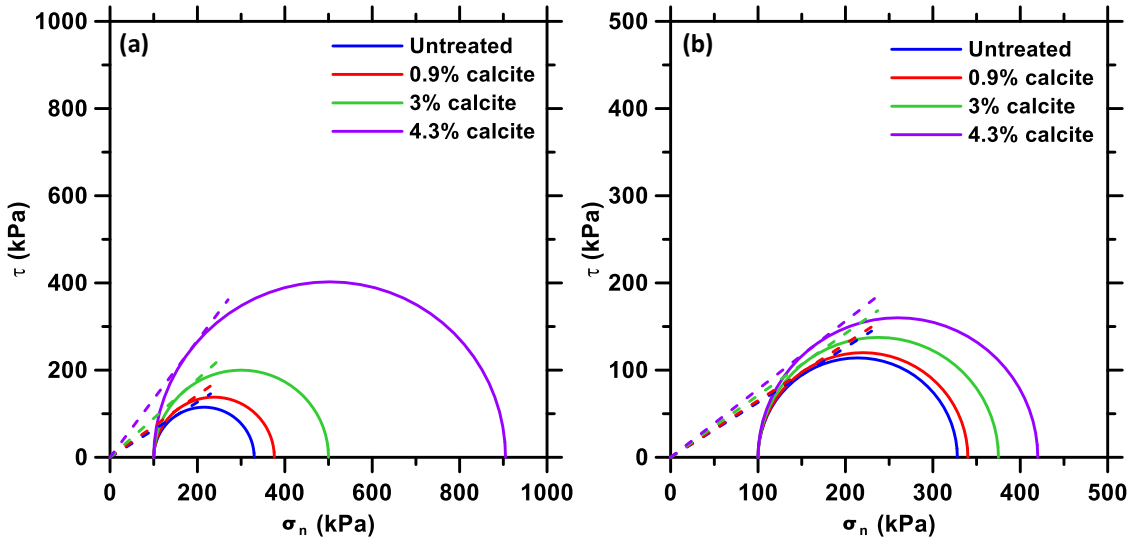

Figure 3.15: Mohr circles for: (a) peak friction angle, and (b) residual friction angle extracted from the DEM simulation for untreated and MICP-modified sands.

Table 3.6: Comparison of friction angle between DEM simulation and experimental results.

Calcite content (%)	Peak friction angle (°)			Residual friction angle (°)		
	Experimental (Feng and Montoya 2015b)	Simulated	Error (%)	Experimental (Feng and Montoya 2015b)	Simulated	Error (%)
0	32.8	32.3	1.5	32.2	32.2	0
0.9	34.2	35.4	3.5	32.8	33.1	0.9
3.0	39.5	41.8	5.8	34.5	35.4	2.6
4.3	53.1	53.2	0.2	38.2	38.0	0.5

3.5. Summary and Conclusions

A DEM model was developed to represent the behavior of untreated sand and sand treated using microbially induced carbonate precipitation (MICP). The open source DEM environment YADE was used for the model. A moment transfer law was used along with a radii expansion-based sphere packing procedure to create virtual specimens for simulation of triaxial compression under drained conditions. The five microscale (two elastic and three rupture) parameters required for DEM simulations were determined based on experimental deviator stress-axial strain and volumetric strain-axial strain behavior reported in the literature for two different sands. Guidance regarding the evaluation of the five microscale parameters using the DEM model presented herein were obtained from a sensitivity analysis.

The triaxial response of MICP-modified sands containing both low (~0.5% by mass) and high (>1% by mass) amounts of precipitated calcite were simulated under drained triaxial compression conditions. For low calcite contents, because the precipitated calcite forms on particle surfaces and does not contribute to bridging (cementation) of the sand particles, the sand grains and calcite together were considered as homogenized particles in the DEM

simulations. The DEM model was shown to accurately reproduce the experimentally-observed deviatoric and volumetric stress-strain behavior of these MICP-modified sands with low calcite content, including the increased dilatancy of the treated sand.

For high (>1% by mass) calcite contents, the DEM model was modified by assigning a cohesive shear strength to the particle contacts. It was assumed that the shear stress between two cemented particles was completely carried by the calcite bridges until they break. After the breaking of calcite bridges, the broken particle contacts along with new contacts generated during the simulation were treated as contacts between uncemented soil particles. Three different MICP-modified sands, with calcite contents ranging from 0.9% to 4.3% by mass, were simulated using this technique, with satisfactory results. The peak and residual friction angles predicted by the simulations were very comparable to the experimental results. However, there were some discrepancies between the predicted and observed volumetric response at larger strains for the two highest calcite contents. Visualization of the compressive normal contact force distributions demonstrated their increasingly non-uniform nature as calcite content increased, showing that there are a few heavily loaded particle contacts that transmit a large share of the load in the cemented sand.

The DEM model and the simulations showed that the model is capable of reproducing the macroscale properties of granular materials with simplified descriptors of its microstructure. The contribution of precipitated calcite to the mechanical behavior of the MICP strengthened sand was based upon the micro-structural nature of the precipitated calcite (e.g., whether calcite just coats the particles so that a homogenized particle can be assumed, or creates distinct interparticle contacts). The model is expected to useful in identifying the desired levels of cementation for the design of MICP treatment strategies

without a large number of trial-and-error experiments. The DEM simulations may also be useful as predictive tools for macroscale soil behavior depending on available computation capacity.

4. PARTICLE-SCALE MECHANISMS IN UNDRAINED TRIAXIAL COMPRESSION OF BIO-CEMENTED SANDS: INSIGHTS FROM 3D DEM SIMULATIONS WITH FLEXIBLE BOUNDARY

4.1. Introduction

Microbially induced carbonate precipitation (MICP) is emerging as a promising means of improvement of granular soil. Bacteria mediates the precipitation of calcium carbonate that cements the soil grains in this method (DeJong et al. 2006, 2010, 2013; Mortensen and DeJong 2011), thereby improving its properties including mechanical strength and stiffness, and resistance to liquefaction (DeJong et al. 2006; van Paassen et al. 2010; Kavazanjian and O'Donnell 2015). MICP is a complex biochemical process. There are several geomicrobiological processes capable of inducing MICP, including hydrolysis of urea (ureolysis) and dissimilatory reduction of nitrogen (denitrification). The details of these two processes have been extensively reported (DeJong et al. 2006, 2013; Hamdan et al. 2017).

Whether uncemented or cemented, granular materials such as sands consist of contacting grains – their arrangement varies based on the sand characteristics and levels of compaction. Continuum models are unable to provide useful information on the physical processes occurring at the particle scale in granular systems because of its inherently discontinuous and heterogeneous nature. Hence, discrete element methods (DEM) have been used in a number of studies to understand the response of sands under several conditions including drained and undrained triaxial testing (Gong 2008; Belheine et al. 2009; Wang and Li 2014; Kozicki et al. 2014; Cil and Alshibli 2014). In the DEM environment, the individual particles are allowed to rotate, slide, and separate. These studies have demonstrated the

immense potential of DEM simulations to predict the behavior of soil during triaxial compression.

While several studies exist on DEM simulations of unbonded particles, they are limited with respect to simulations on cemented granular media (Wang and Leung 2008b; Yang et al. 2016). In order for simulations on bio-cemented media to be realistic, considerations of the microstructure, especially the particle bonds (de Bono et al. 2015; Camusso and Barla 2009; Feng et al. 2017; Obermayr et al. 2013; Vallejos et al. 2016), are required. Our recent work (Yang et al. 2016) described the DEM simulations of sand strengthened using MICP via denitrification under drained triaxial conditions. Multiple microstructural bonding scenarios were considered based on the carbonate content and microscopic evidence. Here, we examine the particle-scale mechanisms in triaxial compression of MICP strengthened sands under undrained conditions. The same five-parameter DEM model used in our earlier work, consisting of two elastic and three rupture parameters, is used. A cohesive bond model is used to describe calcite bridging (i.e., cementation) between particles. A simplified modeling scheme with a representative bond strength between the particles (rather than a range of bond strengths, which probably is more realistic) is implemented. A unique particle facet (PFacet)-based flexible membrane is used to perform virtual undrained triaxial compression tests under constant volume conditions to provide adequate representation of the macroscale constitutive response under undrained loading. Microstructural features during the triaxial test, such as strain localization (i.e., shear band formation), variation in the number of nearest neighbor particles (i.e., coordination numbers), and evolution of force chains between the particles, are examined in detail to provide fundamental insights into the behavior of MICP strengthened sands.

4.2. Numerical Modeling Using Discrete Element Method (DEM)

The discrete element method (DEM) (Cundall and Strack 1979) is a micromechanical method that is extensively used to investigate the behavior of granular materials. Since granular materials such as soils are inherently discontinuous, DEM, where each grain is considered independently, is an appropriate modeling tool. The macro mechanical response of the material such as strength, stiffness, dilatancy, and strain localization can be predicted using microscale properties of the material. Five microscale parameters are generally required for DEM simulations of granular materials. These parameters include the normal and tangential contact stiffness, the interparticle friction angle, the rolling stiffness coefficient, and the plastic moment limit coefficient (Plassiard et al. 2009). A number of commercial and open-source software platforms are commonly used to implement DEM simulations of granular materials. In this chapter, we use the open-source platform YADE (Kozicki and Donzé 2009) to simulate the response of untreated and MICP strengthened sands. YADE enables the implementation of particle generation, packing algorithms, and boundary schemes to simulate experiments on granular materials.

Below, we recall the generic aspects of DEM for simulating a family of spheres. Detailed description and formalisms can be found elsewhere (Belheine et al. 2009; Plassiard et al. 2009; Widuliński et al. 2009; Yang et al. 2016). To represent the surface roughness and irregularity of sand grains, a Moment Transfer Law (MTL) is introduced in the formalisms of classical DEM. MTL enables the modification of the local constitutive law of classical DEM by introducing an additional component at each contact point through which rolling resistance can be specified. The rolling resistance indicates that a couple that resists particle rotations can be transferred between the discrete elements through a contact.

Figure 4.1 shows two spheres A and B with radii of r_A and r_B in contact. The interaction force between the particles can be decomposed into a normal force, a shear force and a contact moment, represented by vectors $\vec{F}_n$, $\vec{F}_s$ and M, respectively. The normal and shear forces as well as the contact moment are related to displacements through the normal stiffness k_n, shear stiffness k_s and rolling stiffness k_r as:

$$\vec{F}_n = k_n U \vec{n} \tag{4.1}$$

$$\Delta \vec{F}_s = k_s \Delta \vec{U}_s \tag{4.2}$$

$$\Delta M_e = k_r \Delta \theta \tag{4.3}$$

In the above equations, U is the relative normal displacement between two spheres, $\vec{n}$ is the unit normal vector, $\Delta \vec{U}_s$ is the incremental tangential displacement, and $\Delta\theta$ is the rotational increment between two spheres. The tangential force $\vec{F}_s$ is obtained through the summation of Equation 4.2 and the elastic moment is obtained through summation of Equation 4.3. The elastic rolling is limited by a plastic moment M_p that is related to the normal force through a dimensionless plastic moment limit coefficient (η), thus simulating the elastic-plastic behavior of rolling contact.

Since every particle in a single-phase system has the same properties, the relationships between normal stiffness, shear stiffness and rolling stiffness can be written as:

$$k_s = \alpha k_n \tag{4.4}$$

$$k_r = \beta k_s r_A r_B \tag{4.5}$$

Here, the shear-to-normal stiffness ratio (k_s/k_n) is defined as α. β is a dimensionless coefficient defined as the rolling stiffness coefficient.

For non-cohesive materials, shearing (sliding) begins at the contact point where $\vec{F}_n$ and $\vec{F}_s$ satisfies the Mohr-Coulomb rupture criterion:

$$\|\vec{F}_s\| - \|\vec{F}_n\| tan\, \mu \leq 0 \tag{4.6}$$

where μ is the inter-particle friction angle.

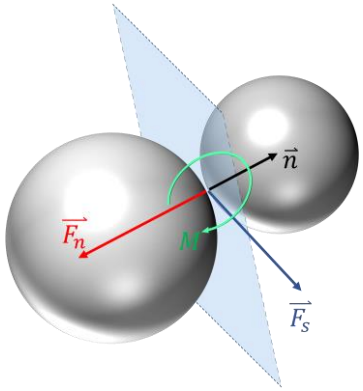

Figure 4.1: Two spheres in contact, showing the normal ($\vec{F}_n$) and tangential ($\vec{F}_s$) contact force vectors, the contact moment vector ($\vec{M}$) and the unit normal vector ($\vec{n}$).

To simulate cemented granular materials such as sands strengthened by MICP, a cohesive bond model was adopted in our previous work (Yang et al. 2016). To model the cementation bonds between the particles, a cohesive shear strength (bond strength) was assigned to all the existing contacts after the particles were packed under the desired confining stress. The bond strength is considered to increase with the degree of cementation. No attempt was made in this study to assign varying strengths to different bonds because it would have necessitated packing of different particle types separately, which introduces system instability and increases the computational expense significantly. However, distribution of bond strengths is likely to influence the material response (de Bono et al. 2015) and is a topic of an ongoing investigation. In addition, another open question is

whether changes in the quantity of bonds reflect the cementation levels either independently or in conjunction with a bond strength distribution.

Shear cohesion (c_s) is defined for the existing contacts as:

$$c_s = C_s min(r_A, r_B)^2 \tag{4.7}$$

Here, C_s is the unit shear strength of the bonds. For uncemented sand grains, $C_s = 0$.

The cementing bridges between the particles restrict sliding and rotational motions. Thus the frictional effects of all existing cohesive contacts are ignored as long as the particles are bonded. The maximum shear force between two bonded particles is then equated to the force of cohesion.

$$\left\|\overrightarrow{F_s}\right\|_{max} = c_s \tag{4.8}$$

It is assumed here that the shear stress is completely carried by the bond between the sand particles until the bond breaks (i.e., it is assumed that cementation bond cohesion is mobilized before frictional resistance is mobilized). Drained triaxial compression tests on cemented sands have shown that increasing cementation generally increases the cohesion intercept of the Mohr-Coulomb failure envelope while the friction angle remains relatively unchanged (O'Donnell 2016), indicating that the above-mentioned assumption is realistic. Once the shear force between any two particles exceeds the cohesive force $\left\|\overrightarrow{F_s}\right\|_{max}$, the bond breaks, and consequently c_s between those particles is assigned a value of zero, similar to that in the uncemented case, and rolling friction governs particle interaction. Any other particle contacts created after the breaking of the bonds during the simulation due to relative movement of particles are considered to be cohesionless and follow the Mohr-Coulomb failure criterion.

4.3. Simulation of Undrained Triaxial Response of Saturated Sand

Simulation methods for consolidated isotopically undrained triaxial compression (CIUC) testing of granular materials can be generally classified into two broad categories: (i) constant volume methods, and (ii) coupled methods. In the former, the solid and the pore water phases are assumed to be incompressible. Thus the sample volume remains constant during the loading process to maintain the undrained condition. This method has been widely used to simulate the CIUC test because the constant volume condition is easier to attain through controlling the volumetric deformation of the sample and is computationally straightforward (Gong et al. 2011; Liu et al. 2015). The constant volume method, though, is limited to saturated samples. The coupled methods consider fluid and fluid-particle interactions directly and the equations for fluid flow and particle motions are solved simultaneously (Catalano et al. 2014). It has been shown that the results from the constant volume and coupled methods agree reasonably well for CIUC test (Liu et al. 2015). However, there are certain situations where the assumption of constant volume is not always valid – prominent of these being the cases of highly dense samples and high strain rate testing (Hanley et al. 2013).

4.3.1. Simulation with Rigid Boundaries

The constitutive response of untreated and MICP-modified sands under CIUC is numerically modeled in this section using the constant volume method. Rigid boundaries, the most commonly employed boundary type in DEM simulations (Cheung and O'Sullivan 2008) were used in the first set of simulations. The tests being modelled were fully saturated ($B > 0.95$, where B is the ratio of the increase in pore water pressure to the increase in isotropic confining pressure; samples with $B > 0.95$ are assumed to be fully

saturated (Kavazanjian and O'Donnell 2015)). To maintain constant volume of the numerical sample, strain-controlled boundary conditions were introduced by assuming a zero volumetric strain, given as:

$$\varepsilon_v = \varepsilon_1 + 2\varepsilon_3 = \dot{\varepsilon_1}\Delta t + 2\dot{\varepsilon_3}\Delta t = 0 \tag{4.9}$$

where ε_v is the volumetric strain, ε_1 and ε_3 are the axial and lateral strains, and $\dot{\varepsilon_1}$ and $\dot{\varepsilon_3}$ are the corresponding strain rates. From the above equation, the strain rate of side walls can be related to the axial strain rate (which corresponds to the loading speed) as:

$$\dot{\varepsilon_3} = -0.5\dot{\varepsilon_1} \tag{4.10}$$

The simulation was carried out in three major stages. First, the numerical sample is generated by assigning random positions to a fixed number of spheres in a prismatic volume. Second, a gravity-free radii growth process is introduced along with adjustment of inter-particle friction angle to result in the target void ratio at the initial effective confining stress, σ'_{3_ini}. The initial confining stress is the difference between the cell pressure and the internal pore pressure. More details on the particle generation and packing process can be found in (Yang et al. 2016). After the generation of the target virtual sample, undrained deviator loading was imposed under a gravity-free condition in the third stage. The bottom and top boundaries move vertically while the lateral boundaries are controlled by Equation 4.10 to maintain a constant volume within the sample. Figure 4.2 illustrates these different stages. During the loading stage, while the cell pressure is maintained constant, the internal pore pressure changes due to axial loading, which causes a change in the effective lateral stress, σ'_3. Thus the excess pore water pressure u_g can be calculated by monitoring the stresses in side walls of the sample:

$$u_g = \sigma'_{3\_ini} - \sigma'_3 \tag{4.11}$$

σ'_{3_ini} and σ'_3 are the initial effective stress and the effective stress in the side walls during the simulation, respectively. All the simulations were carried out at a strain rate of 0.1/s.

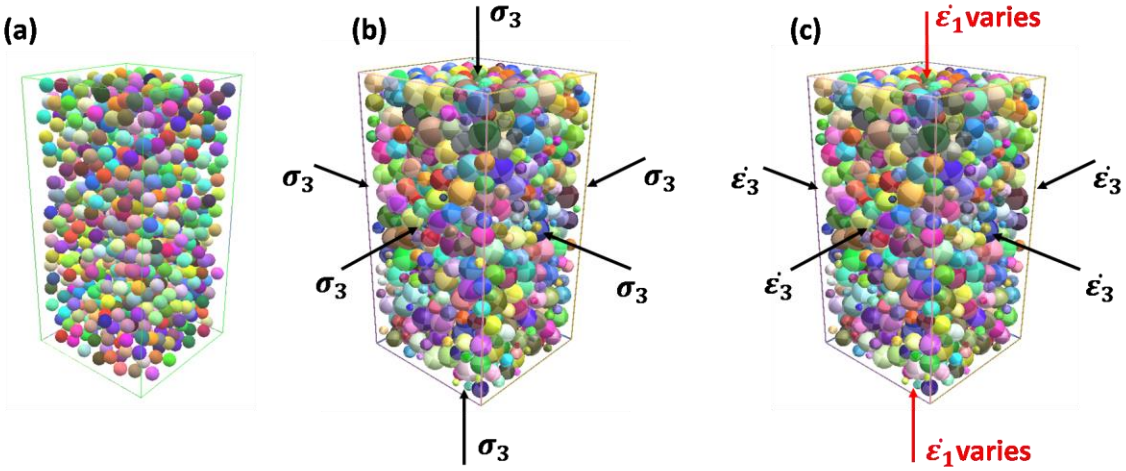

Figure 4.2: (a) Initial volume of spherical particles with random positions; (b) virtual specimen after radii expansion with desired void ratio and confining stress; and (c) deviator loading with constant volume method.

Two sets of experimental data from (Montoya and DeJong 2015) were selected for numerical simulations: one untreated sand specimen with a relative density (D) of 37% as the control case, and a strengthened sand specimen with a D of 45% treated by ureolysis. The calcite content of the latter was 5.31% by mass. The Ottawa 50/70 sand had a median particle size (d_{50}) of 0.22 mm. The undrained test specimen diameter was 72 mm, with a height-to-diameter ratio of 2. All the specimens were back pressure saturated (B > 0.95) at an effective confining stress of 100 kPa before conducting an undrained triaxial compression test. The microscale parameters used for the simulation are listed in Table 4.1. Note that a value of 9 MPa is used for the bond strength of the cemented samples. It is rather difficult to directly measure the calcite bond strength from experiments, and hence

an estimated value of bond strength is used, which results in the simulation matching the experimental data. The simulation volume measured 7.2 mm in diameter, with a height-to-diameter ratio of 2, and consisted of 1000 particles, which was found to be adequate to simulate the mechanical behavior of cemented and uncemented sands from an earlier study (Yang et al. 2016). Extensive details on determining and calibrating the micromechanical parameters for DEM simulations of sand under triaxial compression can also be found in (Yang et al. 2016).

Table 4.1: DEM parameters used to simulate the macroscale response of untreated and treated Ottawa 50/70 sand under undrained triaxial compression (Montoya and DeJong 2015).

Microscale parameters	Untreated	Treated
Void ratio (e_0)	0.75	0.73
Normal stiffness (k_n) (MPa)	100	2000
Stiffness ratio ($\alpha = k_s/k_n$)	0.3	0.3
Inter-particle friction angle (μ) (°)	25	47
Rolling stiffness coefficient (β)	0.1	0.8
Plastic moment limit coefficient (η)	0.002	0.003
Bond strength C_s (MPa)	--	9
Confining stress (kPa)	100	100

Figure 4.3 shows the comparison of the experimental and simulated deviator stress and excess pore pressure as functions of axial strain. The deviator stress response shows oscillations which can be attributed to the larger particle sizes in the simulation, as reported in (Lee et al. 2012). Each particle in the simulation volume is about 20 times larger than the actual particles used in these tests to minimize the computational cost. It can be noticed from Figure 4.3 that while both the deviator stress and excess pore pressure predicted by the numerical model for the untreated sand specimen are in good agreement with the experimental results, the model fails to predict the response of MICP strengthened sand

specimen, particularly with respect to pore pressure at strains greater than 1 percent. Both the deviator stress and excess pore pressure are incorrectly estimated at strains greater than 5% for the MICP strengthened sample; the excess pore pressure more so. The simulation for the cemented sand indicates a strain hardening type behavior while the experimental data shows a strain softening behavior as the cementation degrades within a zone of strain localization (i.e., within a shear band (Montoya and DeJong 2015)). The rigid boundary does not apply a uniform lateral pressure and thus hinders the onset and growth of strain localization in numerical simulation. Thus, while this boundary condition is acceptable in the case of untreated, loose sands where strain localization was not very pronounced, it is clearly an improper approach to simulate heavily cemented granular media which develop prominent shear bands. Thus instead of the rigid wall boundary, a flexible boundary is needed to enable accurate representation of the stress-strain relationships and the prediction of strain localization in cemented media.

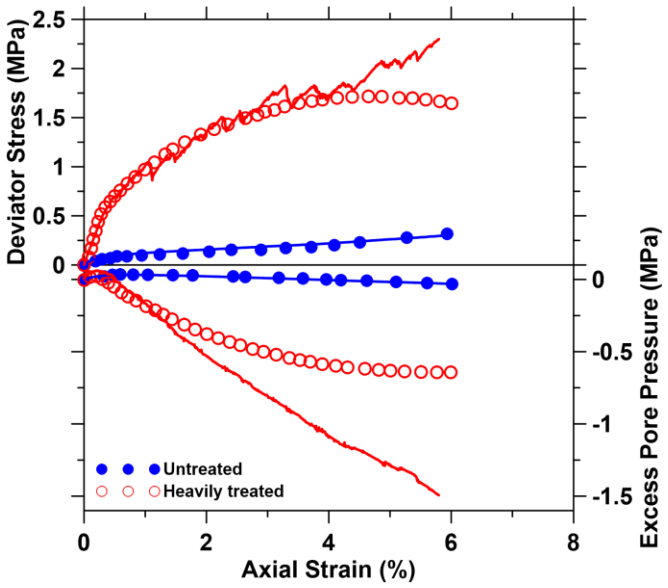

Figure 4.3: Deviator stress and excess pore pressure predicted by the DEM model (continuous lines) for uncemented sand and heavily cemented sand and its comparison with experimental data (symbols) from (Montoya and DeJong 2015).

4.3.2. Simulation with Flexible Boundaries

The limitations of a rigid boundary in triaxial simulations have led to the development of virtual flexible boundaries that behave like the latex membrane used in laboratory experiments. However, there are only a limited number of studies that involve the use of flexible boundaries (Cheung and O'Sullivan 2008; Cil and Alshibli 2014; Iwashita and Oda 1998, 2000; Jiang et al. 2011; O'Sullivan 2011; Wang and Tonon 2009). A bonded particle approach is generally used to mimic the flexible membrane (Iwashita and Oda 1998, 2000; Cil and Alshibli 2014). However, it has been reported that a bonded particle model that consists of clusters of small spherical particles introduces numerical roughness at the interfaces and compromises predictive capability (Effeindzourou et al. 2016). Flexible membranes have been modeled with rigid discrete elements having constrained degrees of freedom with limited success (Lee et al. 2012). Hence, this chapter employs a recently developed methodology that uses Minkowski sums of polytopes and spheres to describe the topology of the objects (Effeindzourou et al. 2016).

4.3.2.1. PFacet element to create deformable membrane

A new element called PFacet (particle facet), which is geometrically constructed by the Minkowski sum of a triangular facet and a sphere, is used as the fundamental element to model a flexible boundary (Effeindzourou et al. 2016). This is based on the cylinder elements developed in (Bourrier et al. 2013). The PFacet element, shown in Figure 4.4(a), is composed of three similarly-sized nodes (spheres) and three connections (cylinders). The introduction of PFacet element accounts for sphere-PFacet, cylinder-PFacet, and PFacet-PFacet interactions. Both the facets and the cylinders are deformable and can be connected to form membrane-like structures. These discrete elements have been developed in YADE

to simulate deformable objects such as membranes within the DEM framework. In a DEM simulation, once a contact between particle and P-facet element is detected, a virtual sphere (with same size as nodal sphere) will be generated within the P-Facet element under the contact point to interact with the particle. The movement and force of the virtual sphere is then distributed to the three nodal spheres. Thus, each of the P-facet elements will have different kinetic movements and will essentially allow free deformation under particle-element interactions. More details on the element itself, how the interactions are accounted for, contacts are tracked, and time integration sequence are presented in (Effeindzourou et al. 2016). A schematic view of a flexible membrane boundary constructed by PFacet elements is shown in Figure 4.4(b).

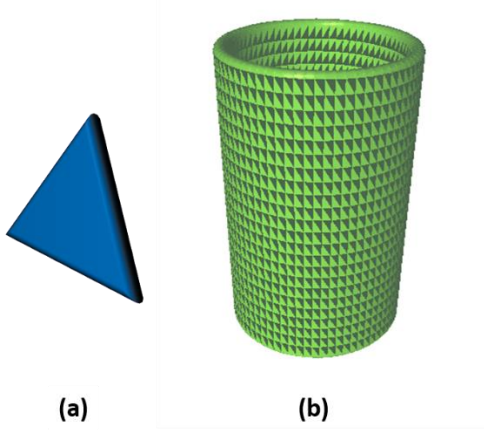

Figure 4.4: (a) PFacet element, and (b) cylindrical membrane created using PFacet elements. Spheres form the vertices of the triangular facet and deformable cylinders, the sides.

4.3.2.2. Virtual specimen preparation and numerical CIUC testing

Four main steps are required to simulate the CIUC triaxial test using a flexible membrane boundary: (1) generation of the packed particles for the desired void ratio under rigid boundaries, (2) replacement of rigid lateral walls with the flexible membrane, (3) isotropic compression of the specimen until the desired confining stress is reached, and (4) axial

compression of the specimen. Figure 4.5 demonstrates the sequence of virtual CIUC experiments.

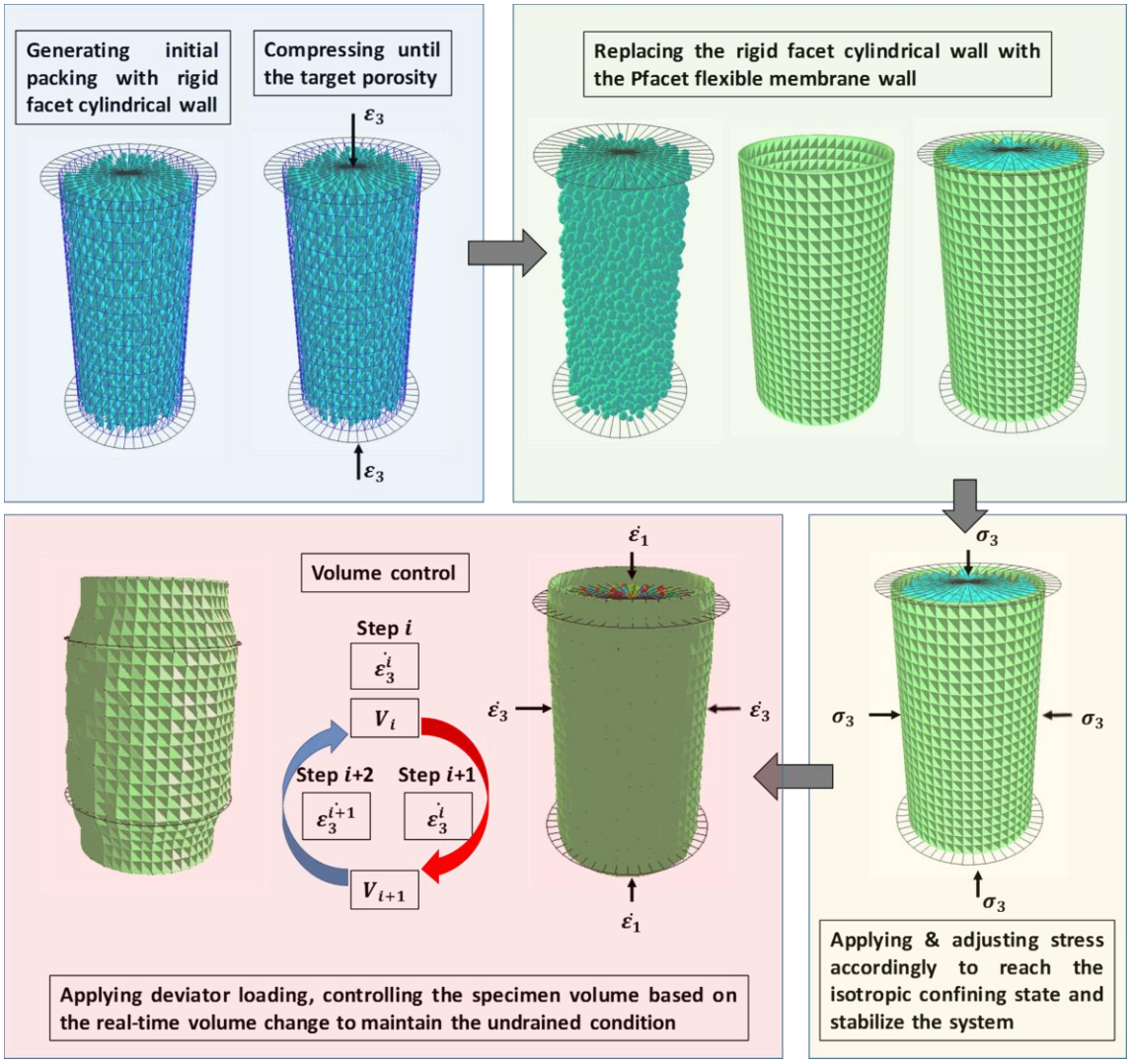

Figure 4.5: Flowchart depicting numerical simulation of undrained compression test using a flexible membrane boundary. (1): particle packing for desired porosity in a rigid container; (2): replacing the rigid container with a PFacet flexible membrane wall; (3) arriving at isotropic confinement, and (4) applying deviator loading and implementing the constant volume condition in every step.

In the first phase, the top and bottom platens that apply compression and cylindrical wall that encloses the specimen were generated using rigid facet elements. The desired particle size distribution of the sand was generated in the cylinder using random dense sphere

packing. The top and bottom platens were then subjected to a velocity to compress the sample slowly to attain the target void ratio while keeping the lateral wall fixed. During this stage, the interparticle friction angle is set to a small value (typically around 1^{o}) and the boundary walls are assumed frictionless to ensure that the stresses applied on the walls remain normal. After the generation of packed particles with the desired void ratio, the lateral cylindrical wall is replaced by the flexible membrane wall made of PFacet elements. The interaction between the spherical sand particles and the PFacet elements that make up the cylindrical wall are established during this stage while the interactions between the PFacet elements and the rigid facet elements that make up the top and bottom platens are disabled to ensure that the deformation of lateral membrane is entirely due to the interaction between sand particles and flexible membrane.

Centripetal velocity was then applied to all the nodes of the membrane as well as to the top and bottom platens to simulate the isotropic consolidation process in two steps. The average stress on the flexible membrane (over all the nodes in the membrane; nodes being the spheres in the PFacet elements) and the stress in the axial loading platen were monitored as the confining stresses in lateral and axial directions respectively. In the first step, a relative high velocity was assigned to both the PFacet nodes and the platens to quickly approach the desired confining stress. In the second step, the sample was consolidated and stabilized through application of small velocities to the PFacet nodes and the platens. During both steps, the velocities of membrane and the platens were adjusted in accordance with the difference between the axial and lateral confining stresses to maintain the isotropic stress status of the sample (i.e., 100 kPa in all directions).

Once the sample is ready for deviator loading, the rigid loading platens are moved in the axial direction. To maintain the constant volume condition for the undrained compression test, the lateral velocity applied on the membrane nodes is adjusted after each time step while the axial velocity acting on the loading platens is kept constant. The initial volume (V_0) of the sample is recorded before the deviator loading stage. Then the real-time volume (V_i) is recorded after every time step and compared with the sample volume from the previous time step (V_{i-1}). The difference in volumes (ΔV) is then determined and the lateral velocity of each node in the membrane is adjusted accordingly and applied to the next time step to correct the volume difference.

4.3.3. Comparison Between Simulated Results Under Different Boundary Conditions

The procedure for the undrained compression test discussed in the previous section was implemented for the same uncemented and cemented sand test results shown in Figure 4.3. The micromechanical parameters provided in Table 4.1 were used. Figure 4.6 shows the deviator stress-axial strain, and excess pore pressure-axial strain relationships when rigid or flexible boundaries are used. Better agreement between the numerical simulation and the experimental data was achieved for both uncemented and cemented specimens than achieved using the constant volume method.

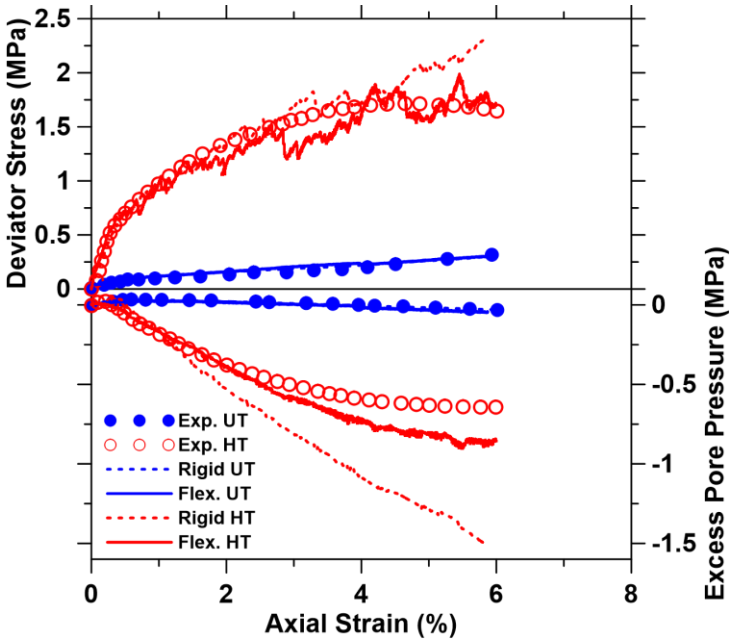

Figure 4.6: Deviator stress and excess pore pressure predicted by the DEM models employing rigid or flexible boundaries, for uncemented sand and heavily cemented sand. The experimental data comes from (Montoya and DeJong 2015). In the legend, UT indicates untreated, and HT, heavily treated.

In simulations of triaxial compression tests, the elastic stage of the deviator stress-axial strain relationship is predicted well, irrespective of the boundary conditions. The rigid wall boundary condition is found to result in a higher strength than the membrane boundary. Beyond the initial elastic stage, which is similar under both boundary conditions, the material stiffness degrades faster for the flexible membrane boundary case. Both these observations can be linked to the overly constraining nature of the rigid boundary (that does not allow shape change) that introduces an inhomogeneous state of stress in the material.

As noted earlier, the use of a rigid boundary adequately captured the response of the uncemented sand, which shows minimal dilatancy (typical behavior for a loose to medium dense sand). However, the use of flexible boundary provides a better prediction for both the stress-strain and volumetric (pore pressure) responses (including dilation and early

contraction) of the heavily cemented sand. The inelastic micromechanical parameters of DEM simulation (especially the rolling stiffness coefficient β and plastic moment limit coefficient η) can be further tuned to provide a closer match between the numerical analysis and the experimental results, especially at larger strains, for the excess pore pressure. Simulations using the flexible boundary approach are able to capture the trend in excess pore pressure of the cemented sand sample, which the rigid boundary model is incapable due to its inability to apply a uniform lateral pressure that hinders strain localization.

Examining the contact force distributions under conditions of rigid and flexible boundaries is also very instructive. Figure 4.7(a) and (b) show the contact force chains corresponding to 5% of axial strain as extracted from YADE simulations of heavily cemented sands under rigid and flexible boundary conditions, respectively. The fact that the rigid wall cannot apply a uniform confining pressure along the boundary results in large contact forces and stress concentrations in the lateral direction, as can be noticed from Figure 4.7(a). The particles near the boundary are constrained by the rigid wall, which results in higher stresses in those particles as seen in the figure. For the flexible membrane case, the contact forces are much more uniformly distributed. There are very few lateral forces close to the boundary because the confining pressure is absorbed by the particles that tend to expand out, resulting in minimal stresses in the other boundary particles (Cook et al. 2004).

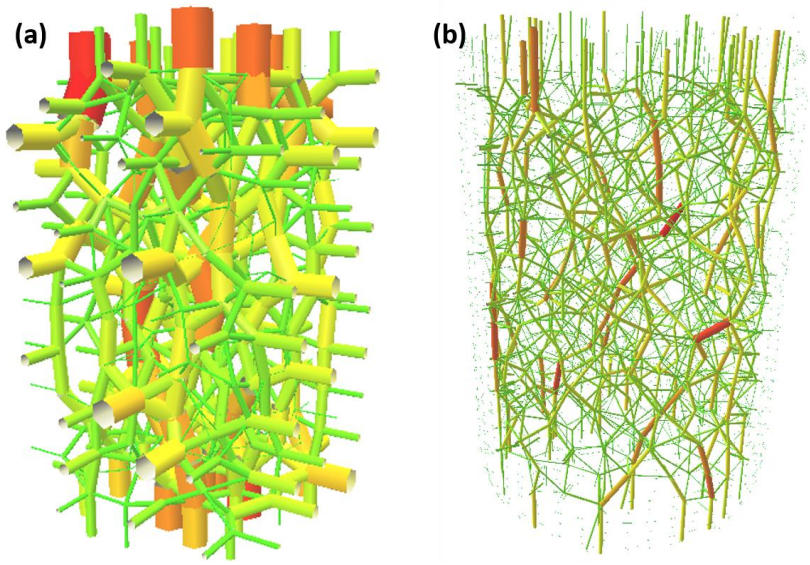

Figure 4.7: Force chains in highly cemented sand samples subjected to unconfined triaxial compression: (a) rigid boundary, (b) flexible membrane boundary. Line thickness and colors are indicative of contact force magnitude.

Figure 4.8(a) and (b) depict vertical cross sections of the simulation volume enclosed by rigid and flexible boundaries respectively at 6% axial strain. It is known that particles inside the zone of strain localization experience severe rotations compared to those outside this region (Iwashita and Oda 1998, 2000). The particles are colored in these figures according to their normalized rotation degrees, with dark blue representing the lowest rotation level and dark red representing the highest rotation level. The normalization is carried out with respect to rotation under a particular test condition, and thus the color schemes cannot be compared between different cross-sections of samples. Figure 4.8(a) shows that for the rigid boundary, due to the constraints imposed, particles with large rotations are distributed all throughout the sample and a defined region of strain localization is not visible. It is also well reported that the rigid boundaries hinder strain localization (Cil and Alshibli 2014). The use of a flexible membrane boundary allows the orientation of the highly rotated

particles in a distinct zone (i.e., the development of a shear band), which is captured by the DEM simulations. More discussion on shear bands is provided in the forthcoming section.

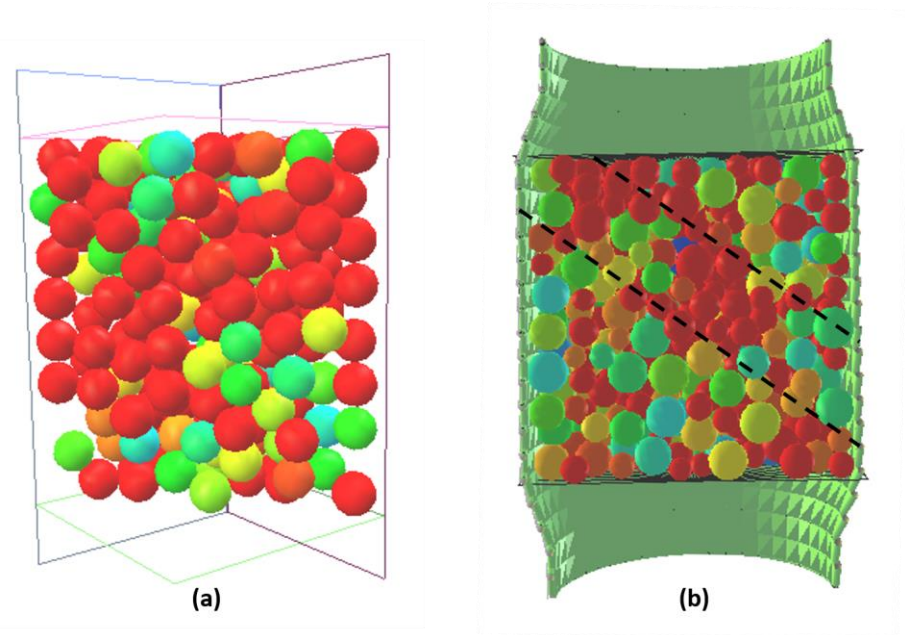

Figure 4.8: Strain localization predicted by the DEM model for heavily cemented sand: (a) rigid boundary, and (b) flexible membrane boundary. The red color represents the heavily rotated particles while light blue represent particles with a lower rotation degree. A tentative shear band is shown here; however this is by no means an accurate representation. This is used only for illustration.

4.4. Simulating Undrained Triaxial Compression Test of MICP-Strengthened Sand

The DEM model adopting flexible membrane boundary conditions is used to simulate the response of MICP-treated sands with varying cementation levels under undrained triaxial compression. Four specimens treated by MICP via ureolysis with calcium carbonate contents varying from 1.01% to 5.31% by mass and one untreated specimen were simulated. The experimental results are from (Montoya and DeJong 2015). All the virtual specimens were prepared with 1,000 particles and an isotropic confining stress of 100 kPa, following the procedure mentioned in the section dealing with simulation using rigid boundaries. The micromechanical parameters used for the five numerical simulations are listed in Table 4.2.

Table 4.2: DEM parameters used to simulate the macroscale response of untreated and treated Ottawa 50/70 sand reported by (Montoya and DeJong 2015).

Microscale parameters	Untreated	Mass of calcite in the treated samples (%)			
		1.01	Unavailable	1.3	5.31
	UT190	LT300	MT450	MT650	HT1400
Initial shear wave velocity (V_s)	190	300	450	650	1400
Void ratio (e_0)	0.75	0.76	0.74	0.76	0.73
Normal stiffness (k_n) (MPa)	100	100	350	600	2000
Stiffness ratio ($\alpha = k_s/k_n$)	0.3	0.3	0.3	0.3	0.3
Inter-particle friction angle (μ) (°)	25	30	40	33	47
Rolling stiffness coefficient (β)	0.1	0.1	0.5	0.0001	0.8
Plastic moment limit coefficient	0.002	0.0005	0.01	0.0001	0.03
Bond strength C_s (MPa)	0	0.5	1.5	2.5	9
Confining stress (kPa)	100				

Figure 4.9 shows the stress-strain responses of all the specimens from the simulation and compares them with the experimental data. The experimental results from (Montoya and DeJong 2015) report the different amounts of carbonates in the samples and the corresponding shear wave velocities. The specimens are identified as untreated (UT), lightly treated (LT), moderately treated (MT), and heavily treated (HT), along with the corresponding shear wave velocities, in Figure 4.9 and Table 4.2. The DEM model captures the macroscale experimental constitutive response of both the treated and untreated sands well. Additional dilation in the MICP strengthened specimens due to roughening of the particles are observed.

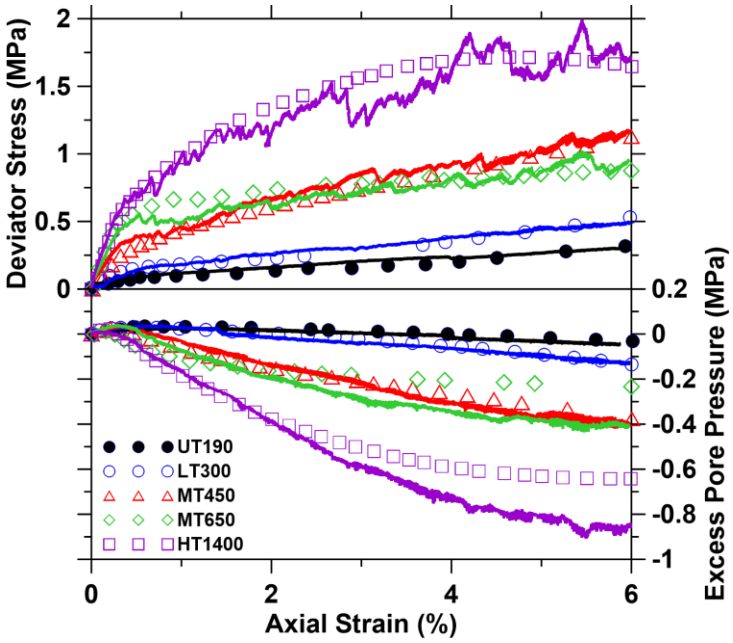

Figure 4.9: Simulation of constitutive response of sand strengthened using different amounts of carbonates through MICP. The symbols indicate the experimental results and the continuous lines, the simulated response. The numbers next to the legend indicates the shear wave velocity through the samples. Experimental results from (Montoya and DeJong 2015).

It can be noticed from Table 4.2 that the normal contact stiffness (k_n) for the simulations needed to be increased from 100 MPa to 2000 MPa as the cementation level increases (denoted by an increase in shear wave velocity). The stiffness ratio (α) was kept constant and thus the shear stiffness increased in a similar manner as the normal stiffness. The bond strength (C_s) was increased from 0 for the untreated sand to 9 MPa for the heavily cemented case. Figure 4.10 shows that the shear stiffness and the bond strength used in the simulations scale linearly with the shear wave velocity. Since the MICP process enhances the contact stiffness between particles (Montoya and DeJong 2015), and because the shear wave velocity is proportional to the shear stiffness (Santamarina et al. 2001), this behavior is expected. The shear stiffness is also related to the normal particle contact stiffness,

thereby allowing for the use of shear wave velocity as a guide in determining the elastic micromechanical parameters for the DEM simulation of MICP treated sands.

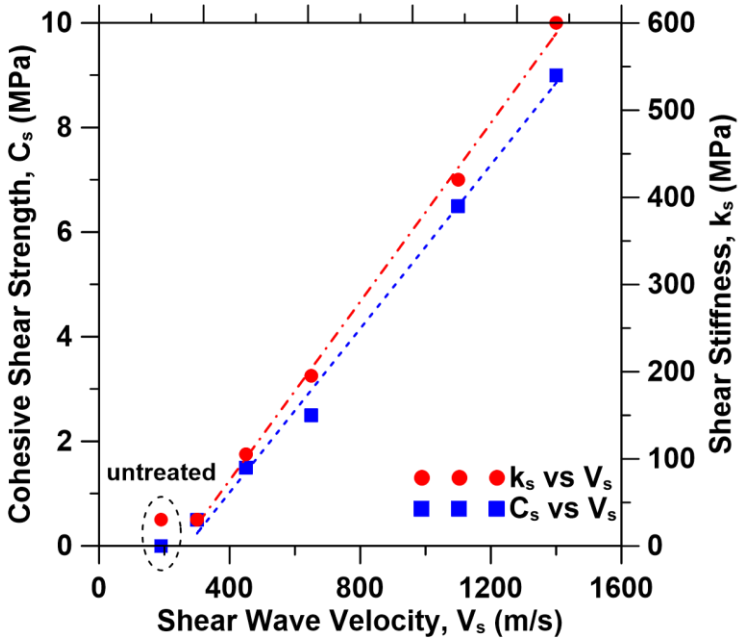

Figure 4.10: Relationships between initial shear wave velocity (which is a function of the degree of cementation) and the shear stiffness of particles and cohesion bond strength between the contacted particles used in the simulations. Experimental values of shear wave velocity from (Montoya and DeJong 2015).

It is also noticed that the inter-particle friction angle and the rolling stiffness coefficient generally increase when cementation level increases to provide simulation results that agree with the experiments. This is founded on the fact that a higher cementation level (higher carbonate content) contributes to enhanced particle surface roughness and thus to increased resistance to sliding. The exception here is the moderately treated sample with a shear wave velocity of 650 m/s (MT650). This sample requires a lower friction angle (33° as opposed to 40° for MT450 sample), an extremely low rolling stiffness coefficient (0.0001 vs 0.05), and an extremely low plastic moment limit coefficient (0.0001 vs 0.01 for MT450 sample) in order to match the experimental data. While the elastic parameters scaled well with the carbonate contents, the rupture parameters deviated significantly from

the expected trends for the MT650 sample. This can be explained by the behavior transition from global failure to localized shear banding between the MT450 and MT650 samples as reported by (Montoya and DeJong 2015) and as numerically shown later in this chapter. A closer observation of the experimental data supports this observation. The experimental post-peak deviator stress and the excess pore pressure for the MT650 sample, after 2% axial strain, are lower than those of the MT450 sample.

To further examine the stress-strain response of the cemented sands, particle rotation during CIUC simulations was monitored for the virtual samples. High particle rotations occur within the zones of strain localization and large voids appear in the shear band (Iwashita and Oda 1998, 2000). Figure 4.11 shows the cross-sectional view of the five virtual samples at an axial strain of 10%. This relatively high axial strain was used to increase the chances of strain localization, especially for the cemented sands. The sand particles are colored in accordance with their rotation degrees, with dark blue indicating the lowest level of rotation and dark red representing the highest level of rotation. Figure 4.11(a) shows that there are very few particles subjected to heavy rotation in the untreated sample, consistent with the physical observations at this strain level for uncemented loose and medium dense samples (Montoya and DeJong 2015). However, further increase in strain may still induce a shear band in this specimen. The lightly and moderately treated samples shown in Figure 4.11(b) and (c) demonstrate the occurrence of heavily rotated particles but they are randomly distributed in the sample. No clear zone of localization is noted, and such specimens have been reported to exhibit classic barreling failure (uniform expansion in the radial direction, concentrated near the mid-height) (de Bono et al. 2015; Wang and Leung 2008a). With a further increase in carbonate content, Figure 4.11(d)

shows that the highly rotated particles tend to develop a preferred orientation. Careful observation of Figure 4.11(d) reveals the likely presence of conjugate shear bands. It has been reported that moderately cemented sand samples at confining pressures comparable to that used in this study exhibit such a behavior (de Bono et al. 2015). As the cementation level further increases, Figure 4.11(e) illustrates strain localization in a distinct, narrower zone which is caused by the breakage of a large number of bonds within the highly localized zone, indicative of a brittle material. Experimental observations also confirm the presence of a narrower localization zone for highly cemented sands (Montoya and DeJong 2015). Note that the simulations shown in Figure 4.11 were carried out at a confining stress of 100 kPa. Shear zones are generally absent under much larger confining stresses (of the order of a few thousand kPa).

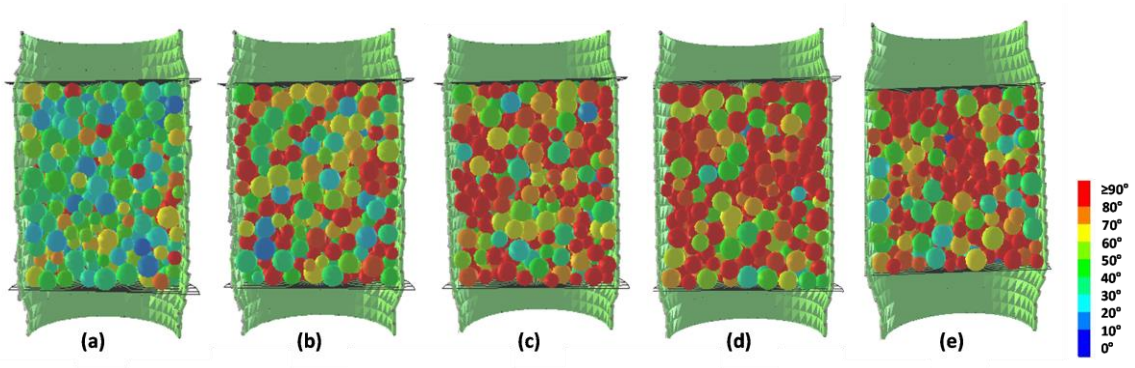

Figure 4.11: Particle rotations obtained from DEM simulations at different cementation levels: (a) untreated (UT190), (b) lightly treated (LT300), (c) moderately treated (MT450), (d) moderately treated (MT650), with likely conjugate shear banding and (e) heavily treated (HT1400), with a narrow shear band. Note that the shear band locations are determined from a visual observation since the use of 1000 particles for simulation is not enough to clearly delineate the shear bands. However one can easily discern the gradual localization from these figures as the cementation increases.

Figure 4.12 provides a 3D visualization of contact network distributions and microscale normal force chains for all the specimens listed in Table 4.2. All the force chains shown here correspond to an axial strain of 6% and are scaled from 0 to 1200 N with a color map

where dark blue represents very small contact forces and dark red indicates contact force closer to 1200 N. Randomly oriented homogenous distributions of contact force networks are observed, both in the vertical and horizontal directions, for all the five samples while the magnitude of contact forces varies with changes in cementation levels. For the untreated and lightly treated sands (Figure 4.12(a) and Figure 4.12(b)), the normal contact forces are relatively small (< 300 N). As the level of cementation increases, stronger force chains that resist the applied axial stress, mostly concentrated in the vertical direction, are noticed (e.g., in Figure 4.12(e) for heavily treated sand). The stronger inter-particle contacts resulting from the MICP treatment sustain higher contact forces in this case. Note the significant increase in contact forces between the MT560 and HT1400 samples.

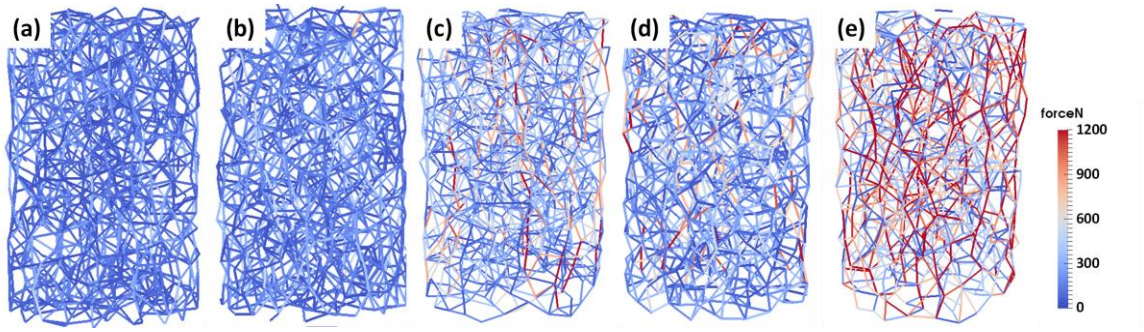

Figure 4.12: Force chains at 6% axial strain for specimens with different cementation levels: (a) untreated (UT190), (b) lightly treated (LT300), (c) moderately treated (MT450), (d) moderately treated (MT650), and (e) heavily treated (HT1400).

Figure 4.13 shows the evolution of force chains under simulated CIUC testing for lightly (LT300) and heavily (HT1400) treated sand specimens. In the initial stage (at 0% strain), both the LT300 and HT1400 samples display similar contact force chain networks, both in magnitude and orientation, due to the isotropic consolidation applied to the samples. These force chains are randomly distributed. During the triaxial compression stage, the force chains continuously restructure with increases in their magnitude and changes in

orientation, resulting from interactions between particles under external applied load. Increasing degree of anisotropy is also noticed with increasing strains, and stronger force chains are noticed to develop in vertical direction to resist the axial loading whereas the lateral contacts are less stressed. This can be particularly noticed in the case of cemented samples. By comparing the force chain evolution process of the LT300 and HT1400 specimens, it can also be noticed that, as the cementation level increases, the enhanced inter-particle contacts transmit significantly higher loads, which eventually contributes to the enhanced macroscale stress-strain behavior.

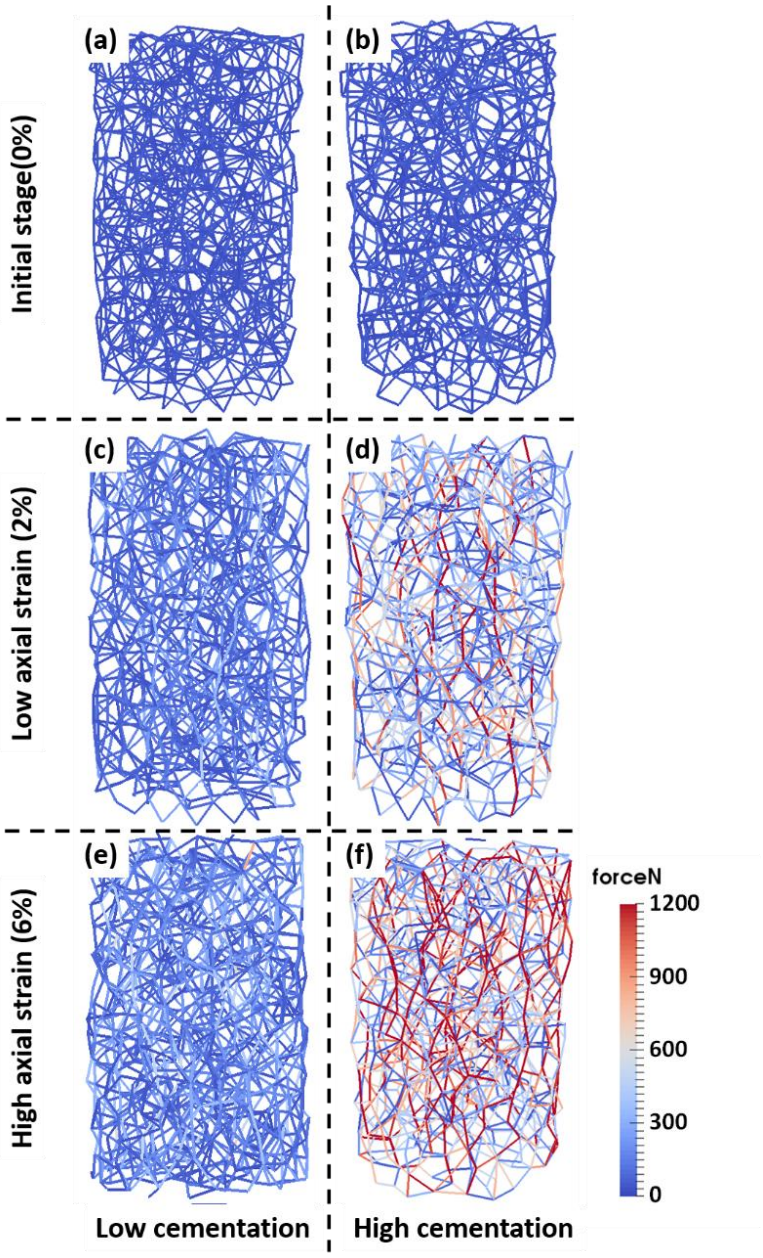

Figure 4.13: Evolution of force chains for lightly treated (low cementation, LT300) and heavily treated (high cementation, HT1400) specimens.

Another quantifiable particle-scale parameter of significance in granular materials behavior is the coordination number. This has been related to the stability of the granular system (Gong et al. 2011; Thornton 2000). Simply defined, the coordination number is the average number of contacts per particle for the whole system. Equation 12 is used to

calculate the coordination number (Z) of a particulate system that by virtue of its packing (i.e., gravity-free packing as is done in the simulations) might contain particles with no contact or only one contact (Thornton 2000).

$$Z = \frac{2C - N_1}{N - N_1 - N_0} \tag{4.12}$$

where C is the number of contacts, N is the number of particles, and N_1 and N_0 represent the number of particles with one or zero contact, respectively.

Figure 4.14 shows the evolution of coordination number as a function of applied axial strain for the untreated and MICP treated samples. The initial coordination number, in general, decreases with increase in cementation. The likely reason for such a response is that the increase in cohesive bond strength between the contacted particles, with increase in cementation, restricts the ability of particles to move during the initial packing and consolidation stage and thus reduces the total number of contacts. During the initial phase of the CIUC test, the coordination number decreases for all the samples until a minimum value is reached. This phenomenon is caused by particle rearrangement and loss of contacts in extensional principal strain directions (Cundall and Strack 1983). The minima in the coordination number also loosely corresponds to the elastic strain in these samples. New contacts are likely to develop during the deviator loading stage with the breakage of cohesive bonds and thus the coordination number increases after the initial drop for all the cemented samples. This is more pronounced for the heavily treated specimen where the coordination number increase is more noticeable, attributed to the breakage of a large number of stronger bonds. Note that, after the initial rearrangement, the untreated sample shows a relatively constant coordination number (Gong et al. 2011). At a large enough

axial strain, the coordination numbers are rather invariant for the moderately and heavily treated samples at around 5.5 and for the untreated and lightly treated samples at around 5.6.

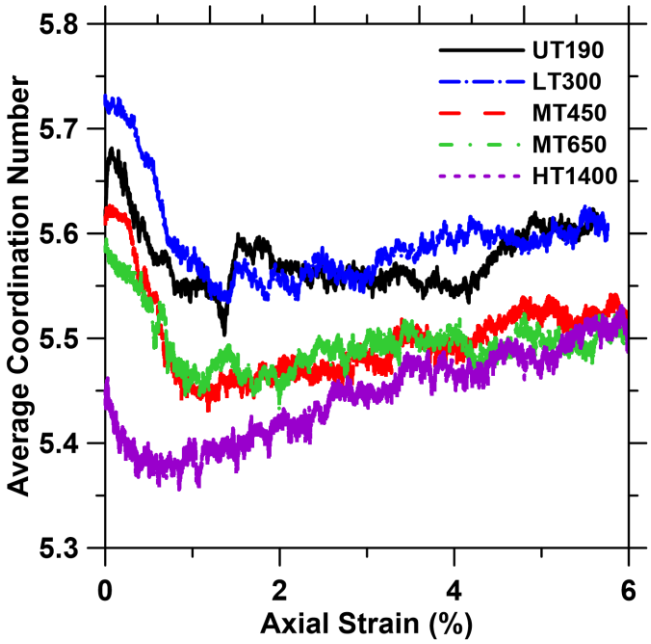

Figure 4.14: Average coordination number as a function of axial strain for the simulated samples.

4.5. Summary and Conclusions

DEM simulations of MICP strengthened sands subjected to consolidated isotopically undrained triaxial compression (CIUC) have been presented in this chapter. A five parameter DEM model, previously calibrated and verified, was used to simulate the response of untreated and treated sands. Cementation was accounted for by assigning cohesive shear strengths to all the existing (initial) contacts. A constant volume method was used to simulate CIUC testing of saturated specimens. Simulations using rigid boundaries indicated that the methodology was able to accurately match the experimentally observed relationships of deviator stress and excess pore pressure with axial strain for untreated samples, whereas it was less than satisfactory for the cemented samples. The

discrepancy was attributed to the fact that the rigid boundary hinders the onset and growth of strain localization, which is dominant in cemented samples.

A novel methodology which uses particle facets (PFacets) to create flexible membranes was also employed in this study. The particle packing and initial consolidation to obtain the desired void ratios were carried out in a rigid cylinder and the packed particles were then enclosed by a flexible membrane. Deviator loading was carried out by applying velocity control to the axial platens as well as to the nodes of the membrane to maintain constant volume. The use of a flexible boundary was found to better predict both the stress-strain and volumetric response of the MICP treated sand. With appropriate choice of elastic and rupture parameters, simulations for all the treated and untreated sands using this procedure yielded satisfactory simulations of the response under CIUC loading. The cohesive bond shear strengths selected for the simulations were found to be linearly related to the experimental shear wave velocity of the samples, providing a means to choose the bond strength values for simulations.

DEM simulations provided further insights into the particle scale mechanisms occurring during CIUC tests in MICP-cemented sands. Monitoring of particle rotations during the virtual tests helped the identification of zones of strain localization based on the knowledge that heavy rotations occur in shear bands. The lack of localized zones in untreated and lightly treated sands and their gradual evolution within a narrow concentrated zone for the highly treated sample was evident from particle rotations. Thus, DEM simulations such as these help provide insights into the failure mode of granular media (e.g., whether barreling failure or shear banding occurs) under different conditions of testing, e.g., different confining stresses, particle packing, and cementation level. Randomly oriented

homogenous contact force networks were observed, and their magnitude increased with increase in cementation levels. The coordination number initially decreased for all the treated and untreated specimens and after local minima gradually increased for all the cemented samples because of particle rearrangements after bond breaking. In addition to serving as predictive tools for the macromechanical behavior of bio-cemented soils, the DEM simulations described in this study also elucidates several particle scale responses in such media, potentially resulting in better design of MICP treatment strategies.

5. DISCRETE ELEMENT SIMULATIONS TO PREDICT RESPONSE OF UNCEMENTED AND CEMENTED SANDS: INFLUENCE OF MATERIAL AND TEST PARAMETERS, AND BOUNDARY CONDITIONS

5.1. Introduction

The response of granular materials to extreme events such as earthquakes and landslides has captured the attention of geotechnical engineers for several decades. One of the emerging technologies to mitigate the impacts of earthquake-induced soil liquefaction is the use of bio-cemented sand. Microbially induced carbonate precipitation (MICP) or enzyme induced carbonate precipitation (EICP) are very actively being researched as bio-cementing methods (DeJong et al. 2006; Kavazanjian and Hamdan 2015; Kavazanjian and O'Donnell 2015a; Montoya and DeJong 2015; Mortensen and DeJong 2011). Development of discrete element method (DEM)-based simulation and response prediction methodologies for cemented granular media is thus of great interest in enabling optimized design of these technologies for interventional strategies in earthquake-prone locations. However, accurate determination of microscale parameters to use in the DEM models to obtain macroscale response is a challenging task.

The discrete element method (Cundall and Strack 1979; Strack and Cundall 1978) is a powerful numerical tool to study the macroscale mechanical behavior of granular materials. DEM offers a viable and sometimes preferred alternative to continuum-based methods for the study of particle assemblages. By computing the motions and interactions of individual discrete elements that represent granular particles at the microscale, DEM enables constitutive modeling of granular media such as sands. A variety of inter-particle contact laws have been developed to capture the characteristics of particle contacts in granular

media, facilitating robust DEM models for predictive purposes (Iwashita and Oda 1998, 2000). The development of fluid-coupled DEM models has enabled accurate description of fluid-particle contacts (Catalano et al. 2014; Chareyre et al. 2012; Shafipour and Soroush 2008; Tong et al. 2012). DEM models that consider particle shape and roughness, clumped particles, packing density, and microscopic stress states have been developed, which helps to predict the mechanical behavior of both cohesive and cohesionless granular materials (de Bono et al. 2015; Kozicki and Tejchman 2011; Sayeed et al. 2011; Shen et al. 2016; Wang and Leung 2008b; Widuliński et al. 2009).

While significant advances have been made in modeling and simulation of both bonded and unbonded granular media, there are several aspects that influence the quality of simulations and the reliability of predictions. For instance, the type of boundary (rigid vs. flexible; rigid being more common because of its ease in use) adopted in the DEM simulations not only influences the macroscopic stress-strain response, but also provides very different indicators of failure. While tweaking the particle-scale input parameters helps accomplish numerically satisfactory solutions, this does not always lead to a physically consistent response. For highly cemented sands where a very localized failure mode with a distinct shear band is experienced in practice (Montoya and DeJong 2015), adequate predictive capability necessitates the use of a flexible boundary to simulate the deformation of the physical membrane boundary and allow for the generation of strain localization (Yang et al. 2018).

Thus, this chapter examines in detail, the influence of boundary and testing conditions, and material types on the constitutive response of uncemented and cemented sands as predicted using DEM. The applicability of different types of DEM models (e.g., classical DEM and

fluid-coupled DEM) for different soil types (cemented vs. uncemented) or different test conditions (drained vs. undrained triaxial compression) are examined. The influence of confining stress on the response of cemented sand under undrained conditions and the use of classical DEM approach to simulate the unconfined compressive strength test of heavily cemented sand are also discussed. Finally, a model employing multiple particle types (having low, medium, and high degree of bond strengths to represent varying levels of cementation) is proposed based on the understanding that not all inter-particle contacts in a cemented medium will have the same bond strength.

5.2. Mathematical Background

In this section, brief descriptions of the discrete element method (DEM), pore-scale finite volume (PFV) method and the algorithms for coupling PFV method with DEM are provided. The open-source DEM software YADE (J. Kozicki and F.V. Donzé 2009) is used as the simulation environment in this study. YADE allows the use of different numerical models within a single simulation environment. More details on the implementation of YADE for problems in granular mechanics can be found in (J. Kozicki and F.V. Donzé 2009; Šmilauer and Chareyre 2010).

5.2.1. A Brief Overview of the Discrete Element Method

Consider a system consisting of N spherical particles. The kinematics of each particle can be described by six degrees of freedom (DOFs) - three translational and three rotational. $\mathbf{X}_i = \{\mathbf{x}_i, \theta_i\}$ is used to represent the position of particle i. Here, $\mathbf{x}_i$ denotes the position of particle's center of mass, and θ_i represents the rotation as an R^3 vector (Catalano et al. 2014).

Newton's second law governs the translational motion of each particle as:

$$m_i \ddot{\mathbf{x}}_i = \int_{\delta\Gamma_i} \sigma^s \boldsymbol{n} ds + \int_{\Gamma_i} \rho^s \boldsymbol{g} dv \tag{5.1}$$

where m_i is the mass of a particle occupying volume Γ_i, $\sigma^s \boldsymbol{n}$ is the stress applied on the particle surface in the direction of the unit normal vector $\boldsymbol{n}$, ρ^s is the particle density and $\boldsymbol{g}$ is the gravitational acceleration.

In Equation 1, the first integral represents the total external force applied on particle *i* from its contacts with other particles, and is denoted as $\mathbf{F}_i^c$. Considering the contact areas between particles to be negligible (a consequence of spherical particle assumption), Equation 5.1 can be rewritten as:

$$m_i \ddot{\mathbf{x}}_i = \sum_{k=0}^{n_c} f_{ik}^c + m_i \boldsymbol{g} \tag{5.2}$$

Here, f_{ik}^c represents the contact force acting on particle *i* from *k*-th contact point and n_c is the total number of contact points on particle *i*.

To describe the translational motion of the whole system, global vectors $\mathbf{x} = \{\mathbf{x}_i\}$ and $\mathbf{F}^c = \{\mathbf{F}_i^c\}$ containing the positions and forces for 3 x *N* translational DOFs of all the particles included in the system are introduced (Catalano et al. 2014). Equation 5.1 can be restated as:

$$\ddot{\mathbf{x}} = \mathbf{M}^{-1}(\mathbf{F}^c + \mathbf{G}) \tag{5.3}$$

Here, $\mathbf{M}$ is the global mass matrix, $\mathbf{G}$ represents the gravitational term and $\mathbf{F}^c = B(\mathbf{X}, \dot{\mathbf{X}})$, where *B* defines the constitutive behavior of the contacts, which will be discussed in the following section.

While the above equations describe the translational motion of the system, similar relations can be developed for rotational motion by replacing force and mass with torque and inertia respectively. Thus, Equation 5.3 should be supplemented with another 3 x *N* rotational DOFs to completely define the kinetic behavior of the system.

$$\ddot{\mathbf{X}} = \mathbf{J}^{-1}(\mathbf{T}^{c} + \mathbf{G}) \tag{5.4}$$

Here, **J** is the generalized inertia matrix, and $\mathbf{T}^{c}$ represents the generalized force vector.

5.2.2. Contact Law

This section recalls the contact law that defines the constitutive behavior of contacts between particles. The interaction force between spherical particles A and B shown in Figure 5.1 can be decomposed into a normal force, a shear force and a contact moment represented by $\vec{F}_n$, $\vec{F}_s$ and *M* respectively. Relationships between all the three decomposed components and the relative displacement can be defined through the normal stiffness k_n, shear stiffness k_s, and rolling stiffness k_r as:

$$\vec{F}_n = k_n U \vec{n} \tag{5.5}$$

$$\Delta\vec{F}_s = k_s \Delta\vec{U}_s \tag{5.6}$$

$$\Delta M_e = k_r \Delta\theta \tag{5.7}$$

$$M_p = \eta \bar{r} \left\| \vec{F}_n \right\| \tag{5.8}$$

where, U is the relative normal displacement between two spheres, $\vec{n}$ is the unit normal vector, $\Delta\vec{U}_s$ is the incremental tangential displacement, and $\Delta\theta$ is the rotational increment between two spheres. The tangential force $\vec{F}_s$ is obtained by summation of Equation 6 and the elastic moment is obtained through the summation of Equation 5.7. The elastic moment,

together with a plastic moment M_p related to the normal force through a dimensionless plastic moment limit coefficient (η) (Equation 5.8), is used to simulate the elastic-plastic behavior of rolling contact that represents the surface roughness and irregularity of granular materials (Belheine et al. 2009; Plassiard et al. 2009; Yang et al. 2016).

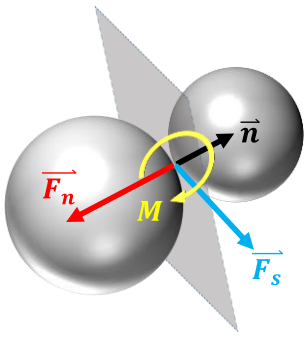

Figure 5.1: Two spheres in contact, showing the normal ($\vec{F}_n$) and tangential ($\vec{F}_s$) contact force vectors, the contact moment vector ($\vec{M}$) and the unit normal vector ($\vec{n}$).

For unbonded granular materials, such as sand, shearing (sliding) behavior satisfies the Mohr-Coulomb rupture criterion:

$$\|\vec{F}_s\| - \|\vec{F}_n\| tan\, \mu \leq 0 \tag{5.9}$$

Here, μ is the inter-particle friction angle.

For cemented granular materials, such as MICP or EICP strengthened sand, a cohesive bond model was employed in a previous work by the authors (Yang et al. 2016). To model the bonding effect between particles, a cohesive strength (bond strength), c_s, was assigned to all the inter-particle contacts after the particles were packed in the virtual sample at the desired packing density. It is assumed that the cohesive bond completely carries the normal and shear stress until the bond breaks. Although it has been reported that the cementation at particle contacts can transmit both the force and the moment (Potyondy and Cundall 2004), it is assumed that the cohesive bond cannot sustain any bending or twisting moment

so that: (a) the contact law is simplified, and (b) the number of parameters that require calibration are reduced. Thus, before the breakage of bond, the frictional effects of the contact are ignored and the maximum shear force between two bonded particles is equated to the cohesive bond strength.

$$\left\|\overrightarrow{F_s}\right\|_{max} = c_s \tag{5.10}$$

Once the bond breaks, the cohesive contact no longer exists and the particles behave in a cohesionless manner and follow the Mohr-Coulomb failure criterion. More details can be found in (Yang et al. 2016).

5.2.3. The Pore-scale Finite Volume (PFV) Method

The pore-scale finite volume (PFV) method is used to simulate the flow of incompressible fluids in a pore space (Catalano et al. 2014; Chareyre et al. 2012). The pore space is discretized by regular triangulation and its dual Voronoi space (Catalano et al. 2014). The discretized domain is constructed by tetrahedrons. Each tetrahedron represents a pore, and the vertices are the center of spherical particles (Figure 5.2), ensuring that deformations of tetrahedral elements are related to the displacements of particles (Catalano et al. 2014). In this scheme, Θ_i is defined as a portion of the tetrahedral domain not occupied by spherical particles, and has a volume of V_i^f. Since saturated porous media is considered here, the volume Θ_i is filled by the fluid (Figure 5.2). The relationship between the time derivative of V_i^f (i.e., volume change rate) and the fluid velocity is established through the divergence theorem as:

$$\dot{V_i^f} = \int_{S_{ij}} (\boldsymbol{u} - \boldsymbol{v})\boldsymbol{n} ds = \sum_{j=j_1}^{j_4} q_{ij} \tag{5.11}$$

Here, $\boldsymbol{n}$ is the outward pointing unit vector normal to $\partial\Theta_i$, and $(\boldsymbol{u}-\boldsymbol{v})$ is the relative velocity between fluid and the solid phases. The integral on facet S_{ij} represents the flux exchange between adjacent tetrahedrons, noted as q_{ij} (where j_1 to j_4 represents the four adjacent tetrahedrons). The pore volume change rate, $\dot{V_i^f}$, is computed through consideration of the motion of particles (i.e., velocities of the vertices). Thus, Equation 5.11 establishes the relationship between fluid fluxes and the deformation of the solid phase.

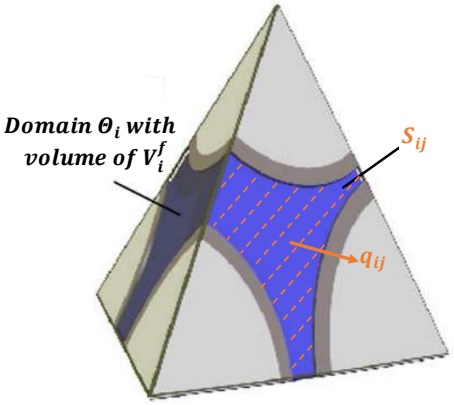

Figure 5.2: Tetrahedral element of the finite volume discretization (Chareyre et al. 2012).

Considering the linear relation between pressure gradient and flux as given by the Stokes equation, the flux q_{ij} can be expressed as:

$$q_{ij} = h_{ij}\frac{p_i - p_j}{l_{ij}} \tag{5.12}$$

Here, $p_i - p_j$ is the pressure drop, l_{ij} is the Euclidean distance between the Voronoi vertices related to each pore domain, and h_{ij} is the hydraulic conductance. A validated expression for h_{ij} is given as (Chareyre et al. 2012; Tong et al. 2012):

$$h_{ij} = \frac{S_{ij}^f {R_{ij}^h}^2}{2\mu} \tag{5.13}$$

where R_{ij}^{h} is the hydraulic radius, S_{ij}^{f} is the area occupied by fluid in facet S_{ij} and μ is the fluid viscosity.

Combining Equations 5.11 and 5.12, the relationship between the discrete pressure field and volume change rate (which in turn is related to the particle velocities) can be given as (Catalano et al. 2014):

$$\dot{V_i^f} = \sum_{j=j_1}^{j_4} \frac{h_{ij}}{l_{ij}} (p_i - p_j) \tag{5.14}$$

The total force $\mathbf{F_i^f}$ acting on the particle *i* by the fluid phase can be expressed as:

$$\mathbf{F_i^f} = \int_{\partial\Gamma_i} (-p^a \boldsymbol{n} + \boldsymbol{\tau n}) ds \tag{5.15}$$

Here $\partial\Gamma_i$ denotes the solid surface of particle *i*, p^a is the absolute pressure and $\boldsymbol{\tau}$ represents the viscous shear stress tensor.

It is reported that the flow regime can be assumed to be a slow viscous flow because of the effects of its interaction with the particles (Catalano et al. 2014). The piezometric pressure, p, is therefore expressed as:

$$p = p^a - \rho^f g z \tag{5.16}$$

Thus, $\mathbf{F_i^f}$ can be expressed as a summation of three terms:

$$\mathbf{F_i^f} = \int_{\partial\Gamma_i} -\rho^f g z \boldsymbol{n} ds + \int_{\partial\Gamma_i} p \boldsymbol{n} ds + \int_{\partial\Gamma_i} \boldsymbol{\tau n} ds \tag{5.17}$$

The first term in the RHS of Equation 5.17 represents the buoyancy force, the second term is the integral of piezometric pressure, and the third term is the integral of the viscous stress. The global fluid force vector can be expressed as:

$$\mathbf{F}^f = \mathbf{SP} \tag{5.18}$$

Here, **P** is the pressure field and **S** is the matrix reflecting the local geometry of sphere packing (Catalano et al. 2014).

5.2.4. PFV-DEM Coupling

There are two relations that are required for coupling the PFV and DEM models. They are expressed as:

$$\mathbf{HP} = \mathbf{E}\dot{\mathbf{x}} + \mathbf{Q}_q + \mathbf{Q}_p \tag{5.19}$$

$$\mathbf{M}\ddot{\mathbf{x}} = \mathbf{F}^c + \mathbf{G} + \mathbf{F}^f \tag{5.20}$$

Equation 5.19 corresponds to mass conservation. **H** is the conductivity matrix denoted by the expression $\frac{h_{ij}}{l_{ij}}$, **P** is the column vector containing all pressure values, and **E** is the matrix corresponding to the volume change rate. $\mathbf{Q}_q$ and $\mathbf{Q}_p$ are flux vectors representing boundary conditions, with $\mathbf{Q}_q$ representing the imposed fluxes and $\mathbf{Q}_p$ representing the imposed pressures, respectively. Equation 20 is obtained by simply adding fluid forces to the contact forces in Newton's equation. Using Equations 5.18 and 5.19, Equation 5.20 can be expressed as:

$$\ddot{\mathbf{x}} = \mathbf{M}^{-1}\left(\mathbf{F}^c + \mathbf{G} + \mathbf{S}\mathbf{H}^{-1}\left(\mathbf{E}\dot{\mathbf{x}} + \mathbf{Q}_q + \mathbf{Q}_p\right)\right) \tag{5.21}$$

This is an ordinary differential equation with **x** as the unknown and can be explicitly solved.

5.3. Simulation of Triaxial Compression of Uncemented and Lightly Cemented Sands Using Rigid Boundaries with and without PFV Coupling

The constitutive responses of uncemented and lightly cemented sands under both drained and undrained triaxial compression are modeled in this section using both the classical

DEM model and the coupled PFV-DEM model, considering that the system is fully saturated. The system is assumed to have rigid boundaries, which is the most commonly employed boundary type in DEM simulations (Belheine et al. 2009; Gong et al. 2011; Liu et al. 2015; Widuliński et al. 2009; Yang et al. 2016). The cemented sands simulated in this section have calcite contents of 1% or lower (thus classified as lightly cemented). The response of heavily cemented sands cannot be accurately simulated using the rigid boundary conditions because of the formation of zones of strain localization (shear bands) (Yang et al. 2018). When strain localization is present as in the case of cemented sands, the cementation degrades within this zone, and a flexible membrane approach is needed for accurate simulations (Yang et al. 2018). The radii growth method, described in detail in our previous work (Yang et al. 2016), is used to prepare a virtual sample with the target porosity at the effective isotropic confining stress for both models.

5.3.1. Classical DEM Method

The classical DEM method was used to simulate the drained triaxial compression test of uncemented and lightly cemented sands. In a drained triaxial test, the top and bottom boundaries move vertically to simulate the loading platens in a strain-controlled condition while the lateral boundaries are controlled by a servomechanism to maintain a constant effective confining stress (Figure 5.3(a)). For the simulation of an undrained triaxial compression test, the constant volume method is applied to prevent volumetric strain during the deviator loading stage. The top and bottom boundaries move vertically while the lateral boundaries are controlled by Equation 5.22 to maintain a constant volume within the sample (Figure 5.3(b)):

$$\dot{\varepsilon}_3 = -0.5\dot{\varepsilon}_1 \tag{5.22}$$

Where $\dot{\varepsilon}_1$ and $\dot{\varepsilon}_3$ are the strain rates of the axial and lateral boundaries. More details on the simulation can be found elsewhere (Lee et al. 2012; Liu et al. 2015; Shafipour and Soroush 2008).

5.3.2. Coupled PFV-DEM Method

After the generation of the target virtual specimen, the pore-scale finite volume (PFV) model is activated during the deviatoric loading stage and the coupling between the PFV and DEM models is established to simulate the triaxial compression test. The top and bottom boundary walls move vertically at a constant strain rate to simulate the loading platens in a strain-controlled test. The boundary conditions of PFV model vary based on the test conditions. For drained triaxial compression, both the top and bottom boundaries are subjected to zero boundary pressure while all the lateral boundaries are subjected to a zero-flux (impermeable boundary) condition to simulate drainage (Figure 5.3(c)). For the undrained triaxial compression, all the boundaries are subjected to a zero-flux condition and an initial internal pressure of zero is imposed (Figure 5.3(d)).

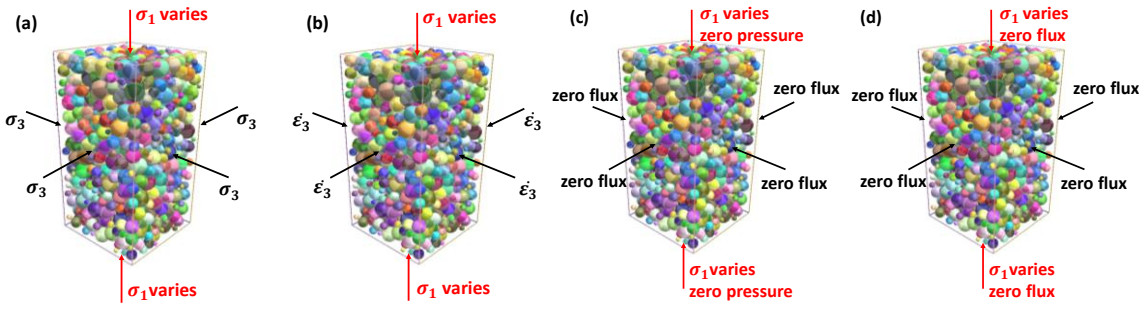

Figure 5.3: Boundary conditions during the deviator loading stage for: (a) DEM simulation of drained triaxial compression test, (b) DEM simulation of undrained triaxial compression test, (c) coupled PFV-DEM simulation of drained triaxial compression test, and (d) coupled PFV-DEM simulation of undrained triaxial compression test.

5.3.3. Comparison of Response from both the Methods

Both the DEM and the coupled PFV-DEM methods were used to simulate the drained and undrained triaxial compression tests of plain and lightly cemented sands with the micro-scale input parameters listed in Table 5.1. A 5000-particle system was used for all the simulations carried out in this section in order to balance the computational cost (time) and simulation accuracy. For lightly cemented sands, the microscale parameters chosen for the drained and undrained test simulations are different because the corresponding experimental data came from different sources.

Table 5.1: DEM parameters used to simulate the drained/undrained triaxial compression test of plain and lightly cemented sands.

Microscale parameters	Untreated (Yang et al. 2016)	Lightly cemented	
		Drained (Mortensen and DeJong 2011)	Undrained (Montoya and DeJong 2015)
Number of particles	5000	5000	5000
Void ratio (e_0)	0.73	0.73	0.76
Normal stiffness (k_n) (MPa)	120	300	100
Stiffness ratio ($\alpha = k_s/k_n$)	0.30	0.30	0.30
Inter-particle friction angle	19	30	30
Rolling stiffness coefficient	0.05	0.20	0.10
Plastic moment limit	0.50	0.12	0.0005
Confining stress (kPa)	100	100	100
Bond strength C_s (MPa)	--	0.50	0.50

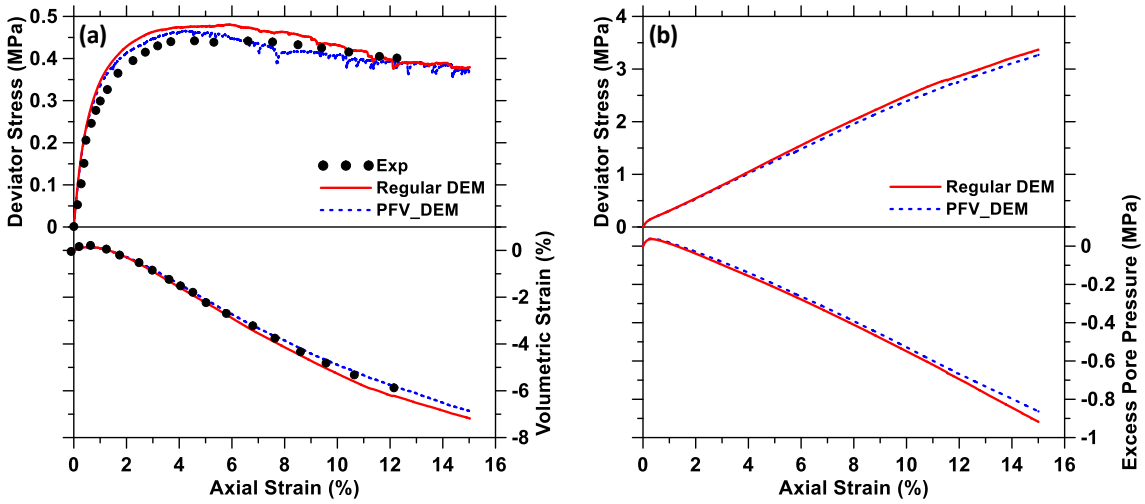

Figure 5.4: Comparison of DEM and PFV-DEM methods for: (a) drained triaxial compression test and (b) undrained triaxial compression test, for uncemented sands.

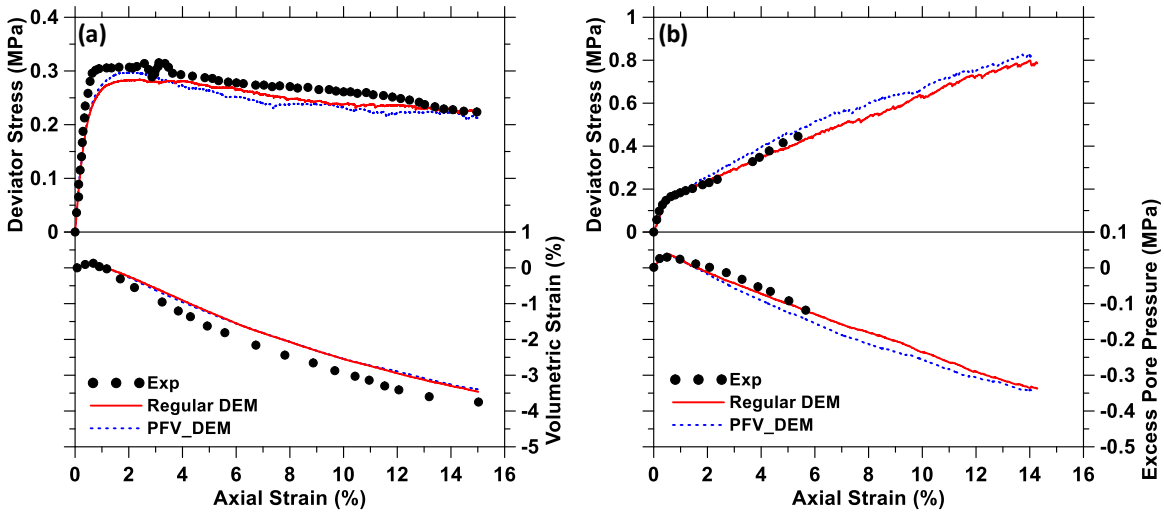

Figure 5.5: Comparison of DEM and PFV-DEM methods for: (a) drained triaxial compression test and (b) undrained triaxial compression test, for lightly cemented sands. Note that the data for (a) and (b) came from different sources.

Figure 5.4 shows the comparison between the simulation results using classical DEM and PFV-DEM models for both the drained and undrained triaxial compression tests of plain sand. Figure 5.5 shows the corresponding results for lightly cemented sand (carbonate mass fraction ~ 1%). The simulations were carried out until an axial strain of 16%. The figures

show that, for both the drained and undrained conditions, the simple DEM and coupled PFV-DEM models yield very similar results, in line with those reported in (Liu et al. 2015). However, a significant difference in computational cost between these two methods exists as can be seen from Figure 5.6. The computational time has been calculated based on the simulations carried out on a dual 16-core system having a 2.6 GHz CPU and 128 GB RAM. For both the drained and undrained triaxial compression tests, the simulations using the simple DEM model only took to 20 minutes to complete while those using the PFV-DEM model took about 2 hours for drained triaxial compression and 3 hours for undrained triaxial compression. Thus, by introducing the pore-scale finite volume method to discretize and represent the fluid phase, the computational cost noticeably increases without significant improvements in the simulation accuracy. Hence, for the remainder of this chapter, the DEM model without fluid coupling is chosen to simulate the triaxial compression test of saturated sands. Notwithstanding this comparison, it should be noted that PFV coupling extends the applications of the classical DEM method and enables the prediction of the pressure field of the liquid phase in a multi-phase media, which the classical DEM cannot provide (Catalano et al. 2014). PFV coupling is also essential in simulating the behavior of unsaturated sands where both the liquid and void phases can be introduced (Yuan and Chareyre 2017).

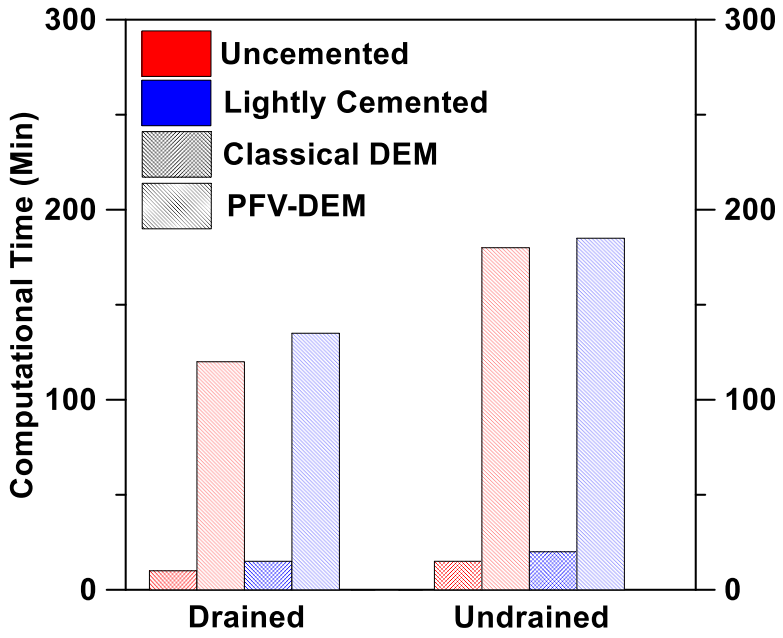

Figure 5.6: Comparison of the computational cost (time) of DEM and PFV-DEM models for the drained and undrained compression tests on plain and lightly cemented sands.

5.4. Simulation of Triaxial Compression of Cemented Sands Using Flexible Boundaries

Previous studies have shown that, in contrast to uncemented sand, cemented systems (either chemically bonded such as through the addition of portland cement, or biologically bonded through bacterially delivered carbonates) tend to fail in a brittle manner, with pronounced strain localization (Montoya and DeJong 2015; Wang and Leung 2008b). Recent studies (Yang et al. 2016) have shown that the classical DEM simulation with rigid boundaries, as explained in the previous section, cannot capture such brittle behavior of highly cemented sands (Yang et al. 2016, 2018) due to the non-uniform lateral pressure applied by the rigid boundary. Thus it is necessary to introduce virtual flexible lateral boundaries to accurately capture the deformation along the side walls under stress as well as to enable the growth of the shear band (Iwashita and Oda 1998, 2000; Yang et al. 2018). The virtual flexible boundaries are idealizations of the latex membranes used to confine the sample laterally in the laboratory experiments. Most studies use a bonded particle

approach (Cil and Alshibli 2014; Iwashita and Oda 1998, 2000) or rigid discrete elements having constrained degrees of freedom (Lee et al. 2012) to simulate the flexible membrane.

5.4.1. Introducing PFacet-based Flexible Membrane

A new element called PFacet (particle facet) was introduced recently by (Effeindzourou et al. 2016). Such an element is geometrically constructed by the Minkowski sum of a triangular facet and a sphere, and is composed of three spheres (as nodes) and three cylinders (as connections) as illustrated in Figure 5.7(a). The contacts between the PFacet element and particles (Figure 5.7(b)) are then translated into sphere-plane or sphere-cylinder interactions by tracking the relative positions of the particle and the coordinates of vertices of the PFacet element (Figure 5.7(c)). A virtual sphere having a radius that is the same as that of the vertex node created at the projection point (from particle to PFacet) interacts with the particle. The movement (displacement and rotation) of the virtual sphere is linearly interpolated between three vertex nodes and the force carried by the virtual sphere is distributed to vertex nodes based on the barycentric coordinates of the projection points.

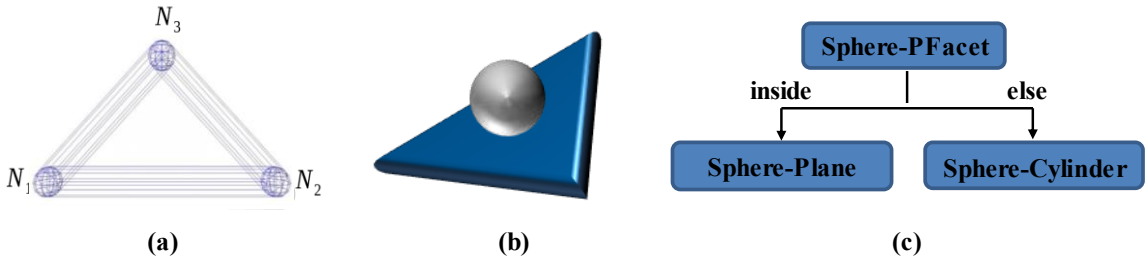

Figure 5.7: (a) Geometric construction of PFacet element, (b) Sphere-PFacet contact and (c) Diagram representing decomposition of sphere-PFacet interaction.

5.4.2. Simulating Undrained Triaxial Compression of Cemented Sands Under Different Confining Stress Levels

The DEM model of bio-cemented sands confined by a flexible membrane boundary was used to simulate the behavior of cemented sands at varying cementation levels when subjected to varying confining stresses under undrained triaxial compression. The reason for carrying out these simulations under undrained conditions is that, in general, bio-mediated carbonate precipitation is employed to mitigate liquefaction-induced damage during earthquakes. Under such fast loading rates, even saturated coarse-grained soils that otherwise experience drained conditions (e.g., under normal loads such as construction loads) may experience undrained loading. Since experimental data on undrained triaxial compression tests of bio-cemented sand under different confining stresses are lacking, one specimen treated by MICP via ureolysis with a calcium carbonate content of ~1.0% by mass tested in undrained triaxial compression at 100 kPa (Montoya and DeJong 2015) is employed as a baseline case for simulations. Two other cases are simulated with the same micro-scale properties and varying confining stresses. Virtual specimens were prepared with 5,000 particles and isotropic confining stresses of 100 kPa, 200 kPa and 300 kPa, following the procedure mentioned in (Yang et al. 2016). The micromechanical parameters used for the three numerical simulations are listed in Table 5.2. Figure 5.8 shows the deviator stress-strain and excess pore pressure-strain responses from all the three simulations and their comparison with the experimental data for the 100 kPa confining stress case. It can be noticed that the DEM model that incorporated the flexible boundary accurately captures the macroscale experimental constitutive response of the bio-cemented sand at 100 kPa, as discussed in our recent work (Yang et al. 2018). The simulated response

of the specimens under higher confining stresses is in line with the expected behavior; the higher the confining stress, the higher the deviator load the specimen can carry, which is classical for a confined system.

Table 5.2: DEM parameters used to simulate the undrained triaxial compression test.

Microscale parameters	Undrained
Number of particles	5000
Void ratio at 100 kPa (e_0)	0.73
Normal stiffness (k_n) (MPa)	350
Stiffness ratio ($\alpha = k_s/k_n$)	0.3
Inter-particle friction angle (μ) (°)	40
Rolling stiffness coefficient (β)	0.5
Plastic moment limit coefficient (η)	0.01
Cohesive Strength (MPa)	1.5
Confining stress (kPa)	100, 200, 300

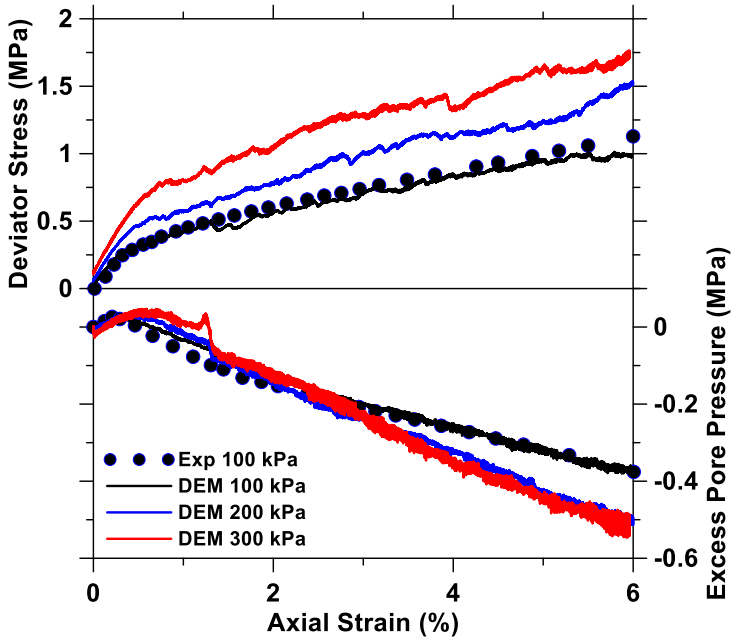

Figure 5.8: Deviator stress and excess pore pressure predicted by DEM model under varying confining stresses.

Figure 5.9 and Figure 5.10 show 3D visualizations of the microscale contact force network distributions as a function of confining pressure for the cemented sand before the start of

deviator loading, i.e., at 0% axial strain, and at an axial strain of 6%. All the force chains are colored with a uniform color map scaled from 0 to 130 N for the 0% strain case (Figure 5.9) and 0 to 400 N for the 6% strain case (Figure 5.10) to facilitate proper comparison of the material responses. A dark blue color in the color map represents near-zero contact force and a dark red color indicates the highest contact force. Figure 5.9 displays the contact force network before the deviator loading starts, and it can be seen that higher contact forces exist in the specimens subjected to a higher confining pressure, which is expected. Randomly oriented homogeneous contact force network distributions and uniform distribution of force chains are noticed for all the specimens as a result of the isotropic consolidation. During the deviator loading stage (Figure 5.10), the contact force networks and the magnitude of force chains evolve, resulting in a more anisotropic contact force network with increasing axial strain. A closer look at Figure 5.10 indicates stronger force chains in the vertical direction to resist the applied external loading, while in the lateral direction, the force chain magnitudes are more uniform and the contact network distribution is more homogeneous. This is a result of the P-Facet flexible membrane applying a uniform confining pressure in the lateral direction.

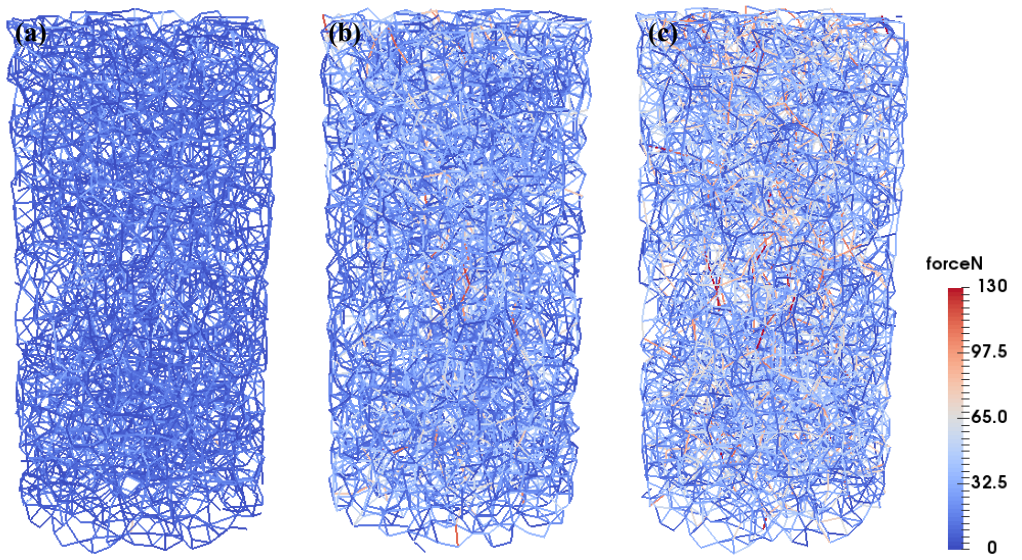

Figure 5.9: Force chains at 0% axial strain for cemented sand specimens (~1% by mass of calcite) at different confining stresses: (a) 100 kPa, (b) 200 kPa and (c) 300 kPa.

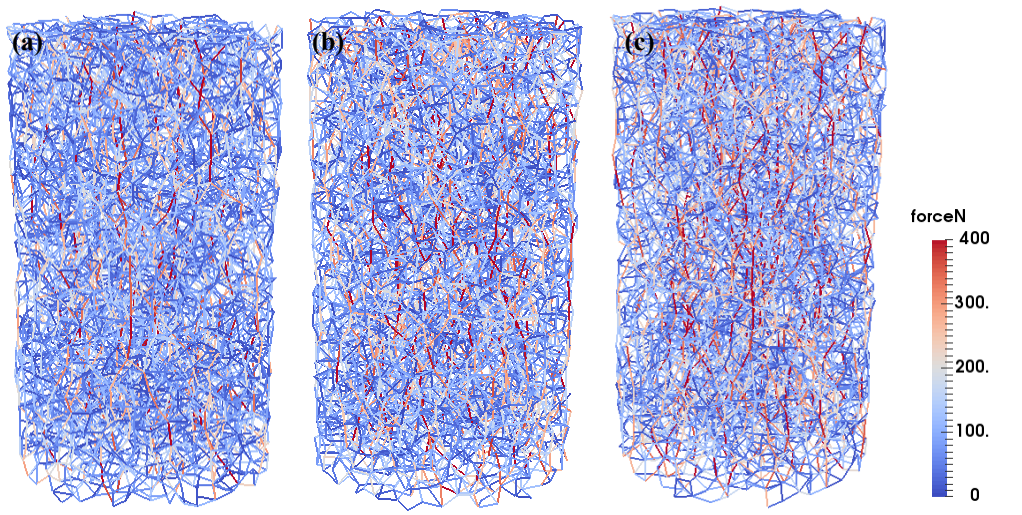

Figure 5.10: Force chains at 6% axial strain for cemented sand specimens (~1% by mass of calcite) at different confining stresses: (a) 100 kPa, (b) 200 kPa and (c) 300 kPa.

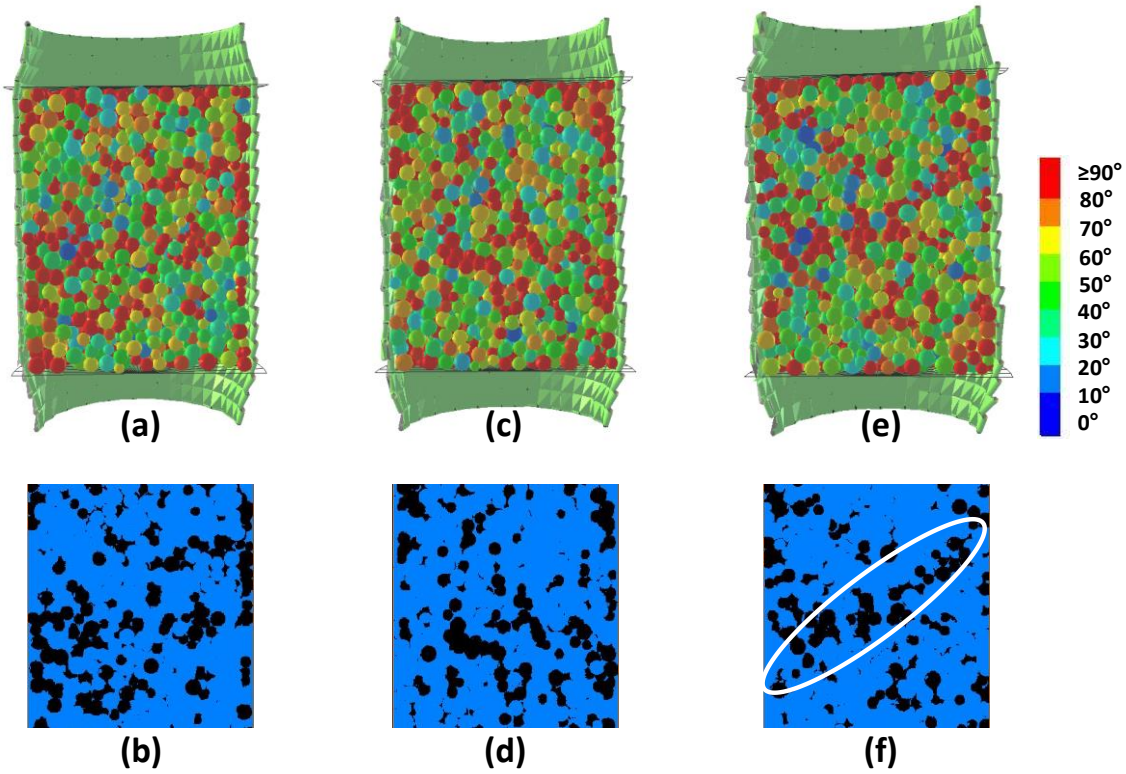

Figure 5.11: Particle rotations obtained from DEM simulations of undrained triaxial compression tests on cemented sand (~1% by mass of calcite) at different confining levels: (a) and (b) 100 kPa, (c) and (d) 200 kPa, and (e) and (f) 300 kPa. Figures (b), (d), and (f) are thresholded images that show only the particles with the highest rotation. A less random organization of these particles can be noticed with increasing confining stress, and at a confining stress of 300 kPa, a reasonably well-formed shear band can be seen.

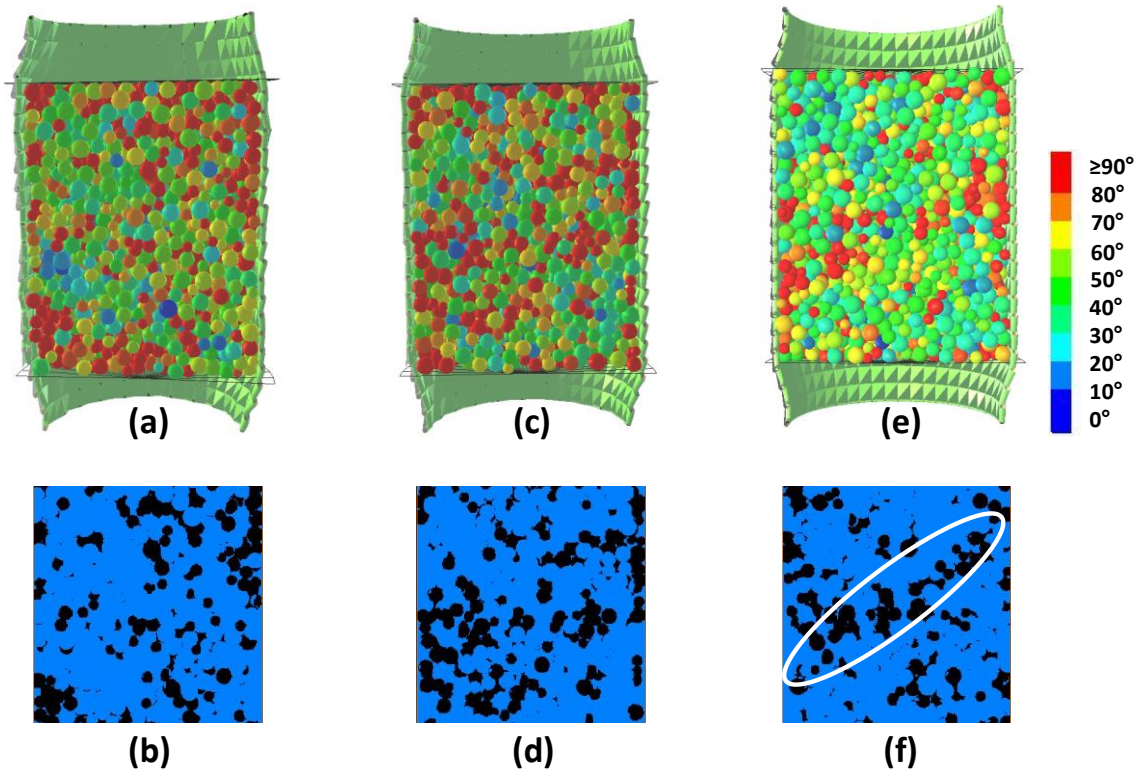

Figure 5.12: Particle rotations obtained from DEM simulations of undrained triaxial compression tests at different cementation levels: (a) and (b) lightly cemented (LT190), (c) and (d) moderately cemented (MT450) and (e) and (f) heavily cemented (HT1400) (Yang et al. 2018). Figures (b), (d), and (f) are thresholded images that show only the particles with the highest rotation, which shows a more organized distribution of these particles with increasing cementation levels. A distinct shear band can be seen for the highly cemented case. All virtual specimens subjected to a confining pressure of 100 kPa. The identifiers LT190, MT450, and HT1400 refer to lightly, moderately, and highly treated sands, with the numbers representing the shear wave velocities through the sample. Please refer to (Yang et al. 2018) for more details.

To further examine the influence of the confining stress levels on the undrained triaxial compression tests, particle rotations during simulated triaxial compression tests were monitored. The distinct zone with highly rotated particles indicate the zone of strain localization. Figure 5.11 (a), (c), and (e) show the cross-sectional views of the virtual specimen with ~1% calcite content, subjected to three different confining stresses at an axial strain of 15%. In this figure, the particles are colored according to their normalized

rotation degrees, with dark blue representing the lowest rotation level (close to 0°) and dark red representing the highest rotation level (≥90°). Figure 5.11 (b), (d), and (f) show the thresholded images corresponding to Figure 5.11 (a), (c), and (e) that show only the particles that have suffered the maximum rotation, in order to obtain a better visual picture on their orientations. Under a confining stress of 100 kPa, the heavily rotated particles are randomly distributed in the sample. However, with an increase in confining stress, the highly rotated particles are organized in a narrower region, corresponding to the formation of a shear band. By confining the specimen at a higher stress level, localized failure behavior results, rather than the barreling failure under low confinement because the cohesive bonds between particles are more likely to break within a localized zone of higher shear strain. Figure 5.12 shows the particle rotations at 15% axial strain obtained from DEM simulations of undrained triaxial compression tests of three virtual specimens having different cementation levels, subjected to a confining stress of 100 kPa. Increasing the cementation level also contributes to strain localization. The influence of cementation on shear band formation has been extensively described in (Yang et al. 2018).

5.4.3. Simulating Unconfined Compressive Strength (UCS) Test of Bio-Cemented Sand

While confined compressive strengths are generally reported for soils, carbonate precipitation makes the bio-cemented soils behave similar to bound granular media, for which unconfined compressive strengths are commonly used. A series of unconfined compressive strength (UCS) tests on Itterbeck sand with very high calcite contents (~10-to-20 % by mass) has been reported in a study by (van Paassen et al. 2009). In this section, a specimen that provided an ultimate UCS of 2.43 MPa at a calcite content of 16.8% by mass (van Paassen et al. 2009) is used for simulation.

To simulate the UCS test, 5000 particles were used to assemble a virtual sample with a target porosity of 0.38. After preparing the virtual sample as described previously (Yang et al. 2018), the lateral wall was removed and all the contacts were assigned a cohesive strength. The top and bottom platens were then assigned a constant velocity to represent a strain-controlled testing condition. The micro-scale parameters used for simulation are listed in Table 5.3. Figure 5.13(a) shows the deformed sample at 4% axial strain. It is clearly observed that the virtual sample failed along a plane of strain localization. Figure 5.13(b) shows the comparison between the experimental stress-strain response and that from the DEM simulation. The response predicted by the DEM model is very consistent with the experimental result. However, it is noticed from Table 5.3 that for such a bio-cemented system, the normal contact stiffness (k_n) value required for the simulation is 180 MPa and the cohesive strength needed is 6 MPa, which is inconsistent with the simulation parameters reported in our earlier research (Yang et al. 2018), where a normal contact stiffness (k_n) of 1400 MPa and a cohesive strength of 9 MPa were needed to reach a peak deviator stress of ~1.7 MPa in an undrained triaxial compression test of MICP-strengthened sand with a calcite content of 5.31% by mass. Such a difference can be attributed to two main factors. First, the initial porosity in this case is much smaller than the earlier case, corresponding to a denser packing with a higher initial coordination number. This indicates that a larger number of cohesive contacts will be established, thereby requiring a lower contact stiffness and cohesive strength to achieve a higher unconfined compressive strength. Second and perhaps more pertinent, the treatment methodology reported in (van Paassen et al. 2009) has been shown to lead to the generation of significantly larger calcite crystals; sometimes of size comparable to that of sand grains. This is inconsistent with the

assumption made in the current DEM model where the existence of calcite (or the cementing material) is simplified by homogenizing the properties of the "calcite-cladded sand" through the assignment of cohesive bonds to particle contacts (Yang et al. 2018) without introducing an additional phase. Thus, it can be concluded that for bio-cemented sands where calcite crystals are large (comparable to the size of sand), the current DEM model, though able to predict the bulk behavior adequately, might be incapable of elucidating the particle physics involved. Such a consideration requires the DEM model to explicitly consider multiple phases, with differing phase and inter-phase properties, to simulate the macro-mechanical response of very heavily cemented sands. This chapter attempts such a simulation as described below.

Table 5.3: DEM parameters used to simulate the UCS test.

Microscale parameters	Unconfined compression
Calcite content (% by mass)	16.8
Number of particles	5000
porosity (φ)	0.38
Normal stiffness (k_n) (MPa)	180
Stiffness ratio ($\alpha = k_s/k_n$)	0.3
Inter-particle friction angle (μ) (°)	30
Rolling stiffness coefficient (β)	0.5
Plastic moment limit coefficient (η)	0.07
Cohesive Strength (MPa)	6
Confining stress (kPa)	N/A

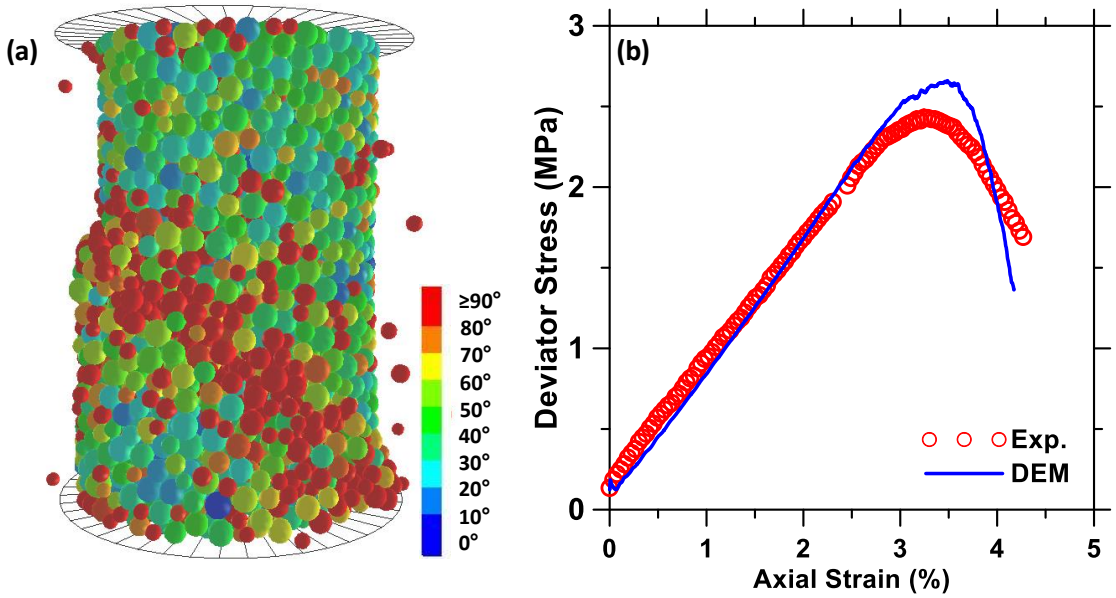

Figure 5.13: (a) 3D visualization of particle rotations and sample deformation under unconfined compression at 4% axial strain, and (b) deviator stress-strain relationship predicted by DEM model and its comparison with experimental data from (van Paassen et al. 2009).

5.4.4. Simulating the Response of Multi-Phase Particulate Systems: A Preliminary Investigation

As described earlier, the cemented sands simulated thus far in this chapter considered that the effect of cementation was to induce a cohesive bond between particles before deviator loading stage and that there was a uniform cohesive strength for all these bonds. The cohesive strength used in the simulations to sufficiently predict the constitutive response was found to scale uniformly with the experimental shear wave velocity through the samples, thus validating this approach (Yang et al. 2018). However, in the case of sands containing high amounts of calcite, as well as in cases where different precipitation techniques are employed, some of the calcite grains could be as large as the sand grains (van Paassen et al. 2009), invalidating the assumption that all cohesive contacts have the same strength. For such cases, it is hypothesized that the distribution of bond strengths is

likely to influence the material response. In this section, we introduce simulations using a multi-phase particle system, where the particle packing consists of multiple particle types with distinct cohesive bond strengths between each of the particle types. In order to understand the response of bio-cemented sands in such a scenario, a parametric study on a three-phase system is carried out here. No attempt is made here to compare the simulation results with any experimental data since specific information on cohesive strength distribution is not available in the literature. The authors expect that with the availability of advanced microstructural and micromechanical characterization tools such as X-ray tomography and micro/nano-indentation, experimental information on cohesive bond strength distribution can be obtained, which can then be used as inputs into the simulations described here. The following sub-sections describe the methodology adopted to simulate the constitutive response of bio-cemented sands with multiple cohesive bond strengths.

5.4.4.1. Multi-phase particle packing

Although preparing a particle packing system with multiple material properties can be achieved with built-in functions in other DEM software (e.g., Particle Flow Code (PFC)), it is slightly more involved to implement this in YADE. However the fact that YADE is an open-source software with the flexibility to build-in unique functionalities, lends it attractive for novel applications.

To prepare a multi-phase particle packing system with the desired properties in YADE, four main steps are required. Here, a system with three distinct particle types is prepared. First, three sets of seeds with desired particle numbers and material properties are randomly assigned within a prismatic volume. Second, the radii growth method is employed to grow the all the seeds under gravity-free condition until the target porosity and confining stress

are obtained (Yang et al. 2016). Third, since the flexible membrane boundary requires the use of a cylindrical virtual sample, the packing within the prismatic geometry is transferred to a cylindrical geometry that was constructed using regular rigid facet elements. This process is achieved through the following steps: (a) virtually placing the cylinder under the bottom of the prism, (b) removing the bottom wall of the prism, and (c) activating gravity as well as assigning a downward velocity to the top plate in the prismatic geometry. Finally, the cylindrical multi-phase particle packing is prepared along with the flexible membrane boundary following the procedure detailed in (Yang et al. 2018). Figure 5.14 shows a packing containing a total of 999 particles belonging to three distinct phases (identified as A, B, and C). The different phases are distributed uniformly in the simulation volume as can be noticed from Figure 5.14. Among the three phases, phase A is assigned the lowest cohesive bond strength, and phase C, the highest. The cohesive strengths of particle types are assumed to follow the relationship: $c_s^A < c_s^B < c_s^C$. The active cohesive contacts between the three phases are considered to follow the following relationships:

$$c_s^{A-A} = c_s^{A-B} = c_s^{A-C} = c_s^A$$

$$c_s^{B-B} = c_s^{B-C} = c_s^B \tag{5.23}$$

$$c_s^{C-C} = c_s^C$$

Where c_s^{i-j} represents the cohesive bond strength of particle contacts. Such relationships are used to ensure that the strengths of the bonds are determined by the conservative condition, i.e., by the particle type that has the lower cohesive strength. Thus, in a three-phase system, all the cohesive particle contacts can be classified into three types: low, medium, and high cohesive bond strength contacts.

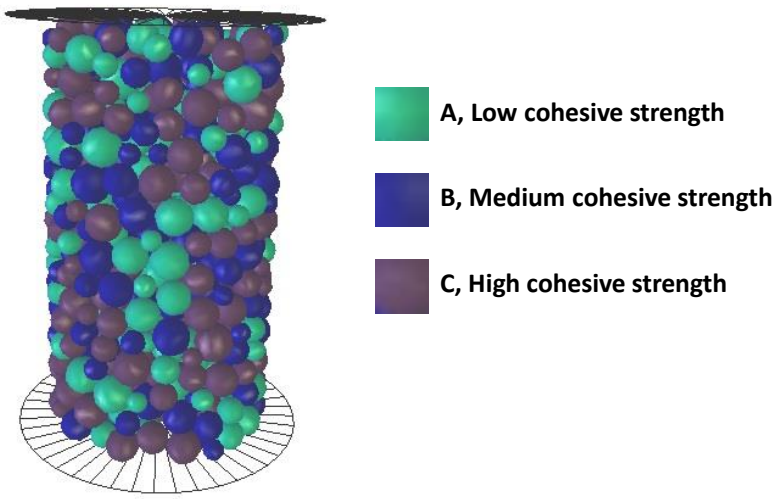

Figure 5.14: Packing in a multi-phase system with three particle types, each having different cohesive bond strengths.

5.4.4.2. Parametric studies

Two parametric studies were carried out to investigate the influence of the cohesive bond strength distribution on the constitutive response of sands under undrained triaxial compression. The micro-scale properties shared by all the three phases are listed in Table 5.4. These properties are in the range of those reported for sands (Belheine et al. 2009; Kozicki et al. 2014; Yang et al. 2016).

Table 5.4: DEM parameters used to simulate the undrained triaxial compression test of the virtual specimen.

Microscale parameters	
Normal stiffness (k_n) (MPa)	200
Stiffness ratio ($\alpha = k_s/k_n$)	0.3
Inter-particle friction angle (μ) (°)	35
Rolling stiffness coefficient (β)	0.1
Plastic moment limit coefficient (η)	0.0001
Confining stress (kPa)	100

The cohesive strength of particles belonging to each phase and the number of particles in each phase controls the cohesive strength distribution based on the relationships detailed

in Equation 23. In the first parametric study, the number of particles belonging to each phase was fixed (333 particles), while the cohesive strength of each phase was varied. Table 5.5 lists five cases where the cohesive bond strengths of phases A and B were varied between 0 and 5 MPa, and that of C varied between 0 and 20 MPa. Case 1 corresponds to an uncemented sand, and Case 5 corresponds to a cemented sand with uniform cohesive bond strength assigned to all contacts, as was done in the previous section of this chapter. Figure 5.15 shows the deviator stress-axial strain relationship of the simulated multi-phase systems. It can be found from Figure 5.15 that, an increase in cohesive strength of the phases results in higher deviator stress and greater negative pore pressure. Note that the cohesive strengths of phases A and B increases from simulation 1 to simulation 5. The cohesive strength of phase C is rather irrelevant in these simulations because, as a conservative estimate, the inter-particle cohesive strength is taken as lowest of the corresponding particle types, as described earlier. Thus even by drastically increasing the cohesive strength of phases B and C (Cases 3 and 4), only a slight increase is observed in both the deviator stress and excess pore pressure when the volume fractions of the phases remain unchanged. This indicates that the mechanical behavior of multi-phase systems predicted by the DEM model is dominated by the phase with the lowest cohesive strength, assuming the number of particles in each phase is the same.

Table 5.5: Simulation parameters: variation in cohesive strength of particle types.

Group ID	Phases		
	A	**B**	**C**
	Num. of Particles		
	333	333	333
	c_s^A(MPa)	c_s^B(MPa)	c_s^C (MPa)
1	0	0	0
2	0.1	0.2	0.5
3	0.5	2	10
4	0.5	5	20
5	5	5	5

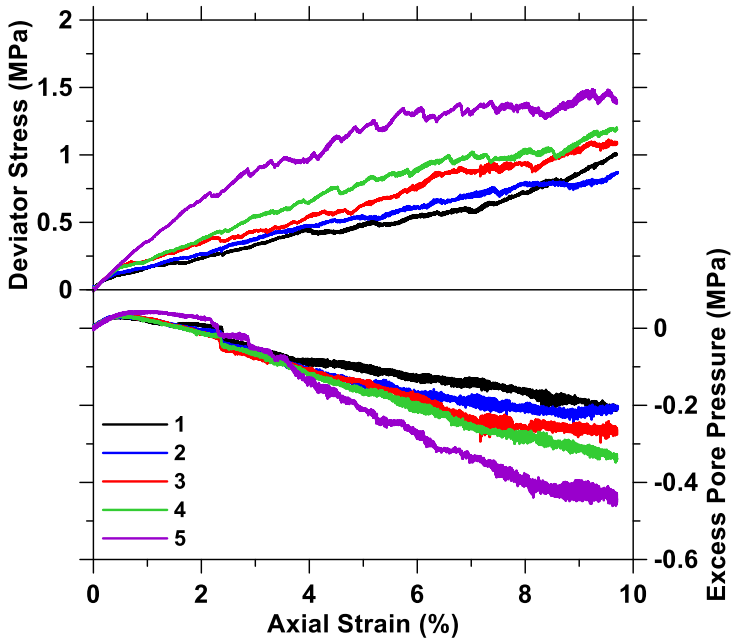

Figure 5.15: Deviator stress-axial strain-excess pore pressure relationships for simulated systems when the cohesive strengths of phases are varied (case number corresponds to that listed in Table 5.5).

In the second parametric study, the cohesive bond strength of each of the three phases were fixed and the volume fractions of each of the phases were changed from simulation 1 to simulation 4 (Table 5.6) to investigate the effect of cohesive strength distribution on the constitutive response of cemented sands. Case 2, with equal volume fractions of all particle types, serves as the baseline case while the other three cases have variable volume fractions.

Figure 5.16 indicates that Case 1 and Case 2 demonstrate similar deviator stress-strain and excess pore pressure-strain relationships despite the fact that the distributions of phases A, B and C are totally different. Case 1 has a high volume fraction of phase A and small volume fractions of phases B and C while Case 2 has the same number of particles belonging to all three phases. Such observation is consistent with the conclusions drawn earlier that phase A dominates the mechanical behavior predicted by the DEM model when it governs the largest number of cohesive contacts. Case 1 and Case 4 are mirror images of each other, where the volume fractions of the least and most cohesive phases are interchanged. The enhancement in deviatoric stress that can be sustained with a larger number of more cohesive contacts is obvious from this comparison. Unsurprisingly, Case 3 where the medium cohesion particles are dominant demonstrates a response that is in between those of Cases 1 and 4. Thus, unlike in the case of a system with equal number of particles belonging to different phases where the particle with lowest bond strength dominated the response, here, the volume fractions of the phases are more instrumental in dictating the constitutive response. Higher volume fractions of phases with medium and high cohesive strength are seen to provide a significant improvement on the mechanical behavior. The simulations using multiple phases of particles thus become very useful in understanding the response of heterogeneous granular media where the binding material (e.g., calcite) is large enough to be considered a “discrete” element rather than just a contact between the primary grains by modeling the binding material as a separate phase and not just as a cohesive bond. However, this effect was not modeled in the present study.

Table 5.6: Simulation parameters: variation in volume fraction of particle types.

Group ID	Phases		
	A	**B**	**C**
	c_s^A(MPa)	c_s^B(MPa)	c_s^C (MPa)
	0.5	5	20
	Volume Fraction		
1	0.62	0.19	0.19
2	0.33	0.33	0.33
3	0.19	0.62	0.19
4	0.19	0.19	0.62

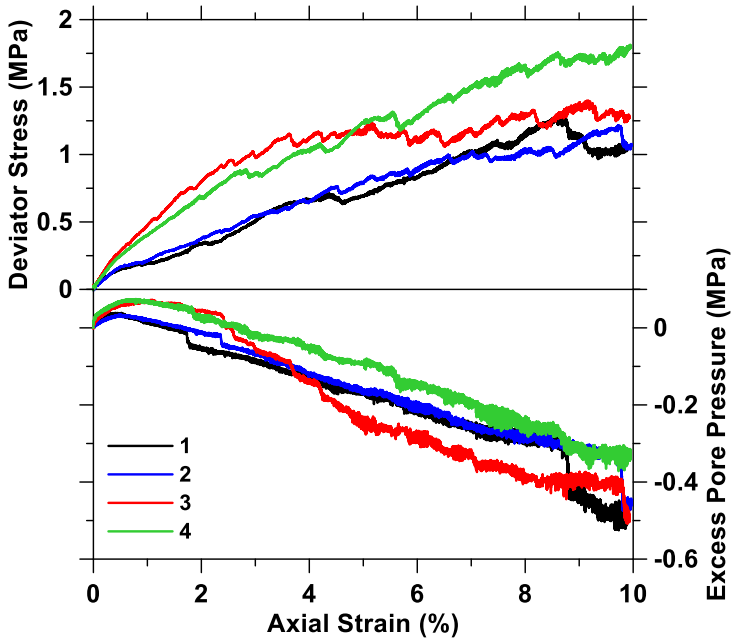

Figure 5.16: Deviator stress-axial strain-excess pore pressure relationships for simulated systems when the volume fraction of phases are varied (case number corresponds to that listed in Table 5.6).

5.5. Summary and Conclusions

The influence of boundary conditions, loading and testing conditions, and material types on the response of bio-cemented sands are explored using DEM simulations in the YADE environment. Both the classical DEM model and the pore scale finite volume (PFV)-coupled DEM model were used to simulate the response of saturated uncemented and

lightly cemented sands bound by rigid walls under both drained and undrained triaxial compression. A comparison between classical DEM and PFV coupled DEM models showed that for all the test cases evaluated, the simulation outcomes were very similar, albeit at a higher computational cost for the PFV-DEM method. Even though PFV coupling endows additional capabilities such as the prediction of the pressure field of the liquid phase in a multi-phase media, when the trade-off between computational cost, expediency, and accuracy is considered, the classical DEM emerges as the preferred option for simulations of the type discussed in this chapter.

For moderately and highly cemented sands, rigid boundary cannot be used for simulation because of its inability to capture strain localization. A novel methodology which uses PFacet elements to create a flexible membrane boundary was adopted in this work to simulate undrained triaxial compression tests of moderately cemented sands (cementation levels of ~1%). The influence of confining stress on the macroscale mechanical response of such sands were simulated. 3D visualization of normal contact force networks in the samples demonstrated non-uniform distribution of axial force chains as the confining stress increased, and a uniform force distribution in the lateral direction was observed, which is attributed to the flexible wall. Monitoring of particle rotations helped identify the zone of strain localization, which indicates that shear banding is the preferred failure mode in cemented sands. The transition from barreling failure to shear banding with increased confining stress or cementation degree was illustrated through the distributions of heavily rotated particles.

The unconfined compressive strength (UCS) test of a very heavily cemented sand was also simulated using the classical DEM model. This model used a virtual cohesive bond of

uniform strength to describe the cementation level. Even though the macroscale mechanical response was sufficiently simulated using the classical DEM model, the particle physics involved was not adequately represented, especially when large calcite grains bind the sand particles. To overcome this limitation, this chapter presents a multi-phase particle packing model with differing phase and inter-phase properties to simulate the response of very heavily cemented sands or similar granular media (including cement-based materials). A three-phase system was developed. Parametric studies showed that increasing the volume fraction of particles with a higher cohesive strength is more effective than increasing the cohesive strength of a smaller number of particles, in attaining higher stress capacity for the cemented sands. This paves the way for the design of bio-cementing methods whereby larger calcite crystals are formed (through MICP or EICP) rather than just producing stronger bonds.

6. DEM SIMULATIONS ON THE INFLUENCE OF CARBONATE PRECIPITATION ON LIQUEFACTION MITIGATION OF SAND

6.1. Introduction

Earthquake-induced liquefaction of soil is a major hazard to structures located in seismically active zones, and thus its mitigation has been an active topic of research for several decades. Liquefaction of loose, saturated, cohesionless soil around existing infrastructure can result in different types of soil failure including bearing failure, lateral spreading, and excessive/differential settlements (O'Donnell et al. 2017a). Earthquake loading induces multiple load cycle reversals, resulting in changes in particle packing of the soil leading to a compressional volumetric strain and increase in pore fluid pressure approaching the confining stress on the soil particles. Some of the conventional techniques to improve the performance of liquefiable soils include densification techniques, discrete reinforcing, or injection of binding agents (Keramatikerman et al. 2018; Kumari et al. 2018; Porcino et al. 2015; Shahir et al. 2016; Shen et al. 2018). Sustainable solutions of cementing soil through biological means to mitigate liquefaction such as microbially induced carbonate precipitation (MICP), enzyme induced carbonate precipitation (EICP), or a combined process of desaturation and carbonate precipitation (MIDP) are being actively researched (DeJong et al. 2006; Kavazanjian and Hamdan 2015; Kavazanjian and O'Donnell 2015a; Montoya and DeJong 2015; Mortensen and DeJong 2011; Xiao et al. 2018). MICP is among the most popular of these solutions, where microbes in a calcium rich medium are used to precipitate calcite in the voids of the soil (DeJong et al. 2006; van Paassen et al. 2010). Centrifuge models have demonstrated that MICP-cemented sands demonstrate reduced excess pore pressure, reduced settlements, and greater surface

accelerations when compared to untreated sands (Montoya et al. 2013). It has also been reported that even a small amount of calcite precipitation can significantly enhance the liquefaction resistance of sands (O'Donnell et al. 2017b).

Modeling of the dynamic response of water saturated granular materials is a complex problem requiring complex multiphysics models. Continuum formulations based on phenomenological observations of the soil skeleton and the pore water phase are commonly used to model liquefaction (Elgamal and Yang 2000; Liyanapathirana and Poulos 2002; Sawicki and MierczyĹ 2006). Another well-studied option is to use discrete element method (DEM)-based models. Here, the movement of particles and their rearrangement are used to represent the macroscale deformation and response of the soil. DEM-based models have been used to simulate the undrained and drained response of granular media in a number of recent studies including those of authors (Belheine et al. 2009; Feng et al. 2017; Gong et al. 2011; Kozicki et al. 2014; Liu et al. 2015; Widuliński et al. 2009; Yang et al. 2016, 2018). Even though the saturated soil is a two-phase medium comprising of solid sand grains and fluid in the pores, most of the DEM simulations employ a constant volume method to simulate the undrained saturated soil tests (Gong et al. 2011; Liu et al. 2015; Yang et al. 2018a). It has been shown by multiple studies that a computationally more expensive coupled fluid-particle interaction DEM model provides similar results as a constant volume model (Gong 2015; Yang et al. 2018).

DEM-based models can be valuable towards an in-depth understanding of the liquefaction phenomenon because of its capacity to track microscale particle movements that dictate the macroscale soil deformation, which is the fundamental mechanism of liquefaction. Previous studies have reported the use of DEM-based models for the simulation of

liquefaction of loose sands (Bernhardt and Biscontin 2016; Dabeet et al. 2012; El Shamy and Zeghal 2007; Shi et al. 2010); however liquefaction simulations of bio-cemented sands have received little attention. In this chapter, we develop a verified and validated method in the open-source YADE DEM environment (J. Kozicki and F.V. Donzé 2009) to model the cyclic direct simple shear (DSS) test on sands in an effort to understand their behavior under cyclic shear loading. A six-parameter contact model which includes the normal and tangential contact stiffness, the interparticle friction angle, the rolling stiffness coefficient, the plastic moment limit coefficient and cohesion is used to simulate the mechanical response of untreated and MICP-cemented sands using appropriate microscale parameters that capture the underlying physics of the system. For non-cohesive materials (i.e., untreated sand), shearing (sliding) begins at the contact point where the Mohr-Coulomb rupture criterion is satisfied. For cohesive materials (i.e., MICP-cemented sand), a cohesive bond with specified shear strength (bond strength) is assigned to the existing contacts after the particle packing stage. As discussed in our previous work, the bond strength is related to the degree of cementation and the shear wave velocity (Yang et al. 2018a). The dynamic response is numerically solved using an explicit finite difference algorithm in YADE, keeping the velocities and accelerations constant at each time step. This allows YADE to efficiently follow the non-linear interaction between the particles in the system. Numerical models like the one described here can be used to design the levels of cementation to mitigate liquefaction as a function of the sand type, its size distribution, cyclic stress ratio, and effective vertical stress. Validated DEM models also aid in the development of cyclic strength curves for different types of sands, providing engineers with useful information on prioritizing mitigation measures.

6.2. Simulating the Cyclic Direct Simple Shear (DSS) Test Using DEM

The direct simple shear (DSS) test as well as the direct shear test have been extensively modeled using DEM (Bernhardt et al. 2014; Bernhardt and Biscontin 2016; Dabeet 2014; Huang et al. 2015; O'Sullivan et al. 2004), because of its ability to interrogate particle-scale mechanisms and localized evolution of constitutive relationships. Previous studies have used a rectangular 2D geometry with four rigid walls as boundaries to simulate the cyclic DSS test (Shi et al. 2010). Studies have also considered both hinged and laminar walls to simulate the different types of DSS devices often used in laboratory studies (Bernhardt and Biscontin 2016; Xue et al. 2015). The boundary walls influence the microscopic response, even when the macroscopic response is similar, indicating the importance of boundary conditions in modeling the DSS test. However, the three-dimensional response and out-of-plane deformations present in real granular materials are not accounted for in such simulations even though the macroscale response is captured (Bernhardt and Biscontin 2016). 3D DEM model with a cylindric geometry restricted by layers of ring-like lateral walls (stacked ring, or laminar configuration) has been used to simulate the mechanical response of granular materials under both DSS and cyclic DSS conditions (Dabeet 2014; Dabeet et al. 2012). While this method has been shown to be able to closely duplicate the boundary conditions that are generally applied in laboratory tests, it is computationally intensive due to the need to execute user-defined functions at regular intervals to control the velocities and positions of each layer of ring-like lateral walls. In this chapter, we initially model the cyclic DSS test with a 3D shear box constructed using six rigid walls as well as a cylindrical geometry restricted by laminar boundary walls (stacked rings). While 2D DEM model comparisons of DSS test using the

stacked ring and shear box geometries have been reported (Shen et al. 2011), it is interesting to examine the performance of these two models under dynamic loading in 3D.

6.2.1. General Modeling Process for Shear Box and Stacked Ring DEM Tests

The overall modeling process consists of four major steps. First, boundary walls are created for both the models. As shown in Figure 6.1(a), six connected rigid walls are created to assemble the shear box. For the cylindrical model with laminar boundary walls, a predefined number of layers of cylindrical facet-walls are created to represent the stacked-rings (as shown in Figure 6.1(d)), and the top and bottom rigid walls are created in the same manner as for the shear box. Second, radii expansion method (Belheine et al. 2009) is used to generate the target particle parking. The numerical specimen is initially generated by randomly assigning a fixed number of fine spheres within a prismatic volume to generate a loosely packed state, as illustrated in Figure 6.1(a) and (b). The sizes of these spherical particles are then numerically increased until the designed grain size distribution and the desired void ratio are reached. A small inter-particle friction angle is applied during this stage to help reach the target void ratio (Huang et al. 2014; Potyondy and Cundall 2004; Thornton 2000). Gravity-free condition, as well as zero-friction wall condition are also imposed during the growth procedure to ensure a homogeneous stress state (Yang et al. 2016). After generating the target particle packing, appropriate properties are assigned to all the existing contacts. While maintaining the other boundary walls fixed, displacement is assigned to the top and bottom walls to achieve the desired vertical effective stress, σ_v'. After the consolidation of the numerical specimen, the inter-particle friction angle is then set back to target value before shearing is started.

Cyclic shearing is then imposed on the specimen. During the cyclic shearing stage, different boundary conditions are imposed for the two models. For the shear box model, the bottom boundary wall as well as the front and back walls are fixed while the top boundary wall moves horizontally at a specified velocity to simulate the cyclic shear condition. The side boundary walls (left and right walls) are controlled by a servo-mechanism to rotate correspondingly to ensure contact with top and bottom walls. For the cylindrical model, while the bottom boundary wall is fixed and the top boundary wall moves horizontally at the specified velocity, the laminar boundary walls move independently with linearly increasing speeds (from bottom to top) to achieve uniform boundary shear strain, as illustrated in Figure 6.1(e). During the cyclic shearing simulation, constant volume conditions are enforced by fixing the vertical translation to represent the undrained condition. It has been reported that the change of the vertical stress acting on the top wall is equivalent to the variation of pore water pressure (Dyvik et al. 1987; Finn 1978). Thus, the excess pore water pressure (Δu) can be defined as:

$$\Delta u = \sigma'_{v\_ini} - \sigma'_v \tag{6.1}$$

where σ'_{v_ini} is the initial vertical effective stress before shearing.

The excess pore water pressure ratio (r_u), which is one of the parameters used to define the occurrence of liquefaction (O'Donnell et al. 2017a), can be expressed as:

$$r_u = \frac{\Delta u}{\sigma'_{v\_ini}} \tag{6.2}$$

For a stress-controlled cyclic DSS test, the cyclic stress ratio (CSR) is defined as:

$$CSR = \frac{\tau_{cy}}{\sigma'_{v\_ini}} \tag{6.3}$$

where τ_{cy} is the horizonal stress sustained by the top wall during the simulation.

Figure 6.1(c) and (f) illustrate the contact force network for both the shear box and cylindrical models after the consolidation stage, where the thickness of the lines is proportional to the magnitude of contact force. Uniform distribution of contact forces is observed for both the models, indicating a fairly homogeneous stress distribution at the end of consolidation for both the simulation schemes.

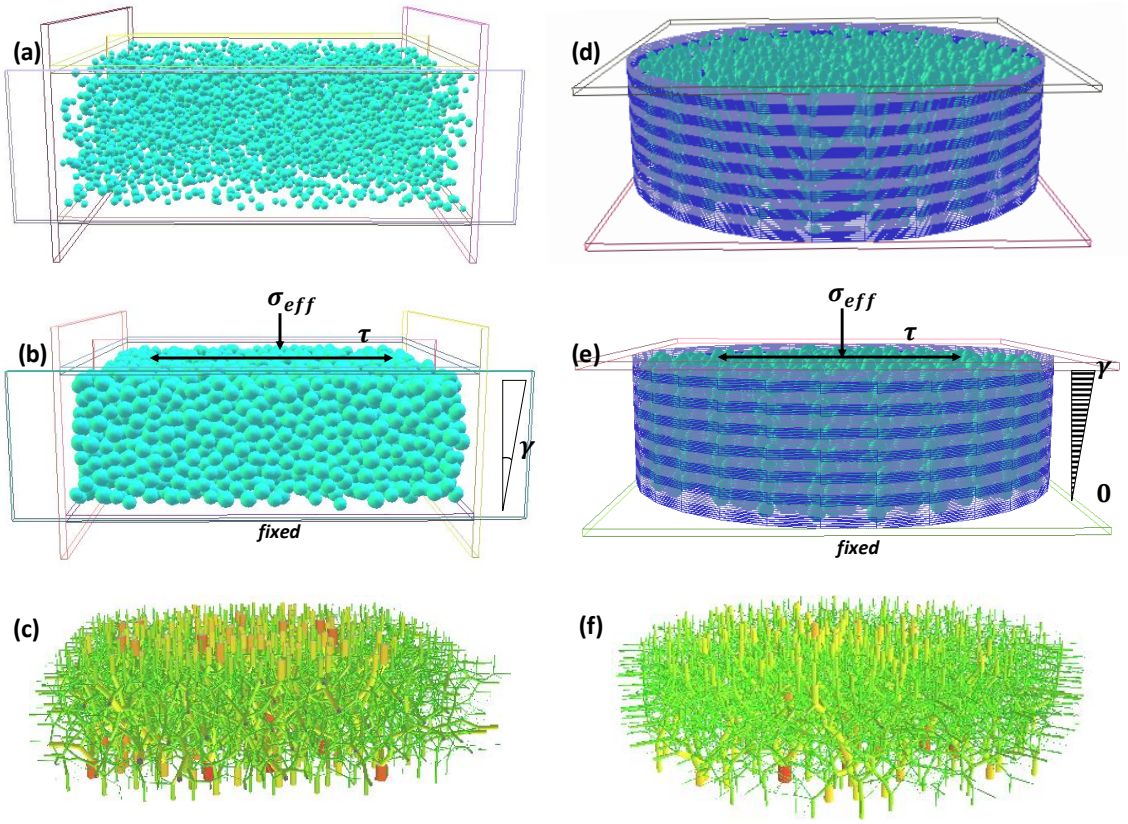

Figure 6.1: Simulation schemes for the shear box and cylindrical models: (a) loose packing state before radii growth process, (b) confined state along with boundary conditions applied for cyclic DSS simulation, (c) contact force network as the end of consolidation for shear box model and (d) loose packing state before radii growth process, (e) confined state along with boundary conditions, (f) contact force network after consolidation for cylindrical model.

6.2.2. Comparing the Performance of the Shear Box and Laminar Wall DEM Models

The experimental results of cyclic DSS tests on Fraser River sand reported in (Wijewickreme et al. 2005) with a cyclic stress ratio (CSR) of 0.10 were used to examine the performance of both the shear box and cylindrical models developed here. A shear box 60 x 20 x 60 mm (length x height x width) (roughly the same as that reported in (Wijewickreme et al. 2005)) was used for the simulations, with ~5,000 mono-sized (2 mm) particles. On the other hand, a cylindrical specimen with 60 mm diameter and 20 mm height was created with same size (2 mm diameter) particles. 14 layers of cylindrical facet-walls each with a thickness of 1.5 mm were created to restrict the deformation of the specimen laterally. Both the numerical specimens were then consolidated with a target vertical effective stress of 100 kPa and the void ratio at the end of consolidation was designed to be 0.67 as is the case in the experimental sample (Dabeet et al. 2012). The cyclic shear resistance is defined as the number of load cycles required to reach a horizontal shear strain (γ) of 3.75% (National Research Council 1985), which has been adopted in many other liquefaction studies (Porcino et al. 2009; Sivathayalan and Vaid 2004; Wijewickreme et al. 2005). All the simulations were stopped when the limiting shear strain of 3.75% was reached.

The shear box model was first used to simulate the cyclic DSS test at CSR of 0.10 to calibrate the micro-scale parameters required to describe the contact law for DEM simulations by matching the simulation results to the experimental data. The inter-particle friction angle (μ) was set to be 18°, which is same as reported in (Thomas 1992) for Fraser River sand. A normal contact stiffness (k_n) of 100 MPa and a stiffness ratio (α) of 0.15 (which results in a tangential contact stiffness (k_s) of 15 MPa) were chosen so that during

the cyclic shearing, the specimen can sustain the target shear stress level (15 kPa). A rolling stiffness coefficient (β) of 0.22 as well as a plastic moment limit coefficient (η) of 0.1, which represent the surface roughness of particles, were used so that during cyclic loading the stress path develops properly and the cyclic shear resistance (number of loading cycles required to reach 3.75% shear strain, (N_{liq})) matches the value in (Wijewickreme et al. 2005). The chosen values of the parameters are in the range reported in the DEM modeling of the constitutive response of sands (Plassiard et al. 2009; Vinod et al. 2013). All the input parameters used for the simulations are listed in Table 6.1. The simulated results are plotted in Figure 6.2 and both the stress path and shear stress – strain relationship simulated by the DEM model with appropriate micro-scale parameters are found to be in good agreement with the experimental data, indicating the capability of the shear box model to adequately capture the dynamic response of sand under cyclic DSS test. The same micro-scale parameters are then used to simulate the cyclic DSS test using the cylindrical model with laminar boundary walls. The simulation results for this case are also shown in Figure 6.2. It is clearly observed that under same CSR, the cylindrical model with laminar boundaries demonstrate a weaker cyclic resistance (3 cycles compared to 7 cycles when simulated using the shear box model, and 8 cycles reported in experiments (Wijewickreme et al. 2005)). Significantly larger vertical effective stress drop in each cycle and larger shear strains were noticed when the simulation was carried out using the cylindrical model.

Table 6.1: DEM parameters used to simulate the Fraser River sand (Wijewickreme et al. 2005).

Parameters	Fraser River sand
Void ratio (e_0)	0.67
Normal stiffness (k_n) (MPa)	100
Stiffness ratio ($\alpha = k_s/k_n$)	0.15
Inter-particle friction angle (μ) (°)	18
Rolling stiffness coefficient (β)	0.22
Plastic moment limit coefficient	0.1
Confining stress (kPa)	100
Number of particles	5000
Sample size (L x H x W in mm) – Shear box model	60 x 20 x 60
Sample size (D x H in mm) – Cylindrical model	60 x 20

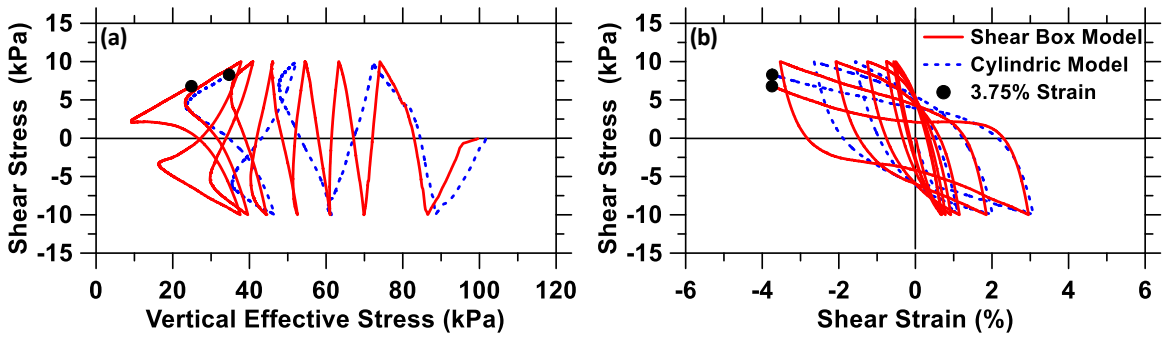

Figure 6.2: Results of numerical simulation of the cyclic DSS test at a CSR of 0.10 for Fraser river sand: (a) stress path, and (b) shear stress-shear strain response.

To further investigate the performance of these two models, the contact force distributions for these models are plotted in Figure 6.3. Figure 6.3(a) and (d) show the contact force chain network after the consolidation and before applying shear load for the shear box and cylindrical geometries respectively. Uniform distribution of contact forces can be noticed for both the shear box and cylindrical models with similar contact force magnitudes, indicating that after consolidation, both the models reach an isotropic stress state. Figure

6.3(b) and (e) compare the contact force distributions at the end of the cyclic DSS simulations for the shear box and cylindrical geometries respectively, while Figures 3(c) and (f) exhibit the view from the right face of those shown in Figure 6.3(b) and (e). A gradually varying contact force distribution with depth can be noticed for the shear box model, where contact forces with a higher magnitude are located near the top of the specimen and lower magnitude contact forces are present near the bottom of the specimen. This correlates well with the shearing level (low level at the bottom and high at the top). For the cylindrical model, the depth-dependent variation of contact forces is not readily observed and the large-magnitude contact forces expected near the shearing surface are largely absent. Such an observation might be attributed to the fact that with the enlarged particle size (2 mm in simulations, as opposed to D_{50} of 0.26 mm of Fraser river sand), the particle size/laminar wall thickness ratio was drastically increased. This resulted in insufficient layers of particles being sheared independently by the movement of laminar walls, which results in a rapid shear strain increase as well as vertical effective stress drop during the simulation. Note that this is an outcome of the numerical simulation parameters considered, and could be overcome by using smaller particles (and a larger number of them). Using a numerical sample that follows the actual grain size distribution of the sand will require approximately 1.5 million particles. This approach will likely solve this issue since significantly a greater number of particles can be sheared and contact forces can be transmitted continuously. However the higher computational demand in such simulations (which has resulted in many laminar wall models using 2D simulations (Shi et al. 2010)) makes 3D DEM simulations using shear box much more efficient, which is hence used further in this study.

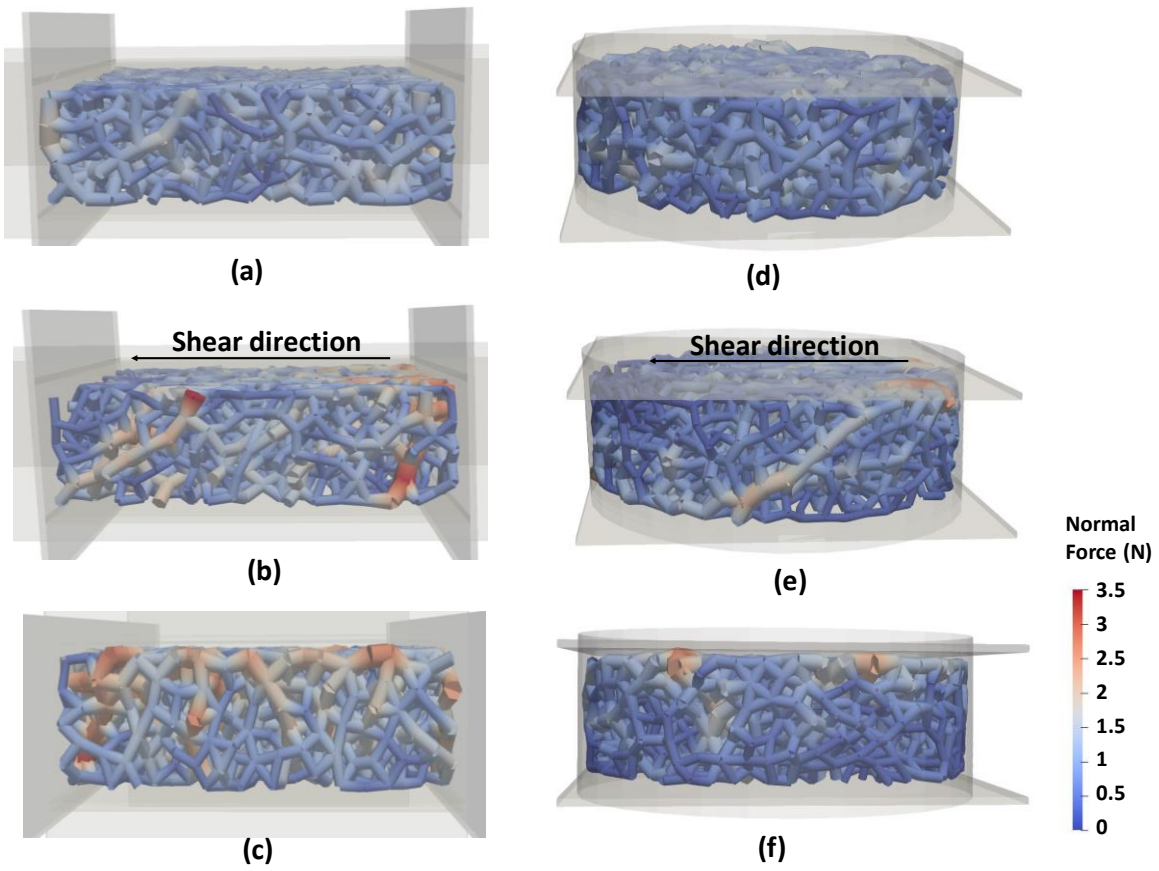

Figure 6.3: Numerically simulated contact force network for the shear box model: (a) after consolidation, (b) after shearing, and (c) side view (right side) of (b); and for the model: (d) after consolidation, (e) after shearing, and (f) side (right side) of (e).

6.2.3. 3D Shear Box Model Validation Using Cyclic DSS Test of Fraser River Sand

In the model verification process described earlier, experimental data from Fraser river sand at a CSR of 0.10 was used. In the model validation described here, stress-controlled, virtual cyclic direct simple shear tests are carried out with cyclic stress ratios (CSR) of 0.08 and 0.12, as reported in the laboratory tests (Wijewickreme et al. 2005). The same microscale parameters listed in Table 6.1 are used for all the simulations since the sand being simulated is the same. Figure 6.4 shows the stress path and shear stress-shear strain response simulated by the DEM model at both the CSR levels. Gradual drop in vertical effective stress is observed in the simulations, followed by a rapid drop in the last few

cycles, similar to that observed in the experimental results. The drop in vertical stress is higher at higher CSR values. Relatively low small shear strains in the initial stages followed by rapid increase is also observed from the stress-strain response, which also closely matches the response reported in (Wijewickreme et al. 2005). Similarly, the number of hysteresis loops in the shear stress-strain response increases with a reduction in CSR, as expected. The microscale parameters that were chosen under the condition that the simulated number of cycles to reach a 3.75% strain is similar to the experimental value, are also found to model the constitutive response of Fraser river sand under cyclic DSS adequately. Figure 6.5 shows the relationship between CSR and the cyclic shear resistance (N_{liq}) of the Fraser river sand at all three CSRs simulated in this work (and in the experimental study). With a decrease in CSR, the number of cycles to initiate liquefaction increases in a linear manner (within the limits of CSR chosen in this work). As noted from this figure, good agreement between the experimental and simulated N_{liq} are obtained, which validates the use of the 3D shear box model and the microscale parameters shown in Table 6.1 to simulate the cyclic DSS test of sands and capture the dynamic mechanical response appropriately.

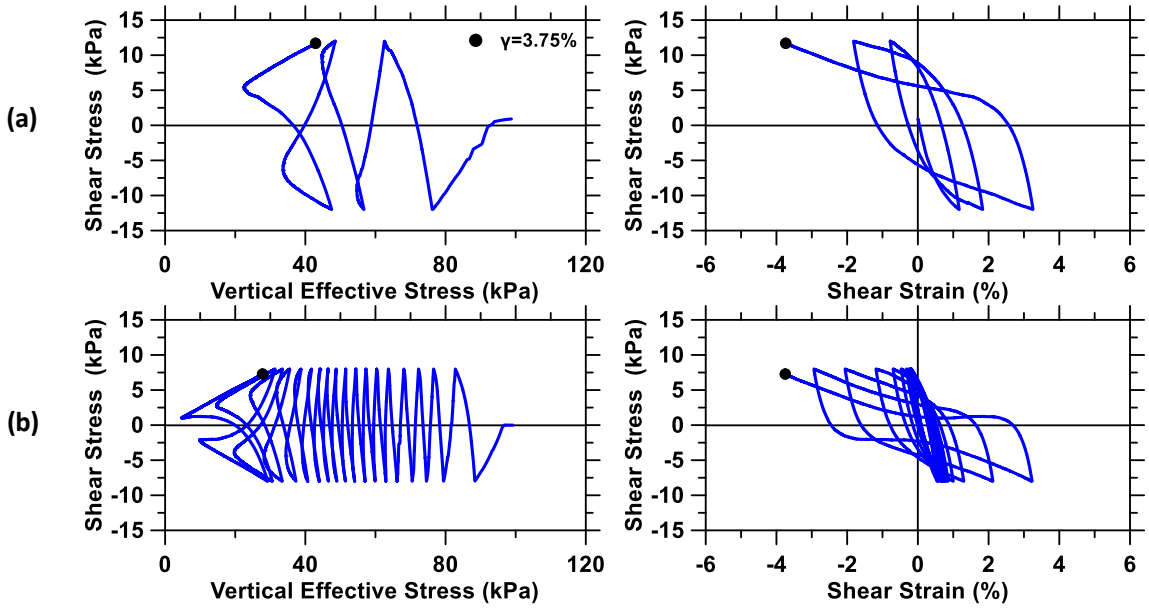

Figure 6.4: Simulated stress path and shear stress-strain response under cyclic DSS tests for Fraser river sand at different CSR: (a) 0.12, and (b) 0.08. Please refer to Figure 6.2 for simulation results corresponding to a CSR of 0.10.

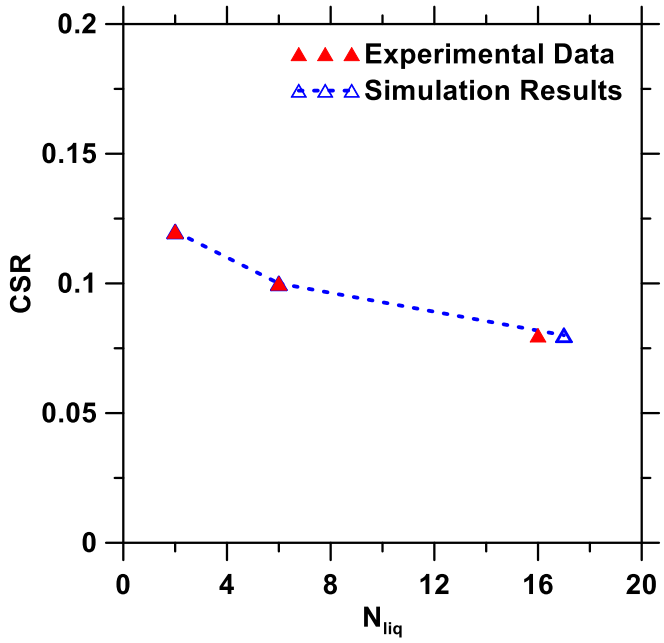

Figure 6.5: Cyclic shear resistance predicted by the numerical simulation and its comparison with experimental results from (Wijewickreme et al. 2005).

6.2.4. Criteria for Determining the Onset of Liquefaction

Different methods have been used to define the occurrence of liquefaction under cyclic DSS tests - for instance, the 3.75% shear strain criterion has been implemented in the development of Figure 6.5. A pore pressure ratio, which is sometimes used, depends on the excess pore pressure generated during cyclic shearing, a key determinant of the cyclic resistance of saturated sands (Ochoa-Cornejo et al. 2016). Based on such a criterion, liquefaction is defined as the state at which the excess pore pressure ratio (r_u) equals 1.0 (Jiaer et al. 2004; O'Donnell et al. 2017a)). Initial liquefaction or partial liquefaction are also the terms used to describe the state when r_u approaches 1.0 since full pore pressure ratio is not achievable in some situations. Furthermore, the onset of liquefaction generally occurs by large shear strains, and not by complete loss of effective stress resulting from the pore pressure build up in loose sands (Porcino and Diano 2016), and hence the possibility of pore pressure ratio attaining a value of 1.0 is rather limited. While the limitations of this parameter as a criterion to establish liquefaction has been detailed in (Jiaer et al. 2004), it has been used in many studies on liquefaction potential of cemented soil deposits (O'Donnell et al. 2017a; Zeghal and El Shamy 2008). Thus, it is instructive to observe the variation in pore pressure ratios as a function of CSR and number of cycles, as is shown in Figure 6.6 for the simulations on Fraser river sand. It is noticed that, as the CSR increases, the pore water pressure ratio reaches a value closer to 1.0 in lesser number of cycles. Rapid change in this ratio is also noticed within the last few cycles, along with significant oscillation that can be attributed to the rapid changes in effective vertical stress shown in Figure 6.4. For a lower CSR level of 0.08, the peak r_u value at the end of simulation (i.e., when the shear strain reached 3.75%) was approximately 0.95. Thus, for sands sustaining

relatively low cyclic shear loads, both the ultimate strain and the pore pressure ratio methods can adequately define the onset of liquefaction. For a higher CSR level of 0.12, the maximum value of r_u was found to be around 0.80 at a shear strain of 3.75%. The rate of increase in r_u is found to be the highest for the latter case. Since, in the simulations, the number of cycles to reach the failure criterion of 3.75% shear strain was always lower than the number of cycles to attain a r_u of 1.0, the former is adopted in the simulations reported further in this chapter. Note that the experimental data used to validate the simulations on carbonate-precipitated sand reported in the following section uses the pore pressure ratio criterion.

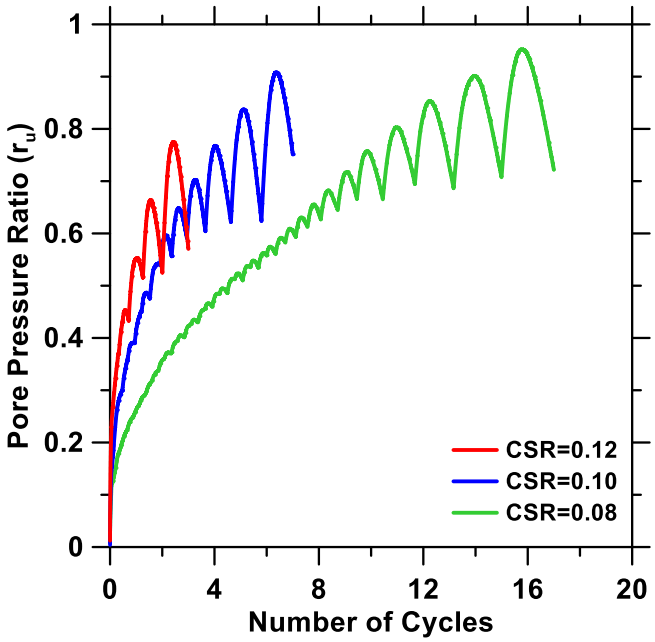

Figure 6.6: Numerically simulated excess pore water pressure ratio (r_u) as a function of number of cycles to reach 3.75% strain.

6.3. DEM Simulations of Sands Strengthened Using Carbonate Precipitation

In this section, DEM model developed and validated in the previous section to simulate the cyclic DSS test on uncemented sands is adopted to evaluate the efficiency of microbially

induced carbonate precipitation (MICP) on liquefaction mitigation. Limited cyclic DSS experiments are reported on sand strengthened using MICP. This modeling effort employs the experimental data reported in (O'Donnell et al. 2017b) towards predicting the liquefaction resistance of MICP-strengthened sands. Four sets of cyclic DSS experimental data reported in (O'Donnell et al. 2017b) are selected for numerical simulations: (i) an untreated Ottawa 20-30 sand specimen (UT) with a relative density (d_r) of 40% as the control case, (ii) MICP-cemented specimen (T) with a d_r of 40% and a calcite content of 0.86% by mass, (iii) the treated specimen reconstituted once after cyclic DSS testing (R1) and (iv), the treated specimen reconstituted once again after the first reconstitution and cyclic DSS testing (R2). The samples R1 and R2 have relative densities of 40% and unchanged calcite contents of 0.86%. The calcite content used in the experimental study is less than 1% because it has been shown that very little calcite precipitation is necessary to result in significant improvements in stiffness and dilatancy of sand (O'Donnell and Kavazanjian 2015). Considering the poor gradation of Ottawa 20-30 sand (see Figure 6.7) and the need for computational efficiency (Feng et al. 2017), a simplified enlarged particle size distribution (PSD) as shown in Figure 6.7 is used to prepare the numerical samples. The simplified PSD has a mean of 4.5 mm and a standard deviation of 0.9 mm. The simplified PSD allows fewer number of particles to be used in the simulations.

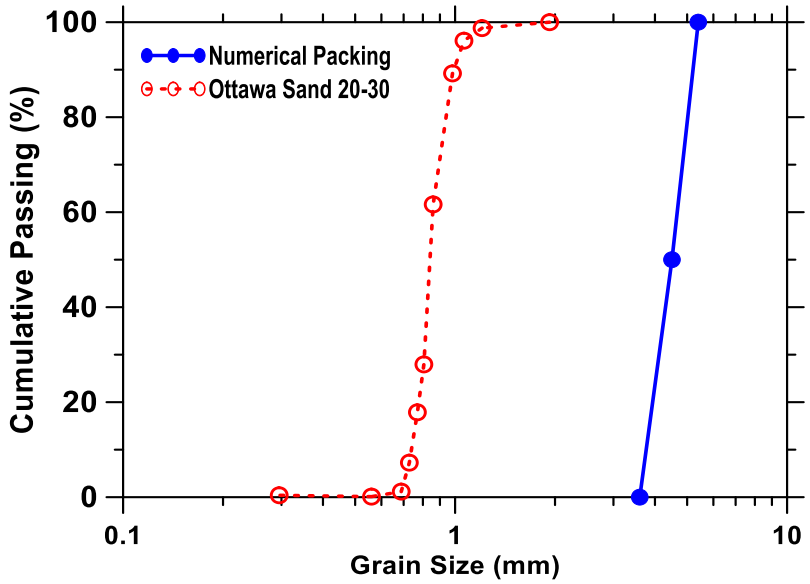

Figure 6.7: Particle size distribution of Ottawa 20-30 sand the corresponding simplified PSD used for simulations.

6.3.1. DEM Model Parameter Identification for Cyclic DSS Simulation of MICP-Cemented Sands

As discussed earlier, cyclic DSS experiments are reported in (O'Donnell et al. 2017b) for four different sets of samples. In Section 3, during the verification of the DEM model, the model parameters were determined by matching the experimental and simulated number of cycles to liquefaction for a given CSR. This was then validated for other CSRs. Here, a different approach is required to calibrate the DEM parameters since the microscale parameters will be different between the UT, T, R1, and R2 samples. Hence the constitutive response of untreated and MICP-strengthened sands under consolidated isotopically undrained triaxial compression (CIUC) is numerically simulated and the simulation results are used for DEM input parameter calibration. While experimental data is available for the untreated Ottawa 20-30 sand (UT sample), CIUC test results are not available for the Ottawa 20-30 sand with 0.86% calcite content and a relative density of 40% (the T sample).

However, from (O'Donnell et al. 2017b) it is seen that Ottawa 20-30 sand with a 0.66% calcite content and a relative density of 50%, for which CIUC data is available, has a very similar shear wave velocity as the T sample. Thus, this experimental data is used to obtain the DEM simulation parameters for the treated (T) Ottawa 20-30 sand.

CIUC test is simulated using a constant volume assumption. This method, applicable for fully saturated granular materials conforming to the incompressible water assumption, is to simulate the undrained test by maintaining a constant sample volume throughout the test (Yang et al. 2018). For the constant volume method, different boundary conditions can be employed (i.e., rigid boundary wall and flexible membrane wall). Our recent work has shown that the performance under CIUC test is not dissimilar for untreated and lightly cemented sands with either of the boundary types, while a flexible membrane boundary is preferred for heavily cemented sands (Yang et al. 2018a). Considering the low calcite content in the treated specimens (~0.86% by mass), the rigid boundary model is used for computational expediency. The strain rate of side walls (lateral strain rate, $\dot{\varepsilon_3}$) can be related to the axial strain rate ($\dot{\varepsilon_1}$) as:

$$\dot{\varepsilon_3} = -0.5\dot{\varepsilon_1} \tag{6.4}$$

The excess pore water pressure u_g can be calculated as:

$$u_g = \sigma'_{3\_ini} - \sigma'_3 \tag{6.5}$$

where σ'_{3_ini} and σ'_3 are the initial effective stress and the effective stress in the side walls during the simulation, respectively. The CIUC simulations are carried out at a strain rate of 0.1/s.

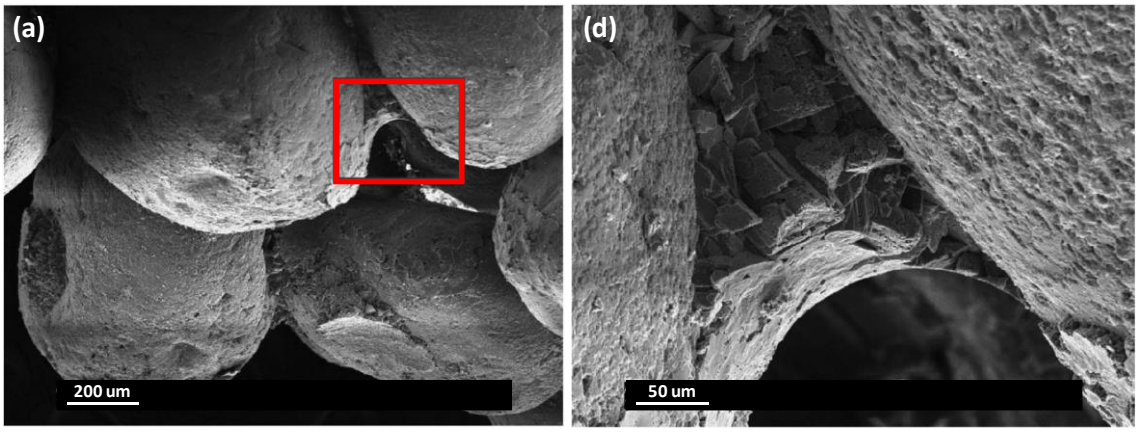

Figure 6.8: SEM images showing CaCO3 precipitation concentrated at particle contacts (O'Donnell et al. 2017b).

Numerical samples of the UT and T specimens are prepared using the particle packing procedure described earlier and consolidated with an effective confining stress of 100 kPa before the CIUC test. The microscopic DEM input parameters used for the UT and T specimens were determined using the methodology described in our previous work (Yang et al. 2016), and are listed in Table 6.2. Normal stiffness and stiffness ratio of 100 MPa and 0.30 respectively were found to adequately represent Ottawa sand in our earlier studies. For the treated specimen, the normal stiffness was left unchanged since the calcite content is very low, and the effect of calcite precipitation is captured through changing the cohesive strength of the bond. Such an approach is acceptable and has been adopted in the past (Yang et al. 2018a) because it was noticed from electron micrographs (Figure 6.8 (O'Donnell et al. 2017b)) that calcite precipitation predominantly occurs at the particle contacts at low cementation levels such as the one examined here. The cohesive bond strength was well correlated to the shear wave velocity in (Yang et al. 2018a), and the chosen bond strength for the treated specimen was based on this relationship and the shear wave velocity provided in (O'Donnell et al. 2017b) to account for the inter-particle

bridging effect of calcite grains. Experience from earlier simulations that demonstrated increase in interparticle friction angle and plastic moment limit coefficient was used to derive appropriate values for these parameters. The increase in interparticle friction angle and the plastic moment limit coefficient from the untreated to the treated samples indicates the effect of calcite crystals on roughening of sand particle surfaces. This increases the resistance to sliding, which contributes to a higher global shear resistance. The CIUC simulation results for the UT and T samples are shown in Figure 6.9 along with the experimental data. It can be noticed from Figure 6.9 that both the deviator stress and excess pore pressure predicted by the numerical model are in good agreement with the experimental results, indicating that the microscale parameters chosen can reasonably predict the constitutive response of untreated and MICP-treated sand.

Table 6.2: DEM input parameters used to simulate the macroscopic response of cyclic DSS tests.

Microscopic parameters	Untreated Ottawa 20-30 sand (UT)	Treated Ottawa 20-30 sand (T)	Reconstituted Ottawa 20-30 sand	
			R1	R2
Relative Density (d_r) (%)	40	40	40	40
Normal stiffness (k_n) (MPa)	100	100	100	100
Stiffness ratio ($\alpha = k_s/k_n$)	0.3	0.3	0.3	0.3
Inter-particle friction angle (μ) (°)	22	29	25	23
Rolling stiffness coefficient (β)	0.3	0.3	0.3	0.3
Plastic moment limit coefficient (η)	0.28	0.35	0.32	0.3
Bond strength C_s (MPa)	0	0.75	0.35	0.13
Initial vertical effective stress (kPa)	100			

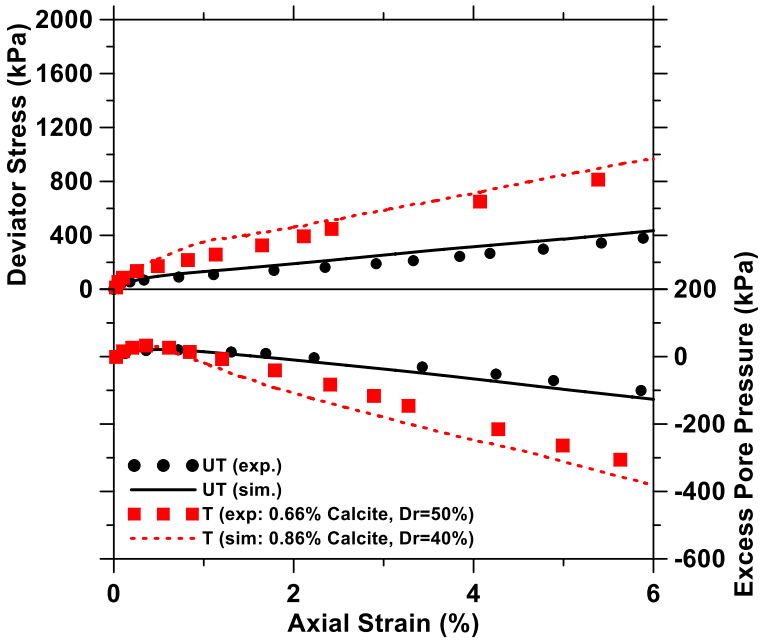

Figure 6.9: Experimental (O'Donnell et al. 2017b) and numerically predicted constitutive relationships for untreated (UT) and treated (T) samples under CIUC test. Note that the experimental data for the actual treated sample used in cyclic DSS test is not available, and a specimen with very similar characteristics is used for DEM parameter identification.

6.3.2. Simulating Cyclic DSS Test of Cemented and Reconstituted Sands

To simulate the cyclic DSS tests, numerical samples were constructed using a shear box of dimension 100 x 33 x 100 mm, which is similar to that used in the laboratory tests. All the numerical samples were packed with ~5,000 particles following the designed PSD shown in Figure 6.7. A small friction angle of 0.1^{o} was applied to prepare the samples with a relative density of 40%. The shearing speed (velocity assigned to the top boundary wall) was controlled by a user-defined function to maintain a cyclic frequency of 1 Hz, which is the same as the frequency used in the experiments. In a dual 16-core system with a 2.6 GHz CPU and 128 GB RAM, which was used to run the simulations described in Section 3, much longer times were needed to carry out the cyclic DSS tests of cemented sands especially for larger number of cycles, attributable to the larger specimen size used. Thus,

the cyclic DSS simulations were implemented in Amazon Web Service (AWS; https://aws.amazon.com/), which is a cloud computing platform that provides various choices of computational power. While for fixed number of particles, the simulation speed mainly depends on the maximum clock speed of the CPU, the most significant advantage of using AWS is the capability to simultaneously run multiple simulations, thereby reducing the total computational time. Details related to implementing YADE on AWS can be found in (Šmilauer et al. 2018).

In addition to the microscale parameters for the UT and T specimens determined as described earlier, microscale parameters needed to simulate the cyclic DSS tests of R1 and R2 samples are also listed in Table 6.2. While keeping the normal stiffness and stiffness ratio constant, the other parameters were initially changed based on the observed trends in the experimental CSR-N_{liq} response given in (O'Donnell and Kavazanjian 2015). Since only a single experimental data point is available for the reconstituted samples (CSR=0.35 for R1 and CSR=0.30 for R2), the numerical simulations were tuned out to match the reported data at the respective CSRs. The cohesive bond strength had to be reduced to 0.35 MPa for the first reconstitution (from 0.75 MPa for the treated case), and then to 0.13 MPa for the second reconstitution, indicating the weakening effects of calcite bridging during repeated shear events.

Since the cyclic strength curve of untreated Ottawa 20-30 sand is reported in (O'Donnell et al. 2017b), three simulations were carried out for the untreated numerical sample with CSRs of 0.30, 0.27 and 0.25. The DEM simulations with the microscale parameters reported in Table 6.2 were carried out to predict the cyclic strength at different CSRs to develop cyclic strength curves as shown in Figure 6.10. Figure 6.10 shows the cyclic

strength curves of the MICP-cemented and reconstituted sands predicted by the numerical models along with the limited available experimental results. It can be noticed that the simulated cyclic strength curves closely match the experimental results, validating the use of CIUC test data to calibrate the microscale parameters of the DEM model. A comparison between the numerically predicted curves for the untreated and treated samples indicates that a relatively small amount of calcite (~0.86 by mass) lends the sand the capability to sustain more liquefaction cycles at the same CSR or higher stresses before failure for the same number of cycles. Simulations of reconstituted sands point to a decrease in cyclic resistance of the cemented sand during multiple shear events. The cyclic resistance of the R2 sample is significantly lower than that of the treated sample, but even after two reconstitutions, it shows higher strength than the untreated sand. The capability of the DEM simulations to develop cyclic strength curves as shown in Figure 6.10 for different sand types and CSRs is expected to be beneficial to engineers in deciding the levels of cementation required to mitigate liquefaction.

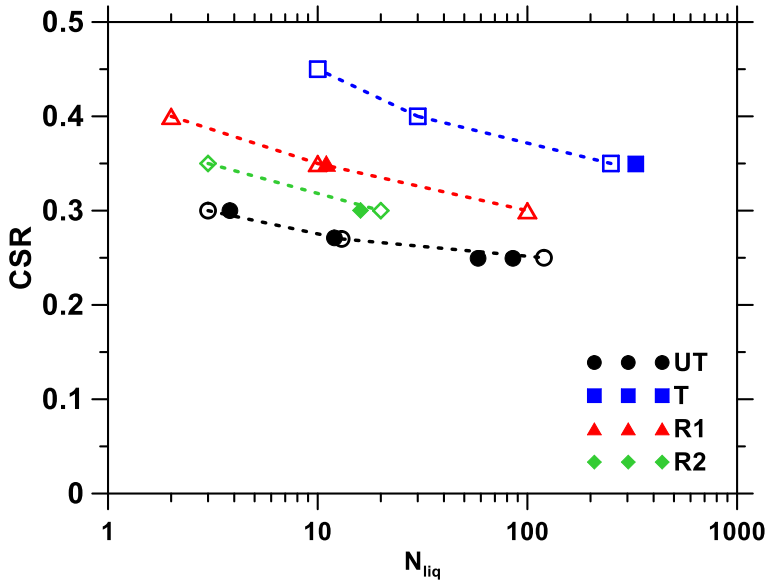

Figure 6.10: Cyclic strength curves developed using the DEM simulations and compared to the experimental data reported in (O'Donnell et al. 2017b). The closed symbols correspond to experimental data and the open symbols to DEM simulations.

To further explore the effect of calcite precipitation on the shear resistance of sand, the simulated stress path as well as the shear stress – shear strain relationship of the UT, T, R1 and R2 samples are shown in Figure 6.11. All the simulations are carried at a cyclic stress ratio of 0.30 and only the response for the first 10 cycles are plotted here. A rapid drop in vertical effective stress and rapid development of shear strain are observed for the untreated specimen within the first four cycles. On the other hand, the simulations point to a significantly better cyclic DSS performance of the MICP-cemented specimen. Reduced vertical effective stress drop and shear strain development are observed in the first ten shearing cycles. The specimen after first reconstitution shows similar performance compared to the treated specimen, while the second reconstitution significantly degrades the cyclic shear strength. It is understood that the liquefaction resistance of the treated sand depends on the strength of calcite and the quality of particle contacts (bonds). Liquefaction does not occur as long as the particles are held in contact by the calcite grains, but once

this bond breaks, as is the case with the second reconstitution, the sand shows brittle behavior and demonstrates insignificant resistance to liquefaction.

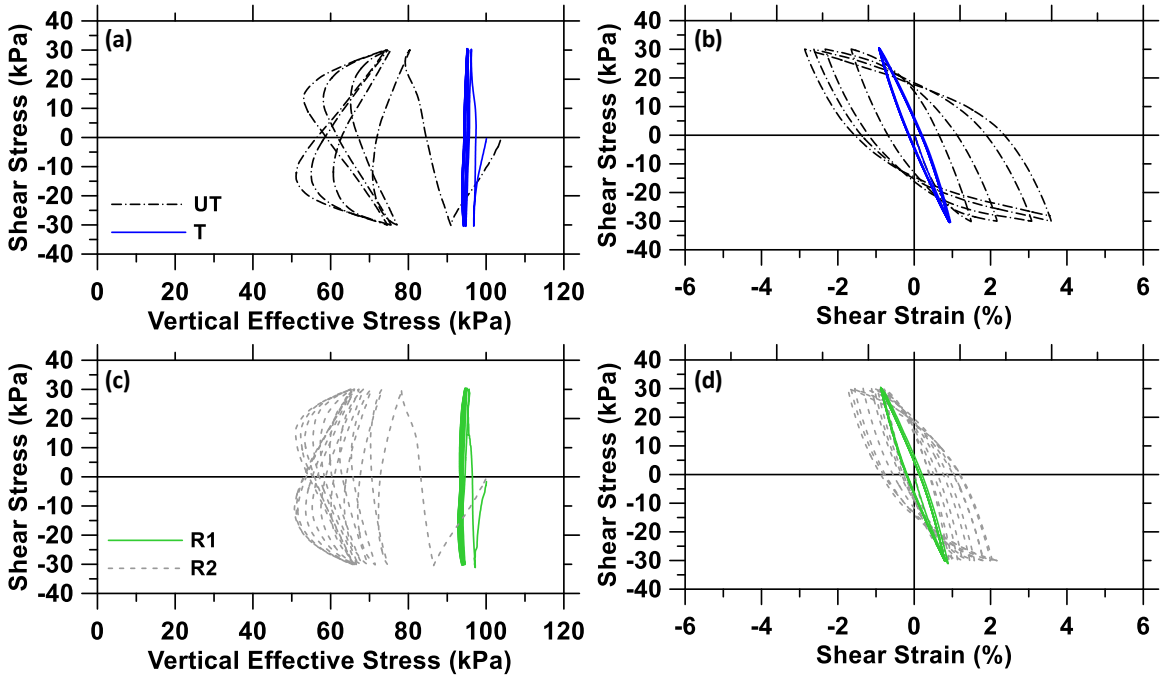

Figure 6.11: Simulated stress path and shear stress – shear strain relationship under cyclic DSS test for untreated, cemented and reconstituted sands with CSR = 0.30, for 10 cycles.

The coordination number, which is related to the stability of the granular system (Gong et al. 2011; Thornton 2000), is also used here to quantify the impact of cementation on liquefaction resistance of sand. It is defined as the average number of contacts per particle for the whole system and can be expressed as shown in Equation 6.6 for numerical systems that were packed in a gravity-free condition.

$$Z = \frac{2C - N_1}{N - N_1 - N_0} \tag{6.6}$$

Here, Z is the coordination number, C is the number of contacts, N is the number of particles, and N_1 and N_0 represent the number of particles with one or zero contact, respectively.

Figure 6.12 shows the evolution of coordination number as a function of the number of shearing cycles for the untreated, cemented, and reconstituted specimens simulated at a CSR of 0.30. Similar initial coordination numbers (between 5.2 and 5.3) are noticed for all the four specimens, which is likely due to the low cementation level as well as the same initial relative density. During cyclic shearing, the coordination number drops until failure (4 cycles) for the untreated specimen. Such a phenomenon is caused by rapid particle rearrangement and loss of contact between particles under relatively high shear stress before failure. On the other hand, the coordination number of both the T and R1 specimens remain relatively constant during the 10 shearing cycles, which indicates that the particle rearrangement is restricted by the combined bridging and roughening effect from the precipitated calcite. The vertical stress drop for these samples are also minimal, which shows that there is no significant contact loss. After the second reconstitution, the coordination number evolves similar to that of untreated sand. However, it is also noticed that while the coordination number of the R2 specimen after 9 cycles drops to a level lower than the coordination number for the untreated specimen at 4 cycles (when it failed), the R2 specimen is capable of sustaining a few more cycles of shearing before failure (20 cycles at a CSR of 0.30 as can be seen from Figure 6.12). This could be attributed to the fact that even after two reconstitutions, the inter-particle contacts can still sustain higher sliding due to influence of remaining calcite.

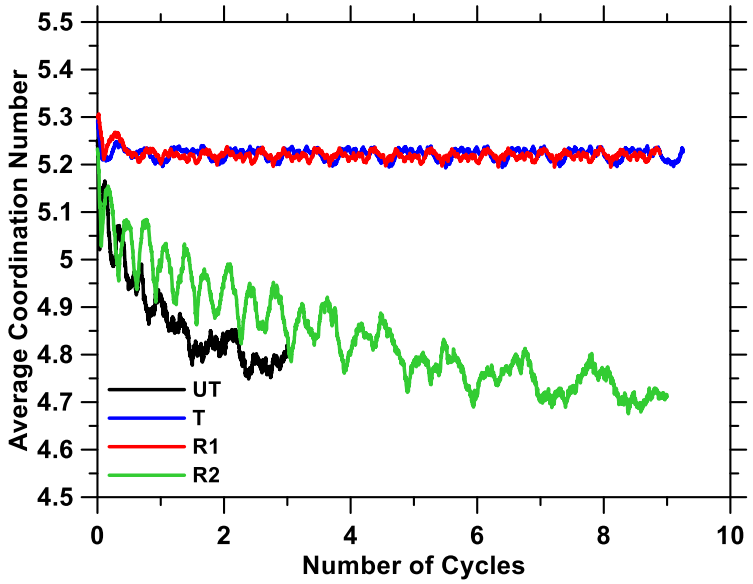

Figure 6.12: Predicted average coordination number of untreated, cemented and reconstituted sands, for the first 10 cycles of cyclic DSS simulation with a CSR of 0.3.

6.4. Summary and Conclusions

This chapter has presented DEM simulations on sands subjected to cyclic direct simple shear tests and evaluated the performance of sands cemented using microbially induced carbonate precipitation (MICP). The use of a previously calibrated and verified six-parameter model in the open-source DEM platform YADE was used. A 3D shear box geometry and a cylindrical geometry restricted by laminar boundary walls (stacked rings) were used to carry out the initial simulations. The DEM model parameters for the chosen Fraser river sand were obtained by matching the simulated number of cycles to failure (i.e., to reach a shear strain of 3.75%) in a DSS test at a CSR of 0.10 to that reported in the experiments. The 3D shear box model was found to be computationally convenient given the larger size of simulated particles, and hence used for the simulations reported in this chapter. To validate the DEM model, stress-controlled, virtual cyclic DSS tests were carried out on Fraser sand at CSRs of 0.08 and 0.12. The experimental and simulated shear

stress-shear strain curves, vertical stress-shear stress curves, and the number of cycles to failure were similar, demonstrating the capability of the model and the parameter selection method to simulate cyclic DSS on sands.

Since extensive experimental data on cyclic DSS test of MICP-cemented sands were not available, microscale DEM model parameters were determined by simulating undrained triaxial compression tests on MICP-cemented sands. Cyclic DSS simulations using the 3D shear box model were carried out on untreated, treated (calcite content of 0.86%), and reconstituted samples using the microscale parameters determined from undrained triaxial simulations. The Cyclic DSS simulations were carried out for multiple CSRs to generate the cyclic strength curves. The simulated cyclic strength curves closely matched the experimental results, demonstrating the capability of the DEM-based model to predict cyclic strength curves to aid engineers in the design of appropriate MICP-strengthening schemes. It was found from the cyclic strength curves and the coordination numbers that a small amount of calcite was enough to resist liquefaction for a significant number of cycles. For reconstituted sands used to capture the influence of multiple shear events, the liquefaction resistance decreased as the number of reconstitutions increased. The cohesive bond strength between the particles decreases with reconstitution, and even when some interparticle sliding and roughness are contributed by the remnant calcite grains, the deterioration in liquefaction resistance is significant. The simulation scheme developed in this study can be used to infer the influence of calcite content on liquefaction mitigation, and help design appropriate MICP strategies.

7. A PRELIMINARY STUDY ON THE CONE PENETRATION TEST (CPT) WITH DISCRETE ELEMENT METHOD (DEM)

7.1. Introduction

The cone penetration test (CPT) is an in-situ testing method that is used for identifying soil types and estimating soil properties (Been et al. 1987; Lunne et al. 1997; Robertson 1986, 2009; Schnaid 2008). CPT has been accepted as one of the major choices for in-situ testing, considering its rapidity, repeatability, reliability and economy. The measured CPT parameters (e.g., cone t-penetration resistance (q_c) and friction resistance (f_s)) are typically analyzed by empirical or semi-empirical methods including bearing capacity theory (Durgunoglu and Mitchell 1973; Terzaghi 1951), cavity expansion methods (Salgado et al. 1997; Vesic 1972; Yu 2013) or steady-state cone-penetration and strain-path methods (Baligh 1985; Houlsby et al. 1985; Sagaseta et al. 1997; Teh and Houlsby 1991). Laboratory tests including centrifuge tests (Bolton et al. 1999; Bolton and Gui 1993) and calibration- chamber tests (Ghionna and Jamiolkowski 1991; Houlsby and Hitchman 1988; Parkin and Lunne 1982) have also been performed to study cone-penetration. However, these laboratory tests are typically laborious and expensive. Finite-element method (FEM) has been adopted by researchers to develop constitutive models for the cone penetration process (Abu-Farsakh et al. 1998; De Borst 1982; Huang et al. 2004; Kouretzis et al. 2014). Partial agreement between physical tests and FEM simulated CPT results has been observed (Susila and Hryciw 2003) while significant mean error (20%) is also found from FEM simulations (Ahmadi et al. 2005).

The discrete element method (DEM), on the other hand, has been recognized as a powerful numerical tool for exploring the penetration mechanism of the CPT by providing insights

into micro-scale mechanical behavior of granular material that governs the macro-scale response. DEM-based simulations have been actively reported for CPT of granular materials. Jiang et al. (2006) reported a two-dimensional (2D) DEM model to study the plane-strain penetration mechanism in granular materials and focused on the effect of the soil–penetrometer interface friction. The difference between two-dimensional and three-dimensional DEM simulations has also been reported (Bakunowicz and Ecemis 2014). Arroyo et al. (2011) built a virtual calibration chamber using a 3D DEM model. The cone soil particle – penetrometer interaction has been investigated by (Kotrocz et al. 2016), where a direct shear simulation was carried out for parameter calibration. A 3D cylindrical numerical model with 90° and 30° segmentations has been reported to simulate the CPT with increased cone-diameter to particle-diameter ratio while maintaining a relative low computational time (Falagush et al. 2015). The effect of particle shape, together with the particle crushing mechanisms are studied in (Ciantia et al. 2016; Falagush et al. 2015).

7.2. Preliminary Study with 2D DEM Model

In this chapter, a preliminary study is carried out on simulating CPT of sands with a 2D DEM model. The influence of on non-material factors (e.g., boundary conditions, velocity, and cone-diameter to particle-diameter ratio) are numerically studied. The results are expected to pave the way for the simulation of CPT on bio-cemented soils and investigate the effect of carbonate precipitation on soil's behavior (such as porosity change and force transmission). Experimental results on CPT of bio-cemented sands are very rare, and there is only a recent study (Gomez et al. 2017) on this topic. In the absence of data for verification and validation, this chapter is concerned with only developing the numerical models for CPT.

7.2.1. Particle Packing and Model Preparation

Random loose packing algorithm (Šmilauer et al. 2018) was employed to generate a random non-contact particle packing (as illustrated in Figure 7.1(a)) with designed particle dimeters (as listed in Table 7.1). A single-size particle packing was employed here considering a poor gradation of the sand reported in (Gomez et al. 2017). The generated particle packing was then allowed to consolidate under the effect of gravitational force into a pre-defined rectangular chamber with rigid boundaries. The initial inter-particle friction angle was adjusted so that the final packing can reach a porosity of 0.14, which is equivalent to a laboratory (three-dimensional) porosity of 0.403 (Bakunowicz and Ecemis 2014) that is commonly observed for loose sand. Once the self-consolidation reached a balanced state, a confining stress can be applied to the particle packing depending on the designed simulation scenario (e.g., deep penetration may require a high confining stress while shallow penetration can be simulated with low confining stress or even no confining stress).

Facet elements (which are triangular rigid elements) (Šmilauer et al. 2018) were then used to assemble the penetrometer with a diameter of 16 mm and a cone tip angle of 60° (as reported in (Gomez et al. 2017)) directly on the top of particle packing. Figure 7.2(b) shows the prepared model before the loading stage. The inter-particle contacts were assigned the input parameters listed in Table 7.1, which are commonly used values in the previous chapters to simulate different test methods on sands. No attempt was made here to match any experimental results since calibrating the contact model may require multiple sets of experimental data from different tests on same type of granular material (Ciantia et al. 2016; Ecemis and Bakunowicz 2018; Kotrocz et al. 2016), and this section only performs a

preliminary study focusing on the influence from non-material factors. A constant velocity was then assigned to the assembled penetrometer to drive it into the particle packing until target depth. Figure 7.1(c) illustrates a typical status at the end of CPT simulation and the corresponding force chain network is plotted in Figure 7.1(d), where a concentrated force network was noticed near the location of cone tip, as expected.

Table 7.1: Geometries information and material properties used for simulation.

Cone diameter (mm)	15		
Particle size (mm)	1	1.5	3
Cone diameter/particle size	15	10	5
Number of particles	1400	5600	12700
Height x width (mm)	100 x 100		
Cone advance speed (mm/s)	20, 200 and 2000		
Porosity	0.14		
Normal stiffness (k_n) (MPa)	100		
Stiffness ratio ($\alpha = k_s/k_n$)	0.15		
Inter-particle friction angle (μ) (°)	18		
Rolling stiffness coefficient (β)	0.25		
Plastic moment limit coefficient (η)	0.1		

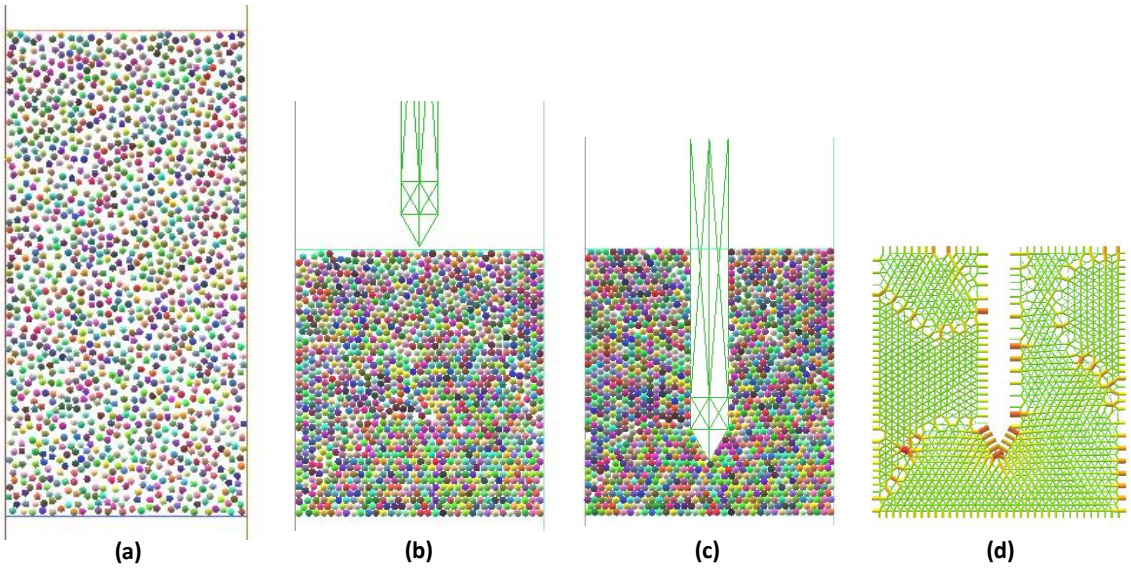

Figure 7.1: (a) Initial loose-state packing, (b) prepared 2D DEM model for CPT simulation, (c) model after CPT simulation (with a cone-diameter/particle-size ratio of 15), and (d) force chain network after simulation of CPT.

7.2.2. Influence of Penetrometer Advance Speed

A typical cone penetration test (CPT) can be carried out with a cone advance speed ranging from 15 mm/s to 25 mm/s and many researchers have reported modeling CPT with a speed in such a range (Ecemis and Bakunowicz 2018; Falagush et al. 2015; Kotrocz et al. 2016). However, it is still interesting to investigate the effect of cone advance speed on the simulation results since other researchers have reported that increased loading rate may not significantly influence the simulation results and thus may help to accelerate the simulation and reduce computational time and effort.

The numerical model with a cone-diameter/particle-size ratio of 15 was used in this study (as illustrated in Figure 7.1). Approximately 1400 particles were used to fill the chamber having a dimension of 100 mm width x 100 mm height. Three different speed of 20 mm/s, 200 mm/s and 2000 mm/s were used here to drive the penetrometer 85 mm into the packed particles. The four rigid boundary walls were fixed during the simulation. Figure 7.2 shows

the simulated penetration resistance, together with the coordination number evolution for the selected three different cone advance speeds. It is observed that both the 200 mm/s and 20 mm/s driving speed simulations predicted similar penetration responses whereas the 2000 mm/s case predicted a higher penetration resistance. Such an observation could indicate that the penetrometer advance speed can be increased within limits for DEM-based numerical simulations to save the computation time, especially for simulations containing large number of particles.

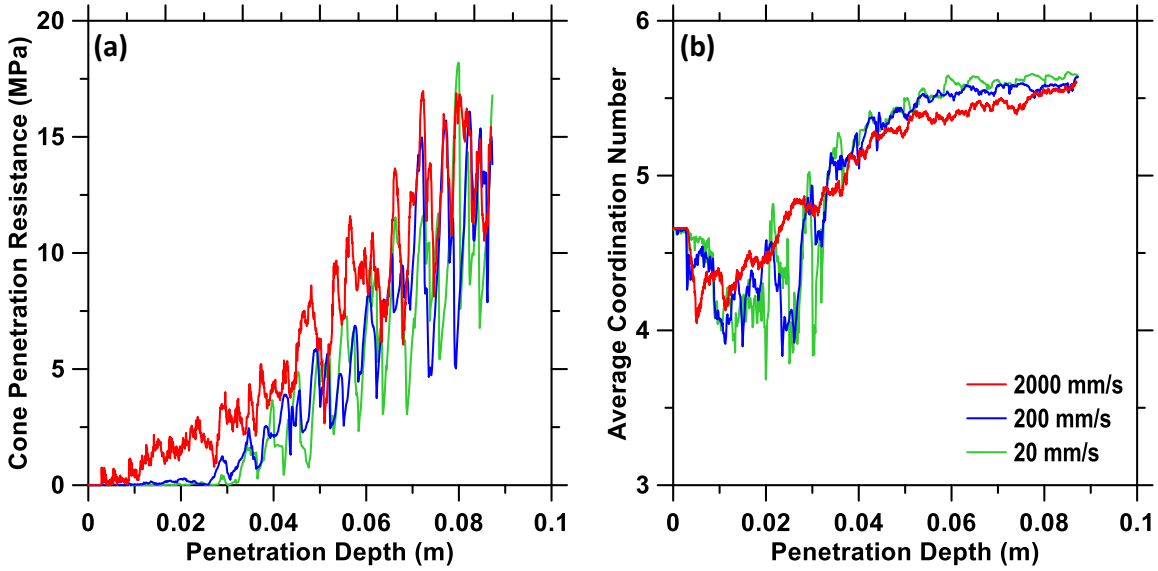

Figure 7.2: Effect of loading speed on: (a) cone penetration resistance and (b) coordination number.

7.2.3. Influence of Cone-diameter to Particle-size Ratio

It has been reported that an increase in particle size (while maintaining the same cone size) is typically required to control the number of particles required in a reasonable simulation volume. Since the cone-diameter to particle size (D_{50} in experiment) in the experiment is significantly larger than that is generally affordable in terms of computational capability (which may require millions of particles to simulate the number of particles encountered

in a field CPT) (e.g., numerical ratios of 3.3 and 2.4 compared to experimental ratio of 36 in (Ciantia et al. 2016) and a numerical ratio of 18 compared to experimental ratio of 45 in (Falagush et al. 2015)), it is necessary to determine the influence of cone-diameter to particle-size ratio to accurately depict the effect of carbonate precipitation on enhancing soil's properties in the future work.

Thus three cone-diameter/particle-size ratios (5, 10 and 15) were adopted in this section, while a ratio of 16 was used for the experiments (Gomez et al. 2017). All the three samples were prepared to a porosity of 0.14 with four fixed rigid boundary walls. The final prepared state contained 1400, 5600 and 12700 particles, corresponding to the three cone-diameter/particle-size ratios in the 100 mm width x 100 mm height chamber. A cone advance speed of 200 mm/s was applied to all the three simulations to drive the cone to penetrate 85 mm into the sample. The simulation results are plotted in Figure 7.3, where reasonably similar penetration resistances are predicted by the three cases, which could result in the conclusion that the enlarged cone-diameter/particle-size ratios selected for this study are acceptable for simulating the reported cone penetration test that has a relatively low cone-diameter/particle-size ratio (Gomez et al. 2017). However it was noticed that the simulated cone penetration resistances showed in both Figure 7.2 and Figure 7.3 are significantly larger than that reported for loose plain sands (Ecemis and Bakunowicz 2018; Gomez et al. 2017; Schnaid 1990), which is mainly due to the fixed boundary conditions that strictly restraints the expansion of particles during the simulation.

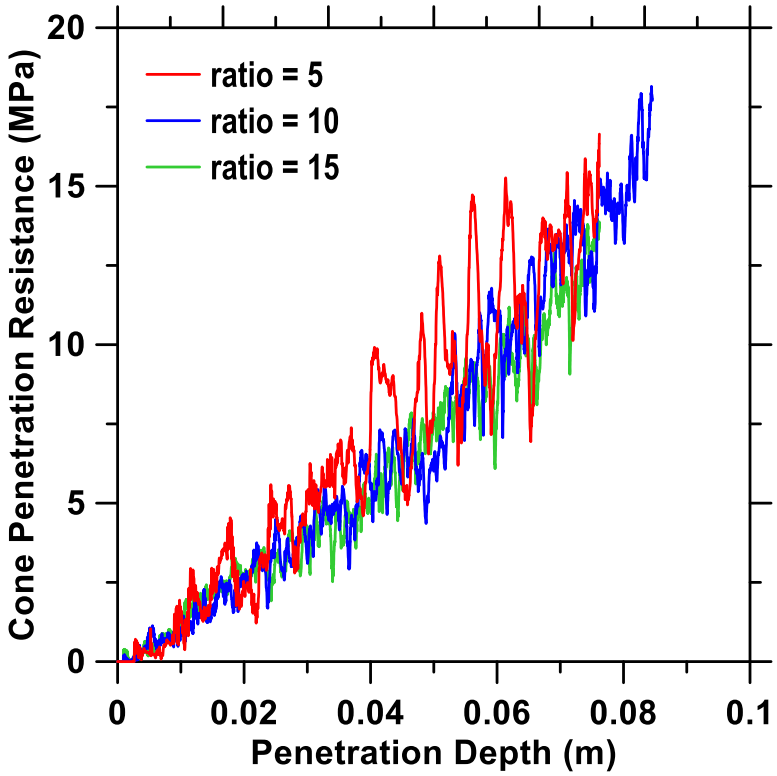

Figure 7.3: Simulated cone penetration resistance for different cone-diameter/particle-size ratios.

7.2.4. Influence of Boundary Conditions

In this section, the influence of boundary conditions on CPT simulations was investigated by introducing four sets of numerical specimens: (1) a numerical chamber with 100 mm width and 100 mm height bounded by four fixed boundary walls; (2) a numerical chamber with 200 mm width and 100 mm height with same boundary conditions as in (1); (3) and (4) were two specimens with same geometry and sizes as that of (1) and (2) while installed with a fixed top boundary wall and a servo-controlled side and bottom boundary walls (Ecemis and Bakunowicz 2018; Falagush et al. 2015). All the specimens were packed with a particle size of 3 mm (corresponding to a cone-diameter/particle-size ratio of 5). A user-defined function was developed under Python environment to control the movement of

side and bottom boundary walls to maintain constant confining stress. The same advance speed of 200 mm/s was employed to drive the penetrometer in to the particle packing.

Figure 7.4 shows the penetration penetration resistance obtained from the four sets of simulations. It can be noticed from the figure that by increasing the chamber width from 100 mm to 200 mm, the predicted cone resistance at the end of simulations was greatly reduced; from 15 MPa to 7 MPa, which indicates a strong boundary effect from the fixed boundary conditions. A further increase of the chamber width may mitigate such boundary effect, but it comes with a corresponding increase in computational cost due to the larger number of particles required to be simulated. It is also observed that by employing the servo-controlled boundary condition, the predicted penetration resistance was drastically reduced from 15 MPa to 1 MPa for the 100 mm wide chamber, which is comparable to the reported experimental results on loose sands (Schnaid 1990). A simulation carried out on the 200 mm wide chamber controlled by constant stress boundaries also predicted a similar response, indicating that by employing the constant stress boundaries to enable the particle expansion during simulation, the boundary effect can be mitigated.

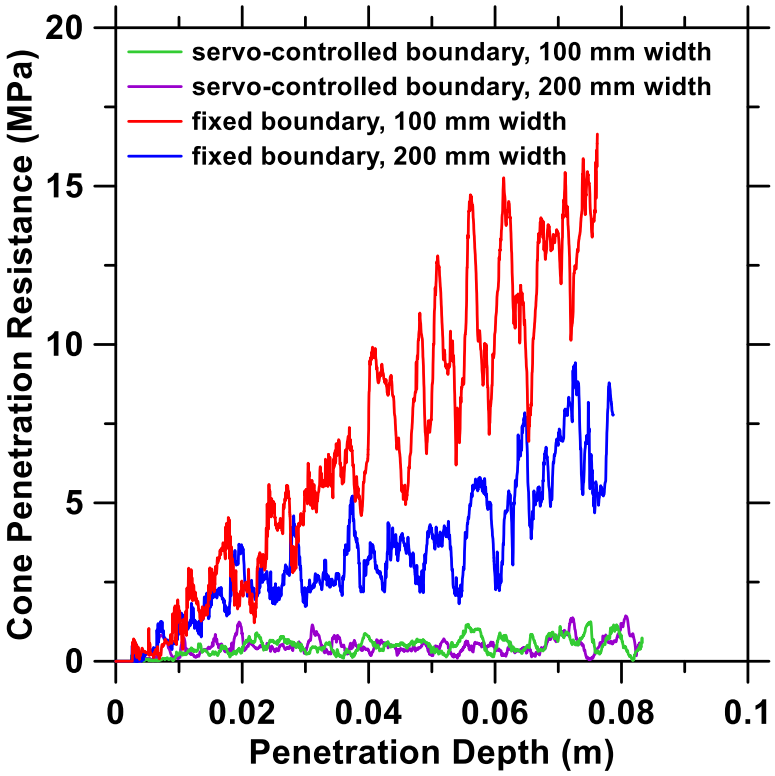

Figure 7.4: Influence of boundary conditions and chamber width.

7.3. Conclusions and Future Work

This chapter has presented a preliminary study on the numerical simulation of cone penetration test using 2D DEM models. The non-material factors such as loading speed, cone-diameter/particle-size ratio, and boundary conditions were parametrically investigated. It is noticed that the loading speed can be increased from the recommended experimental value to accelerate the simulation without significantly compromising accuracy. The cone-diameter/particle-size ratio can also be increased to reduce number of particles required, which can further decrease the computational cost (only applies to the reported experimental work, which will be simulated in a future study). The boundary conditions, on the other hand, can drastically influence the simulation results. A numerical chamber with large width/height ratio is required to reduce such a boundary effect with an

increased number of particles. A servo-controlled boundary condition that can maintain constant stress during simulation can effectively mitigate such an effect without the requirement of enlarging the chamber width/height ratio.

The numerical model developed through this preliminary study will be used to simulate the cone penetration test on bio-cemented sand in an upcoming work. A refined servo-control mechanism will be developed to simulate the multi-layer experimental setup (Gomez et al. 2017). A friction sleeve part will be added to the numerical penetrometer to closely duplicate the experiment. The cone penetration resistance, together with the sleeve friction will be numerically evaluated to determine the micro-scale parameters required for simulation. The verified model will be validated on cemented sands and the influence of cementation degree on the cone penetration resistance will be studied.

8. PREDICTING THE MECHANICAL RESPONSE OF ULTRA-HIGH PERFORMANCE CONCRETE (UHPC) WITH DISCRETE ELEMENT METHOD (DEM)

8.1. Introduction

Ultra-high performance concrete (UHPC) belongs to a special class of cementitious materials that shows very high mechanical properties and enhanced durability. Compressive strengths in excess of 120-150 MPa are generally reported for UHPC mixtures (Graybeal 2011a; Yoo and Banthia 2016). When reinforced with high volumes of steel fibers (in the order of 2-3% by volume), these composites exhibit high tensile strengths and strain hardening (Gesoglu et al. 2016), making them useful for many high-end structural applications. For example, the U.S Federal Highway Administration and several state Departments of Transportation have been investigating the use of UHPC for deck-level connections between modular precast components that are heavily stressed in service (Graybeal 2011b; Saleem et al. 2011). Use of UHPC for blast protection has also been reported (Yi et al. 2012). While immense efforts have focused on the use of UHPC for such special applications, the downside is the high cost of these mixtures. Thus it is critical to develop cost-effective UHPC using commonly available materials and conventional concrete production methods (Wang et al. 2012; Wille et al. 2011; Wille and Boisvert-Cotulio 2015).

During the past years, numerous researchers have reported studies on modeling the constitutive behavior of concrete with finite element method (FEM)-based models, in either two- or three- dimensions (Abed and Alhafiz 2018; Kwak and Filippou 1990; Lou et al. 2014; Naganuma et al. 2004; Palermo and Vecchio 2007; Xiao et al. 2017). However,

simulating the fracture behavior, especially damage evolution (e.g., crack propagation), is always a challenging objective in finite element-based numerical simulation methods. To successfully simulate the fracture performance of concrete, multiple technologies (e.g., using cohesive traction-separation laws along the predetermined element interface and using the extended finite element method (XFEM) to enable a local enrichment of approximation space – which allows element splitting and localized re-meshing) have been widely used (Chao et al. 2012; Du et al. 2014; Zhai et al. 2017). On the other hand, discrete element method (DEM) to investigate the mechanical behavior of concrete from particle scale has also garnered attention (Abbasnia and Aslami 2015; Nagai and Matsumoto 2010; Nitka and Tejchman 2015b; Suchorzewski et al. 2018; Tran et al. 2011). This chapter aims to simulate and predict the mechanical performance of UHPC with DEM models. The commercial software Particle Flow Code 2D (PFC2D) developed by Itasca Group™ was used to develop 2D models constructed by disk particles to simulate the flexure, compression and tension behavior of UPHC. The experimental results that are used in this study are obtained from the results of a recent project at ASU, investigating the development of UHPC from local materials. The results are reported in a recent Ph.D thesis (Arora 2018).

8.2. DEM Methodology

The discrete element method (DEM), originally developed by (Cundall and Strack 1979) for studying mechanical properties of rocks, has been widely extended to simulate the mechanical response of cemented granular materials. By computing the individual motions and inter-particle contacts of sufficient number of particles (the basic element used in DEM), it is able to simulate the macroscale response from microscale interactions. More

significantly, the distinct nature of DEM endows the capability of simulate damage evolution by tracking the evolution of inter-particle contacts.

8.2.1. Contact Model

A so-called flat-joint model which is available as a built-in contact model in PFC 2D DEM package was adopted in this chapter to describe the inter-particle contact characteristics for UHPC. As seen in Figure 8.1, this model provides the macroscopic behavior of a finite-size, linear elastic and either bonded or frictional interface that may sustain partial damage (Cundall 2004). The inter-particle contact interface is discretized into desired number of elements and the contact force as well as bond state (either bonded or unbonded) are determined individually for each of the elements. The force carried by each of the elements is then summed at the centroid of the inter-particle contact interface to update the interaction status of contacted particles. The contact law schematically showed in Figure 8.1 is used to calculate the force carried by a single element.

For each of the contact element with bonded status, the normal force is expressed as:

$$F_n = \int \sigma dA \tag{8.1}$$

Where A is the area of the element and σ is the normal stress acting on the element that can be calculated as:

$$\sigma = k_n d_n \tag{8.2}$$

Here, k_n is the normal contact stiffness and the d_s is the contact distance. When the element sustains tension and the tensile-strength limit (σ_c) is exceeded ($\sigma > \sigma_c$), the bond breaks in tension and all existing contact forces are set to zero (as shown in Figure 8.2(a)). The shear force is calculated incrementally as:

$$\Delta F_s = k_s \Delta d_s \tag{8.3}$$

where k_s is the shear stiffness and Δd_s is the incremental tangential displacement.

The shear stress (τ) is then calculated as:

$$\tau = \frac{F_s}{A} \tag{8.4}$$

If the shear stress exceeds the strength ($\tau_c = c - \sigma \tan \phi$), the bond breaks in shear (as seen in Figure 8.2(b)) and the shear behavior follows the Mohr-Coulomb failure criterion as:

$$\tau - \sigma \cdot \mu \leq 0 \tag{8.5}$$

where μ is the friction coefficient.

The entire failure envelope described by the contact law before debonding is shown in Figure 8.2(c). The detailed description of flat-joint model is documented in (Cundall 2004).

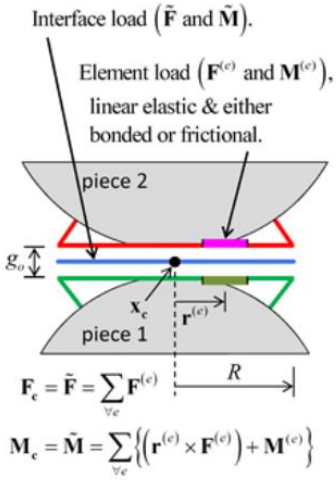

Figure 8.1: Inter-particle contact model used in DEM simulations (Cundall 2004).

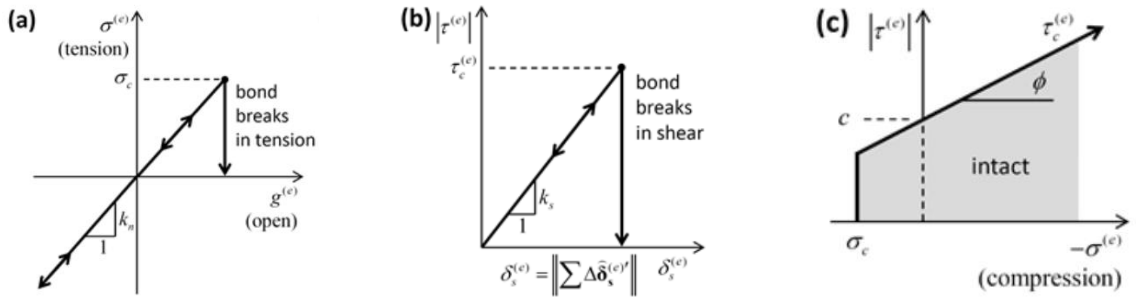

Figure 8.2: Mechanical response of contact law used in DEM simulations: (a) bonded normal contact, (b) bonded tangential contact and (c) bonded failure envelope (Cundall 2004).

8.2.2. Preparing the Numerical Particle Packing

Considering the significant property differences between the cement paste and aggregate in concrete, a two-phase particle packing was adopted to represent the cement paste and aggregate separately. The volume fraction of each phase was same as that reported in experiments (65% by volume of paste and 35% by volume of aggregate) (Arora 2018). Figure 8.3 shows the experimentally measured (solid line) particle size distributions (PSDs) for both the paste (here, the binder particles, though it is known that the particles and the resultant paste have different particle sizes), and aggregate. Significant size difference was noticed from the plot where the aggregate's particle size is approximately two magnitudes larger than that of paste, which can result in the requirement of a significantly large number of particles to assemble the representative DEM model. For example, a 20 mm diameter x 40 mm high numerical specimen will contain more than six million particles if the actual sizes are used, which is computationally unaffordable. Thus, while maintaining the numerical PSD for aggregate the same as in the actual experiment, an enlarged PSD for the paste is needed to reduce the number of particles to a manageable level. With the designed numerical PSD shown in Figure 8.3 (dotted line), the same 20 mm x 40 mm numerical

specimen was constructed using approximately 24,000 particles. The designed numerical PSDs were used in all the DEM simulations in this chapter.

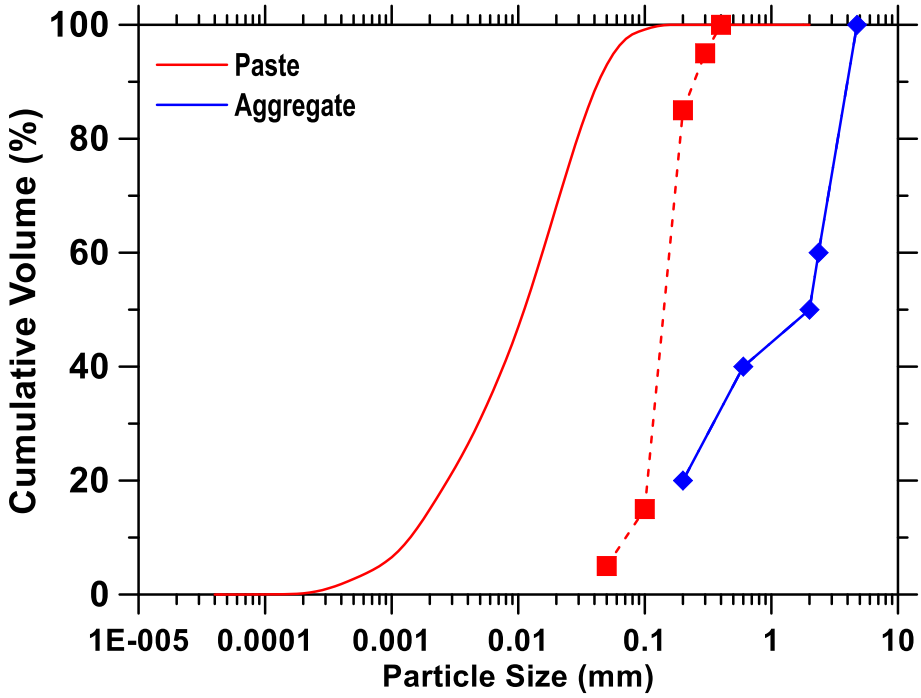

Figure 8.3: Numerically designed and experimentally obtained particle size distributions for cement paste and aggregate, where solid lines represent PSDs obtained experimentally and dot lines with marks represent numerical PSDs.

8.3. Simulating the Mechanical Performance of UHPC

In this section, two-dimensional DEM models are used to simulate the mechanical behavior of UHPC under various loading paths. The four-point bending test is simulated in order to calibrate the particle contact model by matching the numerically obtained results with the experimental data. The calibrated model is then used to simulate the uniaxial compression and tension tests of UHPC to predict the complete tension-compression response of UHPC.

8.3.1. Calibrating the Contact Model Using Compression and Flexure Results

As mentioned in previous section, the contact model adopted in this work for describing inter-particle contact behavior contains six parameters: the normal and shear stiffness (k_n

and k_s), the friction coefficient (μ) for unbonded shear behavior, the tensile strength (σ_c), the cohesion (c) and the friction angle for bonded shear behavior (ϕ). Among all the six parameters, the normal and shear stiffness (k_n and k_s) can be related to the particle's elastic modulus (E_c) and Poisson's ratio (υ_c) (Cundall 2004), where the poisson's ratio can be determined from compression stress-strain experiments and the elastic modulus can be determined through micro-indentation test (Arora 2018). Since no unique solution can be obtained by analytically solving the empirical equation detailed in (Arora 2018), which related the cohesion and friction angle (c and ϕ) to the particle hardness with fitting parameters, the cohesion and related friction angle, together with the tensile strength (σ_c), were determined numerically determined by performing a series of parametric studies for flexural tests, which will be discussed in detail in the following sections. By combining the cohesion and friction angle obtained through analytical solution along with the tensile strength based on values reported in the litearture (Nitka and Tejchman 2015b), a series of simulations were carried out until good correlations were observed between simulation results and experimental data for the flexural tests. A zero friction coefficient (μ) was used with the consideration that the global behavior should be dominated by the bonded inter-particle contact. The particle densities of each phase was set to be same as the corresponding materials' densities. A proper local damping coefficient was required to dissipate the excessive kinetic energy during simulation (Cundall 2004; Nitka and Tejchman 2015a) since an improper value (typically too small) of a damping coefficient may cause accumulation of extremely large excessive kinetic energy and thus influence the accuracy of simulation. The damping coefficient of 0.1 was used in this work to minimize such influence (Nitka and Tejchman 2015a).

Table 8.1: Parameters used in DEM simulations.

Input parameters	Paste	Aggregate
Density (ρ) [Kg/m^3]	2100	2700
Elastic modulus (E_c) [GPa]	32	70
Poisson's ratio (υ_c) [--]	0.2	0.17
Cohesion (c) [MPa]	150	0
Tensile stress (σ_c) [MPa]	16.5	0
Friction angle (ϕ) [°]	24.4	0
Friction coefficient (μ) [--]	0	0

8.3.1.1. Modeling the flexural response of UHPC

To simulate the flexural response of UHPC, numerical specimens with 45 mm length and 10 mm thickness were used to represent the experimental beam having a dimension of 405 mm length x 50 mm depth x 50 mm width. Numerical PSDs shown in Figure 8.3 were used to distribute maximum number of particles into the geometry under gravity-free condition with significant overlap (as illustrated in Figure 8.4(a)). Four rigid boundary walls were created along the specimen outline to restrict the movement of particles within the specimen geometry. A simple linear contact model (Cundall 2004) as well as a high damping coefficient (0.5) were assigned to the generated particles for the purpose of quickly eliminating inter-particle overlap and the particle packing was solved automatically until a balanced state, as seen in Figure 8.4, is attained. After preparing the particle packing, the flat-joint model with input parameters listed in Table 8.1 was assigned to all the existing inter-particle contacts and the model was solved automatically again till a balanced state (Figure 8.4(b)).

The rigid boundary walls were then deleted and four circular rigid walls were created to represent the physical supports and punches. The circular rigid wall supports are located at

the bottom of the numerical specimen, 2.5 mm away from the edge of the beam. The punches were placed on top of the beam with one-third-length intervals, same as that in the experiment to simulate a four-point bending test. The numerical specimen was then allowed to settle under gravity to establish stable contact with supports. An automatic solver was used here again until a balanced state is reached. The prepared numerical specimen before the loading stage is shown in Figure 8.4(c).

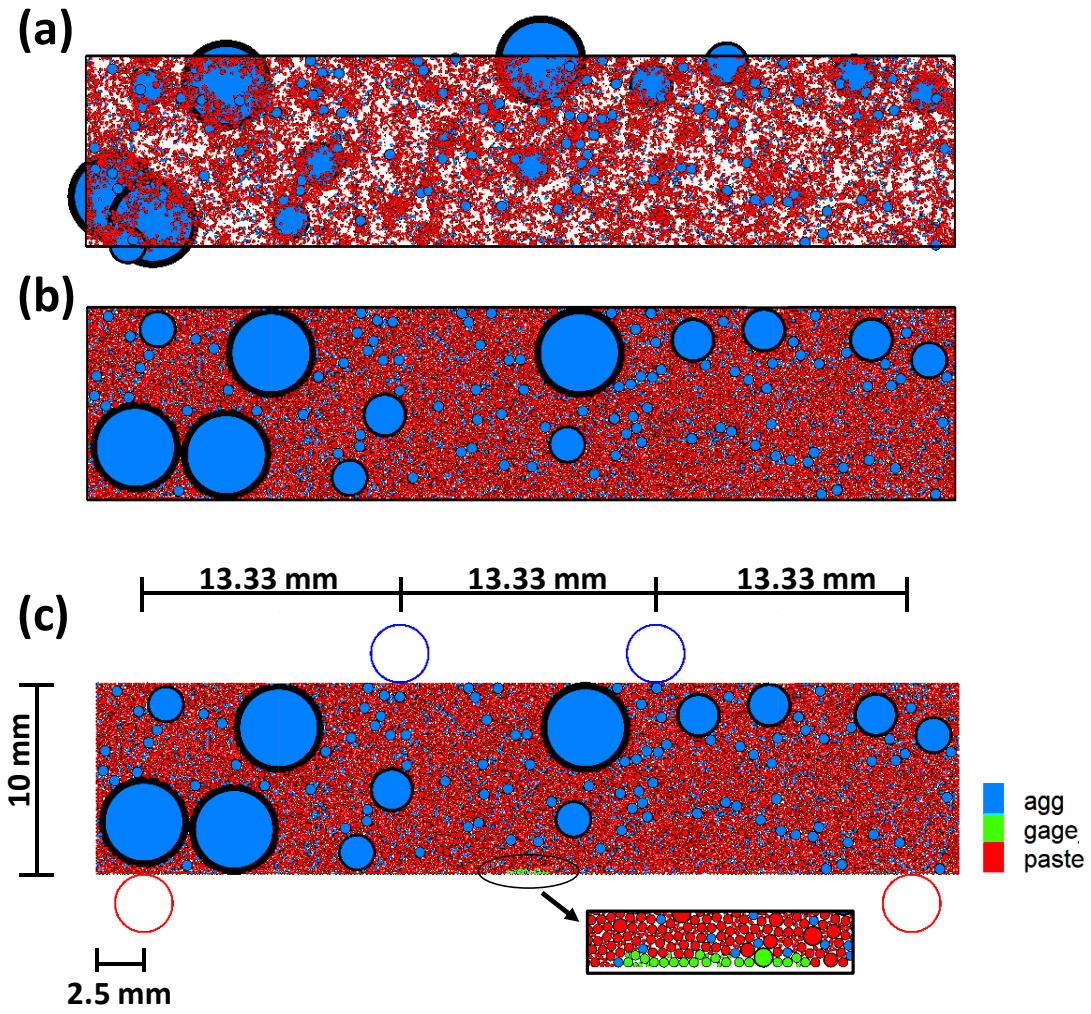

Figure 8.4: Schematic showing: (a) initially distributed particle packing with significant overlaps, (b) particle packing restricted by rigid boundaries after attaining the balanced state, and (c) the prepared numerical specimen before the flexural loading.

A constant velocity of 5 mm/s was assigned to top punches to apply flexure loading to the numerical specimen. Contact force sustained by punch walls were recorded and a small number of particles located in the bottom mid-span section of the specimen were used to record the deflection during the simulation (see the highlighted area in Figure 8.4(c)) and the recorded load-deflection data was used to calculate the stress-strain relationship. The stress-strain relationship obtained numerically and experimentally are plotted in Figure 8.5. A good agreement between simulation results and the experimental data is noticed. Such an observation indicates that after the aforementioned careful parameter calibration process, the DEM model can adequately depict the bending behavior of UHPC.

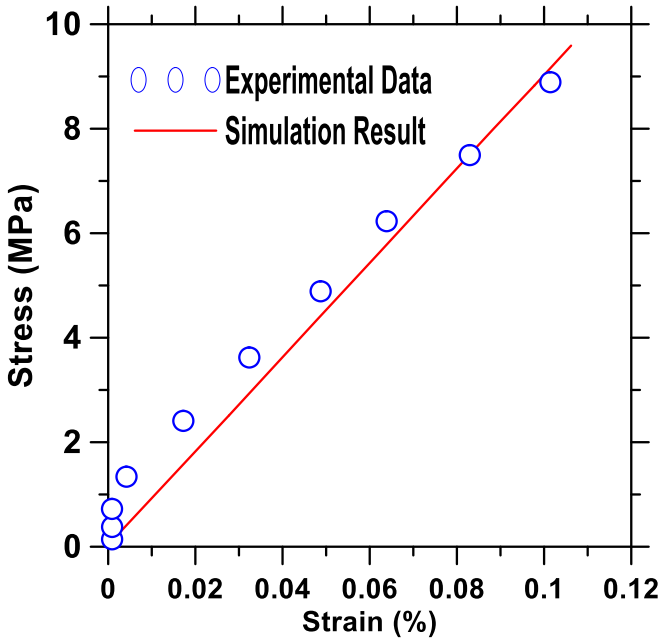

Figure 8.5: Numerically simulated flexural stress-strain response against reported experimental result (Arora 2018).

8.3.1.2. Simulating the compression behavior of UHPC

The same particle packing procedure detailed in the previous section was used here to prepare the numerical specimen for uniaxial compression simulation. The prepared specimen and its geometry can be found in Figure 8.6(a). Top and bottom rigid walls with

zero-friction were attached to the specimen and a constant velocity of 10 mm/s towards the center of the specimen was assigned to top and bottom walls to simulate the axial strain controlled uniaxial compression test until 70% of the peak stress.

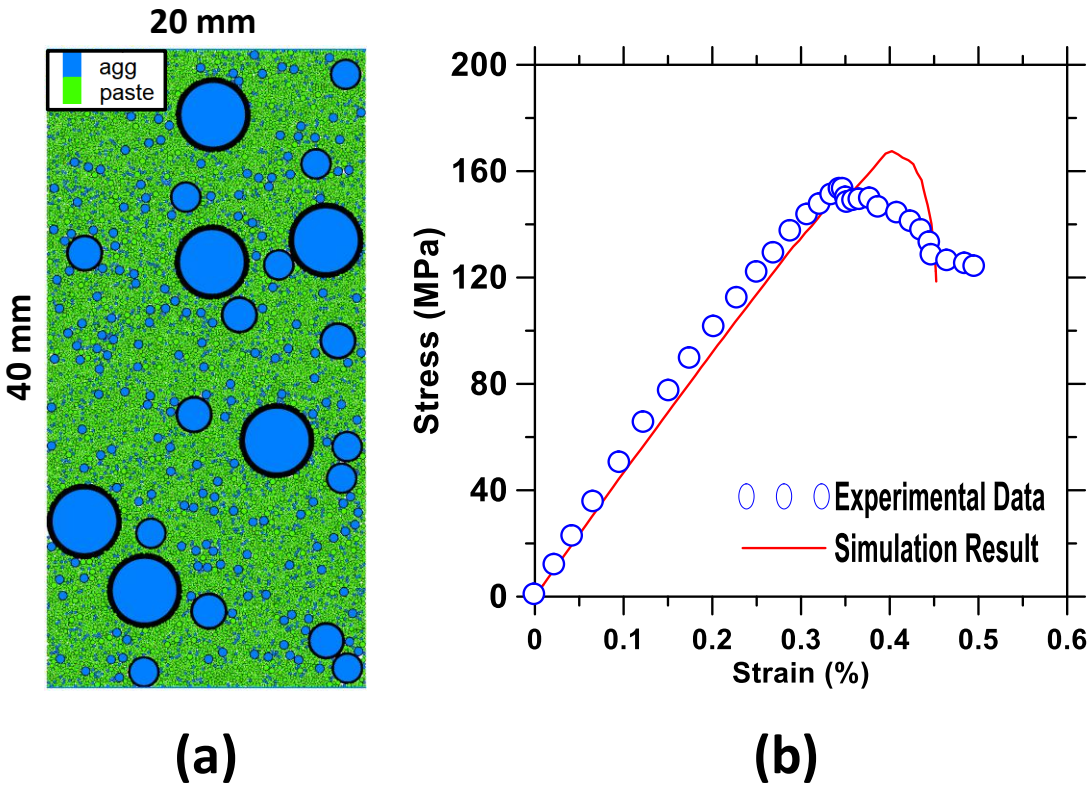

Figure 8.6: (a) Schematic illustration of the numerical specimen, and (b) the simulated stress-strain response under compression against experimental data (Arora 2018).

Figure 8.6(b) plots the axial stress-strain response simulated by the DEM model against the data obtained from the experiment. Good agreement was noticed until the peak stress. However, the DEM model simulated a more brittle post-peak behavior compared to the reported experimental data, which is likely due to the different boundary conditions applied in simulation and experiment – an axial strain-controlled compression test was simulated by the DEM model while a radial-controlled compression test was carried out experimentally.

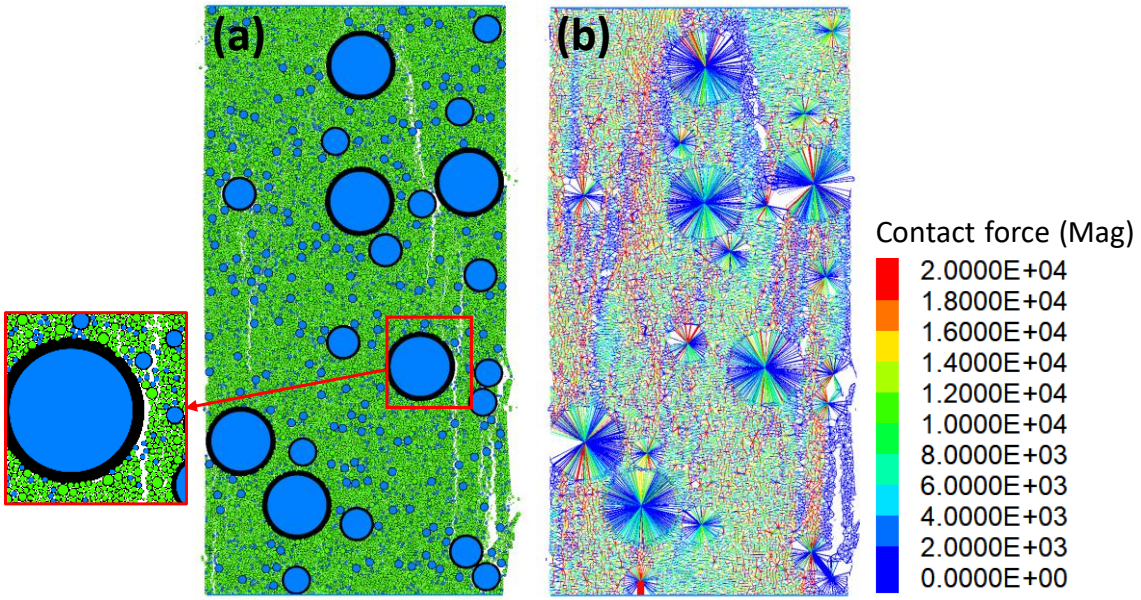

Figure 8.7: (a) Simulated crack patterns and (b) Contact force network distribution at the end of uniaxial compression simulation.

Figure 8.7 shows the numerical specimen with propagated cracks after compression simulation together with the inter-particle contact force network. Multiple splitting cracks were clearly observed in the numerical specimens, as commonly observed in laboratory tests. It was also noticed that the DEM model successfully captures the interphase (aggregate-paste) debonding during crack propagation (zoomed part in Figure 8.7(a)). Figure 8.7(b) clearly indicates that at the end of the compression simulation, the side of the specimen lost the ability to transfer externally applied load and the remaining force was concentrated in the middle of the specimen where it is relatively undamaged. Significant higher vertical contact forces were noticed for paste-aggregate contacts in Figure 8.7(b), which further reveals the fact that during uniaxial compression test, the internal force is mainly transferred vertically.

8.3.2. Predicting the Tension Behavior

In this section, the calibrated DEM model was used to predict the mechanical response of UHPC under uniaxial tension test. Same specimen constructed for uniaxial compression simulation (with dimension of 20 mm width x 40 mm height) was used here with additional modifications. All the rigid walls were removed from the model and the specimen was partitioned into several sections for data-recording and simulation control purpose. As seen in Figure 8.8, the top and bottom sections (marked as 'top_grip' and 'bot_grip' in Figure 8.8) with a thickness of 5% of specimen height were used to apply tension load. All the particles within these sections were assigned with a constant velocity of 10 mm/s to simulate the strain-controlled uniaxial tension test. The section located in the middle portion of the specimen (marked as 'stress_gage' in Figure 8.8) was used to calculate the axial stress and axial strain during the simulation. All the inter-particle contacts located within this section were used to calculate the average axial stress. All those particles located in the top and bottom edge of this section ('stress_gage' section) were identified and the displacement of these particles were used to calculate the axial strain.

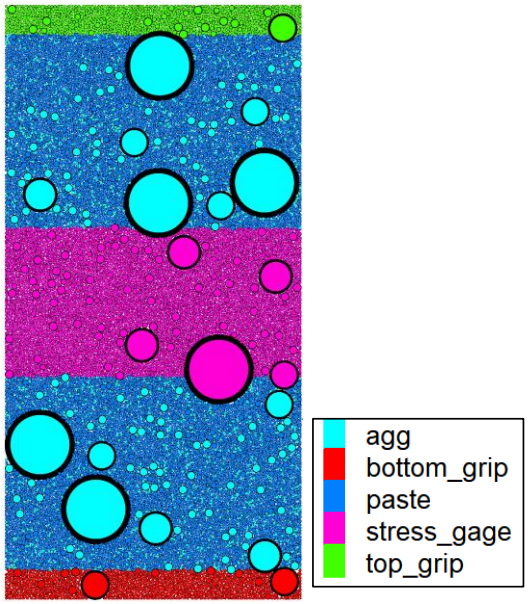

Figure 8.8: The measurement sections indicated in a 2D DEM model for the tension test.

Figure 8.9 shows the predicted axial stress-strain response of the numerical specimens, where a peak tensile stress of 12.3 MPa with a peak strain of 0.0039% was predicted. Figure 8.10 shows particle displacement map together with the y-component particle contact force network at the end of the tensile loading simulation. A main crack propagating through the middle of the specimen with multiple branches is clearly revealed through the change in direction of particle displacements shown in Figure 8.10(a) as well as the magnitude of change in contact forces shown in Figure 8.10(b), which is consistent with the experimental observations from tension tests on concrete.

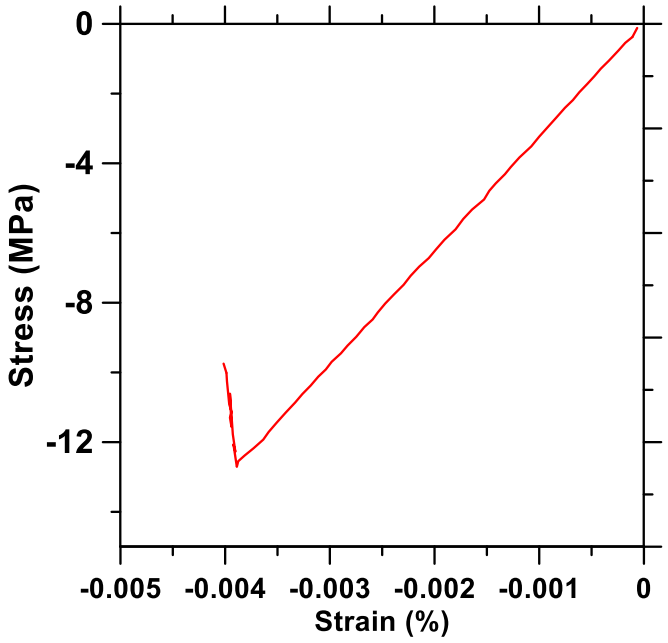

Figure 8.9: Numerically simulated tension behavior of UHPC.

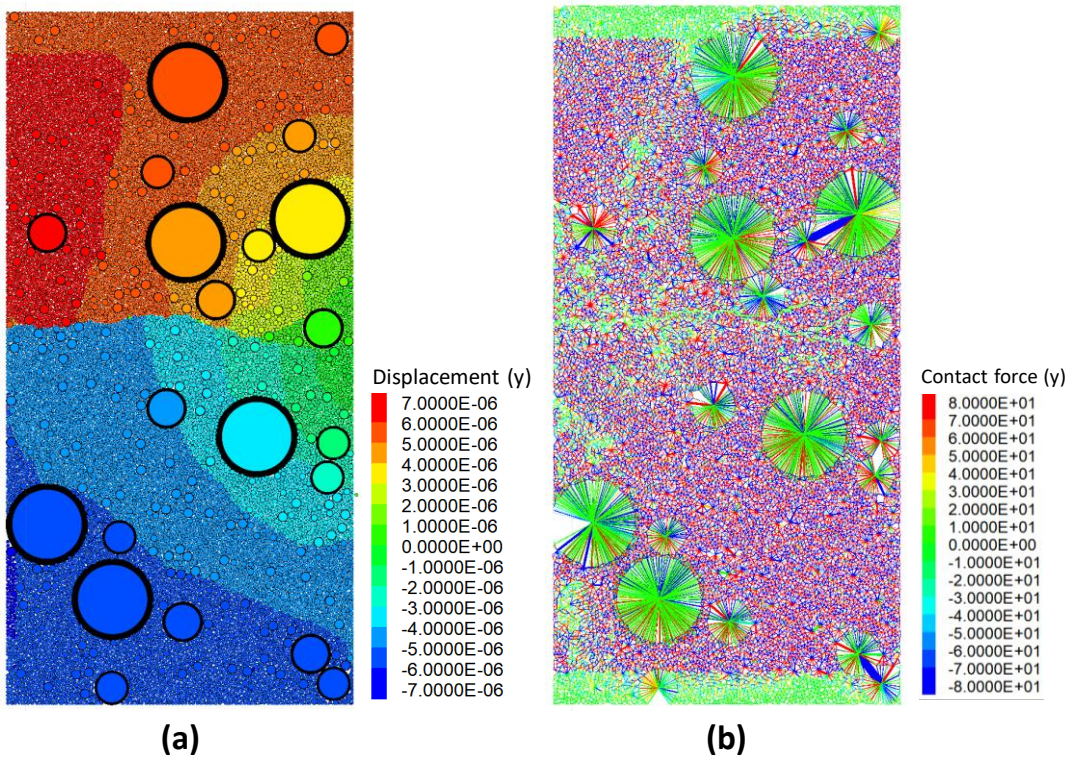

Figure 8.10: (a) Particle displacement and (b) Contact force (in vertical direction) network at the end of the tension simulation.

8.4. Summary and Conclusions

This chapter extends the application of discrete element method (DEM) to simulate the flexural, compressive, and tensile behavior of ultra-high performance concrete (UHPC). Particle Flow Code 2D (PFC2D) was used to develop the 2D DEM models. A flat-joint contact model was employed to describe the inter-particle behavior. A two-phase particle packing was generated to represent the cement paste and aggregates having different material properties. The parameters of the contact model were partially obtained through reported experiments while the remaining parameters (cohesion, friction angle and tensile strength) were obtained by performing a parametric study as reported in (Arora 2018). Four-point bending test was simulated and the results from simulations were used to acquire the appropriate parameters (cohesion, friction angle and tensile strength) required for describing the mechanical performance of UHPC. The compressive stress-strain response of UHPC was simulated to a desirable degree of accuracy, and the calibrated model was then used to predict the behavior of UHPC under uniaxial tension. The DEM modeling reported in this chapter provides a useful avenue towards the design of high strength concretes where an apriori determination of the material's constitutive response can be made, and the influence of the constituents examined in detail.

9. CONSCLUSIONS AND FUTURE WORK

9.1. Conclusions

This thesis uses the discrete element method (DEM) to systematically investigate the particle scale mechanisms governing the mechanical behavior of bio-cemented sands by simulating static and dynamic laboratorial tests that the commonly used to evaluate the performance of sands. A contact model with six parameters representing the behavior in the normal and shear directions, rolling contact, and bonding is used to describe the response of uncemented and bio-cemented sands. An open-source DEM platform, YADE, was used to perform the simulations. The following salient conclusions are arrived at based on this thesis:

- A methodology for three-dimensional simulation of the drained triaxial compression test of plain sand with rigid wall boundaries was carried out and a method established to calibrate the contact model. Drained triaxial compression of bio-cemented sand was simulated with this DEM model. The mismatch between simulation and experimental results was observed for bio-cemented sands displaying high levels of cementation.
- A methodology to simulate flexible boundary walls was developed for the virtual undrained triaxial compression tests of plain and bio-cemented sands employing a constant volume method. The flexible boundary deforms freely on interaction with sand particles, and a uniform confining stress can be applied laterally to allow the formation of shear band. The brittle failure of heavily bio-cemented sand is captured in this manner, thus overcoming the limitations of the rigid wall model. A linear relationship between contact stiffness and cementation level (represented as

a function of the measured shear wave velocity) and a linear relationship between cohesive strength and cementation level are utilized in simulating the undrained triaxial compression behavior of bio-cemented sands with varying cementation levels.

- The performance of multiple DEM models on simulating the drained and undrained triaxial compression tests of sands was examined. The pore-finite-volume (PFV) – coupled DEM model was used to simulate the drained and undrained triaxial compression tests on fully saturated sand. The PFV-coupled model and the regular six-parameter DEM model were found to perform in a similar manner as far as the predictive capacity is concerned, but it was noticed that longer computational times were required for the PFV-coupled model. The influence of cementation levels and confining stress on the response of bio-cemented sands was studied. A novel DEM model is developed to simulate the unconfined compression test of bio-cemented sands with extremely high cementation level. This model is capable of being utilized for a number of cemented granular media, including portland cement concrete for the prediction of compressive response. The use of multiple particles and thereby differing contact responses enables realistic simulation of multi-component granular media.
- The cyclic direct simple shear (DSS) test of sands is numerically modeled using both the shear box model and the cylindrical model, corresponding to the Cambridge-type and NGI-type laboratory tests that are commonly used. The limitations of cylindrical model is brought out - i.e., with a small ring thickness/particle size ratio, the cylindrical model fails to apply uniform shear to

the simulation volume. This can be mitigated through the use of a larger simulation volume or smaller particles, but not without significant investments in computational time and cost. The shear box model was eventually used to predict the response of plain and bio-cemented sands, as well as the sands reconstituted multiple times after a cyclic shearing event. A commercial cloud platform was used to perform simulations that required larger number of cycles.

- A preliminary study on numerical simulation of the cone penetration test (CPT) was performed. Two-dimensional DEM model was developed to parametrically investigate the influence of non-material factors (loading speed, cone-diameter to particle-size ratio and boundary conditions) on the cone penetration resistance of soils. This model will be used in the CPT simulation of bio-cemented sands, for which very limited CPT data is available.
- A 2D DEM model was developed to evaluate the response of ultra-high performance concrete (UHPC) in compression, flexure, and tension. UHPC can be considered as an extremely cemented granular material. 2D DEM models with two-phase packing are developed wherein the model was verified for flexural response using intrinsic materials-related parameters and validated for compression and tension.

9.2. Future Work

The following is a brief overview of proposed activities that will complement and extend the work reported in this dissertation:

- Based on the findings on CPT simulations reported in Chapter 7, 2D DEM models can be used to simulate CPT on bio-cemented sands. 3D DEM models can also be

developed for CPT simulation and the difference between 2D and 3D models (for example, the packing density in 2D and 3D) can be investigated to provide an understanding of the scale and dimension effects on CPT simulations.

- 2D DEM models can be developed to simulate the direct simple shear (DSS) shear test, and the efficiency of such models in relation to 3D tests can be evaluated. The influence of ring thickness/particle ratio needs to be investigated for simulating the NGI-type direct simple shear test and computationally efficient methods need to be arrived at.
- A refined multi-phase particle packing can be used to represent the sand and calcite particles in bio-cemented sands. While preliminary work in this regard has been carried out, refinement of this model can be carried out only with supplementary experimental evidence from advanced imaging techniques (e.g., X-ray synchrotron tomography) that will help identify the salient features the microstructure of bio-cemented sands. The development of multi-phase packing and the capability to assign different contact parameters to these phases are certain to improve the fidelity of the DEM-based models for cemented granular media.
- DEM models with irregular-shape particles can be developed to simulate the performance of granular media containing non-spherical constituents (e.g., aggregates, fibers in concrete). Both the fresh (rheology) and hardened properties (mechanical performance) of granular media can be realistically simulated using such models. Clumps with high aspect ratio can help represent fibers while regular disk particles can be used to represent the aggregates. Such models will help better

understand the influence of constituent geometry and interactions on the performance of concrete or similar granular media.

REFERENCES

Abbasnia, R., and Aslami, M. (2015). "Numerical simulation of concrete fracture under compression by explicit discrete element method." *International Journal of Civil Engineering*, 13(3), 245–254.

Abed, F., and Alhafiz, A. R. (2018). "Finite element simulation of the flexural behavior of BFRP-FRC beams." *Advances in Science and Engineering Technology International Conferences (ASET), 2018*, IEEE, 1–5.

Abu-Farsakh, M. Y., Voyiadjis, G. Z., and Tumay, M. T. (1998). "Numerical analysis of the miniature piezocone penetration tests (PCPT) in cohesive soils." *International Journal for Numerical and Analytical Methods in Geomechanics*, 22(10), 791–818.

Ahmadi, M. M., Byrne, P. M., and Campanella, R. G. (2005). "Cone tip resistance in sand: modeling, verification, and applications." *Canadian geotechnical journal*, 42(4), 977–993.

Arora, A. (2018). "Evaluation of the Performance of Multi-Component Cementitious Composites: Multi-Scale Experimental Characterization and Numerical Simulation." PhD Dissertation, Arizona State University.

Bagi, K. (2005). "An algorithm to generate random dense arrangements for discrete element simulations of granular assemblies." *Granular Matter*, 7(1), 31–43.

Bakunowicz, P., and Ecemis, N. (2014). "Validation of porosity in 2D-DEM CPT model using large scale shaking table tests in saturated sands"." *14th International conference of the International Association for Computer Methods and Advances in Geomechanics, Japan*.

Baligh, M. M. (1985). "Strain path method." *Journal of Geotechnical Engineering*, 111(9), 1108–1136.

Been, K., Jefferies, M. G., Crooks, J. H. A., and Rothenburg, L. (1987). "The cone penetration test in sands: part II, general inference of state." *Geotechnique*, 37(3), 285–299.

Belheine, N., Plassiard, J.-P., Donzé, F.-V., Darve, F., and Seridi, A. (2009). "Numerical simulation of drained triaxial test using 3D discrete element modeling." *Computers and Geotechnics*, 36(1–2), 320–331.

Bernhardt, M. L., and Biscontin, G. (2016). “Experimental validation study of 3D direct simple shear DEM simulations.” *Soils and Foundations*, 56(3), 336–347.

Bernhardt, M. L., Biscontin, G., and O’Sullivan, C. (2014). “3D discrete element method simulations of a laminar-type simple shear apparatus.” *Geo-Congress 2014: Geo-characterization and Modeling for Sustainability*, 614–623.

Bjerrum, L., and Landva, A. (1966). “Direct simple-shear tests on a Norwegian quick clay.” *Geotechnique*, 16(1), 1–20.

Bolton, M. D., and Gui, M. W. (1993). *The study of relative density and boundary effects for cone penetration tests in centrifuge*. University of Cambridge, Department of Engineering.

Bolton, M. D., Gui, M.-W., Garnier, J., Corte, J. F., Bagge, G., Laue, J., and Renzi, R. (1999). “Centrifuge cone penetration tests in sand.” *Géotechnique*, 49(4), 543–552.

de Bono, J., McDowell, G., and Wanatowski, D. (2015). “Investigating the micro mechanics of cemented sand using DEM.” *International Journal for Numerical and Analytical Methods in Geomechanics*, 39(6), 655–675.

Bourrier, F., Kneib, F., Chareyre, B., and Fourcaud, T. (2013). “Discrete modeling of granular soils reinforcement by plant roots.” *Ecological engineering*, 61, 646–657.

Budhu, M. (1984). “Nonuniformities imposed by simple shear apparatus.” *Canadian Geotechnical Journal*, 21(1), 125–137.

Bundeleva, I. A., Shirokova, L. S., Pokrovsky, O. S., Bénézeth, P., Ménez, B., Gérard, E., and Balor, S. (2014). “Experimental modeling of calcium carbonate precipitation by cyanobacterium Gloeocapsa sp.” *Chemical Geology*, 374, 44–60.

Camusso, M., and Barla, M. (2009). “Microparameters calibration for loose and cemented soil when using particle methods.” *International Journal of Geomechanics*, 9(5), 217–229.

Catalano, E., Chareyre, B., and Barthélemy, E. (2014). “Pore-scale modeling of fluid-particles interaction and emerging poromechanical effects.” *International Journal for Numerical and Analytical Methods in Geomechanics*, 38(1), 51–71.

Chang, C. S., and Misra, A. (1990). “Packing structure and mechanical properties of granulates.” *Journal of Engineering Mechanics*, 116(5), 1077–1093.

Chao, Z., Peng, C., Jianbo, L., and Yixiang, C. (2012). “Numerical Simulation to evaluate fatigue fracture behavior of Concrete Beam with Initial Crack.” *Digital Manufacturing and Automation (ICDMA), 2012 Third International Conference on*, IEEE, 566–570.

Chareyre, B., Cortis, A., Catalano, E., and Barthélemy, E. (2012). “Pore-scale modeling of viscous flow and induced forces in dense sphere packings.” *Transport in porous media*, 94(2), 595–615.

Cheung, G., and O’Sullivan, C. (2008). “Effective simulation of flexible lateral boundaries in two-and three-dimensional DEM simulations.” *Particuology*, 6(6), 483–500.

Ciantia, M. O., Arroyo, M., Butlanska, J., and Gens, A. (2016). “DEM modelling of cone penetration tests in a double-porosity crushable granular material.” *Computers and Geotechnics*, 73, 109–127.

Cil, M. B., and Alshibli, K. A. (2014). “3D analysis of kinematic behavior of granular materials in triaxial testing using DEM with flexible membrane boundary.” *Acta Geotechnica*, 9(2), 287–298.

“Comparisons with PFC3D - Yade.” (n.d.). <https://yade-dem.org/wiki/Comparisons_with_PFC3D> (Aug. 4, 2016).

Cook, B. K., Lee, M. Y., DiGiovanni, A. A., Bronowski, D. R., Perkins, E. D., and Williams, J. R. (2004). “Discrete element modeling applied to laboratory simulation of near-wellbore mechanics.” *International Journal of Geomechanics*, 4(1), 19–27.

Cundall, P. A. (2004). “PFC user manual.” *Itasca Consulting Group Inc., Mineapolis*.

Cundall, P. A., and Hart, R. D. (1995). “Numerical modeling of discontinua.” *Analysis and Design Methods*, Elsevier, 231–243.

Cundall, P. A., and Strack, O. D. (1979). “A discrete numerical model for granular assemblies.” *Geotechnique*, 29(1), 47–65.

Cundall, P. A., and Strack, O. D. L. (1983). "Modeling of microscopic mechanisms in granular material." *Studies in Applied mechanics*, Elsevier, 137–149.

Cundall, P. A., and Strack, O. D. L. (2013). "Modeling of microscopic mechanisms in granular material." *Mechanics of granular materials: new models and constitutive relations*, 63(23).

Dabeet, A. (2014). "Discrete element modeling of direct simple shear response of granular soils and model validation using laboratory tests." PhD Thesis, University of British Columbia.

Dabeet, A., Wijewickreme, D., and Byrne, P. (2012). "Simulation of cyclic direct simple shear loading response of soils using discrete element modeling." *Lisbon: proceedings of the 15th World conference on earthquakes engineering*.

Dabeet, A., Wijewickreme, D., and Byrne, P. (2014). "Application of discrete element modeling for simulation of cyclic direct simple shear response of granular materials." *National Conference on Earthquake Engineering*, 21–25.

De Borst, R. (1982). "Finite element analysis of static penetration tests." *Proc. 2nd Eur. Symp. on Penetration Testing*, 457–462.

DeJong, J. T., Fritzges, M. B., and Nüsslein, K. (2006). "Microbially induced cementation to control sand response to undrained shear." *Journal of Geotechnical and Geoenvironmental Engineering*, 132(11), 1381–1392.

DeJong, J. T., Mortensen, B. M., Martinez, B. C., and Nelson, D. C. (2010). "Bio-mediated soil improvement." *Ecological Engineering*, 36(2), 197–210.

DeJong, J. T., Soga, K., Kavazanjian, E., Burns, S., Van Paassen, L. A., Al Qabany, A., Aydilek, A., Bang, S. S., Burbank, M., Caslake, L. F., and others. (2013). "Biogeochemical processes and geotechnical applications: progress, opportunities and challenges." *Geotechnique*, 63(4), 287–301.

Du, X., Jin, L., and Ma, G. (2014). "Numerical modeling tensile failure behavior of concrete at mesoscale using extended finite element method." *International Journal of Damage Mechanics*, 23(7), 872–898.

Durgunoglu, H. T., and Mitchell, J. K. (1973). "Static penetration resistance of soils."

Dyvik, R., Berre, T., Lacasse, S., and Raadim, B. (1987). “Comparison of truly undrained and constant volume direct simple shear tests.” *Geotechnique*, 37(1), 3–10.

Ecemis, N., and Bakunowicz, P. (2018). “Feasible packing of granular materials in discrete-element modelling of cone-penetration testing.” *Geomechanics and Geoengineering*, 1–19.

Effeindzourou, A., Chareyre, B., Thoeni, K., Giacomini, A., and Kneib, F. (2016). “Modelling of deformable structures in the general framework of the discrete element method.” *Geotextiles and Geomembranes*, 44(2), 143–156.

Ehrlich, H. L., Newman, D. K., and Kappler, A. (2015). *Ehrlich’s geomicrobiology*. CRC press.

El Shamy, U., and Abdelhamid, Y. (2014). “Modeling granular soils liquefaction using coupled lattice Boltzmann method and discrete element method.” *Soil Dynamics and Earthquake Engineering*, 67, 119–132.

El Shamy, U., and Zeghal, M. (2007). “A micro-mechanical investigation of the dynamic response and liquefaction of saturated granular soils.” *Soil Dynamics and Earthquake Engineering*, 27(8), 712–729.

El Shamy, U., Zeghal, M., Dobry, R., Abdoun, T., Thevanayagam, S., and Elgamal, A. (2010). “DEM Simulation of Liquefaction-Induced Lateral Spreading.”

Elgamal, A.-W., and Yang, Z. (2000). “Numerical modeling of liquefaction-induced lateral spreading.” *12th World Conference on Earthquake Engineering, Auckland*.

Falagush, O., McDowell, G. R., and Yu, H.-S. (2015). “Discrete element modeling of cone penetration tests incorporating particle shape and crushing.” *International Journal of Geomechanics*, 15(6), 04015003.

Fazekas, S., Török, J., Kertész, J., and Wolf, D. E. (2005). “Computer simulation of three dimensional shearing of granular materials: Formation of shear bands.” *Powders and Grains*, 223–226.

Feng, K., and Montoya, B. M. (2015a). “Influence of Confinement and Cementation Level on the Behavior of Microbial-Induced Calcite Precipitated Sands under Monotonic

Drained Loading." *Journal of Geotechnical and Geoenvironmental Engineering*, 142(1), 04015057.

Feng, K., and Montoya, B. M. (2015b). "Drained shear strength of MICP sand at varying cementation levels." *American Society of Civil Engineers (ASCE)*.

Feng, K., Montoya, B. M., and Evans, T. M. (2014). "Numerical investigation of microbial-induced cemented sand mechanical behavior." *American Society of Civil Engineers (ASCE)*.

Feng, K., Montoya, B. M., and Evans, T. M. (2017). "Discrete element method simulations of bio-cemented sands." *Computers and Geotechnics*, 85, 139–150.

Finn, W. D. L. (1978). "Constant volume cyclic simple shear testing." *Proc. 2nd Int. Conf. on Microzonation, San Francisco*, 839–851.

Gesoglu, M., Güneyisi, E., Muhyaddin, G. F., and Asaad, D. S. (2016). "Strain hardening ultra-high performance fiber reinforced cementitious composites: Effect of fiber type and concentration." *Composites Part B: Engineering*, 103, 74–83.

Ghionna, V. N., and Jamiolkowski, M. (1991). "A critical appraisal of calibration chamber testing of sands." *Proceedings of the 1st International Symposium on Calibration Chamber Testing (ISOCCTI), Potsdam, NY Elsevier*, 13–39.

Gomez, M. G., DeJong, J., and Anderson, C. M. (2017). "Effect of bio-cementation on geophysical and cone penetration measurements in sands." *Canadian Geotechnical Journal*, (ja).

Gong, G. (2008). "DEM [Discrete Element Method] simulations of drained and undrained behaviour." University of Birmingham.

Gong, G. (2015). "DEM Simulations of Granular Soils under Undrained Triaxial Compression and Plane Strain." *Journal of Applied Mathematics and Physics*, 3(08), 1003.

Gong, G., Thornton, C., and Chan, A. H. (2011). "DEM simulations of undrained triaxial behavior of granular material." *Journal of Engineering Mechanics*, 138(6), 560–566.

Gong, G., and Zha, X. (2012). "DEM simulation of liquefaction for cohesionless media at grain scale." *Journal of Central South University*, 19(9), 2643–2649.

Graybeal, B. (2011a). "FHWA TECHNOTE: Ultra High Performance Concrete." *FHWA Publication No: FHWA-HRT-11-038: Federal Highway Administration*.

Graybeal, B. A. (2011b). "Fatigue Response in Bridge Deck Connection Composed of Field-Cast Ultra-High-Performance Concrete." *Transportation Research Record*, (2251), 93–100.

Hamdan, N., Kavazanjian Jr, E., Rittmann, B. E., and Karatas, I. (2017). "Carbonate mineral precipitation for soil improvement through microbial denitrification." *Geomicrobiology Journal*, 34(2), 139–146.

Hamidi, A., and Haeri, S. M. (2008). "Stiffness and deformation characteristics of a cemented gravely sand." *International Journal of Civil Engineering*, 6(3), 159–173.

Hanley, K. J., Huang, X., O'Sullivan, C., Kwok, F., Yu, A., Dong, K., Yang, R., and Luding, S. (2013). "Challenges of simulating undrained tests using the constant volume method in DEM." *AIP Conference Proceedings*, AIP, 277–280.

Houlsby, G. T., and Hitchman, R. (1988). "Calibration chamber tests of a cone penetrometer in sand." *Géotechnique*, 38(1), 39–44.

Houlsby, G. T., Wheeler, A. A., and Norbury, J. (1985). "Analysis of undrained cone penetration as a steady flow problem."

Huang, A.-B., Ma, M. Y., and Lee, J. S. (1993). "A micromechanical study of penetration tests in granular material." *Mechanics of materials*, 16(1–2), 133–139.

Huang, W., Sheng, D., Sloan, S. W., and Yu, H. S. (2004). "Finite element analysis of cone penetration in cohesionless soil." *Computers and Geotechnics*, 31(7), 517–528.

Huang, W.-C., Sung, C.-Y., Liao, H.-Y., and Chu, S.-S. (2015). "Micromechanical behavior of granular materials in direct shear modeling." *Journal of the Chinese Institute of Engineers*, 38(4), 469–480.

Huang, X., Hanley, K. J., O'Sullivan, C., and Kwok, F. C. (2014). "Effect of sample size on the response of DEM samples with a realistic grading." *Particuology*, 15, 107–115.

Iwashita, K., and Oda, M. (1998). "Rolling resistance at contacts in simulation of shear band development by DEM." *Journal of engineering mechanics*, 124(3), 285–292.

Iwashita, K., and Oda, M. (2000). "Micro-deformation mechanism of shear banding process based on modified distinct element method." *Powder Technology*, 109(1), 192–205.

J. Kozicki, and F.V. Donzé. (2009). "YADE-OPEN DEM: an open-source software using a discrete element method to simulate granular material." *Engineering Computations*, 26(7), 786–805.

Janda, A., and Ooi, J. Y. (2016). "DEM modeling of cone penetration and unconfined compression in cohesive solids." *Powder Technology*, 293, 60–68.

Jerier, J. F., Donze, F. V., Imbault, D., and Doremus, P. (2008). "A geometric algorithm for discrete element method to generate composite materials." *Discrete element group for Hazard mitigation, Annual Report*, 4, A1–A8.

Jiaer, W. U., Kammerer, A. M., Riemer, M. F., Seed, R. B., and Pestana, J. M. (2004). "Laboratory study of liquefaction triggering criteria." *13th World Conference on Earthquake Engineering, Vancouver, BC, Canada, Paper*.

Jiang, M. J., Yan, H. B., Zhu, H. H., and Utili, S. (2011). "Modeling shear behavior and strain localization in cemented sands by two-dimensional distinct element method analyses." *Computers and Geotechnics*, 38(1), 14–29.

Jiang, M., Liu, F., and Zhou, Y. (2014). "A bond failure criterion for DEM simulations of cemented geomaterials considering variable bond thickness." *International Journal for Numerical and Analytical Methods in Geomechanics*, 38(18), 1871–1897.

Karatas, I. (2008). "Microbiological improvement of the physical properties of soils." PhD Dissertation, Arizona State University.

Karatas, I., Kavazanjian, E., and Rittmann, B. E. (2008). "Microbially induced precipitation of calcite using Pseudomonas denitrificans." *Proc. of 1st Int. Conf. on Bio-Geo-Civil Engineering, 23–25 June 2008, Delft, The Netherlands*, 58–66.

Kavazanjian, E., and Hamdan, N. (2015). "Enzyme Induced Carbonate Precipitation (EICP) Columns for Ground Improvement." American Society of Civil Engineers, 2252–2261.

Kavazanjian, E., and O'Donnell, S. T. (2015a). "Mitigation of Earthquake-Induced Liquefaction via Microbial Denitrification: A Two-Phase Process." *IFCEE 2015*, 2286–2295.

Kavazanjian, E., and O'Donnell, S. T. (2015b). "Mitigation of Earthquake-Induced Liquefaction via Microbial Denitrification." *American Society of Civil Engineers (ASCE)*.

Keramatikerman, M., Chegenizadeh, A., Nikraz, H., and Sabbar, A. S. (2018). "Effect of flyash on liquefaction behaviour of sand-bentonite mixture." *Soils and Foundations*.

Kjellman, W. (1951). "Testing the shear strength of clay in Sweden." *Geotechnique*, 2(3), 225–232.

Kotrocz, K., Mouazen, A. M., and Kerényi, G. (2016). "Numerical simulation of soil–cone penetrometer interaction using discrete element method." *Computers and electronics in agriculture*, 125, 63–73.

Kouretzis, G. P., Sheng, D., and Wang, D. (2014). "Numerical simulation of cone penetration testing using a new critical state constitutive model for sand." *Computers and Geotechnics*, 56, 50–60.

Kozicki, J., and Tejchman, J. (2011). "Numerical simulations of sand behaviour using DEM with two different descriptions of grain roughness." *II International Conference on Particle-based Methods—Fundamentals and Applications. Particles*.

Kozicki, J., Tejchman, J., and Mühlhaus, H.-B. (2014). "Discrete simulations of a triaxial compression test for sand by DEM." *International Journal for Numerical and Analytical Methods in Geomechanics*, 38(18), 1923–1952.

Kumara, J., Hayano, K., Shigekuni, Y., and Sasaki, K. (2013). "Physical and mechanical properties of sand-gravel mixtures evaluated from DEM simulation and laboratory triaxial test." *International Journal of GEOMATE,* 4(2), 546–551.

Kumari, S., Sawant, V. A., and Mehndiratta, S. (2018). "Effectiveness of Stone Column in Liquefaction Mitigation Geotechnical Earthquake Engineering and Soil Dynamics V." *Geotechnical Earthquake Engineering and Soil Dynamics*.

Kwak, H.-G., and Filippou, F. C. (1990). *Finite element analysis of reinforced concrete structures under monotonic loads*. Department of Civil Engineering, University of California Berkeley, CA.

Lee, S. J., Hashash, Y. M., and Nezami, E. G. (2012). "Simulation of triaxial compression tests with polyhedral discrete elements." *Computers and Geotechnics*, 43, 92–100.

Li, B. (2015). "Geotechnical properties of biocement treated sand and clay." Thesis, Nanyang Technological University.

Li, Y., Yang, Y., Yu, H.-S., and Roberts, G. (2016). "Monotonic direct simple shear tests on sand under multidirectional loading." *International Journal of Geomechanics*, 17(1), 04016038.

Liu, G., Rong, G., Peng, J., and Zhou, C. (2015). "Numerical simulation on undrained triaxial behavior of saturated soil by a fluid coupled-DEM model." *Engineering Geology*, 193, 256–266.

Liyanapathirana, D. S., and Poulos, H. G. (2002). "A numerical model for dynamic soil liquefaction analysis." *Soil Dynamics and Earthquake Engineering*, 22(9–12), 1007–1015.

Lou, T., Lopes, S. M., and Lopes, A. V. (2014). "A finite element model to simulate long-term behavior of prestressed concrete girders." *Finite Elements in Analysis and Design*, 81, 48–56.

Lunne, T., Powell, J. J., and Robertson, P. K. (1997a). *Cone penetration testing in geotechnical practice*. CRC Press.

Lunne, T., Robertson, P. K., and Powell, J. J. M. (1997b). *Cone penetration testing in geotechnical practice. Blackie Academic. Chapman*. Hall Publishers, UK.

Mahboubi, A., Ghaouti, A., and Cambou, B. (1996). “La simulation numérique discrète du comportement des matériaux granulaires.” *Revue française de géotechnique*, (76), 45–61.

Mayne, P. W. (2007). “NCHRP synthesis 368.” *Cone Penetration Testing. A synthesis of highway practice. Washington. DC: Transportation research board*.

Montoya, B. M., and DeJong, J. T. (2015). “Stress-strain behavior of sands cemented by microbially induced calcite precipitation.” *Journal of Geotechnical and Geoenvironmental Engineering*, 141(6), 04015019.

Montoya, B. M., DeJong, J. T., and Boulanger, R. W. (2013). “Dynamic response of liquefiable sand improved by microbial-induced calcite precipitation.” *Géotechnique*, 63(4), 302.

Mortensen, B. M., and DeJong, J. T. (2011). “Strength and stiffness of MICP treated sand subjected to various stress paths.” *Geo-Frontiers 2011: Advances in Geotechnical Engineering*, 4012–4020.

Nagai, K., and Matsumoto, K. (2010). *Static and fatigue failure simulation of concrete material by dirscrete analysis*. FraMCoS-7, Seoul, Korea Concrete Institute.

Naganuma, K., Yonezawa, K., Kurimoto, O., and Eto, H. (2004). “Simulation of nonlinear dynamic response of reinforced concrete scaled model using three-dimensional finite element method.” *13th WCEE Proceedings*, 1–6.

National Research Council. (1985). *Liquefaction of Soils During Earthquakes, Committee on Earthquake Engineering, Commission on Engineering and Technical Systems*. National Academy Press, Washington, DC.

Nitka, M., and Tejchman, J. (2015a). “Modelling of concrete behaviour in uniaxial compression and tension with DEM.” *Granular Matter*, 17(1), 145–164.

Nitka, M., and Tejchman, J. (2015b). “Modelling of concrete fracture at aggregate level using FEM and DEM based on X-ray μCT images of internal structure.” *Engineering fracture mechanics*, 147, 13–35.

Obermayr, M., Dressler, K., Vrettos, C., and Eberhard, P. (2013). “A bonded-particle model for cemented sand.” *Computers and Geotechnics*, 49, 299–313.

Ochoa-Cornejo, F., Bobet, A., Johnston, C. T., Santagata, M., and Sinfield, J. V. (2016). "Cyclic behavior and pore pressure generation in sands with laponite, a super-plastic nanoparticle." *Soil Dynamics and Earthquake Engineering*, 88, 265–279.

O'Donnell, S. T. (2016). "Mitigation of Earthquake-Induced Soil Liquefaction via Microbial Denitrification: A Two-Stage Process." PhD Dissertation, Arizona State University.

O'Donnell, S. T., and Kavazanjian, E. (2015). "Stiffness and dilatancy improvements in uncemented sands treated through MICP." *Journal of Geotechnical and Geoenvironmental Engineering*, 141(11), 02815004.

O'Donnell, S. T., Kavazanjian, E., and Rittmann, B. E. (2017b). "MIDP: Liquefaction mitigation via microbial denitrification as a two-stage process. II: MICP." *Journal of Geotechnical and Geoenvironmental Engineering*, 143(12), 04017095.

O'Donnell, S. T., Rittmann, B. E., and Kavazanjian, E. (2017a). "MIDP: Liquefaction mitigation via microbial denitrification as a two-stage process. I: Desaturation." *Journal of Geotechnical and Geoenvironmental Engineering*, 143(12), 04017094.

O'Sullivan, C. (2011). "Particle-based discrete element modeling: geomechanics perspective." *International Journal of Geomechanics*, 11(6), 449–464.

O'Sullivan, C., Cui, L., and Bray, J. D. (2004). "Three-dimensional discrete element simulations of direct shear tests." *Numerical Modeling in Micromechanics via Particle Methods*, 373–382.

van Paassen, L. A., Ghose, R., van der Linden, T. J., van der Star, W. R., and van Loosdrecht, M. C. (2010). "Quantifying biomediated ground improvement by ureolysis: large-scale biogrout experiment." *Journal of Geotechnical and Geoenvironmental Engineering*, 136(12), 1721–1728.

van Paassen, L. A., van Loosdrecht, M. C. M., Pieron, M., Mulder, A., Ngan-Tillard, D. J. M., Van der Linden, T. J. M., and others. (2009). "Strength and deformation of biologically cemented sandstone." *ISRM Regional Symposium-EUROCK 2009*, International Society for Rock Mechanics.

Palermo, D., and Vecchio, F. J. (2007). "Simulation of cyclically loaded concrete structures based on the finite-element method." *Journal of Structural Engineering*, 133(5), 728–738.

Parkin, A. K., and Lunne, T. (1982). “Boundary effects in the laboratory calibration of a cone penetrometer for sand.” *Norwegian Geotechnical institute publication*, (138).

Plassiard, J. P. (2007). “Modélisation discrète d’impacts de blocs rocheux sur structures de protection type merlons.” PhD Thesis, Joseph Fourier University, Grenoble.

Plassiard, J.-P., Belheine, N., and Donzé, F.-V. (2009). “A spherical discrete element model: calibration procedure and incremental response.” *Granular Matter*, 11(5), 293–306.

Plassiard, J.-P., Belheine, N., and Donzé, F.-V. (n.d.). “Calibration procedure for spherical discrete elements using a local moment law.”

Poganski, J., Schweiger, H. F., Kargl, G., and Kömle, N. I. (2017). “DEM modelling of a dynamic penetration process on Mars as a part of the NASA InSight Mission.” *Procedia engineering*, 175, 43–50.

Porcino, D., and Diano, V. (2016). “Laboratory study on pore pressure generation and liquefaction of low-plasticity silty sandy soils during the 2012 earthquake in Italy.” *Journal of Geotechnical and Geoenvironmental Engineering*, 142(10), 04016048.

Porcino, D., Marcianò, V., and Granata, R. (2015). “Cyclic liquefaction behaviour of a moderately cemented grouted sand under repeated loading.” *Soil Dynamics and Earthquake Engineering*, 79, 36–46.

Porcino, D., Marcianò, V., and Nicola Ghionna, V. (2009). “Influence of cyclic pre-shearing on undrained behaviour of carbonate sand in simple shear tests.” *Geomechanics and Geoengineering: An International Journal*, 4(2), 151–161.

Potyondy, D. O., and Cundall, P. A. (2004). “A bonded-particle model for rock.” *International journal of rock mechanics and mining sciences*, 41(8), 1329–1364.

Rees, S. (2013). “Part One: Introduction to Triaxial Testing.” www.gdsinstruments.com.

Robertson, P. K. (1986). “In situ testing and its application to foundation engineering.” *Canadian Geotechnical Journal*, 23(4), 573–594.

Robertson, P. K. (2009). “Interpretation of cone penetration tests—a unified approach.” *Canadian geotechnical journal*, 46(11), 1337–1355.

Roscoe, K. H. (1953). “An apparatus for the application of simple shear to soil samples.” *Proc. 3rd ICSMFE*, 186–191.

Sagaseta, C., Whittle, A. J., and Santagata, M. (1997). “Deformation analysis of shallow penetration in clay.” *International journal for numerical and analytical methods in geomechanics*, 21(10), 687–719.

Saleem, M. A., Mirmiran, A., Xia, J., and Mackie, K. (2011). “Ultra-High-Performance Concrete Bridge Deck Reinforced with High-Strength Steel.” *Aci Structural Journal*, 108(5), 601–609.

Salgado, R., Mitchell, J. K., and Jamiolkowski, M. (1997). “Cavity expansion and penetration resistance in sand.” *Journal of Geotechnical and Geoenvironmental Engineering*, 123(4), 344–354.

Sawicki, A., and MierczyĹ, J. (2006). “Developments in modeling liquefaction of granular soils, caused by cyclic loads.” *Applied Mechanics Reviews*, 59(2), 91–106.

Sayeed, M. A., Suzuki, K., Rahman, M. M., and others. (2011). “Strength and deformation characteristics of granular materials under extremely low to high confining pressures in triaxial compression.” IJENS Publishers.

Schnaid, F. (1990). “A study of the cone-pressuremeter test in sand.” PhD Thesis, University of Oxford.

Schnaid, F. (2008). *In situ testing in geomechanics: the main tests*. CRC Press.

Shafipour, R., and Soroush, A. (2008). “Fluid coupled-DEM modelling of undrained behavior of granular media.” *Computers and Geotechnics*, 35(5), 673–685.

Shahir, H., Pak, A., and Ayoubi, P. (2016). “A performance-based approach for design of ground densification to mitigate liquefaction.” *Soil Dynamics and Earthquake Engineering*, 90, 381–394.

Shen, C.-K., O’Sullivan, C., and Jardine, R. J. (2011). “A micromechanical investigation of drained simple shear tests.” *Deformation Characteristics of Geomaterials:*

Proceedings of the Fifth International Symposium on Deformation Characteristics of Geomaterials, IS-Seoul 2011, 1-3 September 2011, Seoul, Korea, IOS Press, 314.

Shen, M., Martin, J. R., Ku, C.-S., and Lu, Y.-C. (2018). "A case study of the effect of dynamic compaction on liquefaction of reclaimed ground." *Engineering Geology*, 240, 48–61.

Shen, Z., Jiang, M., and Thornton, C. (2016). "DEM simulation of bonded granular material. Part I: Contact model and application to cemented sand." *Computers and Geotechnics*, 75, 192–209.

Shi, D., Zhou, J., Xue, J., and Zhang, J. (2010). "A Micro-Mechanical Simulation of Sand Liquefaction Behavior by DEM." *Soil Behavior and Geo-Micromechanics*, 204–211.

Sivathayalan, S., and Vaid, Y. P. (2004). "Cyclic resistance and post liquefaction response of undisturbed in-situ sands." *Proceedings of the 13th world conference on earthquake engineering*.

Skar_zyn´ ski, M., Nitka, M., and Tejchman, J. (2015). "Modelling of concrete fracture at aggregate level using FEM and DEM based on X-ray μCT images of internal structure." *Engineering fracture mechanics*, 147, 13–35.

Šmilauer, V., Catalano, E., Chareyre, B., Dorofeenko, S., Duriez, J., Dyck, N., Eliáš, J., Er, B., Eulitz, A., Gladky, A., Guo, N., Jakob, C., Kneib, F., Kozicki, J., Marzougui, D., Maurin, R., Modenese, C., Scholtès, L., Sibille, L., Stránský, J., Sweijen, T., Thoeni, K., and Yuan, C. (2018). "Yade Documentation 2nd ed."

Šmilauer, V., Catalano, E., Chareyre, B., Dorofeenko, S., Duriez, J., Gladky, A., Kozicki, J., Modenese, C., Scholtès, L., Sibille, L., and others. (2010). "Yade reference documentation." *Yade Documentation*.

Šmilauer, V., and Chareyre, B. (2010). "Yade dem formulation." *Yade Documentation*.

Strack, O. D. L., and Cundall, P. A. (1978). *The distinct element method as a tool for research in granular media*. Department of Civil and Mineral Engineering, University of Minnesota.

Suchorzewski, J., Tejchman, J., and Nitka, M. (2018). "Discrete element method simulations of fracture in concrete under uniaxial compression based on its real internal structure." *International Journal of Damage Mechanics*, 27(4), 578–607.

Susila, E., and Hryciw, R. D. (2003). “Large displacement FEM modelling of the cone penetration test (CPT) in normally consolidated sand.” *International Journal for Numerical and Analytical methods in geomechanics*, 27(7), 585–602.

Teh, C. I., and Houlsby, G. T. (1991). “Analytical study of the cone penetration test in clay.” *Geotechnique*, 41(1), 17–34.

Terzaghi, K. (1951). *Theoretical soil mechanics*. Chapman And Hall, Limited.; London.

Thomas, J. (1992). “Static, cyclic and post liquefaction undrained behaviour of Fraser River sand.” PhD Thesis, University of British Columbia.

Thornton, C. (2000). “Numerical simulations of deviatoric shear deformation of granular media.” *Géotechnique*, 50(1), 43–53.

Tong, A.-T., Catalano, E., and Chareyre, B. (2012). “Pore-scale flow simulations: model predictions compared with experiments on bi-dispersed granular assemblies.” *Oil & Gas Science and Technology–Revue d’IFP Energies nouvelles*, 67(5), 743–752.

Tran, V. T., Donzé, F.-V., and Marin, P. (2011). “A discrete element model of concrete under high triaxial loading.” *Cement and Concrete Composites*, 33(9), 936–948.

Utili, S., and Nova, R. (2008). “DEM analysis of bonded granular geomaterials.” *International Journal for Numerical and Analytical Methods in Geomechanics*, 32(17), 1997–2031.

Vallejos, J. A., Salinas, J. M., Delonca, A., and Mas Ivars, D. (2016). “Calibration and verification of two bonded-particle models for simulation of intact rock behavior.” *International Journal of Geomechanics*, 17(4), 06016030.

Van der Star, W. R. L., Van Wijngaarden, W. K., Van Paassen, L. A., Van Baalen, L. R., and Zwieten, G. (2011). “Stabilization of gravel deposits using microorganisms.” *Proceedings of the 15th European Conference on Soil Mechanics and Geotechnical Engineering, Athens, Greece, 5-9 October 2011*, IOS Press.

Van Paassen, L. A., Daza, C. M., Staal, M., Sorokin, D. Y., van der Zon, W., and van Loosdrecht, M. C. (2010). “Potential soil reinforcement by biological denitrification.” *Ecological Engineering*, 36(2), 168–175.

Vesic, A. S. (1972). “Expansion of cavities in infinite soil mass.” *Journal of Soil Mechanics & Foundations Div*, 98(sm3).

Vinod, J. S., Indraratna, B., and Sitharam, T. G. (2013). “DEM modelling of granular materials during cyclic loading.” *International Conference on Case Histories in Geotechnical Engineering*

Wang, C., Yang, C., Liu, F., Wan, C., and Pu, X. (2012). “Preparation of Ultra-High Performance Concrete with common technology and materials.” *Cement and Concrete Composites*, 34(4), 538–544.

Wang, X., and Li, J. (2014). “Simulation of triaxial response of granular materials by modified DEM.” *Science China Physics, Mechanics & Astronomy*, 57(12), 2297–2308.

Wang, Y. H., and Leung, S. C. (2008a). “Characterization of cemented sand by experimental and numerical investigations.” *Journal of geotechnical and geoenvironmental engineering*, 134(7), 992–1004.

Wang, Y., and Tonon, F. (2009). “Modeling triaxial test on intact rock using discrete element method with membrane boundary.” *Journal of engineering mechanics*, 135(9), 1029–1037.

Wang, Y., and Wang, Y.-L. (2017). “Liquefaction characteristics of gravelly soil under cyclic loading with constant strain amplitude by experimental and numerical investigations.” *Soil Dynamics and Earthquake Engineering*, 92, 388–396.

Wang, Y.-H., and Leung, S.-C. (2008b). “A particulate-scale investigation of cemented sand behavior.” *Canadian Geotechnical Journal*, 45(1), 29–44.

Wei, J., and Wang, G. (2016). “Evolution of fabric anisotropy in cyclic liquefaction of sands.” *Journal of Micromechanics and Molecular Physics*, 1(03n04), 1640005.

Whiffin, V. S., van Paassen, L. A., and Harkes, M. P. (2007). “Microbial carbonate precipitation as a soil improvement technique.” *Geomicrobiology Journal*, 24(5), 417–423.

Widuliński, L., Kozicki, J., and Tejchman, J. (2009). “Numerical simulations of triaxial test with sand using DEM.” *Archives of Hydro–Engineering and Environmental Mechanics*, 56(3–4), 149–172.

Wijewickreme, D., Sriskandakumar, S., and Byrne, P. (2005). “Cyclic loading response of loose air-pluviated Fraser River sand for validation of numerical models simulating centrifuge tests.” *Canadian Geotechnical Journal*, 42(2), 550–561.

Wille, K., and Boisvert-Cotulio, C. (2015). “Material efficiency in the design of ultra-high performance concrete.” *Construction and Building Materials*, 86, 33–43.

Wille, K., Naaman, A. E., and Parra-Montesinos, G. J. (2011). “Ultra-High Performance Concrete with Compressive Strength Exceeding 150 MPa (22 ksi): A Simpler Way.” *Materials Journal*, 108(1), 46–54.

Xiao, P., Liu, H., Xiao, Y., Stuedlein, A. W., and Evans, T. M. (2018). “Liquefaction resistance of bio-cemented calcareous sand.” *Soil Dynamics and Earthquake Engineering*, 107, 9–19.

Xiao, Y., Chen, Z., Zhou, J., Leng, Y., and Xia, R. (2017). “Concrete plastic-damage factor for finite element analysis: Concept, simulation, and experiment.” *Advances in Mechanical Engineering*, 9(9), 1687814017719642.

Xue, J., Zhao, Z., and Shi, J. (2015). “A DEM investigation on simple shear behavior of dense granular assemblies.” *Journal of Central South University*, 22(12), 4844–4855.

Yang, P., Kavazanjian, E., and Neithalath, N. (2018). “Particle-Scale Mechanisms in Undrained Triaxial Compression of Bio-Cemented Sands: Insights from 3D DEM Simulations with Flexible Boundary.” *International Journal of Geomechanics*.

Yang, P., O’Donnell, S., Hamdan, N., Kavazanjian, E., and Neithalath, N. (2016). “3D DEM Simulations of Drained Triaxial Compression of Sand Strengthened Using Microbially Induced Carbonate Precipitation.” *International Journal of Geomechanics*, 17(6), 04016143.

Yi, N.-H., Kim, J.-H. J., Han, T.-S., Cho, Y.-G., and Lee, J. H. (2012). “Blast-resistant characteristics of ultra-high strength concrete and reactive powder concrete.” *Construction and Building Materials*, 28(1), 694–707.

Yoo, D.-Y., and Banthia, N. (2016). “Mechanical properties of ultra-high-performance fiber-reinforced concrete: A review.” *Cement and Concrete Composites*, 73, 267–280.

Yu, H.-S. (2013). *Cavity expansion methods in geomechanics*. Springer Science & Business Media.

Yuan, C., and Chareyre, B. (2017). “A pore-scale method for hydromechanical coupling in deformable granular media.” *Computer Methods in Applied Mechanics and Engineering*, 318, 1066–1079.

Zeghal, M., and El Shamy, U. (2008). “Liquefaction of saturated loose and cemented granular soils.” *Powder Technology*, 184(2), 254–265.

Zeng, C. (2014). “DEM modeling of dense grain shear characteristic in silo.” *Electronic Journal of Geotechnical Engineering*, 19, 7061–7070.

Zhai, C., Wang, X., Kong, J., Li, S., and Xie, L. (2017). “A sophisticated simulation for the fracture behavior of concrete material using XFEM.” *Earthquake Engineering and Engineering Vibration*, 16(4), 859–881.

APPENDIX A

PYTHON SCRIPT FOR SIMULATING UNDRAINED TRIAXIAL COMPRESSION TEST WITH FLEXIBLE MEMBRANE

```
# import corrosponding yade modulus
from yade import pack
from yade import geom
from yade import plot
from yade import ymport
from yade import qt
from yade.gridpfacet import *
import gts, os.path, locale
locale.setlocale(locale.LC_ALL, 'en_US.UTF-8')
#################################################################################
#      A. DEFINING VARIABLES, MATERIALS' PROPERTIES AND PACKING       #
#################################################################################
# A.a). define variables
key = 'Triaxial_Undrained'      # file name to be saved
young=550e6               # normal contact stiffness
compFricDegree = 1.8   # initial contact friction during the confining phase
finalFricDegree = 43      # contact friction during the deviatoric loading
poisson = 0.3               # shear-to-normal stiffness ratio
isoStress = 110000        # confining stress
conStress = 100000        # confining stress for deviatoric loading stage
width = 1.4e-1              # sample width
height = 2.8e-1             # target sample height(after consolidation)
height_0 = 3.2e-1         # initial sample height
num_spheres=1000        # number of spheres
R_p = 0.0084              # mean particle radius
rCoff = 10                  # thickness of top and bot sphere cap (based on rParticle)
rParticle = 0.02e-1       # membrane grid seed size
alpha = 8
rate = 0.1                  # loading rate (strain rate)
damp = 0.3                  # damping coefficient
targetPorosity = 0.43     # target porosity
thresholdvalue = 0.05     # threshold unbalance force
final_rate = 0.1            # strain rate for deviator loading
thresholdstrain = 0.06     # threshold axial strain for terminate
enlargefactor = 1.00

# A.b). create materials for sand spheres and plates
Sand = O.materials.append(CohFrictMat(
        young=young,poisson=poisson,frictionAngle=radians(compFricDegree),
        alphaKr=0.25,alphaKtw=0,etaRoll=0.005,etaTwist=0,
        normalCohesion=5e6,shearCohesion=5e6,
        momentRotationLaw=True,density=2650,label='spheres'
))

# A.c). create membrane materials
```

```
GridMat = O.materials.append(CohFrictMat(
	young=100e6,poisson=0.3,density=2650,frictionAngle=radians(0),
	alphaKr=0,alphaKtw=0,etaRoll=0,etaTwist=0,
	normalCohesion=1e9,shearCohesion=1e9,
	momentRotationLaw=True,label='gridNodeMat'
))
pFacetMat = O.materials.append(FrictMat(
	young=100e6,poisson=0.3,density=2650,frictionAngle=radians(0),label='pFacet
Mat'
))

# A.d). create TOP & BOT plate materials
frictMat = O.materials.append(FrictMat(
	young=100e6,poisson=0.3,density=2650,frictionAngle=radians(0),label='frictMat'
))

#########################################################################
#                          B. DEFINING GLOBAL ENGINES                   #
#########################################################################

#*************************************************************************#
O.engines=[
	ForceResetter(),
	InsertionSortCollider([
		Bo1_Sphere_Aabb(),
		Bo1_PFacet_Aabb(),
		Bo1_Facet_Aabb(),
		Bo1_GridConnection_Aabb()
	]),
	InteractionLoop(
		[
		Ig2_Sphere_Sphere_ScGeom6D(),
		Ig2_GridNode_GridNode_GridNodeGeom6D(),
		Ig2_GridConnection_GridConnection_GridCoGridCoGeom(),
		Ig2_Sphere_PFacet_ScGridCoGeom(),
		Ig2_Facet_Sphere_ScGeom6D()
		],
		[
		Ip2_FrictMat_FrictMat_FrictPhys(),
		Ip2_CohFrictMat_CohFrictMat_CohFrictPhys(label="cohesiveIp")
		],
		[
		Law2_ScGeom_FrictPhys_CundallStrack(),
		Law2_ScGeom6D_CohFrictPhys_CohesionMoment(useIncrementalForm
	=True,always_use_moment_law=False,label='cohesiveLaw'),
```

```
		Law2_GridCoGridCoGeom_FrictPhys_CundallStrack(),
		Law2_ScGridCoGeom_FrictPhys_CundallStrack(),
		],label="iloop"
	),
	GlobalStiffnessTimeStepper(active=1,timeStepUpdateInterval=25,timestepSafety
Coefficient=0.8),
	NewtonIntegrator(gravity=(0,0,0),damping=0.1,label='newton')
]
#*************************************************************************#
O.engines[2].lawDispatcher.functors[1].always_use_moment_law=False
O.engines[2].physDispatcher.functors[1].setCohesionOnNewContacts=False

#########################################################################
#                              C. GENERATING PACKING                    #
#########################################################################
# C.a). generate random dense sphere pack
pred = pack.inCylinder((0,0,0),(0,0,height_0),.5*width)
sp = pack.randomDensePack(
	pred,spheresInCell=num_spheres,radius=R_p,rRelFuzz=0.3,
	returnSpherePack=True,memoDbg=True,memoizeDb='/tmp/loosePackings11.sqli
te'
)
sand=sp.toSimulation(color=(0,1,1),material=Sand)

# C.b). define different sections of sphere pack
bot = [O.bodies[s] for s in sand if O.bodies[s].state.pos[2]<rParticle*rCoff]
top = [O.bodies[s] for s in sand if O.bodies[s].state.pos[2]>height_0-rParticle*rCoff]
tot = [O.bodies[s] for s in sand if O.bodies[s].state.pos[2]<=height_0]

# C.c). detect the position of particles in top & bot layer
top_limit = 0
top_id = 0
for s in top:
	if s.state.pos[2]>=top_limit:
		top_limit = s.state.pos[2]
		top_id = s.id
bot_limit = height_0
bot_id = 0
for s in bot:
	if s.state.pos[2]<=bot_limit:
		bot_limit = s.state.pos[2]
		bot_id = s.id

# C.d). create facet wall around particle packing
facets = []
```

```
nw = 45
nh = 15
rCyl2 = .5*width / cos(pi/float(nw))
for r in xrange(nw):
	for h in xrange(nh):
		v1 = Vector3( rCyl2*cos(2*pi*(r+0)/float(nw)),
rCyl2*sin(2*pi*(r+0)/float(nw)), height_0*(h+0)/float(nh) )
		v2 = Vector3( rCyl2*cos(2*pi*(r+1)/float(nw)),
rCyl2*sin(2*pi*(r+1)/float(nw)), height_0*(h+0)/float(nh) )
		v3 = Vector3( rCyl2*cos(2*pi*(r+1)/float(nw)),
rCyl2*sin(2*pi*(r+1)/float(nw)), height_0*(h+1)/float(nh) )
		v4 = Vector3( rCyl2*cos(2*pi*(r+0)/float(nw)),
rCyl2*sin(2*pi*(r+0)/float(nw)), height_0*(h+1)/float(nh) )
		f1 = facet((v1,v2,v3),color=(0,0,1),material=frictMat)
		f2 = facet((v1,v3,v4),color=(0,0,1),material=frictMat)
		facets.extend((f1,f2))
wall = O.bodies.append(facets)

# C.e). define different sections of facet wall
for b in wall:
	O.bodies[b].state.blockedDOFs = 'xyzXYZ'
	O.bodies[b].state.vel = (0,0,0)

# C.f). create top & bot facet plate
facets3 = []
nw=45
rCyl2 = (.6*width+2*rParticle) / cos(pi/float(nw))
for r in xrange(nw):
	if r%2==0:
		v1 = Vector3( rCyl2*cos(2*pi*(r+0)/float(nw)),
rCyl2*sin(2*pi*(r+0)/float(nw)), height_0 )
		v2 = Vector3( rCyl2*cos(2*pi*(r+1)/float(nw)),
rCyl2*sin(2*pi*(r+1)/float(nw)), height_0 )
		v3 = Vector3( rCyl2*cos(2*pi*(r+2)/float(nw)),
rCyl2*sin(2*pi*(r+2)/float(nw)), height_0 )
		v4 = Vector3( 0, 0, height_0 )
		f1 = facet((v1,v2,v4),color=(0,0,0),material=frictMat)
		f2 = facet((v2,v3,v4),color=(0,0,0),material=frictMat)
		facets3.extend((f1,f2))
topcap = O.bodies.append(facets3)
facets3 = []
for r in xrange(nw):
	if r%2==0:
		v1 = Vector3( rCyl2*cos(2*pi*(r+0)/float(nw)),
rCyl2*sin(2*pi*(r+0)/float(nw)), 0 )
```

```
                v2 = Vector3( rCyl2*cos(2*pi*(r+1)/float(nw)),
rCyl2*sin(2*pi*(r+1)/float(nw)), 0 )
                v3 = Vector3( rCyl2*cos(2*pi*(r+2)/float(nw)),
rCyl2*sin(2*pi*(r+2)/float(nw)), 0 )
                v4 = Vector3( 0, 0, 0 )
                f1 = facet((v1,v2,v4),color=(0,0,0),material=frictMat)
                f2 = facet((v2,v3,v4),color=(0,0,0),material=frictMat)
                facets3.extend((f1,f2))
botcap = O.bodies.append(facets3)

# C.g). define top & bot wall id
for s in topcap:
        top_id = s

bot_id = 0
for s in botcap:
        bot_id = s

# D.h). calculate porosity
V_sand = 0
num_sand = 0
for b in sand:
        r = O.bodies[b].shape.radius
        V_sand += 1.3333333*3.1416*r*r*r
        num_sand +=1
porosity = 1-V_sand/(.25*width*width*3.1416*height_0)

print 'v_sand= ',V_sand,' number of sand: ',num_sand,'porosity is: ',porosity
O.pause()

#############################################################################
#                          D. DEFINING ADD-ON FUNCTIONS                     #
#############################################################################
# D.a). a function for saving variables
def plotAddData():
        f1 = sum(O.forces.f(b)[2] for b in topcap)
        f2 = sum(O.forces.f(b)[2] for b in botcap)
        f11 = sum(O.forces.f(b.id)[2] for b in top)
        f22 = sum(O.forces.f(b.id)[2] for b in bot)
        fa = abs(.5*(f2-f1))
        fa1 = abs(.5*(f22-f11))
        e = (top[0].state.displ()[2] - bot[0].state.displ()[2])/height_0-e_ini
        f4 = 0
        r_cum = 0
        count = 0
```

```
	Area = 0

	for f in membrane_grid:
		f.shape.color = Vector3(0,0,0)
		x = f.state.pos[0]
		y = f.state.pos[1]
		dist = math.sqrt(x*x+y*y)
		n = Vector3(x/dist,y/dist,0)
		z = f.state.pos[2]
		a = 2*3.1416*dist/(360/alpha)*6*rParticle*(1+e)
		if z<=O.bodies[top_id].state.pos[2] and z>=O.bodies[bot_id].state.pos[2]:
			count += 1
			r_local = dist
			r_cum += r_local
	r_avg = r_cum/count-rParticle
	Area = r_avg*2*3.1416*(O.bodies[top_id].state.pos[2] -
O.bodies[bot_id].state.pos[2])
	area_avg = Area/count
	s = fa/(3.1416*r_avg*r_avg)
	s1 = fa1/(3.1416*r_avg*r_avg)
	for b in membrane_grid:
		x = b.state.pos[0]
		y = b.state.pos[1]
		dist = math.sqrt(x*x+y*y)
		n = Vector3(x/dist,y/dist,0)
		a = 2*3.1416*dist/(360/alpha)*6*rParticle*(1+e)
		z = b.state.pos[2]
		if z<=O.bodies[top_id].state.pos[2] and z>=O.bodies[bot_id].state.pos[2]:
			f_local = O.forces.f(b.id)
			length =
math.sqrt(f_local[0]*f_local[0]+f_local[1]*f_local[1]+f_local[2]*f_local[2])
			cos_theta =
(n[0]*f_local[0]+n[1]*f_local[1]+n[2]*f_local[2])/length
			p_normal = (length*cos_theta/a)
			f4 += (p_normal)
	p = abs(f4/count/1000)
	h = O.bodies[top_id].state.pos[2] - O.bodies[bot_id].state.pos[2]
	VV = h*r_avg*r_avg*3.1416
	dV = VV-V_ini
	ev = -((O.bodies[top_id].state.pos[2] -
O.bodies[bot_id].state.pos[2])*r_avg*r_avg*3.1416-V_ini)/V_ini
	er = (r_avg-R_avg)/R_avg
	if (abs(e*100)>thresholdstrain*100):
		O.pause()
```

```
	plot.addData(
		i = O.iter,
		q = (abs(s)-p*1000)/1000,
		q1 = (abs(s1)-conStress)/1000,
		p = p,
		u = conStress/1000-p,
		e = -e*100,
		ev = ev*100,
	)
	for b in tot:
		b.shape.color=scalarOnColorScale(b.state.rot().norm(),0,pi/2.)
	return (dV,e)

# D.b). a function for adding force (servo-controlled of lateral wall)
def addforce():
	h_sample = O.bodies[top_id].state.pos[2] - O.bodies[bot_id].state.pos[2]
	#print 'height is ',h_sample
	r_cum = 0
	count = 0
	f4 = 0
	for b in membrane_grid:
		x = b.state.pos[0]
		y = b.state.pos[1]
		dist = math.sqrt(x*x+y*y)
		n = Vector3(x/dist,y/dist,0)
		a = 2*3.1416*dist/(360/alpha)*6*rParticle*(1+e)
		z = b.state.pos[2]
		if z<=O.bodies[top_id].state.pos[2] and z>=O.bodies[bot_id].state.pos[2]:
			f_local = O.forces.f(b.id)
			length =
math.sqrt(f_local[0]*f_local[0]+f_local[1]*f_local[1]+f_local[2]*f_local[2])
			cos_theta =
(n[0]*f_local[0]+n[1]*f_local[1]+n[2]*f_local[2])/length
			p_normal = (length*cos_theta/a)
			f4 += (p_normal)
			count += 1
	p = abs(f4/count/1000)
	for f in membrane_grid:
		f.shape.color = Vector3(0,0,0)
		x = f.state.pos[0]
		y = f.state.pos[1]
		dist = math.sqrt(x*x+y*y)
		n = Vector3(x/dist,y/dist,0)
		z = f.state.pos[2]
		a = 2*3.1416*dist/(360/alpha)*6*rParticle*(1+e)
```

```
                if z<=O.bodies[top_id].state.pos[2] and z>=O.bodies[bot_id].state.pos[2]:
                        r_local = dist
                        r_cum += r_local
        r_avg = r_cum/count-rParticle
        Volume = r_avg*r_avg*3.1416*h_sample
        delV = Volume - V_ini
        for b in topcap:
                O.bodies[b].state.blockedDOFs = 'xyzXYZ'
                O.bodies[b].state.vel = (0,0,-vel_a)
        for b in botcap:
                O.bodies[b].state.blockedDOFs = 'xyzXYZ'
                O.bodies[b].state.vel = (0,0,vel_a)
        for f in membrane_grid:
                f.shape.color = Vector3(0,0,0)
                x = f.state.pos[0]
                y = f.state.pos[1]
                dist = math.sqrt(x*x+y*y)
                n = Vector3(x/dist,y/dist,0)
                z = f.state.pos[2]
                a = 2*3.1416*dist/(360/alpha)*6*rParticle#*(1+e)
                if z<=O.bodies[top_id].state.pos[2] and z>=O.bodies[bot_id].state.pos[2]:
                        f.state.blocked = 'z'
                        f.state.vel = (dist/h_sample)*vel_a*n
                        if delV>0:
                                f.state.vel = -3.0*(dist/h_sample)*vel_a*n
                        else:
                                f.state.vel = 3.0*(dist/h_sample)*vel_a*n
                else:
                        f.state.vel = 0*n

# D.c). a function for recording data
def checkrecord():
        plot.saveDataTxt('results_'+key)

# D.d). a function used for consolidation
def confining():
        e_ini = (top[0].state.displ()[2] - bot[0].state.displ()[2])/height_0
        f1 = sum(O.forces.f(b)[2] for b in topcap)
        f2 = sum(O.forces.f(b)[2] for b in botcap)
        f4 = 0
        r_cum = 0
        count = 0
        a = 2*3.1416*(.5*width+rParticle)/(360/alpha)*6*rParticle
        for f in membrane_grid:
                f.shape.color = Vector3(0,0,0)
```

```
                x = f.state.pos[0]
                y = f.state.pos[1]
                dist = math.sqrt(x*x+y*y)
                n = Vector3(x/dist,y/dist,0)
                a = 2*3.1416*dist/(360/alpha)*6*rParticle
                z = f.state.pos[2]
                f.state.vel = -vel_ini_r*n
        for b in topcap:
                O.bodies[b].state.blockedDOFs = 'xyzXYZ'
                O.bodies[b].state.vel = (0,0,-vel_ini_a)
        for b in botcap:
                O.bodies[b].state.blockedDOFs = 'xyzXYZ'
                O.bodies[b].state.vel = (0,0,vel_ini_a)
        for b in membrane_grid:
                x = b.state.pos[0]
                y = b.state.pos[1]
                dist = math.sqrt(x*x+y*y)
                n = Vector3(x/dist,y/dist,0)
                a = 2*3.1416*dist/(360/alpha)*6*rParticle
                z = b.state.pos[2]
                if z<=O.bodies[top_id].state.pos[2] and z>=O.bodies[bot_id].state.pos[2]:
                        f_local = O.forces.f(b.id)
                        length =
math.sqrt(f_local[0]*f_local[0]+f_local[1]*f_local[1]+f_local[2]*f_local[2])
                        cos_theta =
(n[0]*f_local[0]+n[1]*f_local[1]+n[2]*f_local[2])/length
                        p_normal = (length*cos_theta/a)
                        f4 += (p_normal)
                        r_cum += dist
                        count += 1
        r_avg = r_cum/count-rParticle
        fa = abs(.5*(f2-f1))
        p_r = f4/count/1000
        p_a = fa/(3.1416*0.25*width*width)/1000
        e_ini2 = ((O.bodies[top_id].state.pos[2] - O.bodies[bot_id].state.pos[2])-
height_0)/height_0
        V_ini = (O.bodies[top_id].state.pos[2] -
O.bodies[bot_id].state.pos[2])*r_avg*r_avg*3.1416
        R_avg = r_avg
        H_ini = O.bodies[top_id].state.pos[2] - O.bodies[bot_id].state.pos[2]
        porosity = 1-V_sand/((R_avg)*(R_avg)*3.1416*H_ini)
        return (p_r,p_a,e_ini,V_ini,R_avg,H_ini,porosity)

# D.e). a function for stablization
def stable():
```

```
	for f in membrane_grid:
		x = f.state.pos[0]
		y = f.state.pos[1]
		dist = math.sqrt(x*x+y*y)
		n = Vector3(x/dist,y/dist,0)
		a = 2*3.1416*dist/(360/alpha)*6*rParticle
		z = f.state.pos[2]
		f.state.blockedDOFs = 'xyzXYZ'
		f.state.vel = 0*n

	for b in topcap:
		O.bodies[b].state.blockedDOFs = 'xyzXYZ'
		O.bodies[b].state.vel = (0,0,0)

	for b in botcap:
		O.bodies[b].state.blockedDOFs = 'xyzXYZ'
		O.bodies[b].state.vel = (0,0,0)
def compress():
	for b in wall:
		O.bodies[b].state.blockedDOFs = 'xyzXYZ'
		O.bodies[b].state.vel = (0,0,0)

#########################################################################
#           E. APPLYING CONFINING STRESS TO FLEXIBLE MEMBRANE           #
#########################################################################
# E.a). adding corrosponding python function
O.engines=O.engines+[
	PyRunner(command='compress()',iterPeriod=1),
	PyRunner(command='plotAddData',iterPeriod=1)
]

# E.b). compress until target porosity
vel_ini_a = rate*height_0
vel_ini_r = rate*height_0
for b in topcap:
	O.bodies[b].state.blockedDOFs = 'xyzXYZ'
	O.bodies[b].state.vel = (0,0,-vel_ini_a)
for b in botcap:
	O.bodies[b].state.blockedDOFs = 'xyzXYZ'
	O.bodies[b].state.vel = (0,0,vel_ini_a)
while 1:
	O.run(100,True)
	h = (O.bodies[top_id].state.pos[2]-O.bodies[bot_id].state.pos[2])
	V = h*0.25*width*width*3.1416
	porosity = 1-V_sand/V
```

```
        print 'porosity: ',porosity, ' height: ', h
        if (porosity <= targetPorosity):
                print 'compression stage finished!'
                break
h_ini = h # record height after compression

# E.c). ADD CONFINING STRESS
# E.c.1). remove facet wall
for b in wall:
        O.bodies.erase(b)

# E.c.2). create membrane around particle packing by reading mesh file
shiftfactor = O.bodies[bot_id].state.pos[2]-((height-h_ini)/2)
nodesIds,cylIds,pfIds =  gtsPFacet(
        'Mesh_cylinder.gts',shift=(0,0,shiftfactor),scale=1,radius=rParticle,wire=False,fix
ed=False,
        materialNodes='gridNodeMat',material='pFacetMat',color=Vector3(0.5,1,0.5)
)

# E.c.3). define different sections of membrane
membrane_grid = [O.bodies[s] for s in nodesIds ]
membrane_pfacet = [O.bodies[s] for s in pfIds]

# E.c.4). run one interaction
for f in membrane_grid:
        f.shape.color = Vector3(0,0,0)
        x = f.state.pos[0]
        y = f.state.pos[1]
        dist = math.sqrt(x*x+y*y)
        n = Vector3(x/dist,y/dist,0)
        z = f.state.pos[2]
        if z<=O.bodies[top_id].state.pos[2] and z>=O.bodies[bot_id].state.pos[2]:
                f.state.vel = -vel_ini_r*n
O.engines[2].physDispatcher.functors[1].setCohesionNow=True
while 1:
        O.run(1,True)
        break

# E.c.5). redefine engine
#*****************************************************************************#
O.engines=[
        ForceResetter(),
        InsertionSortCollider([
                Bo1_Sphere_Aabb(),
                Bo1_PFacet_Aabb(),
```

```
		Bo1_Facet_Aabb(),
		Bo1_GridConnection_Aabb()
	]),
	InteractionLoop(
		[
		Ig2_Sphere_Sphere_ScGeom6D(),
		Ig2_GridNode_GridNode_GridNodeGeom6D(),
		Ig2_GridConnection_GridConnection_GridCoGridCoGeom(),
		Ig2_Sphere_PFacet_ScGridCoGeom(),
		Ig2_Facet_Sphere_ScGeom6D()
		],
		[
		Ip2_FrictMat_FrictMat_FrictPhys(),
		Ip2_CohFrictMat_CohFrictMat_CohFrictPhys(label="cohesiveIp")
		],
		[
		Law2_ScGeom_FrictPhys_CundallStrack(),
		Law2_ScGeom6D_CohFrictPhys_CohesionMoment(useIncrementalForm
	=True,always_use_moment_law=False,label='cohesiveLaw'),
		Law2_GridCoGridCoGeom_FrictPhys_CundallStrack(),
		Law2_ScGridCoGeom_FrictPhys_CundallStrack(),
		],label="iloop"
	),
	GlobalStiffnessTimeStepper(active=1,timeStepUpdateInterval=25,timestepSafety
Coefficient=0.8),
	NewtonIntegrator(gravity=(0,0,0),damping=0.3,label='newton'),
	PyRunner(command='confining()',iterPeriod=1),
	PyRunner(command='plotAddData',iterPeriod=1)
]
#*************************************************************************#

# set final friction angle, enable cohesion
setContactFriction(radians(finalFricDegree))
O.engines[2].lawDispatcher.functors[1].always_use_moment_law=True
O.engines[2].physDispatcher.functors[1].setCohesionNow=True
O.engines[2].physDispatcher.functors[1].setCohesionOnNewContacts=False

# E.c.6). confining
# some initial parameters
p_a = 0
p_r = 0
e_ini = 0
V_ini = 0
R_avg = 0
H_ini = 0
```

```
porosity = 0
# velocity
vel_ini_a = 0.05*rate*height_0
vel_ini_r = 0.05*rate*height_0
# loops (fast-slow) for reaching target confining stress
while 1:
	O.run(10,True)
	(p_r,p_a,e_ini,V_ini,R_avg,H_ini,porosity)=confining()
	p_r = abs(p_r)
	pressure = max(p_r,p_a)
	dif = p_r-p_a
	if (p_a > isoStress/1000):
		vel_ini_a = -abs(vel_ini_a)
		if (p_r > isoStress/1000):
			vel_ini_r = -abs(vel_ini_r)
		else:
			vel_ini_r = abs(vel_ini_r)
	elif (p_a <= isoStress/1000):
		if (p_r > isoStress/1000):
			vel_ini_a = abs(vel_ini_a)
			vel_ini_r = -abs(vel_ini_r)
		else:
			if (pressure<0.9*isoStress/1000):
				if dif > 5:
					vel_ini_a = 1.05*abs(vel_ini_a)
				elif dif < -5:
					vel_ini_r = 1.05*abs(vel_ini_r)
			if (pressure>=0.85*isoStress/1000 and pressure<=isoStress/1000):
				if dif > 1:
					if dif > 5:
						vel_ini_a = 1.5*abs(vel_ini_a)
					else:
						vel_ini_a = 1.01*abs(vel_ini_a)
				elif dif < -1:
					if dif < -5:
						vel_ini_r = 1.5*abs(vel_ini_r)
					else:
						vel_ini_r = 1.01*abs(vel_ini_r)
	mean = (p_r+p_a)/2
	unb=unbalancedForce()
	print 'p= ',p_r,' q= ',p_a,' porosity= ',porosity,' unbalanced force: ',unb
	if abs(isoStress/1000-mean)/(isoStress/1000)<0.15 and abs(dif) <15:
		print 'initial strain: ',e_ini
		print 'initial volume: ',V_ini
		print 'Confining stage I is finished!'
```

```
                break
while 1:
        for f in membrane_grid:
                f.state.blockedDOFs = 'xyzXYZ'
        O.run(1,True)
        (p_r,p_a,e_ini,V_ini,R_avg,H_ini,porosity)=confining()
        p_r = abs(p_r)
        pressure = max(p_r,p_a)
        dif = p_r-p_a
        if (p_a > isoStress/1000):
                vel_ini_a = -abs(vel_ini_a)
                if (p_r > isoStress/1000):
                        vel_ini_r = -abs(vel_ini_r)
                else:
                        vel_ini_r = abs(vel_ini_r)
        elif (p_a <= isoStress/1000):
                if (p_r > isoStress/1000):
                        vel_ini_a = abs(vel_ini_a)
                        vel_ini_r = -abs(vel_ini_r)
                else:
                        if (pressure<0.9*isoStress/1000):
                                if dif > 5:
                                        vel_ini_a = 1.05*abs(vel_ini_a)
                                elif dif < -5:
                                        vel_ini_r = 1.05*abs(vel_ini_r)
                        if (pressure>=0.9*isoStress/1000 and pressure<=isoStress/1000):
                                if dif > 1:
                                        if dif > 5:
                                                vel_ini_a = 1.1*abs(vel_ini_a)
                                        else:
                                                vel_ini_a = 1.01*abs(vel_ini_a)
                                elif dif < -1:
                                        if dif < -5:
                                                vel_ini_r = 1.1*abs(vel_ini_r)
                                        else:
                                                vel_ini_r = 1.01*abs(vel_ini_r)
        mean = (p_r+p_a)/2
        unb=unbalancedForce()
        print 'p= ',p_r,' q= ',p_a,' porosity= ',porosity,' unbalanced force: ',unb
        if abs(isoStress/1000-mean)/(isoStress/1000)<0.05 and abs(dif) <10:
                print 'initial strain: ',e_ini
                print 'initial volume: ',V_ini
                print 'Confining stage II is finished!'
                break
print 'V_ini= ',V_ini
```

```
# E.c.7). stablize
#*************************************************************************#
O.engines=[
	ForceResetter(),
	InsertionSortCollider([
		Bo1_Sphere_Aabb(),
		Bo1_PFacet_Aabb(),
		Bo1_Facet_Aabb(),
		Bo1_GridConnection_Aabb()
	]),
	InteractionLoop(
		[
		Ig2_Sphere_Sphere_ScGeom6D(),
		Ig2_GridNode_GridNode_GridNodeGeom6D(),
		Ig2_GridConnection_GridConnection_GridCoGridCoGeom(),
		Ig2_Sphere_PFacet_ScGridCoGeom(),
		Ig2_Facet_Sphere_ScGeom6D()
		],
		[
		Ip2_FrictMat_FrictMat_FrictPhys(),
		Ip2_CohFrictMat_CohFrictMat_CohFrictPhys(label="cohesiveIp")
		],
		[
		Law2_ScGeom_FrictPhys_CundallStrack(),
		Law2_ScGeom6D_CohFrictPhys_CohesionMoment(useIncrementalForm
	=True,always_use_moment_law=False,label='cohesiveLaw'),
		Law2_GridCoGridCoGeom_FrictPhys_CundallStrack(),
		Law2_ScGridCoGeom_FrictPhys_CundallStrack(),
		],label="iloop"
	),
	GlobalStiffnessTimeStepper(active=1,timeStepUpdateInterval=25,timestepSafety
Coefficient=0.8),
	NewtonIntegrator(gravity=(0,0,0),damping=0.3,label='newton'),
	PyRunner(command='stable()',iterPeriod=1),
	PyRunner(command='plotAddData',iterPeriod=1)
]
#*************************************************************************#
O.engines[2].lawDispatcher.functors[1].always_use_moment_law=True
O.engines[2].physDispatcher.functors[1].setCohesionNow=True
O.engines[2].physDispatcher.functors[1].setCohesionOnNewContacts=False
vel_a = abs(vel_ini_a)
while 1:
	O.run(100,True)
	unb=unbalancedForce()
```

```
	print 'unbalanced force: ',unb
	e_ini = (top[0].state.displ()[2] - bot[0].state.displ()[2])/height_0
	f1 = sum(O.forces.f(b)[2] for b in topcap)
	f2 = sum(O.forces.f(b)[2] for b in botcap)
	f4 = 0
	r_cum = 0
	count = 0
	for b in membrane_grid:
		x = b.state.pos[0]
		y = b.state.pos[1]
		dist = math.sqrt(x*x+y*y)
		n = Vector3(x/dist,y/dist,0)
		a = 2*3.1416*dist/(360/alpha)*6*rParticle#*(1+e)
		z = b.state.pos[2]
		if z<=O.bodies[top_id].state.pos[2] and z>=O.bodies[bot_id].state.pos[2]:
			f_local = O.forces.f(b.id)
			length =
math.sqrt(f_local[0]*f_local[0]+f_local[1]*f_local[1]+f_local[2]*f_local[2])
			cos_theta =
(n[0]*f_local[0]+n[1]*f_local[1]+n[2]*f_local[2])/length
			p_normal = (length*cos_theta/a)
			f4 += (p_normal)
			r_cum += dist
			count += 1
	r_avg = r_cum/count-rParticle
	fa = abs(.5*(f2-f1))
	p_r = f4/count/1000
	p_a = fa/(3.1416*r_avg*r_avg)/1000
	print 'pr=', p_r, ' pa=',p_a
	if unb <= thresholdvalue:
		break
#############################################################################
#                          F. APPLYING DEVIATOR LOADING                     #
#############################################################################
# F.a). redifine engines
O.engines=[
	ForceResetter(),
	InsertionSortCollider([
		Bo1_Sphere_Aabb(aabbEnlargeFactor=enlargefactor),
		Bo1_PFacet_Aabb(),
		Bo1_Facet_Aabb(),
		Bo1_GridConnection_Aabb()
	]),
	InteractionLoop(
		[
```

```
	Ig2_Sphere_Sphere_ScGeom6D(interactionDetectionFactor=enlargefactor),
		Ig2_GridNode_GridNode_GridNodeGeom6D(),
		Ig2_GridConnection_GridConnection_GridCoGridCoGeom(),
		Ig2_Sphere_PFacet_ScGridCoGeom(),
		Ig2_Facet_Sphere_ScGeom6D()
		],
		[
		Ip2_FrictMat_FrictMat_FrictPhys(),
		Ip2_CohFrictMat_CohFrictMat_CohFrictPhys(label="cohesiveIp")
		],
		[
		Law2_ScGeom_FrictPhys_CundallStrack(),
		Law2_ScGeom6D_CohFrictPhys_CohesionMoment(useIncrementalForm
	=True,always_use_moment_law=False,label='cohesiveLaw'),
		Law2_GridCoGridCoGeom_FrictPhys_CundallStrack(),
		Law2_ScGridCoGeom_FrictPhys_CundallStrack(),
		],label="iloop"
	),
	GlobalStiffnessTimeStepper(active=1,timeStepUpdateInterval=25,timestepSafety
Coefficient=0.8),
	NewtonIntegrator(gravity=(0,0,0),damping=0.3,label='newton')
]
O.engines[2].lawDispatcher.functors[1].always_use_moment_law=True
O.engines[2].physDispatcher.functors[1].setCohesionNow=True
O.engines[2].physDispatcher.functors[1].setCohesionOnNewContacts=False
O.engines=O.engines+[
	PyRunner(command='addforce()',iterPeriod=1,label='force'),
	PyRunner(command='plotAddData()',iterPeriod=1,label='recorder'),
	PyRunner(command='checkrecord()',realPeriod=10,label='checker')
]

# F.b). define the velocity of membrane walls to maintain the volume constant condition
vel_a = final_rate*abs(vel_ini_a)
vel_r = vel_a*.5*width/height
Vel_r = vel_r
conStress = p_r*1000
###############################################################################
#                                   G. UTILITIES                              #
###############################################################################
# G.a). time step (recommanded by YADE)
O.dt=0.3*PWaveTimeStep()
t = O.dt

# G.b). funtion for plot
```

```
plot.plots={'e':('q','p'),'e':('u','ev')}
plot.plot()
O.saveTmp()
O.timingEnabled=1
###########################################################################
#                                   G. RUN                                #
###########################################################################
print '========================='
print "start triaxial simulation"
print '========================='
O.run()
```